Cross-Spectral Analysis For Spatial Point-Lattice Processes

Thesis

UNRESTRICTED

Cross-Spectral Analysis for Spatial Point-Lattice Processes

Mona Kanaan, B.Sc., Dip.[1]
Submitted for the Degree of Doctor of Philosophy
Department of Statistics
Faculty of Mathematics and Computing
The Open University

January 24, 2000

[1]M.N.Kanaan@open.ac.uk

Abstract

In this study, we explore the relationship between the components of a hybrid process consisting of a spatial point process and a lattice process using two-dimensional spectral techniques. Simulated spatial point-lattice patterns are used to demonstrate how the different cross-spectral statistics can reveal correlation between the two components. A method to adjust for jumps that normally occur in the cross-spectral phase statistic is then proposed. Such adjustment is needed to enable us to calculate the slope of the phase spectrum which measures the shift between the two components. Several methods to calculate the slope are investigated. Asymptotic properties of the cross-spectral statistics are derived and their confidence intervals estimated. A test that the components are independent is described.

In a study region, lattice processes are observed at regular grids whereas point processes can be observed anywhere. In order to account for discrepancies that might arise due to this, methods to discretise the point pattern are suggested. Cross-spectral techniques are then applied to analyse the joint process of the discretised point pattern and the lattice pattern.

Finally, we apply the techniques suggested above to study the joint properties of two data sets. The first consists of altitude data of a region in a rain forest in French Guyana together with the locations of a number of tree species in that region. The second set consists of altitude data of the Sahel region of Africa together with location of storms and some of their characteristics. In order to incorporate the storm characteristics in the analysis, cross-spectral tools used to analyse two components are extended to three components.

إهداء الى الراحل الغالي والدي

In Living Memory of My Father

Acknowledgements

I would like to thank my supervisors Paul Taylor and Moira Mugglestone for their support during the last three years. I would like to thank Paddy Farrington for his comments on parts of earlier drafts of this thesis. I would also like to thank my examiners Chris Glasbey and Kevin McConway for their useful comments. Thanks are also due to members of the Department of Statistics at The Open University, in particular to my officemate Jane Warwick.

I would like to thank Michel Goulard, Hélène Dessard and Menghestab Haile for providing the data.

Financial support from The Open University is gratefully acknowledged. Thanks are also due to the Karim Rida Said Foundation for funding my studies at the University of Cambridge.

For moral support I am indebted to my mother Hana Kanaan and my sister Nana and brothers Hasan and Walid. Last but not least, my thanks and gratitude go to Bambos Pattichis for moral and emotional support.

Preface

The relationship between a spatial point process and a lattice process is explored in this study using two-dimensional cross-spectral techniques.

In Chapter 1, we review techniques used to study the individual processes. First- and second-order properties in the spatial and frequency domain for both processes are studied. Estimates and distributional properties of the auto-spectral functions, which represent the frequency domain statistics, are discussed. The estimate of the auto-spectrum, the periodogram, is known not to be consistent. To overcome this undesirable property smoothing techniques are used. Completely spatially random models and possible alternatives are examined. A test for complete spatial randomness based on the maximum periodogram ordinate is also reviewed. A number of simulated examples are provided.

A hybrid process consisting of two components, a spatial point process and a lattice process, is introduced in Chapter 2. We refer to this hybrid process as a spatial point-lattice process. Second-order properties in the spatial and frequency domains are proposed for this hybrid process. By analogy with multivariate time series, see Priestley (1981a), and spatial bivariate point processes, see Mugglestone and Renshaw (1996b), estimates in the frequency domain, known as cross-spectra, are suggested. These estimates are based on the discrete Fourier transforms of both components. A completely spatially random point-lattice process is then introduced. Methods to simulate associated spatial point-lattice processes are also given. Cross-spectral

techniques are then applied to investigate the relationships between the two components of simulated examples.

Several statistics are usually investigated under the flag of cross-spectral analysis. A statistic that is of interest is the slope of the phase spectrum which measures the magnitude and direction of the shift (if it exists) between the two components. However, in most cases the phase spectrum contains several jumps due to the restriction that its values should belong to the interval $(-\pi, \pi)$. A method which extends the one-dimensional adjustment for the phase spectrum of multivariate time series is provided in Chapter 3. Furthermore, methods to calculate the slope of the phase spectrum are supplied. These techniques are then applied to find the slopes of the phase spectra for some of the examples of Chapter 2.

Asymptotic properties of the spectral estimates are derived in Chapter 4. In addition, confidence intervals for these estimates are established. A test for the independence between the two components is given. The test is based on the coherency spectrum and extends the zero coherency test of multivariate time series. Confidence intervals and the zero test for some of the examples in Chapter 2 are also calculated.

In Chapter 5, we investigate a number of methods to discretise the point pattern. This discretisation is suggested in order to account for artefacts that might arise because lattice processes are observed at regular grids whereas events of point processes can be observed at any location in a region. Cross-spectral techniques are then used to study the correlation between the discretised point pattern and the lattice pattern. This approach is then used for some of the examples of Chapter 2.

Chapters 6 and 7 use the suggested cross-spectral techniques to explore the relationships between the components of two data sets. The first data set, the subject of Chapter 6, consists of altitude data of a region in a rain forest in French Guyana together with the locations of a number of tree species in that region. In this chapter, we study in detail the relationship between the altitude data and four of the species. The analyses for the other species versus altitude are provided in Appendix D. The second data set, which is presented in Chapter 7, consists of altitude data of the Sahel region of Africa together with the locations of storms and some of their characteristics. To incorporate the storm characteristics in our study we extend cross-spectral techniques of two components to three components.

General conclusions and suggestions for further research in this area are supplied in Chapter 8. Some appendices are also supplied.

The computations for this thesis were carried out using predominantly my own computer code written for the Splus statistical package and some locally available libraries mmspatial and wanddensity.

Contents

Chapter 1

Point and Lattice Processes: A Summary

In this chapter, we give a summary of point and lattice processes and their properties. In Section 1.1, a brief introduction to point and lattice processes is given. Spatial domain properties of these processes are discussed in Sections 1.2 and 1.3, while frequency domain properties are examined in Section 1.4. The special case of isotropy is reviewed in Section 1.5. The spectral estimates for point and lattice processes and their distributional properties are studied in Sections 1.6 and 1.7. Smoothing techniques for spectral estimates are investigated in Section 1.8. Models for point and lattice processes are discussed in Sections 1.9, 1.10 and 1.11. A formal test based on maximum periodogram ordinates is reviewed in Section 1.12. Examples to illustrate the use of spectral estimates are provided in Section 1.13.

1.1 Spatial Data: Introduction

In this section, we review basic definitions and terminology used for spatial point and lattice processes.

A *spatial point pattern* is a set of locations in the two-dimensional space within a given region, where events have occurred of particular interest to the researcher, for example locations of oak trees at Sherwood forest. We refer to these locations as events and to the region of interest as the study region. The process that generates the point pattern is known as the point process. Several methods are used to analyse the spread of events in the study region, including the following.

- *Distance* methods are based on summaries of distances between either a pair of events or an event and an arbitrary point in the study region. These distances can be used to detect clustering or inhibition of a point pattern. They are discussed by many authors such as Ripley (1981, chapter 8), Diggle (1983, chapter 5) and Upton and Fingleton (1995, chapter 2).

- *Two-dimensional spectral* methods measure spatial periodicities in the data. They have been discussed by, for example, Bartlett (1964), Ripley (1981), Renshaw and Ford (1983) and Mugglestone and Renshaw (1996b). These methods are extensions of one-dimensional spectral methods for point processes (see Bartlett, 1963; Brillinger, 1972; Brillinger, 1981).

A *spatial lattice pattern* is a set of quantitative measurements recorded on a regular lattice, for example measurements of soil fertility for a given area taken at regular spacings in an agricultural study. In general, these patterns arise in planned agricultural trials and in satellite imaging. The process that generates a lattice pattern is called a lattice process. Analysis of a lattice

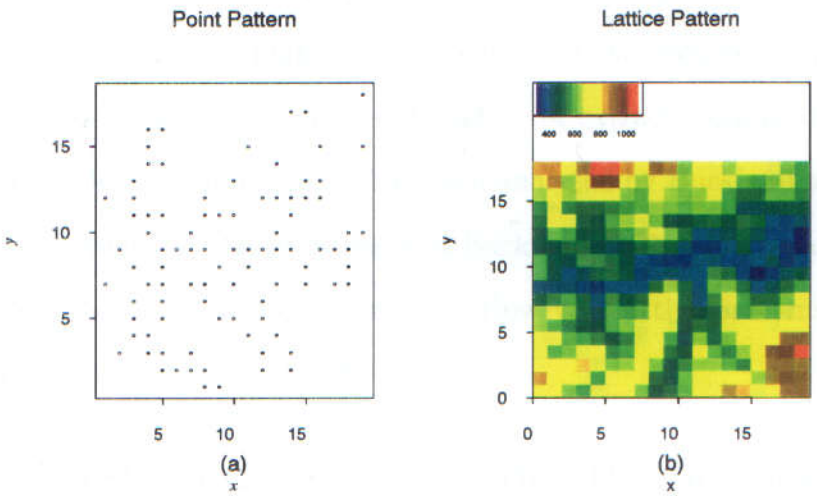

Figure 1.1: Spatial patterns: (a) point pattern represents the red deer occurrence in the Grampian region; (b) lattice pattern is the altitude data of the study region.

process is provided via either a spatial domain approach using *spatial auto-correlation* or a frequency domain approach using *spectral analysis*. Spatial auto-correlation methods measure correlation between measurements at pairs of sites (see Upton and Fingleton, 1995; Cliff and Ord, 1981).

The above terminology is by analogy with time series analysis. Time series analysis in the frequency domain has been studied extensively by many authors such as Rayner (1971, chapter 7), Brillinger (1981, chapter 5), Chatfield (1981, chapter 6), Priestley (1981a, chapter 6) and Diggle (1990, chapter 4). Frequency domain analysis of lattice processes has been discussed by Rayner (1971, chapter 9), Priestley (1981b, chapter 9), Ripley (1981, chapter 5), Renshaw and Ford (1983), Ford and Renshaw (1984) and Mugglestone (1990).

Examples of spatial point and lattice patterns are given in Figure 1.1. The

lattice pattern represents the altitude within a subregion of the Grampian region of Scotland. The point pattern represents the occurrence of red deer within a given grid square. This data set is an extract from data collected by the Red Deer Commission. It has been analysed by Buckland and Elston (1993) and Augustin, Mugglestone and Buckland (1996). So point patterns arise if interest is in locations of events. However, lattice patterns relate to measurements made at grid sites.

1.2 First- and Second-Order Properties in the Spatial Domain

Fundamental functions that describe first- and second-order properties of point and lattice processes in the spatial domain are reviewed in this section.

Consider a point process, say X. The realisation of X is a set of locations of events within a study region. The study region is usually denoted by Ω. In most cases, Ω is assumed to be a rectangular region $[0, \ell_1] \times [0, \ell_2]$, and in this study it is assumed that ℓ_1 and ℓ_2 are integers. The number of events in a region R is denoted by $N_X(R)$. For brevity $N_X(\Omega)$ will usually be written as N_X. The locations of events within Ω will be denoted by $\mathbf{a_j} = (a_{1j}, a_{2j})$ for $j = 1, \ldots, N_X$. Note that vectors will be assumed to be row vectors. Furthermore, the process X is assumed to be orderly, that is only one event is allowed at any location. The *first-order intensity* function for this process is defined as (see Diggle, 1983),

$$\lambda_N(\mathbf{a}) = \lim_{|d\mathbf{a}| \to 0} \left\{ \frac{\mathbb{E}(dN_X(\mathbf{a}))}{|d\mathbf{a}|} \right\} (\mathbf{a} \in \mathbb{R}^2). \tag{1.1}$$

Here $dN_X(\mathbf{a}) = N_X(\mathbf{a} + d\mathbf{a}) - N_X(\mathbf{a})$ is the number of events within a small

neighbourhood of point $\mathbf{a}$, and $|d\mathbf{a}|$ denotes the area of this neighbourhood following the notation of Bartlett (1964). Note here that we will subscript functions summarising the point process by N rather than by X since first- and second-order properties are derived in terms of the number of events.

The *auto-covariance* function is defined as

$$\begin{aligned}\gamma_{NN}(\mathbf{a}_1, \mathbf{a}_2) &= \lim_{|d\mathbf{a}_1|,|d\mathbf{a}_2|\to 0} \left\{ \frac{\mathbb{E}([dN_X(\mathbf{a}_1) - \mathbb{E}(dN_X(\mathbf{a}_1))][dN_X(\mathbf{a}_2) - \mathbb{E}(dN_X(\mathbf{a}_2))])}{|d\mathbf{a}_1||d\mathbf{a}_2|} \right\}, \\ &= \lim_{|d\mathbf{a}_1|,|d\mathbf{a}_2|\to 0} \left\{ \frac{\mathbb{E}(dN_X(\mathbf{a}_1)\, dN_X(\mathbf{a}_2))}{|d\mathbf{a}_1||d\mathbf{a}_2|} \right\} - \lambda_N(\mathbf{a}_1)\lambda_N(\mathbf{a}_2), \\ &\equiv \lambda_{NN}(\mathbf{a}_1, \mathbf{a}_2) - \lambda_N(\mathbf{a}_1)\lambda_N(\mathbf{a}_2) \quad (\mathbf{a}_1 \neq \mathbf{a}_2; \mathbf{a}_1, \mathbf{a}_2 \in \mathbb{R}^2). \end{aligned} \tag{1.2}$$

The function λ_{NN} is known as the *second-order intensity* function. Since the process is orderly we have $\Pr[dN_X(\mathbf{a}) > 1] \to 0$ as $|d\mathbf{a}| \to 0$. Therefore, as $|d\mathbf{a}| \to 0$, $\mathbb{E}(\{dN_X(\mathbf{a})\}^2) = \Pr[dN_X(\mathbf{a}) = 1] = \mathbb{E}\{dN_X(\mathbf{a})\} \approx \lambda_N(\mathbf{a})|d\mathbf{a}|$, see (1.1). Bartlett (1964) includes this term in the *complete covariance density* function, $\kappa(\mathbf{a}_1, \mathbf{a}_2)$, defined as

$$\kappa_{NN}(\mathbf{a}_1, \mathbf{a}_2) = \lambda_N(\mathbf{a}_1)\delta(\mathbf{a}_1 - \mathbf{a}_2) + \gamma_{NN}(\mathbf{a}_1, \mathbf{a}_2), \tag{1.3}$$

where $\delta(z)$ denotes the Dirac delta function, see Section A.2.

Now consider a lattice process $Y = \{Y_{\mathbf{b}}, \text{ for } \mathbf{b} \in \mathbb{R}^2\}$, where $Y_{\mathbf{b}}$ represents a measurement made at $\mathbf{b}$. Usually $\mathbf{b}$ is taken to belong to a subset of $\mathbb{Z}^2$, and measurements made at $Y_{\mathbf{b}} = Y_{(b_1,b_2)}$ are usually associated with the grid square $[b_1, b_1 + 1] \times [b_2, b_2 + 1]$. The term quadrat will usually be used to denote a particular grid square. The first-order moment of a lattice process is summarised by the mean $\mu_Y = \mathbb{E}[Y]$. The auto-covariance function of a lattice process is given by $\gamma_{YY}(\mathbf{b}_1, \mathbf{b}_2) = \mathrm{Cov}\,(Y_{\mathbf{b}_1}, Y_{\mathbf{b}_2})$. In what follows, lattice processes will be corrected for their means.

1.3 Stationarity

In general, a process is *stationary* if all probability statements about the process within a finite region $\Omega \subset \mathbb{R}^2$ are invariant under translations of that region. Stationarity is a fundamental assumption for deriving theoretical properties in the frequency domain. Often this assumption is relaxed and a weaker requirement is allowed. A process is said to be *weakly stationary* if both the original and translated processes possess the same moments up to order k (see Priestley, 1981a). In what follows, *second-order stationarity* will be assumed, unless otherwise stated. For brevity, we will use the term stationarity to indicate second-order stationarity.

For a point process, stationarity implies that the intensity function, $\lambda_N(\mathbf{a})$, is constant throughout the region and the auto-covariance function depends on $\mathbf{a}_1$ and $\mathbf{a}_2$ only through their difference, $\mathbf{c} = \mathbf{a}_1 - \mathbf{a}_2$. Therefore, (1.2) and (1.3) reduce to the following equations, respectively,

$$\gamma_{NN}(\mathbf{a}_1, \mathbf{a}_2) = \gamma_{NN}(\mathbf{a}_1 - \mathbf{a}_2) = \gamma_{NN}(\mathbf{c}) = \lambda_{NN}(\mathbf{c}) - \lambda_N^2,$$
$$\kappa_{NN}(\mathbf{a}_1, \mathbf{a}_2) = \kappa_{NN}(\mathbf{c}) = \lambda_N \delta(\mathbf{c}) + \gamma_{NN}(\mathbf{c}). \tag{1.4}$$

Stationarity for a lattice process Y implies that

$$\begin{aligned} \mathbb{E}[Y] &= \mu_Y, \text{ a constant for all } \mathbf{b}, \\ \mathrm{Var}(Y_{\mathbf{b}}) &= \sigma_{YY}^2, \text{ a constant for all } \mathbf{b}, \\ \text{and } \mathrm{Cov}\,(Y_{\mathbf{b}+\mathbf{c}}, Y_{\mathbf{b}}) &= \gamma_{YY}(\mathbf{c}). \end{aligned}$$

However, the assumption that the lattice process is corrected for its mean implies that $\mu_Y = 0$. Hence, $\gamma_{YY}(\mathbf{c}) = \mathbb{E}[Y_{\mathbf{b}+\mathbf{c}} Y_{\mathbf{b}}]$.

1.4 Spectral Density Function

The *spectral density function* (or spectrum) for a stationary spatial point process is defined as the Fourier transform of the complete auto-covariance function (see Bartlett, 1964; Mugglestone and Renshaw, 1996a; Mugglestone and Renshaw, 1996b). Hence, the auto-spectral density function for process X at frequency $\boldsymbol{\omega}$ is given by

$$\begin{aligned} f_{NN}(\boldsymbol{\omega}) &= \int \kappa_{NN}(\mathbf{c}) \exp\{-i\boldsymbol{\omega}\mathbf{c}^{\top}\} d\mathbf{c} \\ &= \lambda_N + \int \gamma_{NN}(\mathbf{c}) \exp\{-i\boldsymbol{\omega}\mathbf{c}^{\top}\} d\mathbf{c} \quad \text{for} \quad \boldsymbol{\omega} \in \mathbb{R}^2, \end{aligned} \tag{1.5}$$

where $i = \sqrt{-1}$ and $x^{\top}$ denotes the transpose of x. The inverse of (1.5) is given by

$$\kappa_{NN}(\mathbf{c}) = \frac{1}{(2\pi)^2} \int f_{NN}(\boldsymbol{\omega}) \exp\{i\boldsymbol{\omega}\mathbf{c}^{\top}\} d\boldsymbol{\omega}.$$

Similarly, for a stationary lattice process Y the auto-spectral density function is defined by

$$f_{YY}(\boldsymbol{\omega}) = \begin{cases} \sum_{\mathbf{h}} \gamma_{YY}(\mathbf{h}) \exp\{-i\boldsymbol{\omega}\mathbf{h}^{\top}\} & \text{if } \mathbf{h} \in \mathbb{Z}^2, \\ \int \gamma_{YY}(\mathbf{h}) \exp\{-i\boldsymbol{\omega}\mathbf{h}^{\top}\} d\mathbf{h} & \text{if } \mathbf{h} \in \mathbb{R}^2. \end{cases} \tag{1.6}$$

It is worth remarking here that the normalised spectral density function $f_{YY}(\boldsymbol{\omega})d\boldsymbol{\omega}/\sigma_Y^2$, where σ_Y^2 is the variance of the process Y, can be interpreted as the average of the proportion of the total *power* contributed by components with frequencies between $\boldsymbol{\omega}$ and $\boldsymbol{\omega} + d\boldsymbol{\omega}$ by analogy with time series analysis (see Priestley, 1981a, chapter 4).

1.5 Isotropy

A process is said to be *isotropic* if the statistical properties of the process are invariant under rotations. For stationary and isotropic processes the

covariance function depends only on the scalar distance between $\mathbf{a}_1$ and $\mathbf{a}_2$, namely $||\mathbf{a}_1 - \mathbf{a}_2|| = ||\mathbf{c}|| = \sqrt{c_1^2 + c_2^2} = t$. Therefore, the spectral density function of a stationary isotropic point process reduces to

$$f_{NN}(\boldsymbol{\omega}) \equiv f_{NN}(\omega) = \lambda_N + 2\pi \int_0^\infty t\gamma_{NN}(t)J_0(t\omega)dt,$$

where $\omega = \sqrt{\omega_x^2 + \omega_y^2}$ and $J_0(x) = (2\pi)^{-1}\int_{-\pi}^{\pi} \exp\{-ix\sin u\}du$ is an unmodified Bessel function of the first kind of order zero. Similarly, for a stationary isotropic lattice process the spectral function is given by

$$f_{YY}(\boldsymbol{\omega}) \equiv f_{YY}(\omega) = 2\pi \int_0^\infty t\gamma_{YY}(t)J_0(t\omega)dt,$$

where $J_0(x)$ is as defined above.

1.6 Estimation of Spectral Functions

1.6.1 Auto-periodogram of a Point Pattern

Let $X = \{(a_{1j}, a_{2j}); j = 1, \ldots, N_X\}$ denote the set of events within a rectangular study region $\Omega = [0, \ell_1] \times [0, \ell_2]$. An estimate for the auto-spectral function, the *auto-periodogram*, is given in terms of the discrete Fourier transform (DFT) of the co-ordinates of the point process as

$$F_{NN}(\boldsymbol{\omega}_N) \equiv F_{NN}(\omega_p, \omega_q)_N = F_N(p,q)\overline{F}_N(p,q), \text{ where} \tag{1.7}$$

$$\begin{aligned} F_N(p,q) &= A_N(p,q) + iB_N(p,q) \\ &= \frac{1}{\sqrt{\ell_1\ell_2}} \sum_{j=1}^{N_X} \exp\{-2\pi i(pa_{1j} + qa_{2j})/N_X\} \qquad (1.8) \\ &= \frac{1}{\sqrt{\ell_1\ell_2}} \sum_{j=1}^{N_X} \exp\{-i\boldsymbol{\omega}_N \mathbf{a}_j^\top\}, \end{aligned}$$

where $\boldsymbol{\omega}_N = (\omega_p, \omega_q)_N = (2\pi p/N_X, 2\pi q/N_X)$ and $p = 0, \pm 1, \pm 2, \ldots$; $q = 0, \pm 1, \pm 2, \ldots$. Although in principle $F_{NN}(\boldsymbol{\omega}_N)$ can be calculated for all $\boldsymbol{\omega}_N \in$

$\mathbb{R}^2$, it is evaluated only at the frequencies $(\omega_p, \omega_q)_N$ defined above, by analogy with time series analysis (see Priestley, 1981a, chapter 6). The range of frequencies is usually limited by the data analysed.

If X is a homogeneous Poisson process, see Section 1.9.1 for definition, then the bias $B(\boldsymbol{\omega}_N)$ of the estimate $F_{NN}(\boldsymbol{\omega}_N)$ is given by Mugglestone (1990) as

$$B(\boldsymbol{\omega}_N) = 2\ell_1\ell_2\lambda_N^2 \left[\frac{\sin(\frac{\ell_1\omega_p}{2})}{\frac{\ell_1\omega_p}{2}} \times \frac{\sin(\frac{\ell_2\omega_q}{2})}{\frac{\ell_2\omega_q}{2}} \right]^2 . \tag{1.9}$$

This result is an extension of the one-dimensional case which was given by Bartlett (1963). A detailed derivation for the one-dimensional case is given by Cox and Lewis (1968). Computing the bias term gives

$$B(\boldsymbol{\omega}_N) = \begin{cases} 0 & \text{for } \boldsymbol{\omega}_N \text{ or one of its components a non-zero multiple of } 2\pi, \\ 2\ell_1\ell_2\lambda_N^2 & \text{for } \boldsymbol{\omega}_N \to 0, \\ < 2\ell_1\ell_2\lambda_N^2 & \text{otherwise.} \end{cases}$$

Hence, the bias is maximum near zero frequencies. For processes other than the Poisson process the bias does not usually have an explicit representation such as (1.9). However, it is possible to show that the bias is maximum for $\boldsymbol{\omega}_N = 0$ (see Cox and Lewis, 1968, chapter 5). To eliminate the bias near zero, Bartlett (1964) suggests that the co-ordinates be standardised by replacing a_{1j} and a_{2j} by $a'_{1j} = N_X a_{1j}/\ell_1$ and $a'_{2j} = N_X a_{2j}/\ell_2$. Also, if the periodogram values are not standardised they will start to repeat after N_X

rows and/or columns. Using the above standardisation (1.8) reduces to

$$\begin{aligned}\tilde{F}_N(p,q) &= \sum_{j=1}^{N_X} \exp\{-2\pi i(pa_{1j}^* + qa_{2j}^*)\} \\ &= \sum_{j=1}^{N_X} \exp\{-2\pi i(\frac{pa_{1j}}{\ell_1} + \frac{qa_{2j}}{\ell_2})\} \\ &= \sum_{j=1}^{N_X} \exp\{-i(\boldsymbol{\omega}\mathbf{a}_j^\top)\},\end{aligned} \tag{1.10}$$

where $(a_{1j}^*, a_{2j}^*) = (\frac{a_{1j}}{\ell_1}, \frac{a_{2j}}{\ell_2})$ and $\boldsymbol{\omega} = (\omega_p, \omega_q) \equiv (\frac{2\pi p}{\ell_1}, \frac{2\pi q}{\ell_2})$. Moreover, the DFTs of the standardised and original processes are related as follows,

$$\begin{aligned}\tilde{F}_N(p,q) &= \sum_{j=1}^{N_X} \exp\{-2\pi i(pa_{1j}/\ell_1 + qa_{2j}/\ell_2)\} \\ &= \sqrt{\ell_1\ell_2} \times \\ &\qquad \left\{ \frac{1}{\sqrt{\ell_1\ell_2}} \sum_{j=1}^{N_X} \exp\{-2\pi i N_X^{-1}((pN_X/\ell_1)a_{1j} + (qN_X/\ell_2)a_{2j})\} \right\} \\ &= \sqrt{\ell_1\ell_2} F_N(pN_X/\ell_1, qN_X/\ell_2) \\ &= \sqrt{\ell_1\ell_2} F_N(p',q').\end{aligned}$$

Therefore,

$$\begin{aligned}\tilde{F}_{NN}(\boldsymbol{\omega}) \equiv \tilde{F}_{NN}(\omega_p,\omega_q) &= \tilde{F}_N(p,q)\overline{\tilde{F}}_N(p,q) \\ &= \ell_1\ell_2 \times F_N(p',q')\overline{F}(p',q') \\ &= \ell_1\ell_2 F_{NN}(\omega_{p'},\omega_{q'})_N,\end{aligned}$$

where $(\omega_p, \omega_q) = (\frac{2\pi p}{\ell_1}, \frac{2\pi q}{\ell_2})$ and $(\omega_{p'}, \omega_{q'})_N = (\frac{2\pi p N_X}{N_X \ell_1}, \frac{2\pi q N_X}{N_X \ell_2})$. Therefore, $(\omega_p, \omega_q) = (\omega_{p'}, \omega_{q'})_N$. Hence, Bartlett's standardisation not only eliminates the bias near zero but rescales the periodogram as well.

1.6.2 Auto-periodogram of a Lattice Pattern

For a lattice pattern, $Y = \{Y_{(b_1,b_2)}, (b_1 = 0, \ldots, \ell_1 - 1; b_2 = 0, \ldots, \ell_2 - 1)\}$, corrected for its mean, the auto-spectral function can be estimated in terms of the DFT of the process Y by $F_{YY}(\boldsymbol{\omega}) \equiv F_{YY}(\omega_p, \omega_q) = F_Y(p,q)\overline{F}_Y(p,q)$, where

$$\begin{aligned} F_Y(p,q) &= A_Y(p,q) + iB_Y(p,q) \\ &= \frac{1}{\sqrt{\ell_1 \ell_2}} \sum_{b_1=0}^{\ell_1-1} \sum_{b_2=0}^{\ell_2-1} Y_{(b_1,b_2)} \exp\{-2\pi i(\frac{pb_1}{\ell_1} + \frac{qb_2}{\ell_2})\}, \end{aligned} \tag{1.11}$$

with $p = 0, \ldots, \ell_1 - 1$; $q = 0, \ldots, \ell_2 - 1$ and (ω_p, ω_q) defined as before. Since $Y_{(b_1,b_2)}$ is evaluated at integer values only then the highest resolvable frequency, the *Nyquist frequency*, occurs when $p = [\ell_1 - 1]/2$ and $q = [\ell_2 - 1]/2$; here $[c]$ is the greatest integer less than or equal to c. The Nyquist frequency arises since we cannot distinguish between $\exp\{-i(\omega_p b_1 + \omega_q b_2)\}$ and $\exp\{-i([\omega_p + 2k\pi]b_1 + [\omega_q + 2k\pi]b_2)\}$ for integer values (b_1, b_2). Hence, frequencies outside the range $\mathbb{I} = (-\pi, \pi) \times (-\pi, \pi)$ are *aliased* to those inside $\mathbb{I}$. If the dimensions of the study region are highly composite then (1.11) can be estimated efficiently using the fast Fourier transform (FFT), see Brigham (1988, chapters 8 and 11) for more details.

The periodogram is estimated in terms of the DFT of the process itself rather than its auto-covariance function. However, it can be established that the two procedures are equivalent. The equivalence in the time series case is established by Priestley (1981a, chapter 6). In fact, calculating the periodogram directly from the DFT of the lattice process minimises difficulties such as round-off errors that might arise when computing the periodogram from the auto-covariance function. The latter approach would re-

quire calculating the auto-covariance function first and then taking its DFT (see Renshaw and Ford, 1983).

1.6.3 Symmetry of Periodograms

All the periodograms that have been studied exhibit a kind of symmetry. For both point and lattice processes, we have

$$F_{ss}(\omega_{-p}, \omega_{-q}) = F_{ss}(\omega_p, \omega_q) = F_{ss}(-\omega_p, -\omega_q) \text{ and}$$

$$F_{ss}(\omega_{-p}, \omega_q) = F_{ss}(\omega_p, \omega_{-q}) = F_{ss}(-\omega_p, \omega_q) = F_{ss}(\omega_p, -\omega_q),$$

where $s = N$ or Y. Moreover, for a lattice process $F_{YY}(\omega_{\ell_1-p}, \omega_q) = F_{YY}(\omega_p, \omega_{\ell_2-q})$, thus, a suitable form in which to output the lattice periodogram is a matrix with $p = 0, \ldots, [\ell_1/2]$ and $q = -[\ell_2/2], \ldots, [(\ell_2 - 1)/2]$ (see Renshaw and Ford, 1983).

Therefore, one of the frequencies, say p, needs only to vary over positive values, whereas the other, q, varies over both negative and positive values. In what follows, periodograms are usually evaluated at the frequencies $(\omega_p, \omega_q) = (2\pi p/\ell_1, 2\pi q/\ell_2)$ for $p = 0, \ldots, [\ell_1/2]$ and $q = -[\ell_2/2], \ldots, [(\ell_2 - 1)/2]$.

1.7 Distributional Properties of Auto-Spectral Estimates

In this section, we summarise the distributional properties for the auto-spectral estimates. Sampling properties of point spectra have been studied by Bartlett (1964) and Mugglestone (1990), whereas those of lattice spectra have been studied by Grenander and Rosenblatt (1957) and Ripley (1981).

These results are mainly extensions of the one-dimensional cases. The one-dimensional sampling properties of point spectra have been studied by Cox and Lewis (1968) and Brillinger (1972), whereas those of time series have been studied by Priestley (1981a, chapter 6). Note that the results given below hold asymptotically, that is as ℓ_1, ℓ_2 and $N_X \to \infty$.

For a stationary point process, X, it can be shown that the real, $A_N(p,q)$, and imaginary, $B_N(p,q)$, parts of the DFT of X (defined in (1.8)) are asymptotically distributed as $N(0, f_{NN}(p,q)/2)$ for $(p,q) \neq (0,0)$. However, for $(p,q) = (0,0)$ we have $B_N(0,0) \equiv 0$ and $A_N(0,0) \sim N(\lambda_N, f_{NN}(0,0)/2)$. Here $N(\mu, \sigma^2)$ denotes the normal distribution with mean μ and variance σ^2.

For a stationary lattice process, Y, $A_Y(p,q)$ is distributed as

$$A_Y(p,q) \begin{cases} \equiv 0 & \text{if } p = q = 0, \\ \sim N(0, f_{YY}(\omega_p, \omega_q)) & \text{if } (\omega_p, \omega_q) \in \mathbf{\Lambda}, \\ \sim N(0, f_{YY}(\omega_p, \omega_q)/2) & \text{otherwise,} \end{cases} \tag{1.12}$$

where

$$\mathbf{\Lambda} = \begin{cases} (p = 0, q = -\ell_2/2) & \text{if } \ell_1 \text{ is odd and } \ell_2 \text{ is even,} \\ (p = \ell_1/2, q = 0) & \text{if } \ell_1 \text{ is even and } \ell_2 \text{ is odd,} \\ \{(p = \ell_1/2, q = 0), (p = 0, q = -\ell_2/2), \\ \qquad (p = \ell_1/2, q = -\ell_2/2)\} & \text{if } \ell_1 \text{ and } \ell_2 \text{ are even,} \\ \phi & \text{if } \ell_1 \text{ and } \ell_2 \text{ are odd.} \end{cases} \tag{1.13}$$

Here ϕ denotes the empty set. The functions A_Y and f_{YY} are as defined in (1.11) and (1.6), respectively. Furthermore, B_Y has the same distribution as A_Y except for $(\omega_p, \omega_q) \in \mathbf{\Lambda}$ in which case $B_Y \equiv 0$.

In addition, it can be shown that $A_s(p,q)$ and $A_s(p',q')$ for $s = N$ or Y and $(p,q) \neq (p',q')$ are asymptotically independent, and that they are asymptotically independent from $B_s(p,q)$ using orthogonality properties presented

in Appendix A. Similarly, $B_s(p,q)$ and $B_s(p',q')$ are asymptotically independent. Therefore, the auto-periodograms for X and Y are, respectively, asymptotically distributed as follows.

$$F_{NN}(\omega_p,\omega_q)\begin{cases}\sim \lambda_N + \frac{f_{NN}(0,0)}{2}\chi_1^2 & \text{if } p=q=0,\\ \sim \frac{f_{NN}(\omega_p,\omega_q)}{2}\chi_2^2 & \text{otherwise,}\end{cases} \tag{1.14}$$

$$F_{YY}(\omega_p,\omega_q)\begin{cases}\equiv 0 & \text{if } p=q=0,\\ \sim f_{YY}(\omega_p,\omega_q)\chi_1^2 & \text{if } (\omega_p,\omega_q)\in\mathbf{\Lambda},\\ \sim \frac{f_{YY}(\omega_p,\omega_q)}{2}\chi_2^2 & \text{otherwise,}\end{cases} \tag{1.15}$$

where χ_n^2 is the Chi-squared distribution with n degrees of freedom. Furthermore, $F_{ss}(\omega_p,\omega_q)$ and $F_{ss}(\omega_p',\omega_q')$ are asymptotically independent. Thus, for almost all frequencies (ω_p,ω_q), $\mathbb{E}\{F_{ss}(\omega_p,\omega_q)\}\approx f_{ss}(\omega_p,\omega_q)$ and $\mathrm{Var}\{F_{ss}(\omega_p,\omega_q)\}\approx f_{ss}^2(\omega_p,\omega_q)$. So although $F_{ss}(\omega_p,\omega_q)$ is approximately an unbiased estimator of $f_{ss}(\omega_p,\omega_q)$, it is not a consistent estimator since the limit of $\mathrm{Var}\{F_{ss}(\omega_p,\omega_q)\}$ is not zero as $\ell_1,\ell_2\to\infty$ when $s=Y$, and as $N_X\to\infty$ when $s=N$ (see Ripley, 1981, chapter 5). Therefore, $F_{ss}(\omega_p,\omega_q)$ must be smoothed so that consistency is achieved. This is discussed further in Section 1.8.

1.8 Smoothing Techniques

Several techniques for smoothing the periodogram are discussed in the literature. Most are given for the one-dimensional case but can be easily adapted for the two-dimensional case. These techniques can be divided into the following two categories.

- Techniques based on smoothing the covariance function, using lag windows, then calculating the periodogram.

- Techniques based on calculating the periodogram first, usually using the FFT and then averaging the periodogram ordinates to obtain a smoothed periodogram. This technique is usually known as *smoothing the periodogram.*

Chatfield (1981, chapter 7) discusses the comparative merits of three estimation procedures one of which is based on smoothing the periodogram and the others on transforming the covariance function. He concludes that with the advent of high speed computers and the rediscovery of the FFT smoothing the periodogram is being favoured. Moreover, the smoothed periodogram has superior theoretical properties to the periodogram calculated using lag windows. Discussions of time series smoothing techniques are also found in Priestley (1981a, chapter 6) and Diggle (1990, chapter 4). Bartlett (1964) suggests, for the case of spatial point pattern periodograms, the use of either uniform or quadratic weighting for the individual periodogram values.

In what follows, two techniques for smoothing the different spectral estimates are discussed. Both are based on smoothing the periodogram ordinates. The first technique is a modification of the weighted moving average technique discussed by Diggle (1990, chapter 4). It has been used by Mugglestone and Renshaw (1996b) for smoothing the spectral estimates of spatial point patterns with one and two components.

Let $F^\star$ denote either the periodogram F_{NN} or F_{YY}. Assume that $F^\star$ is evaluated for $p = P_1, \ldots, P_2$ and $q = Q_1, \ldots, Q_2$. Let $\tilde{F}$ be the smoothed periodogram where the ordinates of $F^\star$ and $\tilde{F}$ satisfy the following relation-

ship

$$\tilde{F}(p,q) = \sum_{i=-u}^{u} \sum_{j=-v}^{v} w_{(i,j)} F^{\star}(p+i, q+j), \tag{1.16}$$

where $w_{(i,\pm j)} = w_{(-i,\mp j)}$, $w_{(i,j)} = w_{(j,i)}$, $w_{(i,j)} \geq 0$ for $(i,j) \neq \mathbf{0}$, $w_{(0,0)} > 0$, $w_{(i,j)} \geq w_{(i+k,j)}$, $w_{(i,j)} \geq w_{(i,j+k)}$ for k an integer, and $\sum_{i=-u}^{u} \sum_{j=-v}^{v} w_{(i,j)} = 1$. Ideally the values of u and v should be chosen to attain consistency of the spectral estimate and to keep bias to a minimum. In this study, a special case of the weighted moving average technique will be used and will be referred to as *Method A*. In detail, Method A works as follows.

1. Assume that a periodogram, say $F^{\star}$, is to be smoothed such that ordinates are smoothed up to k rows and columns away.

2. Let $u = 1$ and $v = 1$ in (1.16).

3. Calculate the periodogram $\tilde{F}$ derived from $F^{\star}$ by substituting the following values for $w_{(i,j)}$ in (1.16):

$$\begin{aligned} w_{(0,0)} =& 2 \times \begin{cases} 1/6 & \text{for } p \neq (P_1 \text{ or } P_2) \text{ and} \\ & \quad q \neq (Q_1 \text{ or } Q_2) \text{ [Case 1]}, \\ 1/4 & \text{for } p = (P_1 \text{ or } P_2) \text{ and} \\ & \quad q = (Q_1 \text{ or } Q_2) \text{ [Case 2]}, \\ 1/5 & \text{otherwise [Case 3]}, \end{cases} \\ w_{(0,\pm 1)} =& w_{(\pm 1,0)} = w_{(0,0)}/2, \\ w_{(i,j)} =& 0 \quad \text{otherwise.} \end{aligned}$$

   Case 1 corresponds to a typical ordinate, Case 2 corresponds to a corner ordinate and Case 3 corresponds to an edge ordinate (see Figure 1.2 for

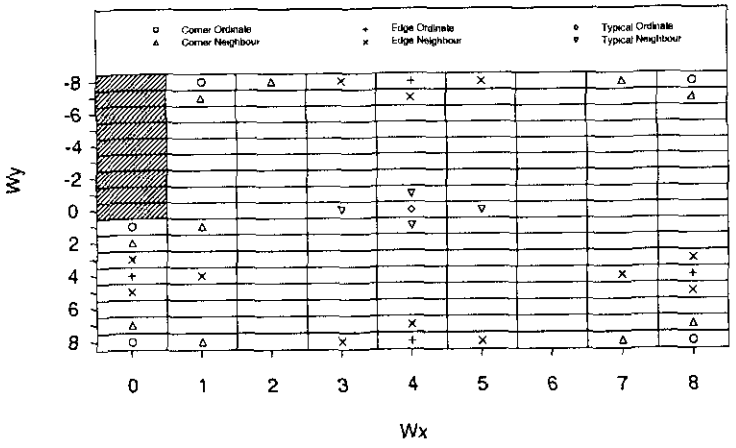

Figure 1.2: A typical periodogram with an illustration of how Method A for smoothing works. For each periodogram ordinate, the ordinates involved in the smoothing depend on whether the ordinate is a corner, edge or typical ordinate. The shaded region represents frequencies that are not usually reported. The values at the other frequencies are masked to clarify the figure.

an illustration). In each case, the ordinate being smoothed is weighted twice as much as its nearest neighbours that are involved in the smoothing.

4. Set $F^{\star} = \tilde{F}$.

5. Repeat steps 3 and 4 $k - 1$ times.

This transformation is similar to that of using a Gaussian kernel with bandwidth equal to the number of repetitions (see Mugglestone and Renshaw, 1996b). An alternative version of Method A uses an enlarged periodogram $F^{\star\star}$ rather than $F^{\star}$ in step 1. The enlarged periodogram is obtained by estimating the periodogram at frequencies outside the range we are interested in. This allows equal weights to be used for the range of frequencies we are

interested in.

The second technique, *Method B*, involves subdividing the data into $s_x \times s_y$ disjoint subregions. Each subregion is of the form $(aR_x, (a+1)R_x) \times (bR_y, (b+1)R_y)$ for $a = 0, \ldots, s_x - 1$ and $b = 0, \ldots, s_y - 1$ where $R_x = \ell_1/s_x$ and $R_y = \ell_2/s_y$. For each $R_x \times R_y$ subregion the periodogram is then computed. After that the periodogram of the entire data set is derived as the average of the periodograms of the subregions. In detail, Method B is as follows.

- Subdivide region into $s_x \times s_y$ disjoint subregions of equal dimensions $R_x \times R_y$ where R_x and R_y are defined above.
- In the case of a point pattern, transform the point pattern such that each subregion is of the form $(0, R_x) \times (0, R_y)$.
- Calculate $F^{\star R_x \times R_y}_{(i,j)}$ for $i = 1, \ldots, s_x; j = 1, \ldots, s_y$, where $F^{\star R_x \times R_y}_{(i,j)}$ is the auto-periodogram of the $R_x \times R_y$ subregion.
- Calculate $\tilde{F}(p,q) = \frac{1}{s_x s_y} \sum_{i=1}^{s_x} \sum_{j=1}^{s_y} F^{\star R_x \times R_y}_{(i,j)}(p,q)$ for the required range of frequencies.

Method B is an extension of the one-dimensional smoothing technique discussed by Brillinger (1981) and Rigas (1996). Further smoothing can be achieved by applying Method A to the output of Method B.

Figure 1.3 represents a lattice pattern. This pattern is a realisation of a cosine wave on a 32 × 32 lattice that repeats twice in the west-east (WE) direction and six times in the south-north (SN) direction plus added noise. The noise is generated from the standard normal distribution.

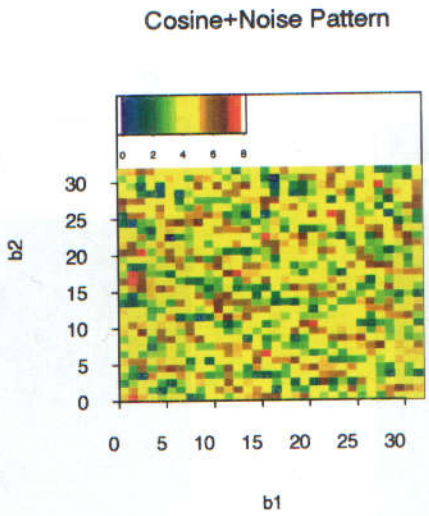

Figure 1.3: A cosine wave plus noise repeating twice in the west-east direction and six times in the south-north direction.

Figure 1.4(a) represents the unsmoothed periodogram of Figure 1.3. As expected, this periodogram exhibits a peak at the frequency $(2, 6)$. Smoothed estimates of the spectral function using Method A two, four and eight times are provided in Figures 1.4(b) to (d). The peak at frequency $(2, 6)$ persists in the smoothed periodograms. However, its power is spread to nearby frequencies. So although smoothing the periodogram results in a consistent estimator, it is obtained at the expense of the relevant information since the bias increases as the degree of smoothing increases.

Figures 1.5(a) to (d) represent the smoothed periodograms of the pattern in Figure 1.3 using Method B. These figures are obtained as follows:

- (a) results from dividing the region where the lattice pattern is observed into 2×2 rectangular subregions of equal dimension and then applying

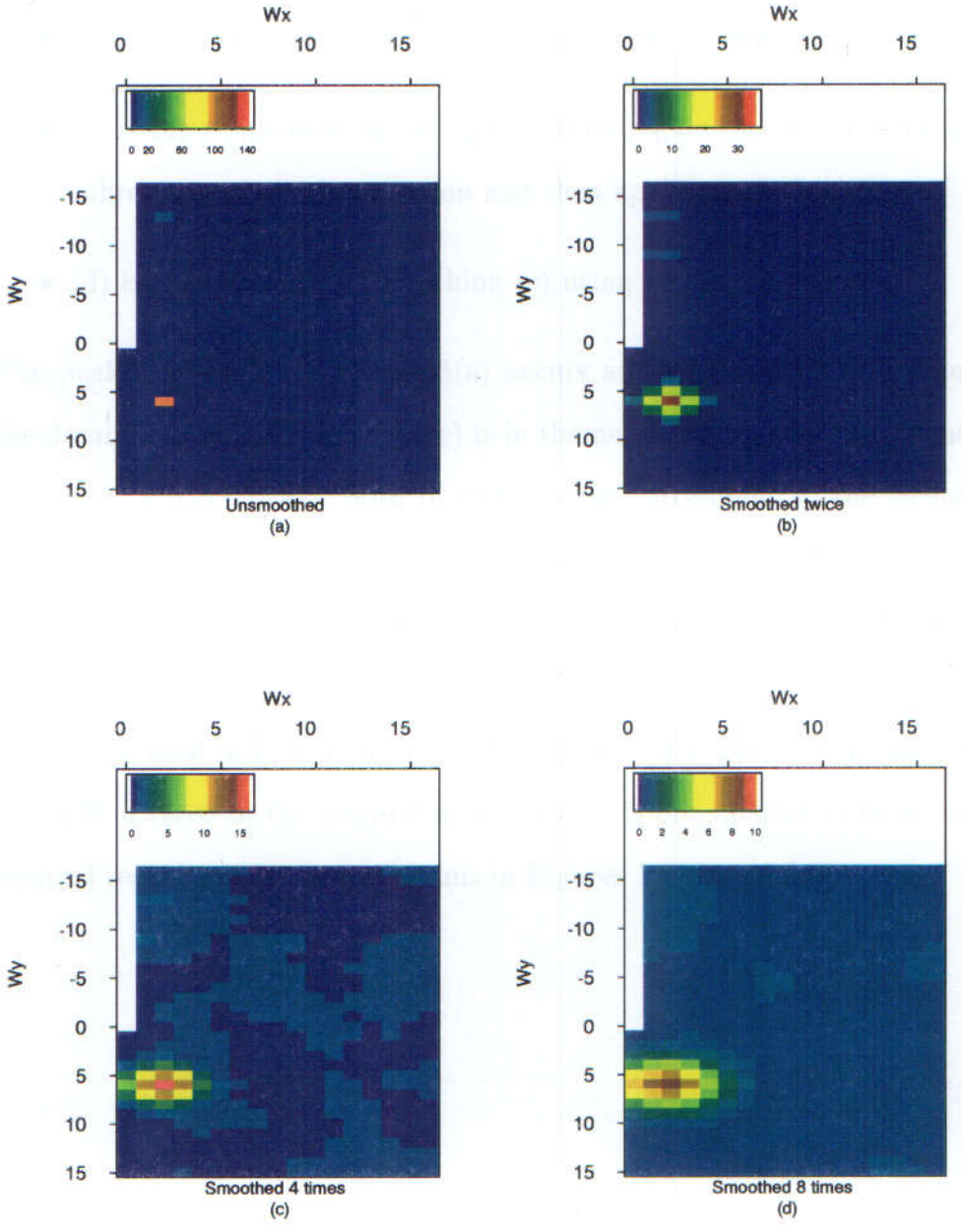

Figure 1.4: Periodograms corresponding to Figure 1.3: (a) unsmoothed; (b) to (d) smoothed using Method A two, four and eight times, respectively.

Method B;

- (b) is obtained by smoothing the outcome of (a) using Method A twice;
- (c) is the result of subdividing the study region into 4×4 rectangular subregions of equal dimension and then applying Method B;
- (d) is the outcome of smoothing (c) using Method A twice.

The peak frequency in Figure 1.5(a) occurs at $(1, 3) = (2/2, 6/2)$, whereas the dominant peak in Figure 1.5(c) is in the neighbourhood of the frequency $(1/2, 3/2) = (2/4, 6/4)$. Both of these peaks correspond to the frequency $(2, 6)$ on the original scale. It can be shown, with the aid of some algebra, that $\tilde{F}(p, q) = F^{\star}(s_x p, s_y q)$. In addition, the frequency ranges in Figure 1.5 are shorter than the range in Figure 1.4. Since the length of the sides of the subregions used in generating the periodograms of Figures 1.5(a) and (b) is one half of those of the original region, and it is one quarter of those of the original region for the periodograms in Figures 1.5(c) and (d).

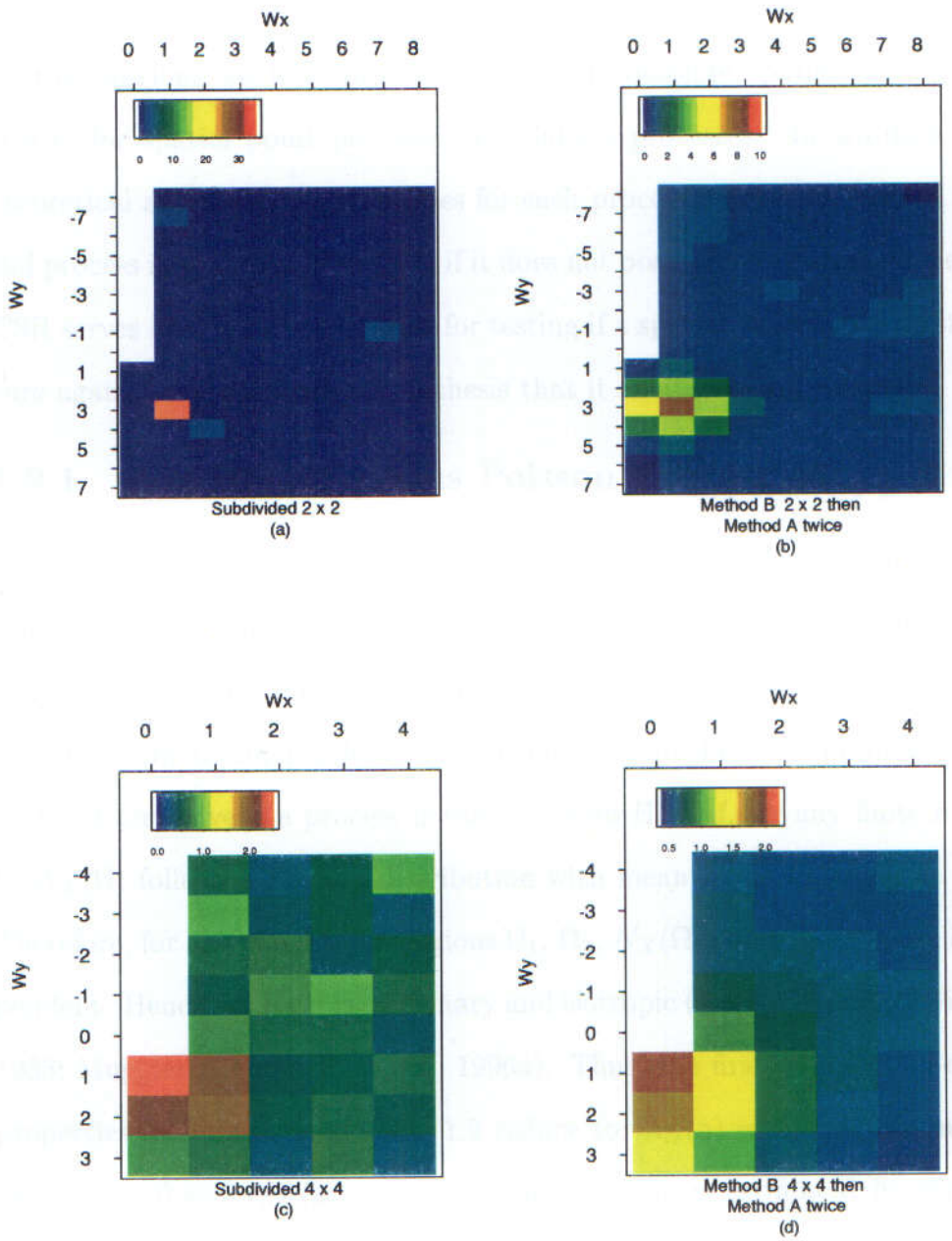

Figure 1.5: Smoothed periodograms corresponding to Figure 1.3 using Method B: (a) by subdividing the region into 2×2 subregions and then applying Method B; (b) by smoothing (a) using Method A twice; (c) by subdividing the region into 4×4 subregions and then applying Method B; and (d) by smoothing (c) using Method A twice.

1.9 Complete Spatial Randomness

In this section, we introduce the notion of complete spatial randomness (CSR) for spatial point processes and lattice processes. In addition, the theoretical and sampling properties for such processes are described. A spatial process is said to exhibit CSR if it does not possess any structure. Hence, CSR serves as the null hypothesis for testing if a spatial process has no structure against the alternative hypothesis that it exhibits some structure.

1.9.1 The Homogeneous Poisson Process

A stochastic model for a completely spatially random point process is the spatial homogeneous Poisson process (HPP) (see, for example, Diggle, 1983, chapter 4). A point process is said to be an HPP if, given $N_X(\Omega) = n$, the n events form an independent random sample from the uniform distribution on Ω. Alternatively, a process is said to be an HPP if, for any finite region Ω, $N_X(\Omega)$ follows a Poisson distribution with mean $\lambda_P|\Omega|$ for some $\lambda_P > 0$. Therefore, for any two disjoint regions Ω_1, Ω_2, $N_X(\Omega_1)$ and $N_X(\Omega_2)$ are independent. Hence, an HPP is stationary and isotropic (see, for example, Diggle, 1983; Mugglestone and Renshaw, 1996a). Thus, the first- and second-order properties introduced in Section 1.2 reduce to: $\lambda_N(\mathbf{a}) = \lambda_P, \lambda_{NN}(\mathbf{a_1}, \mathbf{a_2}) = \lambda_P^2, \gamma_{NN} = 0$ and $f_{NN}(\boldsymbol{\omega}) = \lambda_P$. In practice, λ_P is estimated by the observed intensity, $N_X/|\Omega|$. However as mentioned before, the co-ordinates of the point pattern are standardised before calculating the Fourier transform, hence, $|\Omega| = 1$ and $\hat{\lambda}_P = N_X$.

Furthermore, $\mathbb{E}\{F_{NN}(\boldsymbol{\omega})\} \approx \hat{\lambda}_P = N_X$ implies that the periodogram is

constant for all frequencies under CSR. The term *flat* is usually used in this case. Hence, departures from flatness in periodogram plots would indicate that the process exhibits some structure. In what follows, F_{NN} is scaled by dividing by N_X, unless otherwise stated. Therefore, $\mathbb{E}\{F_{NN}\} \approx 1$ for an HPP.

An HPP in the rectangular region $\Omega = [0, \ell_1] \times [0, \ell_2]$, with a pre-determined number of events, can be simulated as follows (see Lewis and Shelder, 1979).

1. Let n be the pre-determined number of events.

2. Generate $X_1, X_2, \ldots, X_n$ as independent, uniformly distributed random numbers on $[0, \ell_1]$.

3. Generate $Y_1, Y_2, \ldots, Y_n$ as independent, uniformly distributed random numbers on $[0, \ell_2]$.

4. Return $(X_1, Y_1), (X_2, Y_2), \ldots, (X_n, Y_n)$ as the co-ordinates of the two-dimensional HPP in the rectangle.

Figure 1.6(a) is a realisation of an HPP with 500 events on a 32×32 rectangular region. Its sample spectra are calculated for the range of frequencies $p = 0, \ldots, 16$ and $q = -16, \ldots, 15$ as recommended by Mugglestone and Renshaw (1996a). Figure 1.6(b) is the graph of the unsmoothed periodogram; whereas Figure 1.6(c) is the smoothed spectrum using Method A four times. The smoothed periodogram using Method B, where the original region is divided into 2×2 subregions of equal dimension, is given in Figure 1.6(d). Note here that the frequency range is not reduced despite the subdivision of the original region. This is due to the fact that point patterns

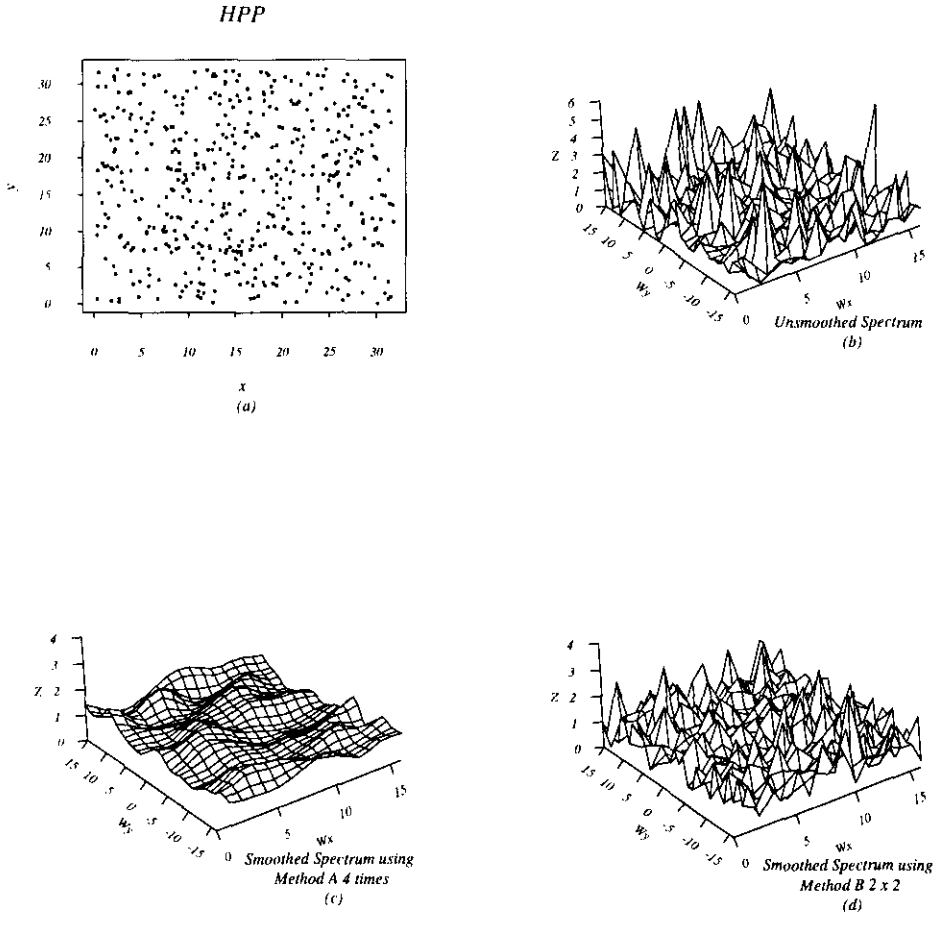

Figure 1.6: (a) A realisation of an HPP; (b) the unsmoothed periodogram of (a); (c) smoothed periodogram using Method A four times; and (d) smoothed periodogram using Method B where the study region is subdivided into 2×2 subregions.

do not have a Nyquist frequency as it is the case for lattice patterns. As expected, the sample spectra of the HPP exhibit no structure. In fact, when smoothed the periodogram becomes almost flat and oscillates around one as in Figure 1.6(c).

1.9.2 White Noise

A lattice process, $\{Y_{\mathbf{b}}\}$, is said to exhibit CSR if its components are identically and independently distributed (IID). Usually the distribution is taken to be the normal distribution with zero mean and variance σ^2_{YY}. Such a process is usually known as *Gaussian white noise*. In this case, it can be shown that $f_{YY}(\omega_p, \omega_q) = \sigma^2_{YY}$ for $(\omega_p, \omega_q) \neq 0$. Hence, the spectrum of a Gaussian process is flat. Therefore, σ^2_{YY} can be estimated by the average value of the periodogram ordinates. However, ordinates $\boldsymbol{\omega} \in \{0, \boldsymbol{\Lambda}\}$, where $\boldsymbol{\Lambda}$ is as defined in Section 1.7, must be excluded from the average since their sampling properties differ from the remaining periodogram ordinates. In addition, ordinates $F_{YY}(\omega_p, \omega_q)$ for $p \in \{0, [\ell_1/2] \text{ if } \ell_1 \text{ is even}\}$ should be excluded for $q < 0$ because they are repeats of ordinates with $q > 0$. Thus, $\hat{\sigma}^2_{YY} = n^{-1} \sum_p \sum_q F_{YY}(\omega_p, \omega_q)$ where summation is over $p = 0, \ldots, [\ell_1/2]$ and $q = -[\ell_2/2], \ldots, [(\ell_2 - 1)/2]$ but excluding the above ordinates and n is the number of ordinates used in the summation. Therefore, the periodogram of a Gaussian process, can be scaled by $\hat{\sigma}^2_{YY}$ to have an expected value of one. In examples to follow, lattice periodograms will be scaled by $\hat{\sigma}^2_{YY}$, unless otherwise stated. Thus, departure from flatness will indicate that the process is not Gaussian white noise. Note that the asymptotic results for lattice processes, reported in Section 1.7, hold exactly for white noise. Priestley

(1981a, chapter 6) gives a detailed derivation of the distributional properties for the one-dimensional white noise.

A realisation of a Gaussian white noise process with mean 10 and standard deviation 2 on a 32×32 lattice is given in Figure 1.7(a). The unsmoothed periodogram for the lattice pattern is presented in Figure 1.7(b). The smoothed periodogram using Method A four times is given in Figure 1.7(c). Figure 1.7(d) represents the smoothed periodogram using Method B after subdividing the region into 2×2 subregions. The spectral estimates do not exhibit any particular structure. In addition, the smoothed spectra fluctuate around the value one as we would expect for white noise.

1.10 Models for Point Processes

A number of alternatives to CSR for point processes are discussed briefly in this section. Mugglestone (1990, chapter 4) gives a more detailed description of possible alternatives to an HPP and their spectral estimates and provides a number of references.

1.10.1 Modified Thomas Cluster Process

A modified Thomas cluster process (MTCP) is an isotropic alternative to CSR where events exhibit a form of aggregation. An MTCP is encountered when parent events distributed as an HPP, with intensity λ_P, give rise to offspring. The number of offspring per parent is generated by a Poisson process with mean μ. The distribution of offspring relative to their parents follows a symmetric Gaussian distribution, $h(\mathbf{a})$, with variance σ^2, that is $h(\mathbf{a}) = (2\pi\sigma^2)^{-1} \exp\{-\mathbf{a}\mathbf{a}^\top/(2\sigma^2)\}$. Note that only the offspring are retained

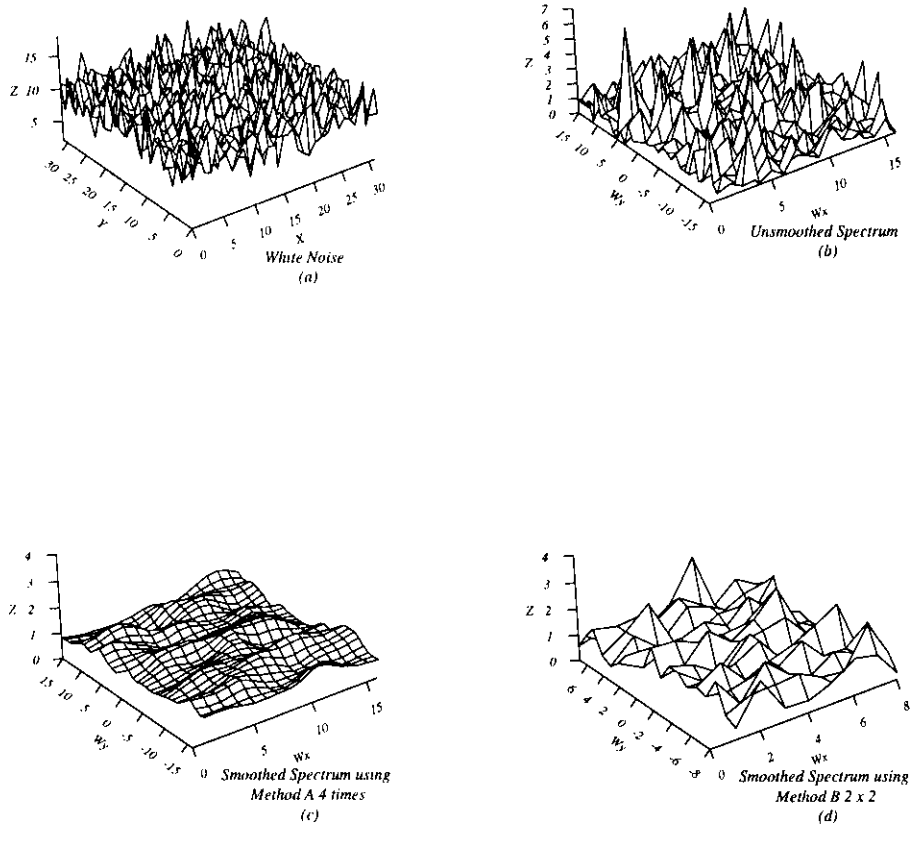

Figure 1.7: (a) A realisation of a white noise process; (b) the unsmoothed periodogram of (a); (c) smoothed periodogram using Method A four times; and (d) smoothed periodogram using Method B where the study region is subdivided into 2×2.

in the final pattern.

The first- and second-order intensity functions of MTCP are given by: $\lambda_C = \lambda_P \mu$ and $\lambda_{CC}(t) = \lambda_C^2 + \lambda_P \mu^2 (4\pi\sigma^2)^{-1} \exp\{-t^2/(4\sigma^2)\}$, for $t > 0$. Hence, the spectral density function is given by

$$f_{CC}(\boldsymbol{\omega}) \equiv f_{CC}(\omega) = \lambda_C (1 + \mu \exp\{-\omega^2 \sigma^2\}).$$

An MTCP is simulated as follows.

1. The n_P parents are determined as a realisation of an HPP, using the simulation method of Section 1.9.1.

2. A sample $\{n_o\}$ of size n_P is generated from the Poisson process with mean μ. The number of offspring per parent is given by n_{o_k} for $k = 1, \ldots, n_P$.

3. The co-ordinates of the offspring are determined by displacing those of their parents by the vectors $(\epsilon_{1jk}, \epsilon_{2jk})$, $j = 1, \ldots, n_{o_i}$ and $k = 1, \ldots, n_P$. Here the $\{\epsilon\}$'s are IID variables from the normal distribution with zero mean and variance σ^2.

1.10.2 Inhibition Processes

Inhibition processes are alternatives to processes that exhibit CSR in which events are regularly spaced. Two types of regularity can be distinguished. One type occurs when events are placed deterministically at a minimum distance from each other, for example, on the intersection points of a regular grid. The other type occurs when random events are constrained not to lie within a minimum distance of each other. An example of the latter type of

inhibition models is given by the simple sequential inhibition process (SSIP). This model is characterised by its dynamic nature (see below). To simulate an SSIP proceed as follows.

1. Generate the first event uniformly on the given region, Ω.

2. Generate a second event uniformly on Ω. Retain the second event only if its distance from the first event is greater than a minimum distance, δ.

3. Generate a third event, and retain this event only if it does not lie within distance δ from the previously retained events.

4. Repeat the procedure of generating and retaining events until the required number of events is generated.

SSIPs are usually parametrised by their packing intensity, $\tau = \lambda\pi\delta^2/4$ where λ is the intensity of the process. The packing intensity represents the proportion of the plane covered by non-overlapping discs of diameter δ (see, for example, Diggle, 1983). SSIPs are easily generated, however, their theoretical statistical properties are intractable. Hence, simulation studies are needed to investigate their properties.

1.10.3 Doubly Stochastic Poisson Processes

A common feature of the previous two models is the assumption that the intensity of the point process is identical throughout the study region. A doubly stochastic Poisson process (DSPP), or Cox process, arises when the intensity of a Poisson process varies within the study region. Specifically,

we talk of a point process driven by the intensity process $\{\Pi(\mathbf{a})\}$ where Π is a continuous stochastic process. The intensity process is usually assumed to be a second-order stationary process. In this case, conditional on Π we have $\mathbb{E}(dN_X(\mathbf{a})) = \mathbb{E}(\Pi(\mathbf{a}))|d\mathbf{a}| = \lambda_\Pi|d\mathbf{a}|$ and $\mathbb{E}(dN_X(\mathbf{a})dN_X(\mathbf{a}')) = \mathbb{E}(\Pi(\mathbf{a})\Pi(\mathbf{a}'))|d\mathbf{a}||d\mathbf{a}'| = (\lambda_\Pi^2 + \gamma_\Pi(\mathbf{a}-\mathbf{a}'))|d\mathbf{a}||d\mathbf{a}'|$. Here λ_Π is the expected value of the process Π and γ_Π is its auto-covariance function. Therefore, the auto-covariance function of the point process is given by

$$\begin{aligned}
\gamma_{NN}(\mathbf{a},\mathbf{a}')|d\mathbf{a}||d\mathbf{a}'| &= \gamma_{NN}(\mathbf{a}-\mathbf{a}')|d\mathbf{a}||d\mathbf{a}'| \\
&= \mathbb{E}\{dN_X(\mathbf{a})dN_X(\mathbf{a}')\} - \mathbb{E}\{dN_X(\mathbf{a})\}\mathbb{E}\{dN_X(\mathbf{a}')\} \\
&= (\lambda_\Pi^2 + \gamma_\Pi(\mathbf{a}-\mathbf{a}'))|d\mathbf{a}||d\mathbf{a}'| - \lambda_\Pi^2|d\mathbf{a}||d\mathbf{a}'| \\
&= \gamma_\Pi(\mathbf{a}-\mathbf{a}')|d\mathbf{a}||d\mathbf{a}'|.
\end{aligned}$$

Thus, the complete covariance function of the process is

$$\kappa_{NN}(\mathbf{a},\mathbf{a}') = \lambda_N\delta(\mathbf{a}-\mathbf{a}') + \gamma_{NN}(\mathbf{a}-\mathbf{a}') = \lambda_\Pi\delta(\mathbf{a}-\mathbf{a}') + \gamma_\Pi(\mathbf{a}-\mathbf{a}').$$

The spectral density function of the point process is

$$f_{NN}(\boldsymbol{\omega}) = \int \kappa_{NN}(\mathbf{v})\exp\{-i\boldsymbol{\omega}\mathbf{v}^\top\}d\mathbf{v} = \lambda_\Pi + \int \gamma_\Pi(\mathbf{v})\exp\{-i\boldsymbol{\omega}\mathbf{v}^\top\}d\mathbf{v}.$$

Bartlett (1964) has shown that the characteristic function of such a process is equivalent to that of an MTCP if $\Pi(\mathbf{a}) = \int h(\mathbf{a}-\mathbf{s})dM(\mathbf{s})$ where M is another Poisson process and h is a bivariate distribution function. Despite the formal equivalence between MTCPs and DSPPs they play different roles. An MTCP reflects the belief that events of the point process tend to form clusters. A DSPP indicates that the point process is heterogeneous, in the

sense that the point process has a variable intensity as opposed to a constant intensity.

In this section, different models for point processes were introduced. These models serve as a benchmark when analysing real data sets. In addition, they are used in simulations of hybrid processes that are discussed in the next chapter. Models for lattice processes are introduced in the next section.

1.11 Models for Lattice Processes

Two major approaches are used to model lattice processes. One is based on the simultaneous specification of the lattice process and the other on conditioning. Cressie (1991, chapter 6) gives a detailed survey of these models with special attention to conditionally specified models. Simultaneous and conditional spatial autoregressive Gaussian (SARG and CARG) models are also discussed by Ripley (1981, chapter 5). Following Ripley's approach SARG and CARG models are defined by matrices S and C, respectively. The diagonals of both matrices are assumed to be identically zero.

Let the lattice process $Y = \{Y_{(b_1,b_2)}, (b_1 = 0, \ldots, \ell_1 - 1; b_2 = 0, \ldots, \ell_2 - 1)\}$ be indexed by $k = 0, \ldots, \ell_1\ell_2 - 1$ where $Y_{(b_1,b_2)} = Y_k$ and $k = b_1 + \ell_1 b_2$. A SARG model is defined by $Y_k = \mu_k + \sum_l S_{kl}(Y_l - \mu_l) + \epsilon_k$ where ϵ_k are IID normal variables with zero mean and variance σ^2; $(I - S)$ is non-singular and I is the identity matrix. It can be shown that $\mathbf{Y} \sim N(\boldsymbol{\mu}, \sigma^2(I-S)^{-1}(I-S^\top)^{-1})$ where $\mathbf{Y} = (Y_0, \ldots, Y_{\ell_1\ell_2-1})^\top$ and $\boldsymbol{\mu} = (\mu_0, \ldots, \mu_{\ell_1\ell_2-1})^\top$.

A CARG model arises if the conditional distribution at a site given all the other sites is Gaussian. Then, $\mathbf{Y} \sim N(\boldsymbol{\mu}, \sigma^2(I - C)^{-1})$, $\mathbb{E}(Y_k | Y_l, k \neq l) =$

$\mu_k + \sum_l C_{kl}(Y_l - \mu_l)$ and $\mathrm{Var}(Y_k|Y_l, k \neq l) = \sigma^2$ where $(I - C)$ is symmetric and strictly positive definite (see, for details, Cressie, 1991). Ripley gives a number of schemes to construct such models. We mention here two particular examples.

The first example is generated by setting S_{kl} to be non-zero only if sites k and l are nearest neighbours and by setting $\boldsymbol{\mu} = \mathbf{0}$. This results in

$$Y_{(b_1,b_2)} = \beta_1 Y_{(b_1-1,b_2)} + \beta_2 Y_{(b_1+1,b_2)} + \beta_3 Y_{(b_1,b_2-1)} + \beta_4 Y_{(b_1,b_2+1)} + \epsilon_{(b_1,b_2)}. \tag{1.17}$$

Bartlett (1975, chapter 2) shows that the spectral density function of the model in (1.17) is proportional to $[1 - 2\beta_1 \cos(\omega_p) - 2\beta_3 \cos(\omega_q)]^{-2}$ for the case where $\beta_1 = \beta_2$ and $\beta_3 = \beta_4$.

The second example is generated by setting the entries of C to be non-zero only for nearest neighbours. This yields the following model

$$\mathbb{E}\left[Y_{(b_1,b_2)}|Y_{(b_1',b_2')}, (b_1,b_2) \neq (b_1',b_2')\right] = \mu_{(b_1,b_2)} + \beta_1 Y_{(b_1-1,b_2)} + \beta_2 Y_{(b_1+1,b_2)} + \beta_3 Y_{(b_1,b_2-1)} + \beta_4 Y_{(b_1,b_2+1)}. \tag{1.18}$$

Bartlett (1975, chapter 2) has also shown that the spectral density function of (1.18) is proportional to $[1 - 2\beta\cos(\omega_p) - 2\beta'\cos(\omega_q)]^{-1}$ where $\beta = \frac{1}{2}(\beta_1 + \beta_2)$ and $\beta' = \frac{1}{2}(\beta_3 + \beta_4)$.

A different type of model is provided via

$$Y_{(b_1,b_2)} \equiv Y_{\mathbf{b}} \equiv \sum_{l=1}^{n} A_l \cos(\boldsymbol{\omega}_l \mathbf{b}^\top + \phi_l) + \epsilon_{\mathbf{b}}. \tag{1.19}$$

Here A_l, $\boldsymbol{\omega}_l$ and n are constants; $\{\phi_l\}$ are IID uniform on $(-\pi, \pi)$ and independent from ϵ where ϵ is defined as before. It is easily proved, using orthogonality relations presented in Appendix A, that the spectral density

function for such processes is discrete with non-zero positive values at the ordinates $\omega_l, l = 1, \ldots, n$. Models generated by (1.19) are usually studied due to their simplicity and to demonstrate the potential of spectral analysis.

1.12 Test for CSR based on the Maximum Periodogram Ordinate

In this section, a formal test of CSR for both point processes and lattice processes is described. It is an adaptation of the test introduced by Fisher (1929) which is based on the maximum periodogram ordinate of a time series. The test developed by Fisher (1929) is summarised as follows. Consider the time series $\{X_t\}$ for $t = 1, \ldots, N$ and suppose that this series can be modelled as

$$X_t = \sum_{j=1}^{J} A_j \cos(\omega_j t + \phi_j) + \epsilon_t, \tag{1.20}$$

where J, A_j, ω_j, $j = 1, \ldots, J$ are constants and the $\{\phi_j\}$ are IID uniform variables on $(-\pi, \pi)$. The $\{\epsilon_t\}$ are IID $N(0, \sigma^2)$ and are independent of the $\{\phi_j\}$.

Fisher (1929) derived the exact distribution for the maximum periodogram ordinate (for the case N odd) based on the statistic

$$g = \frac{\max_p(F_p)}{\sum_{p=1}^{[N/2]} F_p},$$

which is known as Fisher's *g-statistic*. Here, the $\{F_p\}$'s are the periodogram ordinates associated with the time series $\{X_t\}$, and $\{p\}$'s are integers that index frequencies where the periodogram is evaluated. Under the null hypothesis that the time series is Gaussian white noise (that is it contains no

harmonics or equivalently all the A_j's are zero) Fisher (1929) found that

$$\Pr(g > z) = \sum_{k=1}^{[1/z]} (-1)^{k+1} \frac{n!}{k!(n-k)!} (1 - kz)^{n-1},$$

where $n = [N/2]$.

However, under the null hypothesis the periodogram ordinates when standardised by $\sigma^2/2$ can be seen to be independently distributed as χ^2_2 (see Priestley, 1981a, chapter 6). Therefore, for any t non-negative

$$\Pr\left(\frac{F_p}{\sigma^2/2} \leq t\right) = 1 - \exp\{-t/2\}.$$

Since a χ^2_2 is equivalent to an exponential distribution with mean two. In practice, the variance is usually unknown but under the null hypothesis $\mathbb{E}(F_p) = \sigma^2$. Thus, an unbiased estimate of the variance is given by

$$\hat{\sigma}^2 = \frac{1}{n} \sum_{p=1}^{n} F_p,$$

where n is as above. If one can ignore sampling fluctuations as the sample size increases then asymptotically

$$\Pr\left(\frac{\max_p(F_p)}{\hat{\sigma}^2/2} > t\right) \sim 1 - (1 - \exp\{-t/2\})^n. \tag{1.21}$$

Therefore,

$$\Pr(2ng > t) \sim 1 - (1 - \exp\{-t/2\})^n. \tag{1.22}$$

The right hand side of (1.22) is approximately equal to the first term of Fisher's test.

To test for the null hypothesis against the alternative hypothesis that the process contains a sinusoidal component (that is one of the A_j's is not zero)

the following steps are carried out. Let $\alpha\,(0 < \alpha < 1)$ be the chosen level of significance, choose z_α such that $\Pr\,(2ng > z_\alpha) = \alpha$ then compare $2ng$ with z_α. If $2ng > z_\alpha$ conclude that the series contains a harmonic component.

If the first periodogram ordinate is found to be significant then Whittle (1952) suggests that Fisher's test can be used to test the second maximum periodogram ordinate. This is done by removing the maximum ordinate then proceeding as before. The same procedure is repeated until no more significant ordinates are detected.

Fisher's test can be adapted to the lattice process case. This is achieved by extending (1.20) to two dimensions and noting that under the null hypothesis of CSR the standardised periodogram ordinates have similar distributions to those in the one-dimensional case, see Section 1.7.

Next, Mugglestone and Renshaw (2000) note the similarity between the distribution of the periodogram ordinates under the null hypotheses of Gaussian white noise and of an HPP, see Section 1.7. Thus, (1.21) can be used to test for the maximum periodogram ordinate of a spatial point pattern, since $2F_{NN}/\lambda \sim \chi^2_2$ and $\hat{\lambda} = N_X$, see Section 1.9.1. Here λ is the intensity of the process and N_X is the number of events of the pattern. Thus $\hat{\sigma}^2$ is replaced by N_X in (1.21). In addition, Mugglestone and Renshaw (2000) remark that conditional on the intensity of the point process the test based on (1.22) is exact under the null hypothesis of CSR. They also note that a two-tailed test is required for point processes, since periodograms for cluster processes tend to have high values at low frequencies whereas inhibition processes tend to have low values at low frequencies.

1.13 Interpretation of Sample Auto-Spectra

In this section, we will give a brief interpretation of what spectral functions measure. In general, the $(p,q)^{th}$ element of the periodogram represents the extent to which the covariance of the pattern is explained by the cosine wave $\cos(2\pi(pa_{1j}/\ell_1 + qa_{2j}/\ell_2))$, where ℓ_1 and ℓ_2 are the dimensions of the study region. Geometrically, this frequency determines a vector that is perpendicular to the waves (see Rayner, 1971, chapter 9). This vector which is drawn from the origin is defined by its angle from the x-axis, $\theta = \tan^{-1}\left(\frac{q/\ell_2}{p/\ell_1}\right)$, and its length, $k = \sqrt{\left(\frac{p}{\ell_1}\right)^2 + \left(\frac{q}{\ell_2}\right)^2}$.

1.13.1 Point Spectrum

In the case of point processes, possible uses of the auto-periodogram are to detect departures from CSR, to explore whether certain features exist in the data, and to identify what possible processes might have generated the study pattern. Thus, the sample spectrum provides a guide to determine the underlying point process. As mentioned in Section 1.9.1, for a point process that exhibits CSR the auto-periodogram is flat. A peak at low frequencies indicates that the process resembles an aggregated point process. However, a peak at high frequencies indicates that the process is an inhibited process. For a detailed discussion of these issues see Mugglestone and Renshaw (1996a).

Figure 1.8 represents realisations of two point processes and their sample spectra. The point pattern in Figure 1.8(a) is generated from an MTCP on a 32×32 rectangular region. The parameters used to generate this point pattern are: $n_P = 100, \mu = 8$, and $\sigma = 0.5$, where n_P is the number of

parents, μ (labelled as n_C on graph) is the mean number of children per parent, and σ (labelled as *sd* on graph) is the parameter that controls the displacement of children with respect to their parents. Both the raw and smoothed periodograms are characterised by a concentration of power at low frequencies, see Figures 1.8(b) and (c).

Figure 1.8(d) represents the point pattern of an SSIP generated on the unit square with 100 events and a minimum distance 0.08. Thus, the packing intensity for this process is approximately 0.5. The sample spectra for this point process, Figures 1.8(e) and (f), exhibit low values for low frequencies and high values for high frequencies.

Using the two-sided test of Section 1.12, the significance of the peaks detected in Figure 1.8 is given in Figures 1.9(a) and (b) for the clustered and inhibited patterns, respectively. In Figure 1.9 the absolute value of each pixel represents whether the corresponding periodogram ordinate was found to be significant at the level indicated. The levels considered here are 1%, 5% and 10%. The sign represents whether the significant values were detected in the upper or lower tails of the maximum periodogram ordinate distribution with the positive sign corresponding to the upper tail. For the clustered pattern all the significant peaks were detected in the upper tail, whereas for the inhibition pattern they were detected in the lower tail. For relatively low frequencies the clustered pattern exhibits significant values at the 1% level, whereas the inhibited pattern exhibits significant values at the 10% level.

Note here that the range of frequencies in the realisation of the SSIP has been reduced to a smaller range than the typical range for point patterns

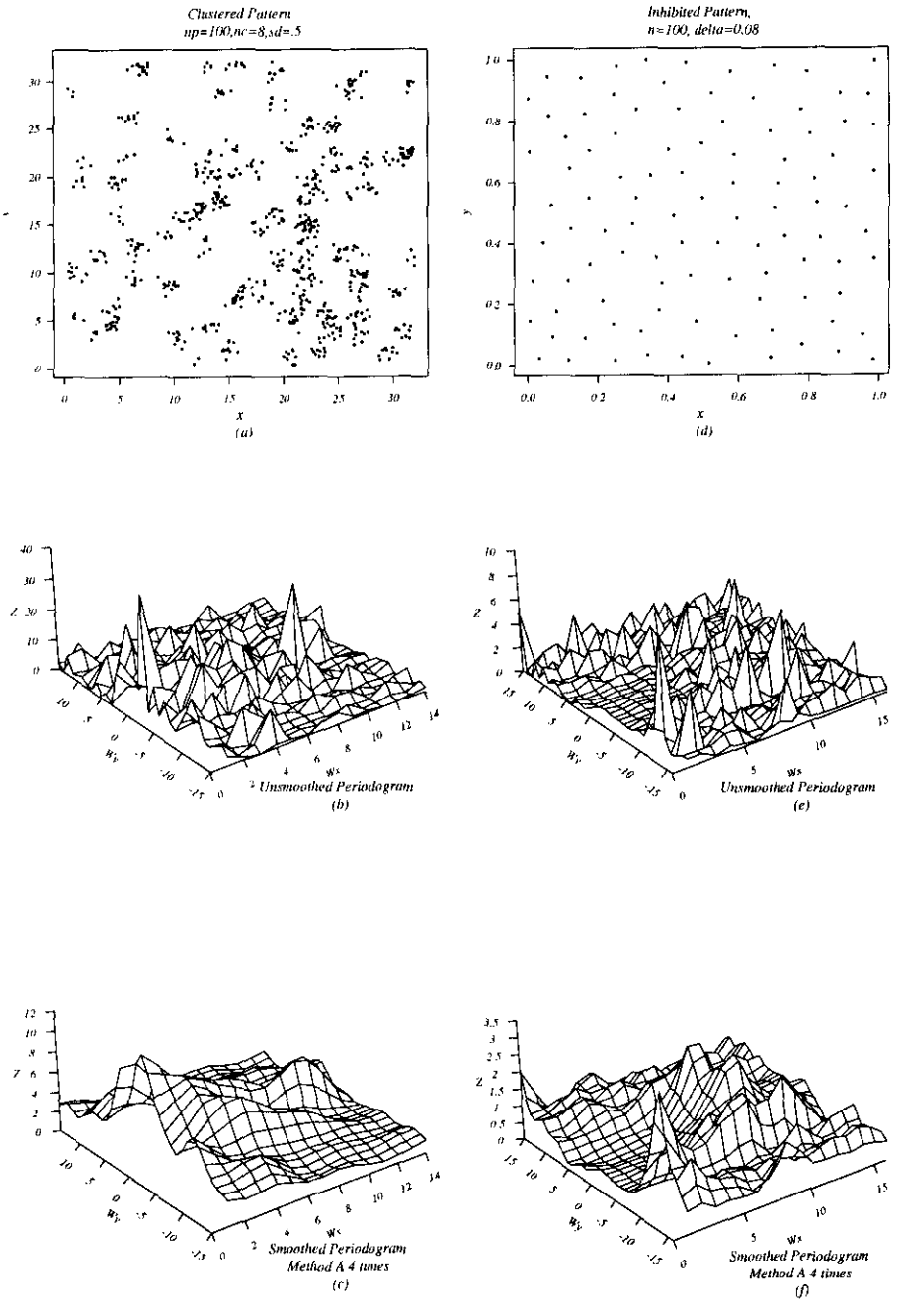

Figure 1.8: (a) A realisation of an MTCP, (b) and (c) unsmoothed and smoothed periodograms of (a); (d) a realisation of an SSIP, (e) and (f) unsmoothed and smoothed periodograms of (d).

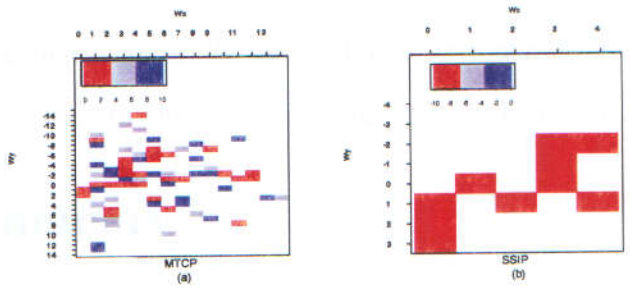

Figure 1.9: (a) Significant periodogram ordinates at the 1%, 5%, and 10% levels for the clustered pattern in Figure 1.8(a). The levels that appear in this graph are the upper tail 1% (red), 5% (grey), and 10% (blue) levels; (b) Significant periodogram ordinates at the 1%, 5%, and 10% levels for the inhibited pattern in Figure 1.8(d). The levels that appear in this graph are the lower tail 10% (red), 5% (grey), and 1% (blue) levels.

$(p = 0, \cdots, 16, q = -15, \cdots, 16)$. This reduction is essential to maintain independence between different periodogram ordinates, since the periodogram is based on $2N_X$ transformations of the data. Mugglestone and Renshaw (2000) give a guideline for the choice of the frequency range in which it is assumed that the events are placed on an $N' \times N'$ lattice with $N' = \sqrt{N}$. For the realisation in Figure 1.8(d) $N_x = 100$ so one considers the frequency range $p = 0, \ldots, [\sqrt{N}/2](= 5)$ and $q = -5, \ldots, 4$.

1.13.2 Lattice Spectrum

For lattice processes the basic use of the periodogram is to detect periodicities that might be present in the data indicating departures from CSR. If the process is white noise then this results in a flat periodogram, see Section 1.9.2. Hence, all frequencies contribute the same power to the periodogram.

Applying Fisher's test to the unsmoothed periodogram, Figure 1.4(a), of the lattice pattern in Figure 1.3 the frequency $(2, 6)$ is found to be the only

significant ordinate at the 1% level. Note that this frequency is the only dominant peak in the periodogram. Hence, one concludes that the lattice process repeats twice in the WE direction and six times in the SN direction.

1.14 Summary

In this chapter, the basic notions and properties of spatial point processes and lattice processes in the spectral domain were described. The asymptotic distributional properties of the sample spectral estimate, the periodogram, were discussed. The periodogram was shown to be an unbiased estimator of the spectral density function but not a consistent one. Thus, smoothing techniques had to be used to attain consistency.

Having established the necessary tools for spectral analysis, models for CSR and possible alternatives were reviewed. For some of these models the theoretical spectral density functions were reported. In addition, algorithms for simulating such models were provided.

A formal test for detecting departures from CSR was then discussed. This test is based on the maximum periodogram ordinate. Examples were also provided to illustrate the potential of spectral estimates as a tool for exploratory analysis of spatial patterns.

In the following chapter, a hybrid process consisting of a point process and a lattice process will be introduced. Spectral analysis techniques will be used to detect patterns for such hybrid processes.

Chapter 2

Point-Lattice Processes: Definitions and Spectral Estimates

In the previous chapter, point and lattice processes were studied as individual processes. In this chapter, a hybrid of the two processes, termed a *point-lattice* process, is introduced. Point-lattice processes are defined in Section 2.1. In Section 2.2, we discuss properties of point-lattice processes both in the spatial domain and in the frequency domain. Cross-spectral estimates for these processes are introduced in Section 2.3. In Section 2.4 the notion of CSR for point-lattice process is considered. Methods for simulating point-lattice processes and simulated examples are provided in Section 2.5.

2.1 Point-Lattice Processes

A spatial point-lattice process is a process with two components: a point process, X, and a lattice process, Y. A realisation of a spatial point–lattice process is called a spatial point–lattice pattern. The region where the point pattern is observed usually coincides with the rectangular region where the

lattice measurements are recorded. Examples of such processes include measurements made on a regular grid in a study region, such as planned agricultural trials, together with events occurring in the same region, such as the growth of a certain species.

To study point-lattice processes we need to explore relationships between their components. Analyses of such spatial processes have been carried out mainly in the parametric domain by considering the lattice process as an explanatory variable in the model used for occurrence of events (see, for example, Buckland and Elston, 1993; Augustin, Mugglestone and Buckland, 1996). In this study, a non-parametric approach based on two-dimensional cross-spectral analysis will be used. However, spectral analysis can be used to identify parameters in a given model.

The cross-spectral analysis approach used in this study is analogous to the analysis carried out by Mugglestone and Renshaw (1996b) to investigate properties of a bivariate point process (a process with two components where each component is a point process). Two-dimensional cross-spectral analysis for point-lattice processes is an extension of the cross-spectral analysis used for one-dimensional hybrid processes: a one-dimensional hybrid process is a process with two components where one component is a one-dimensional point process and the other is a time series (see Rigas, 1983; Brillinger, 1994).

Examples of point-lattice patterns are given in Figure 2.1. Figure 2.1(a) represents occurrence of deer together with altitude within a subregion of the Grampian region of Scotland. Figure 2.1(b) represents occurrence of the tree species *Iryanthera sagotiana* together with altitude within a tropical forest of French Guyana. The latter data set was supplied by Michel Goulard of

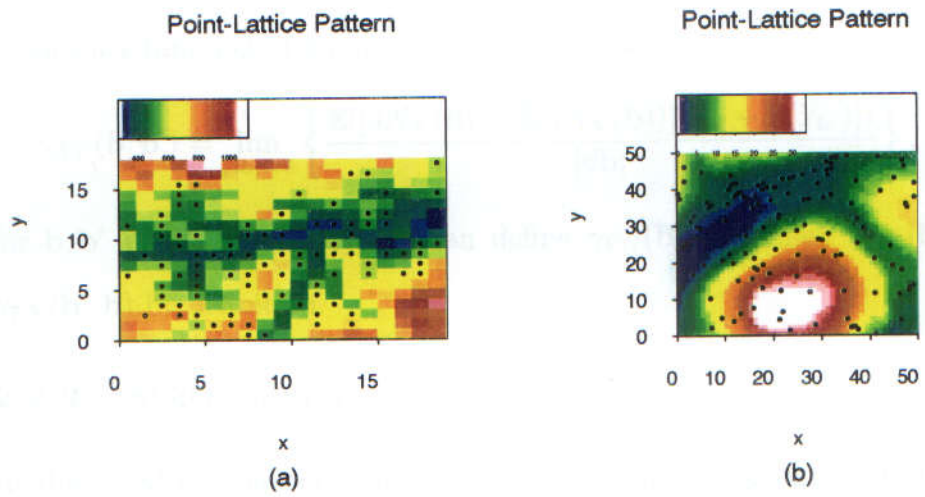

Figure 2.1: Examples of spatial point-lattice patterns: (a) occurrence of red deer superimposed on altitude data of a region of Scotland; and (b) locations of a tree species in a forest of French Guyana together with altitude values of the study region.

Le Centre INRA de Toulouse, France, and Hélène Dessard of *CIRAD-Forêt*, France.

It is worth remarking here that functions used to summarise properties of two or more components will be prefixed with the term *cross*. For example, we say cross-covariance of the spatial point–lattice process $\{X, Y\}$ and auto-covariance of the point process X.

2.2 Assumptions and Definitions

2.2.1 Second-Order Properties in the Spatial Domain

In this section, we define second-order properties of point-lattice processes in the spatial domain. Consider a point-lattice process $\{X, Y\}$ where X is a point process and Y is a lattice process. First- and second-order properties for each component can be investigated using techniques of Chapter 1. However,

to study the relationship between the two components we define the *cross-covariance* function of a point-lattice process as

$$\gamma_{NY}(\mathbf{b}, \mathbf{b}') = \lim_{|d\mathbf{b}|\to 0} \left\{ \frac{\mathbb{E}([dN_X(\mathbf{b}) - \mathbb{E}(dN_X(\mathbf{b}))][Y_{\mathbf{b}'} - \mathbb{E}(Y_{\mathbf{b}'})])}{|d\mathbf{b}|} \right\}, \quad (2.1)$$

for $\mathbf{b}, \mathbf{b}' \in \mathbb{R}^2$. Similarly, we can define $\gamma_{YN}(\mathbf{b}', \mathbf{b})$, where $\gamma_{NY}(\mathbf{b}, \mathbf{b}') = \gamma_{YN}(\mathbf{b}', \mathbf{b})$ by definition.

2.2.2 Stationarity

As discussed in Chapter 1, stationarity is a fundamental assumption for deriving theoretical properties in the frequency domain. In what follows, we will define second-order stationarity for point-lattice processes. A point-lattice process is said to be stationary if both component processes are individually and jointly stationary. Hence, (2.1) reduces to

$$\begin{aligned}
\gamma_{NY}(\mathbf{b}, \mathbf{b}') &= \gamma_{NY}(\mathbf{b} - \mathbf{b}') = \gamma_{NY}(\mathbf{a}) \\
&= \lim_{|d\mathbf{a}|\to 0} \left\{ \frac{\mathbb{E}[dN_X(\mathbf{a}+\mathbf{c}) - \mathbb{E}(dN_X(\mathbf{a}+\mathbf{c}))][Y_{\mathbf{c}} - \mathbb{E}(Y_{\mathbf{c}})]}{|d\mathbf{a}|} \right\} \\
&= \lim_{|d\mathbf{a}|\to 0} \left\{ \frac{\mathbb{E}(dN_X(\mathbf{a}+\mathbf{c})Y_{\mathbf{c}})}{|d\mathbf{a}|} \right\} - \lambda_N \mathbb{E}(Y) \\
&= \lim_{|d\mathbf{a}|\to 0} \left\{ \frac{\mathbb{E}(dN_X(\mathbf{a}+\mathbf{c})Y_{\mathbf{c}})}{|d\mathbf{a}|} \right\}, \quad (2.2)
\end{aligned}$$

since Y is corrected for its mean. Furthermore, stationarity implies that $\gamma_{NY}(\mathbf{a}) = \gamma_{YN}(-\mathbf{a})$.

2.2.3 The Cross-Spectral Density Function

The cross-spectral density function (or spectrum) for a stationary spatial point-lattice process is defined as the Fourier transform of the cross-covariance function, by analogy with point and lattice processes. In principle, for a

point-lattice process two cross-spectra f_{NY} and f_{YN} should be used to investigate the correlation between the two components. However, in the case of stationarity it is sufficient to consider only one cross-spectrum, say f_{NY}. The function f_{NY} at frequency $\boldsymbol{\omega} = (\omega_x, \omega_y)$ is defined by

$$f_{NY}(\boldsymbol{\omega}) = (2\pi)^2 g_{NY}(\boldsymbol{\omega}) = \int \gamma_{NY}(\mathbf{a}) \exp\{-i\boldsymbol{\omega}\mathbf{a}^\top\} d\mathbf{a}. \tag{2.3}$$

The function g_{NY} is defined in (2.3) because some authors use it as the cross-spectral function rather than f_{NY}. Moreover, g_{NY} will be used in Chapter 4 to derive asymptotic properties of the cross-spectral function. The function f_{YN} can be defined by analogy with f_{NY}. Further, $f_{YN}(\boldsymbol{\omega}) = f_{NY}(-\boldsymbol{\omega})$ since $\gamma_{NY}(\mathbf{a}) = \gamma_{YN}(-\mathbf{a})$ for a stationary point-lattice process. In general, $\gamma_{NY}(\mathbf{a}) \neq \gamma_{NY}(-\mathbf{a})$. Thus, f_{NY} will usually be a complex number.

By analogy with bivariate time series analysis, f_{NY} is decomposed into its real and imaginary parts as follows

$$\begin{aligned} f_{NY}(\boldsymbol{\omega}) &= \int \gamma_{NY}(\mathbf{a}) \exp\{-i\boldsymbol{\omega}\mathbf{a}^\top\} d\mathbf{a} \\ &= \int \gamma_{NY}(\mathbf{a}) \cos\{\boldsymbol{\omega}\mathbf{a}^\top\} d\mathbf{a} - i \int \gamma_{NY}(\mathbf{a}) \sin\{\boldsymbol{\omega}\mathbf{a}^\top\} d\mathbf{a} \\ &\equiv c_{NY}(\boldsymbol{\omega}) - i q_{NY}(\boldsymbol{\omega}), \end{aligned} \tag{2.4}$$

see Jenkins and Donald (1968, chapters 8 and 9), Rayner (1971, chapters 8 and 9), Priestley (1981b, chapter 9), Chatfield (1981, chapter 8), and Diggle (1990, chapter 8). The function $c_{NY}(\boldsymbol{\omega})$ is known as the *co-spectrum* and $q_{NY}(\boldsymbol{\omega})$ is known as the *quadrature spectrum*. Alternatively, f_{NY} can be represented in terms of its amplitude α_{NY} (known as the *amplitude spectrum*) and phase ϕ_{NY} (known as the *phase spectrum*). Hence, from (2.4)

$$\begin{aligned} f_{NY}(\boldsymbol{\omega}) &= \sqrt{c_{NY}^2(\boldsymbol{\omega}) + q_{NY}^2(\boldsymbol{\omega})} \exp\left\{i \tan^{-1}(-q_{NY}(\boldsymbol{\omega})/c_{NY}(\boldsymbol{\omega}))\right\} \\ &\equiv \alpha_{NY}(\boldsymbol{\omega}) \exp\{i\phi_{NY}(\boldsymbol{\omega})\}. \end{aligned} \tag{2.5}$$

In addition to the above spectra, the *squared coherency* and *gain* spectra are defined by analogy with bivariate time series respectively as:

$$\upsilon_{NY}(\boldsymbol{\omega}) \equiv \frac{c_{NY}^2(\boldsymbol{\omega}) + q_{NY}^2(\boldsymbol{\omega})}{f_{NN}(\boldsymbol{\omega}) f_{YY}(\boldsymbol{\omega})} = \frac{\alpha_{NY}^2(\boldsymbol{\omega})}{f_{NN}(\boldsymbol{\omega}) f_{YY}(\boldsymbol{\omega})}, \tag{2.6}$$

$$\xi_{Y|N}(\boldsymbol{\omega}) \equiv \sqrt{\frac{f_{YY}(\boldsymbol{\omega})\upsilon_{NY}(\boldsymbol{\omega})}{f_{NN}(\boldsymbol{\omega})}} = \frac{\alpha_{NY}(\boldsymbol{\omega})}{f_{NN}(\boldsymbol{\omega})}, \tag{2.7}$$

$$\xi_{N|Y}(\boldsymbol{\omega}) \equiv \sqrt{\frac{f_{NN}(\boldsymbol{\omega})\upsilon_{NY}(\boldsymbol{\omega})}{f_{YY}(\boldsymbol{\omega})}} = \frac{\alpha_{NY}(\boldsymbol{\omega})}{f_{YY}(\boldsymbol{\omega})}. \tag{2.8}$$

It can be shown that the squared coherency spectrum satisfies the inequality $0 \leq \upsilon_{NY}(\boldsymbol{\omega}) \leq 1$ by using the Cauchy-Schwartz inequality, for any two processes Y and Z we have $[\mathbb{E}(YZ)]^2 \leq [\mathbb{E}(Y)]^2[\mathbb{E}(Z)]^2$

2.2.4 Isotropy

For a stationary, isotropic (isotropy being defined in the same sense as isotropic point and lattice processes) point-lattice process the spectrum defined in (2.3) reduces to

$$f_{NY}(\boldsymbol{\omega}) \equiv f_{NY}(\omega) = 2\pi \int_0^\infty t\gamma_{NY}(t) J_0(t\omega) dt,$$

where $\omega = \sqrt{\omega_x^2 + \omega_y^2}$ and $J_0(x)$ is an un-modified Bessel function of the first kind of order zero, defined in Section 1.5. In this case, $f_{NY}(\omega)$ is a real number which implies that

$$c_{NY}(\omega) = f_{NY}(\omega) = \alpha_{NY}(\omega) \text{ and } q_{NY}(\omega) = \phi_{NY}(\omega) = 0.$$

2.3 Estimation of Cross-Spectral Functions

Consider a point-lattice pattern with components X and Y observed on a study region $[0, \ell_1] \times [0, \ell_2]$ where X denotes the point pattern and Y denotes

the lattice pattern. It is also assumed that Y is corrected for its mean. Define the *cross-periodogram* of the pattern as $F_{NY}(p,q) = F_N(p,q)\overline{F}_Y(p,q)$ where $F_N(p,q)$ and $F_Y(p,q)$ are as defined in (1.10) and (1.11), respectively. Therefore,

$$\begin{aligned} F_{NY}(p,q) &= \left(\sum_{j=1}^{N_X} \exp\left\{-2\pi i(\frac{pa_{1j}}{\ell_1} + \frac{qa_{2j}}{\ell_2})\right\}\right) \times \\ &\quad \left(\frac{1}{\sqrt{\ell_1\ell_2}} \sum_{b_1=0}^{\ell_1-1}\sum_{b_2=0}^{\ell_2-1} Y_{(b_1,b_2)} \exp\left\{2\pi i(\frac{pb_1}{\ell_1} + \frac{qb_2}{\ell_2})\right\}\right) \\ &= (A_N + iB_N)(A_Y - iB_Y) \\ &= (A_N A_Y + B_N B_Y) - i(A_N B_Y - B_N A_Y) \\ &= C_{NY} - iQ_{NY}, \end{aligned} \tag{2.9}$$

where C_{NY} and Q_{NY} are estimates of the co- and quadrature spectra defined in (2.4), respectively. Similarly, estimates of the amplitude (A_{NY}), phase (Φ_{NY}), squared coherency (Υ_{NY}), and gain ($\Xi_{N|Y}, \Xi_{Y|N}$) spectra defined in Section 2.2.3 can be derived by substituting the estimates of the co- and quadrature spectra in (2.5) to (2.8). If the raw estimates of the co- and quadrature spectra are substituted in (2.6) then Υ_{NY} will be equal to one at all frequencies. Therefore, to obtain a useful estimate for the squared coherency one or more of the auto-, co- and quadrature spectra must be smoothed (see, for example, Priestley, 1981b).

2.3.1 Symmetry

The estimates of the cross-spectral functions are symmetric in the following sense:

$$F_{NY}(-p,-q) = \overline{F}_{NY}(p,q), \qquad C_{NY}(-p,-q) = C_{NY}(p,q),$$
$$Q_{NY}(-p,-q) = -Q_{NY}(p,q), \quad A_{NY}(-p,-q) = A_{NY}(p,q),$$
$$\Phi_{NY}(-p,-q) = -\Phi_{NY}(p,q), \quad \Upsilon_{NY}(-p,-q) = \Upsilon_{NY}(p,q).$$

Therefore, one of the frequencies, say p, is needed only to vary over positive values and the other, say q, varies over both negative and positive values, as in the one-component case. In what follows, both the auto- and cross-periodograms are evaluated at the frequencies (ω_p, ω_q) where $p = 0, \ldots, [\ell_1/2]$ and $q = -[\ell_2/2], \ldots, [(\ell_2 - 1)/2]$. It is worth noting here that ω_p and ω_x will be used interchangeably, similarly ω_q and ω_y.

2.3.2 Smoothing and Scaling

It was mentioned above that we need to smooth the cross-periodograms to obtain a meaningful estimate for the squared coherency spectrum. In examples to follow the auto-, co- and quadrature periodograms will be smoothed according to one of the techniques discussed in Section 1.8. On substituting these estimates in (2.5) to (2.8) the smoothed estimates of amplitude, phase, squared coherency, and gain periodograms are obtained.

Furthermore, in Chapter 1 we mentioned that the point and lattice periodograms are scaled such that in the case of CSR the expected values of the estimated auto-spectra are equal to one. The cross-spectra estimates will be scaled similarly. The scaled co- and quadrature spectra are

defined as $\overset{\circ}{C} = C_{NY}/\sqrt{N_X \hat{\sigma}^2_{YY}}$ and $\overset{\circ}{Q} = Q_{NY}/\sqrt{N_X \hat{\sigma}^2_{YY}}$. Calculating the amplitude and gain spectra *after* scaling the co- and quadrature periodograms yields $\overset{\circ}{A} = A_{NY}/\sqrt{N_X \hat{\sigma}^2_{YY}}$, $\overset{\circ}{\Xi}_{N|Y} = \Xi_{N|Y}/\sqrt{N_X/\hat{\sigma}^2_{YY}}$, and $\overset{\circ}{\Xi}_{Y|N} = \Xi_{Y|N}/\sqrt{\hat{\sigma}^2_{YY}/N_X}$. However, the phase and squared coherency are not affected by scaling because the same scaling factor appears in the numerator and denominator of the formulae defining these spectra.

2.3.3 Interpretation of Sample Cross-Spectra

In this section, a brief description of what the different cross spectra measure is given. The following terminology is in accordance with Priestley (1981b, chapter 9) and is based on the result that stationary processes possess spectral representations.

The co-spectrum, C_{NY}, represents the covariance between the coefficients of the *in-phase* components of the two patterns. The quadrature spectrum, Q_{NY}, represents the covariance between the coefficients of the *out-of-phase* components. The amplitude spectrum measures the relative value of the power at the frequency ω in the components X and Y. The squared coherency spectrum measures the square of the linear correlation between the components of the point-lattice process at frequency ω. Moreover, the closer the square root of this value is to unity the stronger the relationship between the two processes is at frequency ω. Gain spectra are used mainly when one suspects there is a causal relationship between the components of a point-lattice process. So $\Xi_{N|Y}(\omega)$ represents the regression coefficient at frequency ω in the linear regression of N_X on Y. An equivalent interpretation holds for $\Xi_{Y|N}(\omega)$. The phase spectrum represents the mean value of the phase shift

between the components X and Y at frequency ω, in the sense described by Priestley (1981b), assuming that the phase and amplitude of the spectral representations for each process are independent random variables.

To demonstrate explicitly what the phase spectrum measures a lattice-lattice process is considered. A lattice-lattice process is a process in which the two components are lattice processes; more details are provided in Chapter 5. Suppose that one of the components is a linear transformation of the other component with a shift and added noise, denoted by say $Y_{\mathbf{b}} = aX_{\mathbf{b}-\mathbf{d}} + \epsilon_{\mathbf{b}}$ where $\mathbf{d}$ is the shift between the two processes. It can be proved that the phase spectrum for this model is a linear function of frequency and that its slope in a specified direction is the magnitude of the shift in that direction.

Figure 2.2(a) is the lattice pattern, X, of Figure 1.3. Figure 2.2(b) is the lattice pattern X shifted to the east by $\mathbf{d} = (d_1, d_2) = (1, 0)$. Denote the shifted process by Y. Figures 2.2(c), (d), and (e) represent the estimated co-, quadrature, and amplitude spectra, respectively, of the lattice-lattice pattern presented in Figures 2.2(a) and (b). The co-spectrum exhibits a positive peak at the frequency $(2, 6)$ indicating that the in-phase components are positively correlated. The quadrature spectrum exhibits a trough at this frequency; this indicates that the components are out of phase. The amplitude spectrum has also a peak at this frequency, thus, confirming that the two processes are correlated. However, whether they are positively or negatively correlated cannot be detected from the amplitude spectrum; one needs to refer to the co-spectrum.

Figure 2.2(f) is the estimated phase spectrum. From this graph one can deduce that the phase spectrum is a linear function of frequency. Further-

more, one can deduce that the two patterns are in phase in the SN direction and that there exists a phase shift in the WE direction. The value of this phase shift can be calculated from the slope of Figure 2.2(f). For example, for the bandwidth $q = 0$, $p = 1, \ldots, 15$ the periodogram values increase from $\frac{62}{1000}\pi$ to $\frac{937}{1000}\pi$ and since $\omega_x = \omega_p = 2\pi p/\ell_1$ then $d_1 = \frac{\frac{(937-62)\pi}{1000}}{\frac{2\pi(15-1)}{32}} = 1$. Therefore, we can deduce empirically from the phase spectrum that the second lattice, Y, is to the east of the first, X, by one unit.

Figures 2.2(g), (h), and (i) represent the estimated squared coherency and gain spectra. These estimates fluctuate around one implying that the two processes are linearly correlated at all frequencies. Since the two components are linear transformations of each other then the gain spectra and the squared coherency must be identically equal to one.

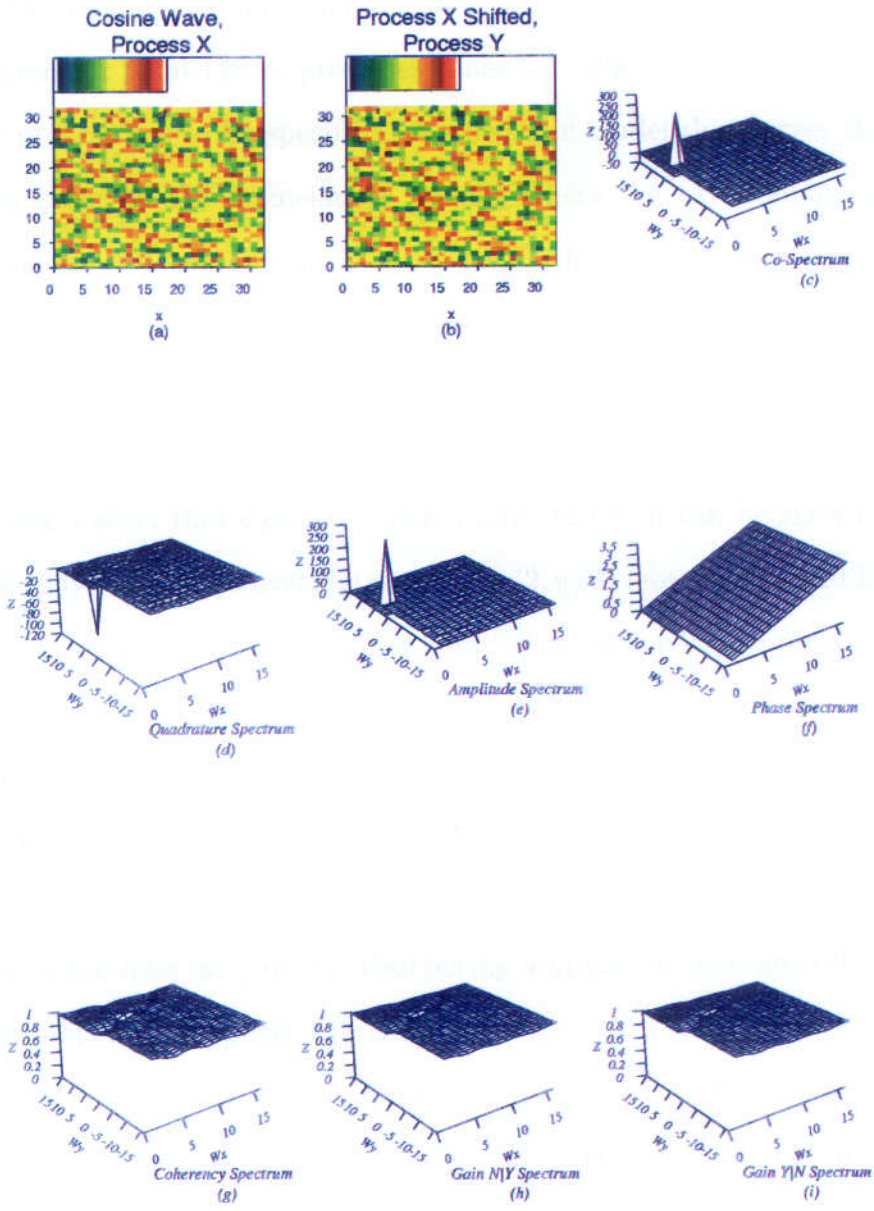

Figure 2.2: (a) Figure 1.3 and (b) the shifted pattern of (a); (c) to (f) are the raw estimates of co-, quadrature, amplitude, and phase spectra; (g) to (i) are the smoothed estimates of the squared coherency and gain spectra.

2.4 CSR for a Point-Lattice Process

As in the case of a single component a model that would serve as a null hypothesis for point-lattice processes is needed. Therefore, CSR for a point-lattice process has to be specified. A stochastic model that serves this purpose is given by the point-lattice process where the two components are independent and component X is an HPP whilst component Y is Gaussian white noise. Thus, $\gamma_{NY} = 0$ where γ_{NY} is defined in (2.2). Therefore, $f_{NY}(\omega) = 0$ for all ω. Consequently, $c_{NY}(\omega) = 0$, $q_{NY}(\omega) = 0$, $\alpha_{NY}(\omega) = 0$, $\upsilon_{NY}(\omega) = 0$, $\xi_{N|Y}(\omega) = 0$, and $\xi_{Y|N}(\omega) = 0$.

It might seem that $\phi_{NY}(\omega)$ is indeterminate but it can be shown that it is uniformly distributed over the range $(-\pi/2, \pi/2)$ (see Jenkins and Donald, 1968, chapter 8). The above results hold for any point-lattice process where the two components are not correlated. Hence, departures from flatness in any of the cross-spectral periodograms except for the phase spectrum indicate that the two components are correlated. It is worth noting that the phase spectrum is defined (mod 2π). However, $\Phi_{NY}(\omega)$ is usually taken to belong to the interval $(-\pi, \pi)$. Restricting $\Phi_{NY}(\omega)$ to this interval leads to discontinuities in the phase spectrum.

Figure 2.3 is a realisation of a point-lattice pattern with two independent components X and Y; X is the realisation of an HPP given in Figure 1.6 and Y is the realisation of a white noise process given in Figure 1.7. This pattern will be referred to as CSRPLE. Figures 2.4 and 2.5 represent the smoothed estimates of the auto- and cross-spectra of CSRPLE using Method A four and eight times, respectively. The auto-spectra are relatively flat and close

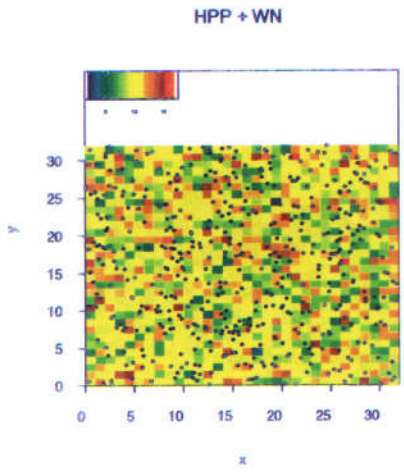

Figure 2.3: CSRPLE: a realisation of a point-lattice process that exhibits CSR.

to the expected value one. The estimates of the co-, quadrature, amplitude, squared coherency, and gain spectra are also flat and fluctuate around the expected value zero. The phase sample spectrum has no structure. In addition to smoothing, all the periodograms are scaled as discussed in Section 2.3.2.

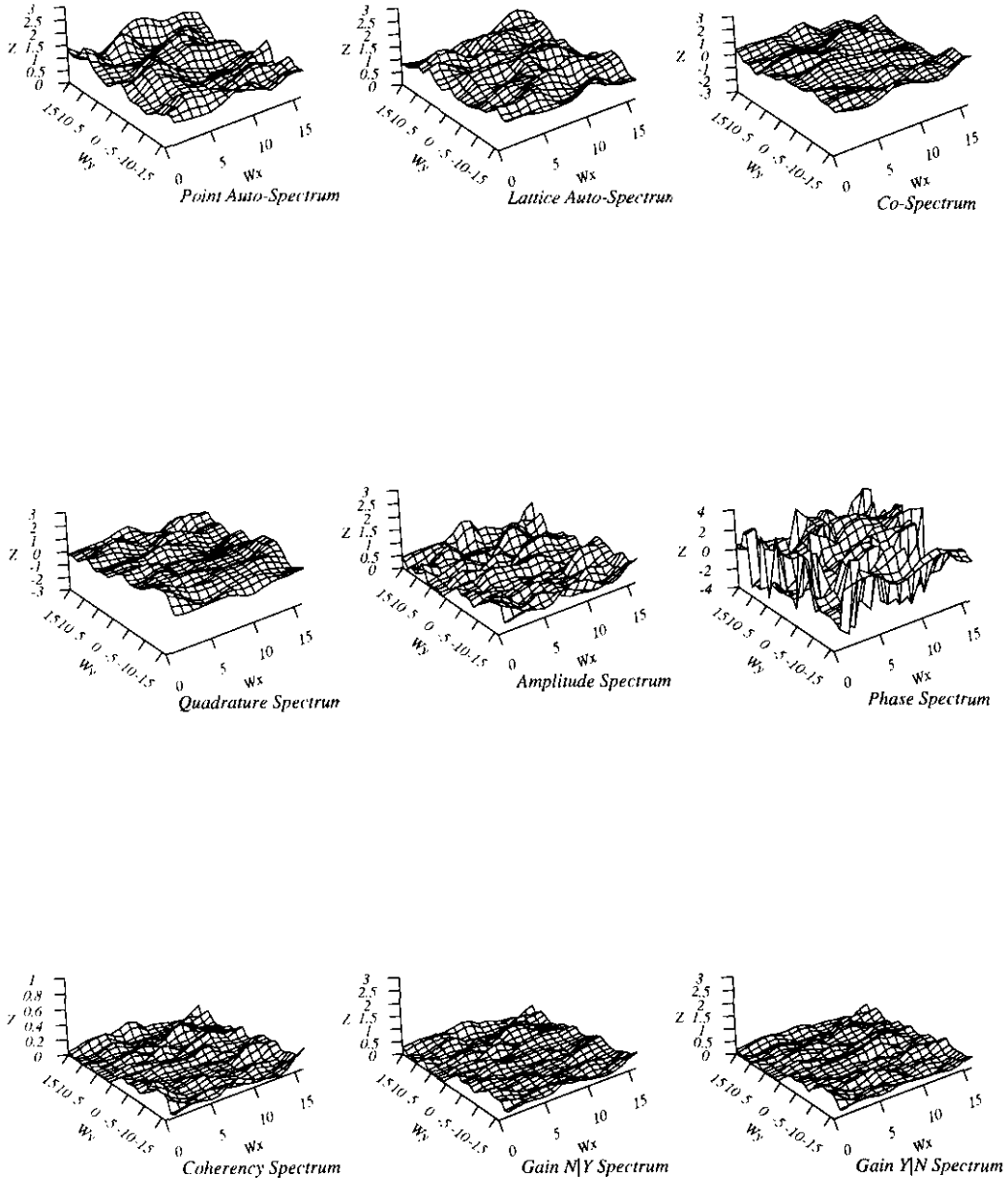

Figure 2.4: Estimated auto- and cross-spectra for CSRPLE. Estimates are smoothed using Method A four times.

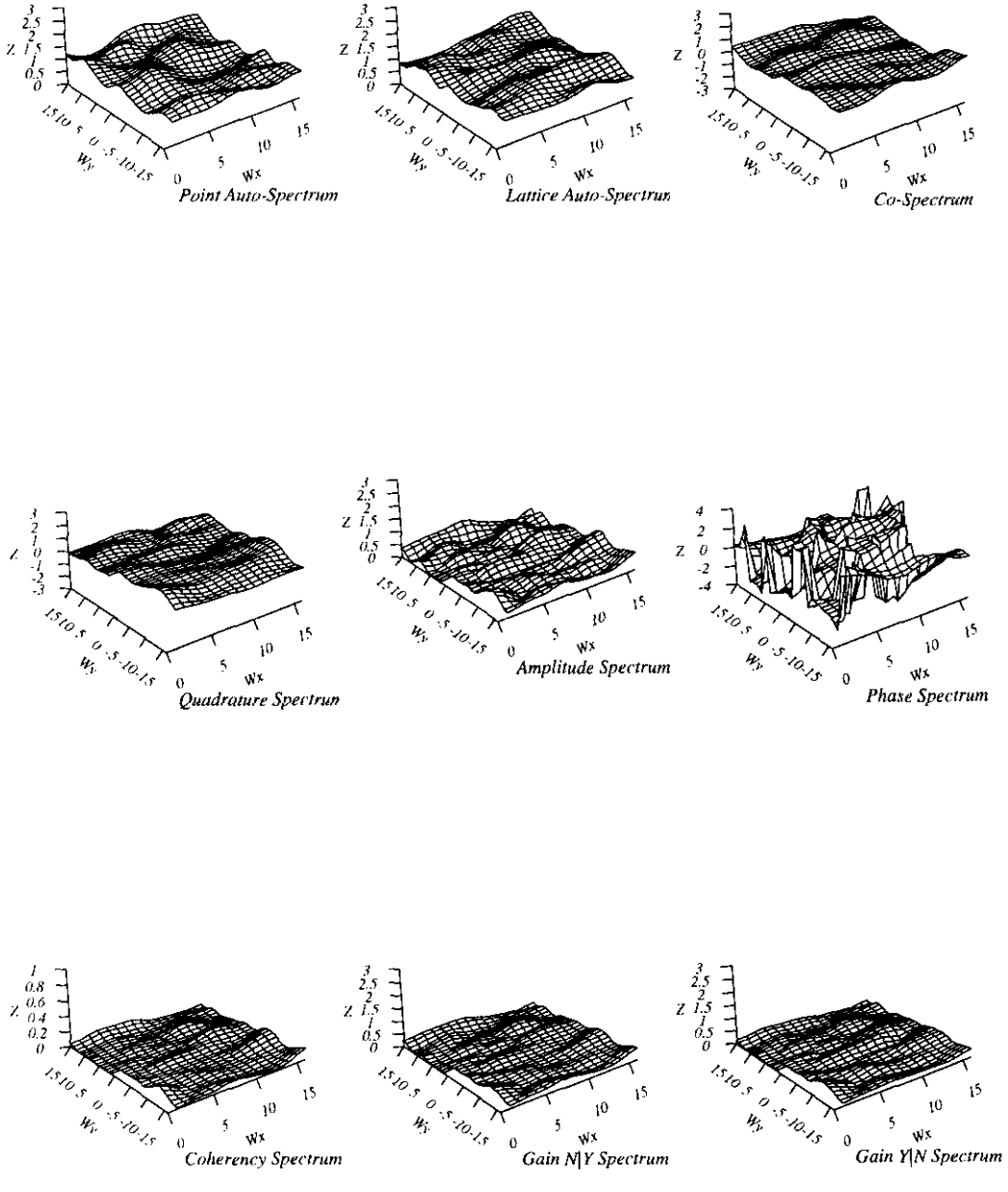

Figure 2.5: Estimated auto- and cross-spectra for CSRPLE. Estimates are smoothed using Method A eight times.

2.5 Simulating a Point-Lattice Process

In this section, methods to simulate point-lattice processes with associated components are introduced. These methods can be divided into two categories. One is based on simulating the lattice pattern first while the second is based on simulating the point pattern first. Potential applications of the first category can be found in forestry. For example, altitude data that are recorded on a lattice might affect the growth of a particular tree species. Examples of the second category might be found in agriculture, such as the composition of soil nutrients, which can be observed on a regular grid, being altered due to the presence of a certain type of vegetation.

For each simulation method an artificial point-lattice example is provided. These examples illustrate how cross-spectral estimates can be used to study the relationship between the two components of a point-lattice pattern. In some of these examples association between the two components is limited to a couple of frequencies, whereas in the rest of the examples association is spread across a wider range of frequencies. These two types of association mirror relationships present in real point-lattice patterns.

2.5.1 Simulating a Point-Lattice Process I

In this section, we propose three methods for simulating a point pattern given a realisation of a lattice process. Two of these methods are based on thresholding the lattice pattern. The first method reflects the belief that the point process is thought to have originated from an HPP, but depending on thresholded values of the lattice pattern only a subset of the events is retained. For

example, seeds spread homogeneously across an agricultural field may not all grow due to variability in soil nutrients. Here seeds are potential events of a point pattern and soil nutrient measurements form a lattice pattern. The second method reflects piecewise homogeneity of the point pattern in which the piecewise intensity function is obtained by thresholding the lattice pattern. In the third method points are thinned according to an intensity function that depends on the lattice pattern.

2.5.1.1 Thresholding

In this section, the two methods that are based on thresholding the lattice pattern are discussed. Given the lattice pattern, the first method which will be referred to as *THRESA* generates the point pattern as follows.

1. Generate an HPP and let K be the number of events of this pattern.

2. Retain a point if the value of the lattice quadrat the point belongs to is within a pre-determined range.

3. Let R denote the total number of events retained. If the number of events is pre-specified, say N_X, then set $K = N_X - R$ and repeat steps 1 and 2 until the required number of events is attained. Otherwise, stop.

Assuming that the lattice pattern is given, the second method involves the following steps to generate a point pattern. This method will be referred to as *THRESB*. Let Y be the lattice pattern and let

$$\Delta_{\mathbf{b}} = \Delta_{(b_1,b_2)} = [b_1, b_1 + 1] \times [b_2, b_2 + 1],$$

for $b_1 = 0, \ldots, \ell_1 - 1$ and $b_2 = 0, \ldots, \ell_2 - 1$, be the quadrats determined by this lattice. Then the point pattern, X, is generated as follows.

1. Let $[\boldsymbol{\lambda}_N]$ denote the matrix generated by thresholding the lattice pattern Y. For example, one can set entries of $\boldsymbol{\lambda}_N$ to be equal to corresponding entries of the lattice pattern if the lattice entry exceeds a given value and set to zero otherwise. Note here that Y is assumed to be non-negative.

2. Generate another matrix, $[\mathbf{N}_X]$, where individual entries $\mathbf{N}_X(b_1, b_2)$ are sampled from a Poisson process with mean $\boldsymbol{\lambda}_N(b_1, b_2)$.

3. In each quadrat, $\Delta_{\mathbf{b}}$, generate an HPP in which the number of events is given by $\mathbf{N}_X(b_1, b_2)$.

Next, we simulate two artificial examples using THRESA and THRESHB, respectively, and study their properties using spectral analysis.

2.5.1.2 Example 1: THRESACOS

In this example, the point and lattice components have simple structures, hence, the association between the two is bound to be simple. Figure 2.6 represents a realisation of a point-lattice process and its spectral estimates are provided in Figure 2.7. The lattice pattern, Y, was generated by setting

$$Y_{(b_1,b_2)} = 2\cos(2\pi(\frac{pb_1}{\ell_1} + \frac{qb_2}{\ell_2})) + \sin(2\pi(\frac{pb_1}{\ell_1} + \frac{qb_2}{\ell_2})) + \epsilon_{(b_1,b_2)},$$

where $\ell_1 = \ell_2 = 64, p = 5, q = 4, b_1 = 0, \ldots, \ell_1 - 1, b_2 = 0, \ldots, \ell_2 - 1$, and $\epsilon_{(b_1,b_2)}$ are IID random variables from the standard normal distribution. The minimum of this realisation was then subtracted to ensure that the lattice

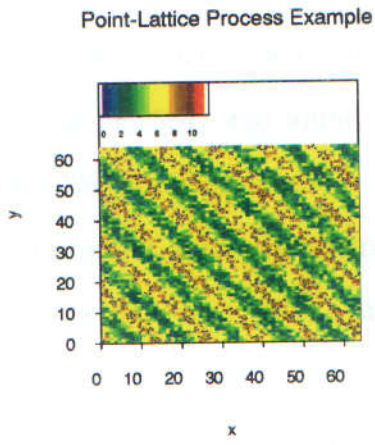

Figure 2.6: THRESACOS: a realisation of a spatial point-lattice process. The lattice pattern is a cosine + sine + noise, and the point pattern is generated using THRESA.

values are positive. The point pattern, X, was then generated according to the method THRESA with $N_X = 1000$. Events were retained only if $7 \leq Y \leq 11$. The lattice pattern ranges from 0 to 11.26, hence, events are associated with relatively large values of the lattice pattern.

Figures 2.7(a) and (b) are the raw estimates of the auto-periodograms of the point and lattice patterns, respectively. Both periodograms exhibit a distinct peak at the frequency $(5, 4)$ corresponding to the deterministic component of the lattice process. The power at this peak contributes to almost 70% of the total power in the lattice spectrum. Thus, the lattice spectrum is composed of waves (stripes in the pattern of Figure 2.6) repeating five times in the WE direction and four times in the SN direction. These waves are perpendicular to the vector that determines an angle of 38.66° with respect to the WE direction. Henceforth, when we report the direction of travel of the waves we will use the terminology that the waves travel in the

direction of the vector with angle θ to mean that the waves are perpendicular to the vector which determines an angle θ with the axis in the WE direction. Using Fisher's test the peak at $(5, 4)$ was found to be the only significant peak at the 1%, 5%, and 10% significance levels.

The peak at $(5, 4)$ in the point auto-periodogram indicates that the pattern resembles a cluster process. Indeed, events are clustered at large values of the lattice pattern. Furthermore, there is a minor peak at $(10, 8)$ which can be attributed to the fact that the clusters exhibit a pattern of regularity. This arises because events belonging to different clusters cannot lie within a minimal distance from each other by construction of the pattern. These two dominant peaks were found to be the only significant ordinates at the 1%, 5%, and 10% significance levels using Fisher's test for point processes. Better insight about the individual components of the point-lattice pattern can be gained by looking at the polar spectra for these processes (see Mugglestone, 1990). However, we are interested mainly in the interaction between the two components of the point-lattice process rather than studying each individually.

Figures 2.7(c) and (d) are the raw estimates of the co- and quadrature spectra, respectively. Both spectra exhibit a peak at the frequency $(5, 4)$. The peak in the co-spectrum implies that events tend to occur at large values of the lattice pattern. Furthermore, the two patterns are out-of-phase as indicated by the peak in the quadrature spectrum. This is expected since the point pattern component peaks/troughs do not coincide exactly with those of the lattice pattern, the point pattern is associated with the upper quartile of the lattice pattern.

Figure 2.7(e) represents the smoothed amplitude spectrum. Again, the peak emphasises the correlation between the two components of the pattern. Figure 2.7(f) is the smoothed phase spectrum. The phase spectrum contains a number of discontinuities which can be attributed to the fact that the phase spectrum is constrained to the interval $(-\pi, \pi)$.

The squared coherency spectrum, Figure 2.7(g), exhibits a peak in the neighbourhood of the frequency $(5, 4)$. Hence, the two components are linearly correlated at this frequency. The gain spectrum of the point pattern given the lattice pattern presented in Figure 2.7(h) has power at most frequencies with a mean of 0.8693 and a median of 0.8309. In contrast, the gain spectrum of the lattice pattern given the point pattern presented in Figure 2.7(i) has its power concentrated at a peak around the frequency $(5, 4)$ and is almost zero elsewhere. Thus, given the lattice process, Y, one can make inferences about the behaviour of the point process, X, for most frequencies. This can be attributed simply to the way the point process was simulated conditionally on the values of the lattice pattern. On the other hand, given the point process inferences about the lattice process can be made only around the frequency $(5, 4)$.

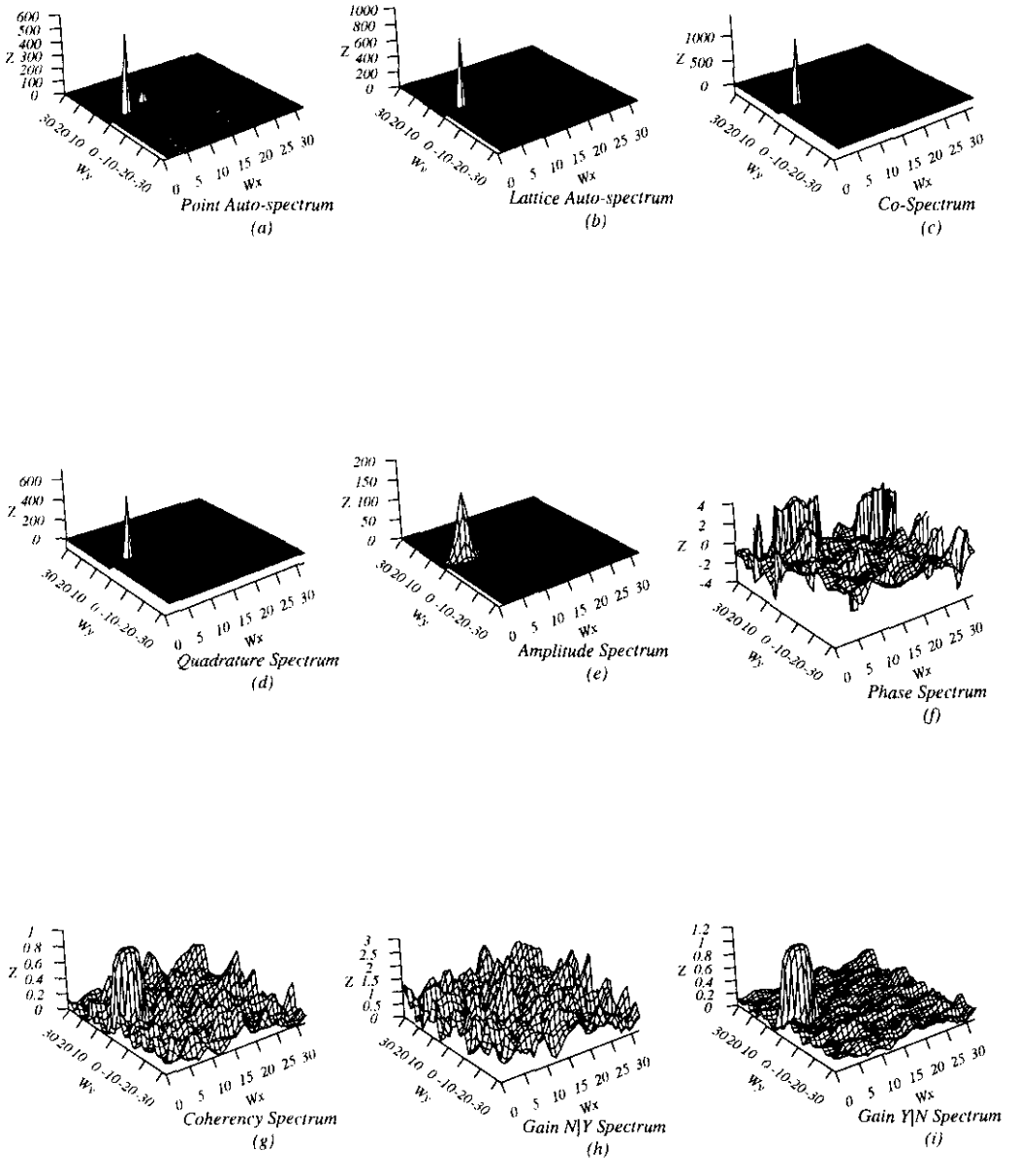

Figure 2.7: Spectra for THRESACOS (Figure 2.6). (a) and (b) Raw auto-periodograms; (c) and (d) raw co- and quadrature spectra; (e) to (i) smoothed amplitude, phase, squared coherency and gain spectra using Method A four times.

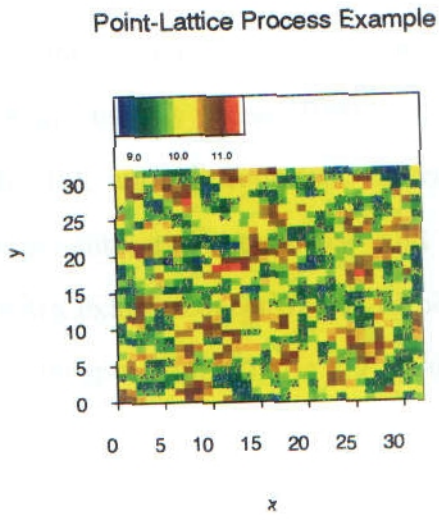

Figure 2.8: THRESBMA: a realisation of a spatial point-lattice process. The lattice pattern is a moving average and the point pattern is generated using THRESB.

2.5.1.3 Example 2: THRESBMA

Figure 2.8 is the graphical representation of a point-lattice pattern where the lattice component is a spatial moving average and the point component is generated using THRESB. The lattice pattern, Y, has been generated by

$$Y_{(b_1,b_2)} = \frac{1}{3}\epsilon_{(b_1,b_2)} + \frac{1}{6}\{\epsilon_{(b_1-1,b_2)} + \epsilon_{(b_1+1,b_2)} + \epsilon_{(b_1,b_2-1)} + \epsilon_{(b_1,b_2+1)}\},$$

where $b_1, b_2 = 0, \ldots, 31$, $\epsilon_{(u,v)}$ are IID from $N(10,1)$, and $u, v = -1, \ldots, 32$. Then THRESB was used to generate an associated point pattern. Events were generated if $0.76 \leq Y/Y^* \leq 0.86$, where $Y^* = 11.35$ is the maximum of the lattice pattern. Note that the minimum of the lattice pattern is 8.669. Thus, events are associated with relatively low values of the lattice pattern. The total number of events generated is 3242. A random sample from the point process of size 742 was then chosen. The number 742 was

itself randomly chosen from integers less than a thousand. The reason for not retaining all the events is that in the real examples discussed later the number of events does not usually exceed 1000 events.

Figures 2.9(a), (b), (c), and (d) represent the raw auto-spectra for the point and lattice components, and the raw co- and quadrature spectra, respectively. These spectra exhibit concentration of power at low frequencies. The smoothed amplitude spectrum, Figure 2.9(e), exhibits the same structure as the above spectra.

Furthermore, the lattice spectrum exhibits concentration of power around the lines $\omega_x = 0$ and $\omega_y = 0$. This feature usually occurs in image analysis when image discontinuities are produced by wrap-round of the image domain. Tapering is then used to remove the artificial vertical and horizontal stripes that occur in the spectra as those in Figure 2.9(b) (for more details see Glasbey and Mardia, 2000; Glasbey and Horgan, 1995; Robinson, 1983). Figure 2.10 gives the significant ordinates of the lattice and point periodograms at the 1%, 5%, and 10% significance levels using Fisher's test.

The negative concentration of power at low frequency magnitudes in the co-spectrum implies that the two components are negatively correlated. Thus, events tend to occur at low lattice values. The quadrature spectrum has negative concentration of power around frequencies with small magnitudes. Therefore, there is a phase shift between the two components.

The phase spectrum, Figure 2.9(f), reveals a negative slope in the WE direction despite the existence of discontinuities at some frequencies. The squared coherency spectrum, Figure 2.9(g), has the same power distribution as most of the above spectra. The values for the squared coherency spectrum

are relatively high for frequencies with small magnitudes. For the frequency band with $p = 0, \ldots, 7$ and $q = -7, \ldots, 7$, the mean and median values of the square root of the squared coherency spectrum are 0.8378 and 0.8468, respectively. Similar behaviour is demonstrated by the gain spectrum presented in Figure 2.9(i). However, the gain spectrum of Figure 2.9(h) has its peaks at high frequencies.

In summary, the two components are negatively correlated and out of phase. In addition, there is some evidence that the two processes are linearly correlated at low frequencies as seen from the squared coherency spectrum.

2.5.1.4 Thinning

Another method to generate a point pattern given the lattice pattern is discussed in this section. This method which will be termed *THIN* uses the techniques of thinning a point process introduced by Lewis and Shelder (1979) to generate a non-homogeneous Poisson process. The idea of thinning was also used by Ogata (1981) who provided a number of algorithms to simulate one-dimensional point processes specified by their conditional intensities. The intensity of the point pattern generated by THIN depends on the lattice pattern as it is the case for THRESB. However, generation of events in THRESB is completely determined by the lattice pattern but this is not true of events generated using THIN. The steps involved in generating a point pattern using THIN are as follows.

1. Define the intensity function, $\{\lambda(\mathbf{a})\}$, of the point pattern to be a function of the lattice pattern. For example, $\lambda(\mathbf{a})$ can be defined as $\lambda(\mathbf{a}) = Y_{[\mathbf{a}]} = Y_{([a_1],[a_2])}$ or as an average of lattice values of neighbour-

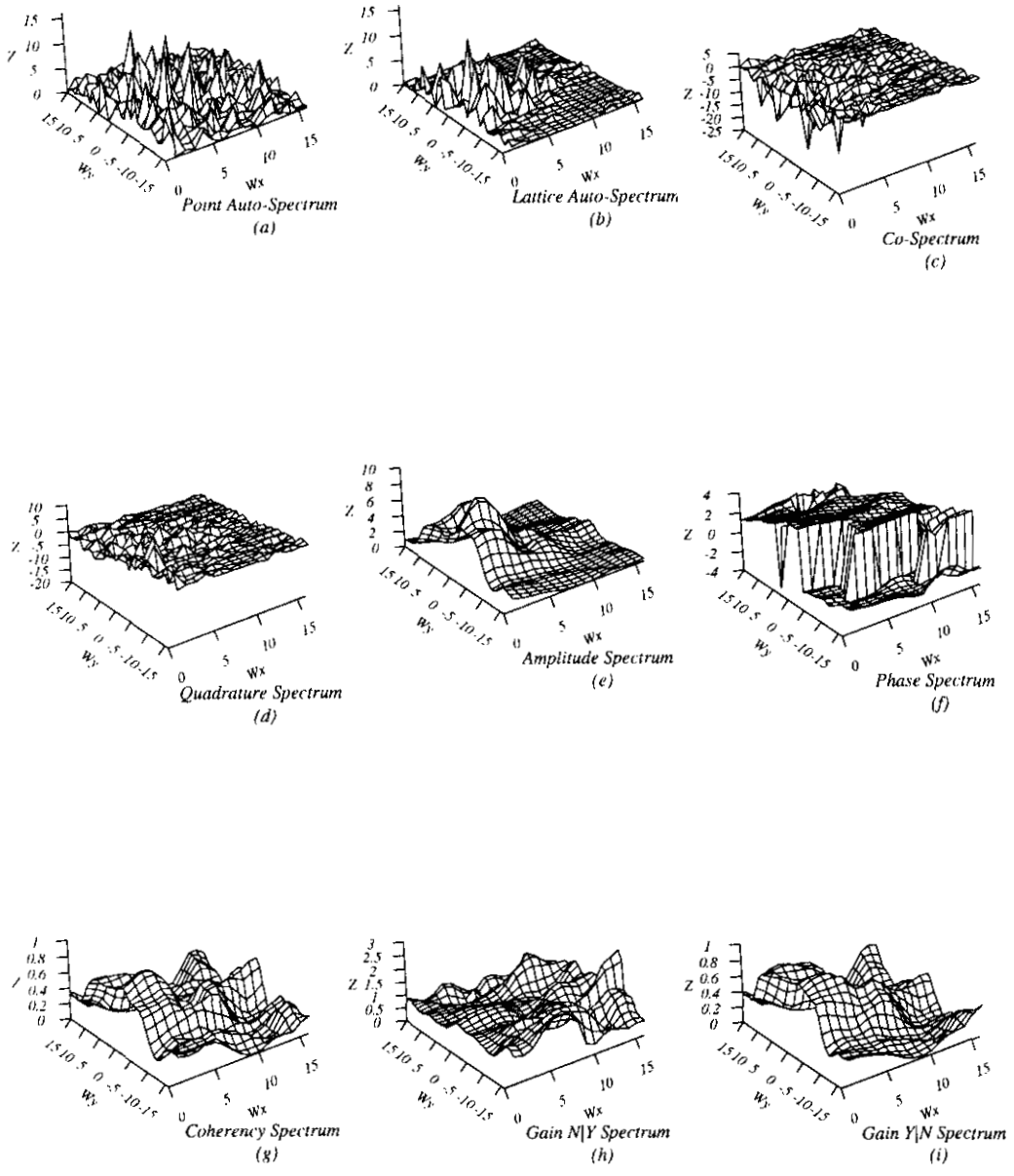

Figure 2.9: Spectra for THRESBMA (Figure 2.8). (a) and (b) Raw auto-periodograms; (c) and (d) raw co- and quadrature spectra; (e) to (i) smoothed amplitude, phase, squared coherency and gain spectra using Method A four times.

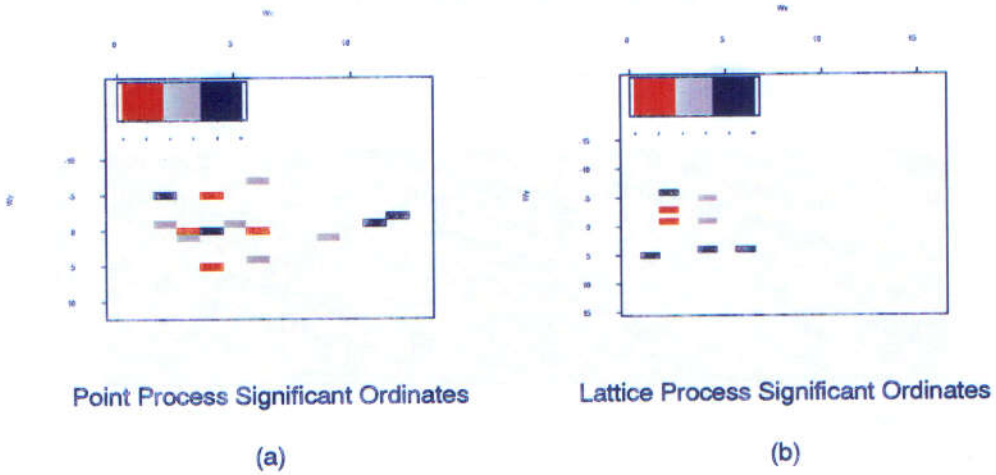

Figure 2.10: (a) Significant ordinates of the sample point spectrum of THRESBMA (Figure 2.9(a)); (b) significant ordinates of the sample lattice spectrum of THRESBMA (Figure 2.9(b)). The pixel value indicates the percentage level of significance.

ing quadrats, assuming that Y is non-negative.

2. Generate a point pattern and let N_X denote the number of events of this pattern. For example, the point pattern can be generated from an HPP with intensity equal to λ^*, the maximum of the intensity function generated in Step 1. Another example is provided by simulating an HPP process of parent events. Then for each parent event generate an integer, j, from a Poisson process with mean equal to the underlying intensity at the location of that event. Next by analogy with simulating an MTCP, for each parent generate j offspring by displacing the parent's co-ordinates by a random variable from the normal distribution with zero mean. In the final pattern retain offspring only.

3. Generate N_X uniformly distributed variables, U, on the interval $(0, 1)$.

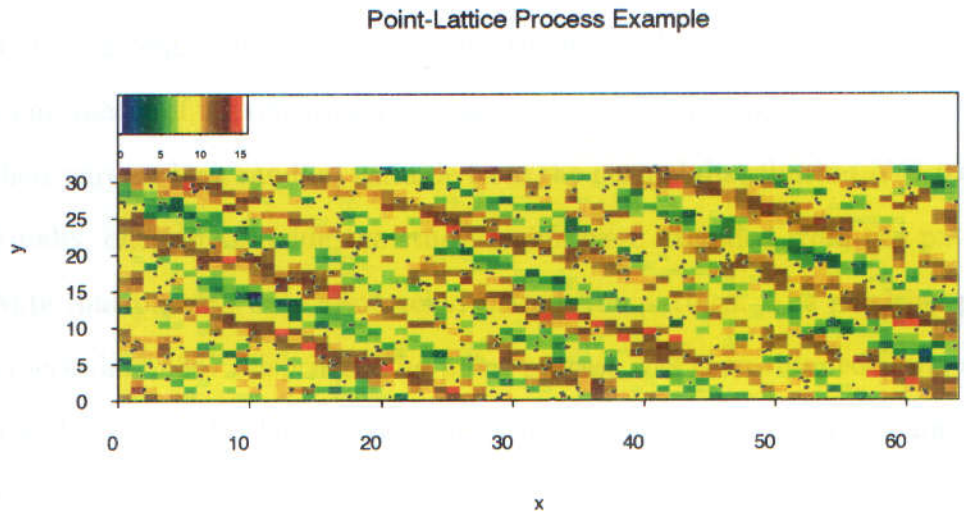

Figure 2.11: THINCOS: a realisation of a spatial point-lattice process. The lattice pattern is cosine + noise and the point pattern is generated using THIN.

4. Retain a point if $U_i \leq \lambda_i/\lambda^*, i = 1, \ldots, N_X$ where λ_i is the intensity at the i^{th} event.

2.5.1.5 Example 3: THINCOS

The lattice pattern in this example exhibits a simple structure, and the point pattern is generated using THIN. Figure 2.11 represents the graph of the point-lattice pattern THINCOS. The lattice pattern component of THINCOS was generated by

$$Y_{(b_1,b_2)} = 2\cos(2\pi(\frac{5b_1}{64} + \frac{4b_2}{32})) + \cos(2\pi(\frac{2b_1}{64} + \frac{3b_2}{32})) + \epsilon_{(b_1,b_2)},$$

where $b_1 = 0, \ldots, 63, b_2 = 0, \ldots, 31$, and $\epsilon_{(b_1,b_2)}$ are IID random variables from the normal distribution $N(0,1)$. The point pattern was generated by first simulating a sample of five hundred parents from an HPP. Next, the

number of offspring for each parent was obtained from a Poisson process with mean equal to the quadrat value the parent belonged to. After that the co-ordinates of the offspring were calculated by displacing the co-ordinates of their parents by a random variable from the normal distribution $N(0, 0.064)$. Finally, offspring outside the study region were excluded from the pattern. Note that parents were also excluded from the pattern. The resulting point process had 4367 offspring. The point process was then thinned using steps 3 and 4 of THIN. The intensity at a particular location was calculated as $Y_{(b_1,b_2)} \times \hat{\lambda}_P$, where $\hat{\lambda}_P = 500/(32 \times 64) \approx 0.244$ is the intensity of the pattern formed by the parents. The number of offspring retained was 2682.

Figure 2.12(a) is the point pattern sample spectrum. Peaks are detected at frequencies $(5, 4), (24, 3)$, and $(24, 5)$. Figure 2.13(a) gives the significant periodogram ordinates using Fisher's test. The peaks in the lattice pattern sample spectrum, Figure 2.12(b), occur at $(5, 4)$ and $(2, 3)$. Note that the magnitude at $(5, 4)$ is greater than that at $(2, 3)$ in agreement with the magnitudes of the cosine components that were used to generate the lattice process.

The co-spectrum, Figure 2.12(c), reveals that the in-phase components of the point-lattice process are positively correlated at the two frequencies $(5, 4)$ and $(2, 3)$. Similarly, the quadrature spectrum, Figure 2.12(d), implies that the out-of-phase components are positively correlated at the same frequencies. Hence, there is a phase shift between the two components. The correlation between the two components is emphasised by the peak in the amplitude spectrum, Figure 2.12(e). No general trend, however, can be detected in the phase spectrum, Figure 2.12(f).

The squared coherency and gain spectra, Figures 2.12(g) and (i), exhibit a peak in the neighbourhood of the frequency $(5, 4)$. However, the other gain spectrum, Figure 2.12(h), has a peak in the neighbourhood of the frequency $(-16, 31)$. Note that the squared coherency is almost zero elsewhere. This can result in an erratic behaviour in the phase spectrum. In Chapter 4, it will be shown that the variance of the phase spectrum is dependent on the inverse of the squared coherency spectrum.

Next, methods to simulate the lattice process given the point process are discussed.

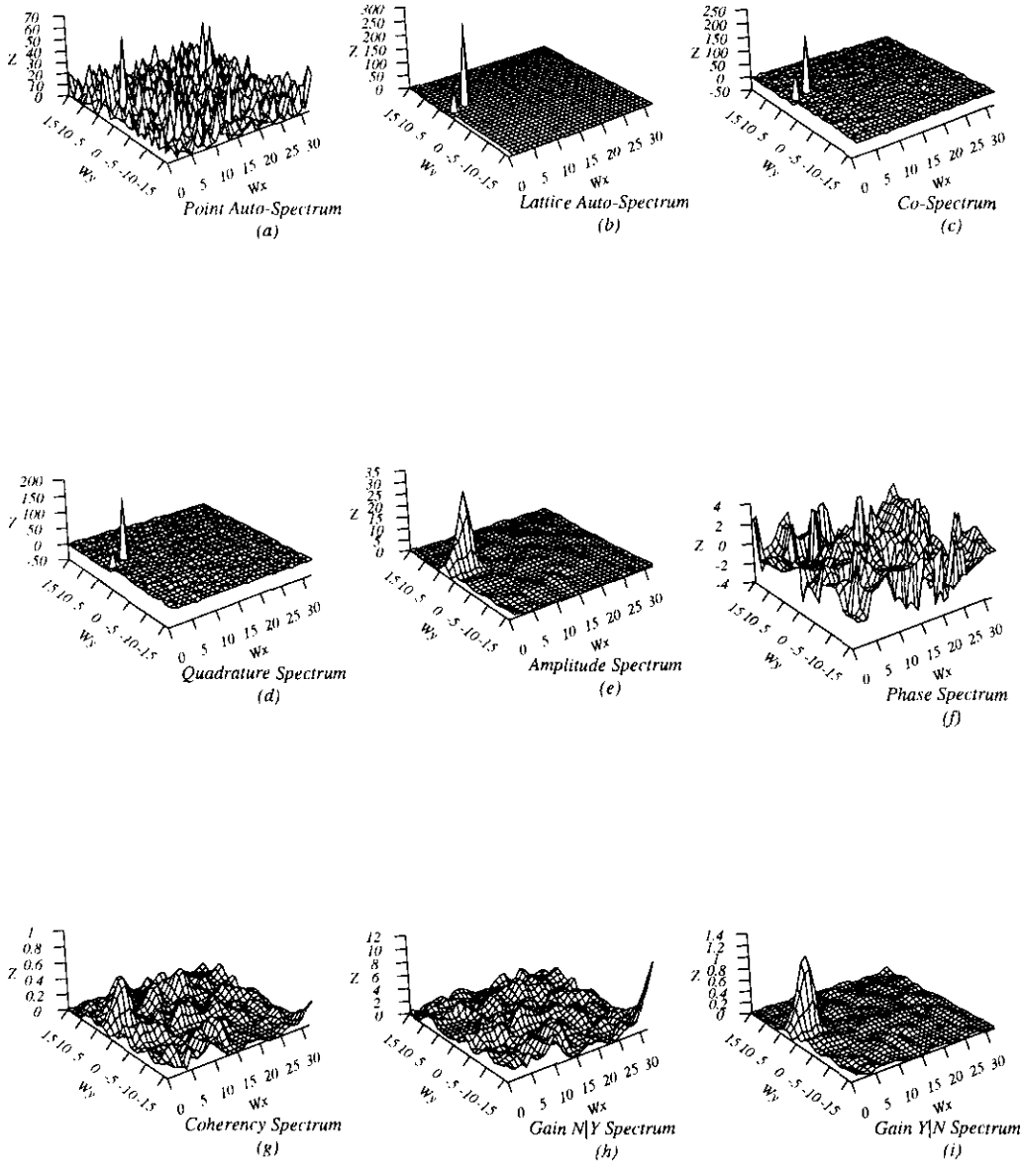

Figure 2.12: Spectra for THINCOS (Figure 2.11). (a) and (b) Raw auto-periodograms; (c) and (d) raw co-and quadrature spectra; (e) to (i) smoothed amplitude, phase, squared coherency and gain spectra using Method A four times.

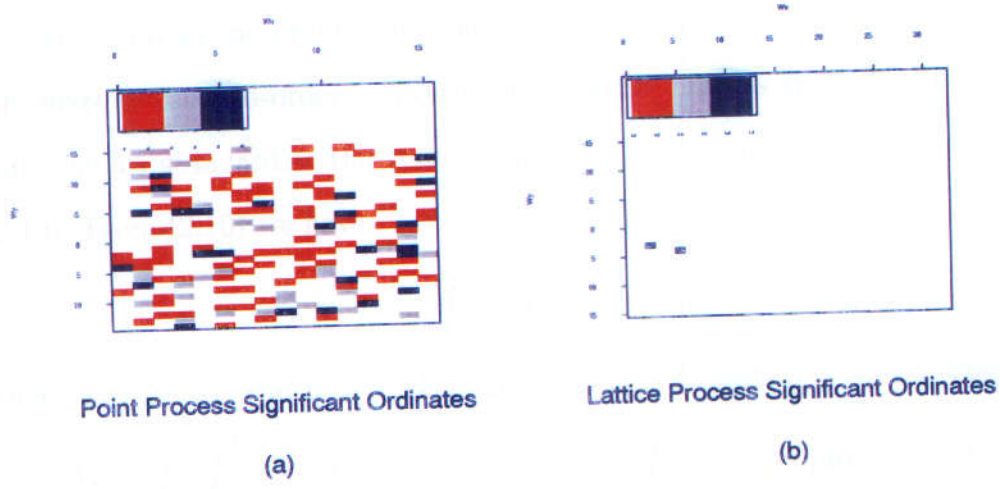

Figure 2.13: (a) Significant ordinates of the sample point spectrum of THINCOS (Figure 2.12(a)); (b) significant ordinates of the sample lattice spectrum of THINCOS (Figure 2.12(b)). The pixel value indicates the percentage level of significance.

2.5.2 Simulating a Point-Lattice Process II

In this section, point-lattice processes where both components are driven by a third stochastic process are considered. These processes will be referred to as doubly stochastic point-lattice processes (DSPLP). Such processes will eventually lead to simulating point-lattice processes by simulating a point pattern then simulating an associated lattice pattern. A model that fits the above characterisation is provided in what follows. Let the point process be a DSPP driven by $\{\Pi(\mathbf{u})\}$ then an associated lattice process can be generated by setting

$$Y_{\mathbf{b}} = \int_{\Delta_{\mathbf{b}}} \Pi(\mathbf{v}) d\mathbf{v}, \tag{2.10}$$

where $\Delta_{\mathbf{b}}$ is as defined in Section 2.5.1. In addition, we assume that Π is stationary and belongs to the class of stochastic processes discussed in

Section 1.10 in which MTCPs and DSPPs are mathematically equivalent. The first- and second-order properties of the DSPP are given in Section 1.10. The first- and second-order properties of the lattice process are derived below. First, let us standardise the span of the integral for the lattice process in (2.10). From (2.10) we have

$$Y_{\mathbf{b}} = \int_{b_1}^{b_1+1} \int_{b_2}^{b_2+1} \Pi(v_1, v_2) dv_2 dv_1,$$

where $\mathbf{v} = (v_1, v_2)$ and $\mathbf{b} = (b_1, b_2)$. Let $u_1 = v_1 - b_1$ and $u_2 = v_2 - b_2$ then

$$Y_{\mathbf{b}} = \int_0^1 \int_0^1 \Pi(u_1 + b_1, u_2 + b_2) du_2 du_1 = \int_{\Delta_0} \Pi(\mathbf{u} + \mathbf{b}) d\mathbf{u}. \qquad (2.11)$$

Thus, $\mathbb{E}[Y_{\mathbf{b}}] = \int_{\Delta_0} \mathbb{E}\Pi(\mathbf{u} + \mathbf{b}) d\mathbf{u} = \int_{\Delta_0} \lambda_\Pi d\mathbf{u} = \lambda_\Pi$ where $\mathbb{E}\Pi(\mathbf{u}) = \lambda_\Pi$ and $\mathbf{u} = (u_1, u_2)$. Also,

$$\begin{aligned}
\mathbb{E}[Y_{\mathbf{b}} Y_{\mathbf{b}'}] &= \mathbb{E}\left[\int_{\Delta_0} \Pi(\mathbf{u} + \mathbf{b}) d\mathbf{u} \int_{\Delta_0} \Pi(\mathbf{u}' + \mathbf{b}') d\mathbf{u}'\right] \\
&= \mathbb{E}\left[\int_{\Delta_0} \int_{\Delta_0} \Pi(\mathbf{u} + \mathbf{b}) \Pi(\mathbf{u}' + \mathbf{b}') d\mathbf{u} d\mathbf{u}'\right] \\
&= \int_{\Delta_0} \int_{\Delta_0} \mathbb{E}[\Pi(\mathbf{u} + \mathbf{b}) \Pi(\mathbf{u}' + \mathbf{b}')] \, d\mathbf{u} d\mathbf{u}' \\
&= \int_{\Delta_0} \int_{\Delta_0} \left[\lambda_\Pi^2 + \gamma_\Pi(\mathbf{u} + \mathbf{b} - (\mathbf{u}' + \mathbf{b}'))\right] d\mathbf{u} d\mathbf{u}',
\end{aligned}$$

where $\mathbb{E}[\Pi(\mathbf{b})\Pi(\mathbf{b}')] = \lambda_\Pi^2 + \gamma_\Pi(\mathbf{b} - \mathbf{b}')$, see Section 1.10 for more details. The second-order properties of the point-lattice process in the spatial domain are summarised by

$$\begin{aligned}
\mathbb{E}\{dN(\mathbf{b}) Y_{\mathbf{b}'}\} &= \mathbb{E}\{\Pi(\mathbf{b}) Y_{\mathbf{b}'}\} |d\mathbf{b}| \\
&= \mathbb{E}\left\{\Pi(\mathbf{b}) \int_{\Delta_0} \Pi(\mathbf{u} + \mathbf{b}') d\mathbf{u}\right\} |d\mathbf{b}| \\
&= \int_{\Delta_0} \mathbb{E}\{\Pi(\mathbf{b}) \Pi(\mathbf{u} + \mathbf{b}')\} d\mathbf{u} |d\mathbf{b}| \\
&= \int_{\Delta_0} \left[\lambda_\Pi^2 + \gamma_\Pi(\mathbf{b} - (\mathbf{u} + \mathbf{b}'))\right] d\mathbf{u} |d\mathbf{b}|. \qquad (2.12)
\end{aligned}$$

Further,

$$\gamma_{NY}(\mathbf{b},\mathbf{b}')|d\mathbf{b}| = \gamma_{NY}(\mathbf{b}-\mathbf{b}')|d\mathbf{b}| = \mathbb{E}\{dN(\mathbf{b})Y_{\mathbf{b}'}\} - \mathbb{E}\{dN(\mathbf{b})\}\mathbb{E}\{Y_{\mathbf{b}'}\} =$$
$$\int_{\Delta_0}\left[\lambda_\Pi^2 + \gamma_\Pi(\mathbf{b}-(\mathbf{u}+\mathbf{b}'))\right]d\mathbf{u}|d\mathbf{b}| - \lambda_\Pi^2|d\mathbf{b}| = \left[\int_{\Delta_0}\gamma_\Pi(\mathbf{b}-\mathbf{b}'-\mathbf{u})d\mathbf{u}\right]|d\mathbf{b}|.$$

Therefore, $\gamma_{NY}(\mathbf{v}) = \int_{\Delta_0}\gamma_\Pi(\mathbf{v}-\mathbf{u})d\mathbf{u}$, setting $\mathbf{b}-\mathbf{b}' = \mathbf{v}$. Thus, the cross-spectral density function is equal to

$$\begin{aligned}
f_{NY}(\boldsymbol{\omega}) &= \int_{R^2}\gamma_{NY}(\mathbf{v})\exp\{-i\boldsymbol{\omega}\mathbf{v}^\top\}d\mathbf{v} \\
&= \int_{R^2}\int_{\Delta_0}\gamma_\Pi(\mathbf{v}-\mathbf{u})\exp\{-i\boldsymbol{\omega}\mathbf{v}^\top\}d\mathbf{u}d\mathbf{v} \\
&= \int_{\Delta_0}\int_{R^2}\gamma_\Pi(\mathbf{v}-\mathbf{u})\exp\{-i\boldsymbol{\omega}\mathbf{v}^\top\}d\mathbf{v}d\mathbf{u} \\
&= \int_{\Delta_0}\int_{R^2}\gamma_\Pi(\mathbf{a})\exp\{-i\boldsymbol{\omega}\mathbf{a}^\top\}\exp\{-i\boldsymbol{\omega}\mathbf{u}^\top\}d\mathbf{a}d\mathbf{u} \\
&= \int_{\Delta_0}\exp\{-i\boldsymbol{\omega}\mathbf{u}^\top\}d\mathbf{u}\int_{R^2}\gamma_\Pi(\mathbf{a})\exp\{-i\boldsymbol{\omega}\mathbf{a}^\top\}d\mathbf{a} \\
&= (f_{NN}(\boldsymbol{\omega}) - \lambda_\Pi)\int_{\Delta_0}\exp\{-i\boldsymbol{\omega}\mathbf{u}^\top\}d\mathbf{u}, \qquad (2.13)
\end{aligned}$$

where $\mathbf{a} = \mathbf{v}-\mathbf{u}$. However,

$$\begin{aligned}
\int_{\Delta_0}\exp\{-i\boldsymbol{\omega}\mathbf{u}^\top\}d\mathbf{u} &= \int_0^1\int_0^1\exp\{-i(\omega_x u_1 + \omega_y u_2)\}du_2du_1 \\
&= \begin{cases}
\left(\frac{e^{-i\omega_x}-1}{-i\omega_x}\right)\left(\frac{e^{-i\omega_y}-1}{-i\omega_y}\right) & \text{for } \omega_x\neq 0;\omega_y\neq 0, \\
\frac{e^{-i\omega_x}-1}{-i\omega_x} & \text{for } \omega_x\neq 0;\omega_y = 0, \\
\frac{e^{-i\omega_y}-1}{-i\omega_y} & \text{for } \omega_x = 0;\omega_y\neq 0, \\
1 & \text{for } \omega_x = 0;\omega_y = 0,
\end{cases} \\
&= e^{-i\left(\frac{\omega_x+\omega_y}{2}\right)}\times\begin{cases}
\frac{\sin(\omega_x/2)\sin(\omega_y/2)}{(\omega_x/2)(\omega_y/2)} & \text{for } \omega_x\neq 0;\omega_y\neq 0, \\
\frac{\sin(\omega_x/2)}{(\omega_x/2)} & \text{for } \omega_x\neq 0;\omega_y = 0, \\
\frac{\sin(\omega_y/2)}{(\omega_y/2)} & \text{for } \omega_x = 0;\omega_y\neq 0, \\
1 & \text{for } \omega_x = 0;\omega_y = 0.
\end{cases}
\end{aligned}$$

Hence, $f_{NY}(\boldsymbol{\omega}) = e^{-i(\frac{\omega_x+\omega_y}{2})}(f_{NN}(\boldsymbol{\omega}) - \lambda_{\Pi})\times$

$$\begin{cases} \frac{\sin(\omega_x/2)\sin(\omega_y/2)}{(\omega_x/2)(\omega_y/2)} & \text{for } \omega_x \neq 0; \omega_y \neq 0, \\ \frac{\sin(\omega_x/2)}{(\omega_x/2)} & \text{for } \omega_x \neq 0; \omega_y = 0, \\ \frac{\sin(\omega_y/2)}{(\omega_y/2)} & \text{for } \omega_x = 0; \omega_y \neq 0, \\ 1 & \text{for } \omega_x = 0; \omega_y = 0. \end{cases} \tag{2.14}$$

In addition, the spectral density function of the lattice process is

$$f_{YY}(\boldsymbol{\omega}) = (f_{NN}(\boldsymbol{\omega}) - \lambda_{\Pi}) \times \begin{cases} \left(\frac{\sin(\omega_x/2)\sin(\omega_y/2)}{(\omega_x/2)(\omega_y/2)}\right)^2 & \text{for } \omega_x \neq 0; \omega_y \neq 0, \\ \left(\frac{\sin(\omega_x/2)}{(\omega_x/2)}\right)^2 & \text{for } \omega_x \neq 0; \omega_y = 0, \\ \left(\frac{\sin(\omega_y/2)}{(\omega_y/2)}\right)^2 & \text{for } \omega_x = 0; \omega_y \neq 0, \\ 1 & \text{for } \omega_x = 0; \omega_y = 0. \end{cases}$$

It is worth noting from (2.14) that the phase spectrum is

$$\phi_{NY}(\boldsymbol{\omega}) = \frac{-\omega_x - \omega_y}{2},$$

since $f_{NN}(\boldsymbol{\omega})$ is real because it is an auto-spectral density function. Hence, the slope in each direction of the phase spectrum is equal to $-1/2$. One can correct for this phase shift, which is an artefact arising from the construction of the process, by multiplying the cross-spectrum by $e^{i(\frac{\omega_x+\omega_y}{2})}$. This is equivalent to translating the co-ordinates of the point process by $(-1/2, -1/2)$. However, translating the point process co-ordinates is bound to create boundary problems when considering realisations within a study region which is why we mutliply by $e^{i(\frac{\omega_x+\omega_y}{2})}$.

To simulate a DSPLP we note the equivalence between MTCPs and a class of DSPPs mentioned in Section 1.10 and that $\mathbb{E}(dN_X(\Delta_{\mathbf{b}})) = \lambda_{\Pi}|\Delta_{\mathbf{b}}| = \lambda_{\Pi} = \mathbb{E}(Y_{\mathbf{b}})$. Thus, one can simulate the point pattern component as an MTCP as discussed in Section 1.10. The lattice pattern is then generated

by assigning to each grid point of the lattice the number of events enclosed within the quadrat associated with that grid point. The resulting lattice will be termed a *count* lattice and will be defined formally in Chapter 5. Noise can be added to the lattice pattern.

Having established the properties of (2.10) one can easily generalise this model. One possibility is to assume that the point process is driven by the process Π_1 and the lattice process is driven by Π_2 such that $\Pi_1 = \alpha\Pi_2$ where $\alpha > 0$. These processes will be termed as *linked* DSPLPs. Note that setting $\alpha = 1$ in the above results in a DSPLP. Another possibility is to assume that $\Pi_1 + \Pi_2 = c$; such processes are termed *balanced* DSPLPs. These generalisations can be viewed as extensions of linked and balanced bivariate Cox point processes as defined by Diggle and Milne (1983). The cross-spectral density functions for the last two models are defined by

$$f_{NY}(\boldsymbol{\omega}) = ke^{-i(\frac{\omega_x+\omega_y}{2})}(f_{NN}(\boldsymbol{\omega}) - \lambda_\Pi) \times \begin{cases} \frac{\sin(\omega_x/2)\sin(\omega_y/2)}{(\omega_x/2)(\omega_y/2)} & \text{for } \omega_x \neq 0; \omega_y \neq 0, \\ \frac{\sin(\omega_x/2)}{(\omega_x/2)} & \text{for } \omega_x \neq 0; \omega_y = 0, \\ \frac{\sin(\omega_y/2)}{(\omega_y/2)} & \text{for } \omega_x = 0; \omega_y \neq 0, \\ 1 & \text{for } \omega_x = 0; \omega_y = 0, \end{cases}$$

where $k = \alpha$ for a linked process and $k = -1$ for a balanced process.

Next, we provide three artificial examples. The first of these examples is a realisation of a linked DSPLP. The second example is a modification of the first one, and the third is a realisation of a balanced DSPLP.

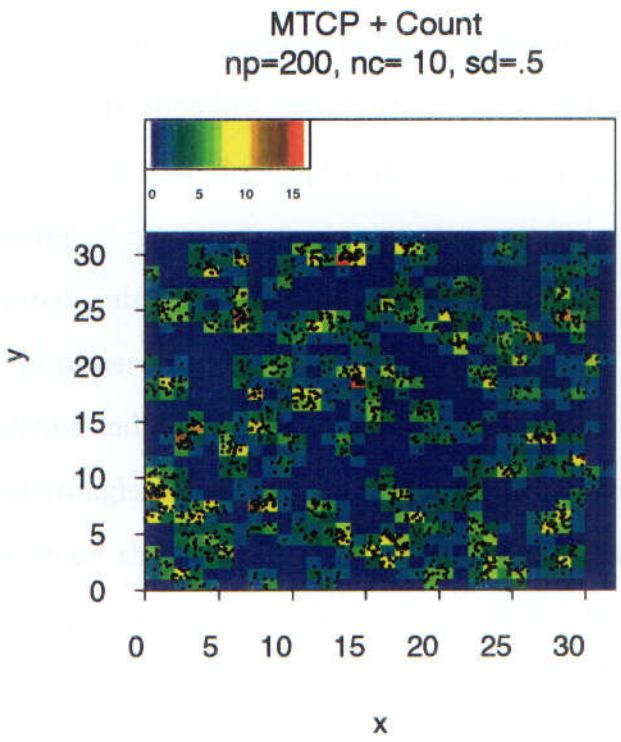

Figure 2.14: LINKED: a realisation of a point-lattice process determined by (2.10). The point pattern is equivalent to an MTCP with the following parameters: $N_P = 200, N_C = 10, \sigma(sd) = 0.5$.

2.5.2.1 Example 4: LINKED

Figure 2.14 is a realisation of a linked DSPLP determined by (2.10). The point pattern is a DSPP which is equivalent to an MTCP with the following parameters: $N_P = 200, N_C = 10$, and $\sigma = 0.5$ on a 32×32 lattice. Note that the distribution function of the intensity of this DSPP is $\Pi(\mathbf{a}) = \lambda_P \sum_{k=1}^{N_P} h(\mathbf{a} - \mathbf{P_k})$ where $\mathbf{P_k}$ denotes the location of a parent, λ_P the intensity of the parent pattern, N_P the number of parents generated, and $h(\mathbf{a})$ is as defined in Section 1.10. The lattice pattern is the count lattice of

the point pattern. The total number of events of the point pattern is 1965.

Theoretical auto- and cross-spectra for this example are given in Figure 2.15 and the corresponding estimates are provided in Figure 2.16. These graphs indicate that the empirical results are in agreement with the theoretical results.

The estimated auto-, co-, and amplitude spectra are characterised by concentration of power for relatively low frequencies. The peaks in the estimated co-spectrum indicate that the two components are positively related. The peaks and troughs in the estimated quadrature spectrum indicate the existence of a phase shift between the two patterns. The estimated phase spectrum is linear and the mean of its slopes in the WE direction is approximately -0.5, and in the SN direction is approximately -0.5 as expected. The values of the squared coherency spectrum are close to one across most frequencies. Thus, the two components are strongly related for most frequencies.

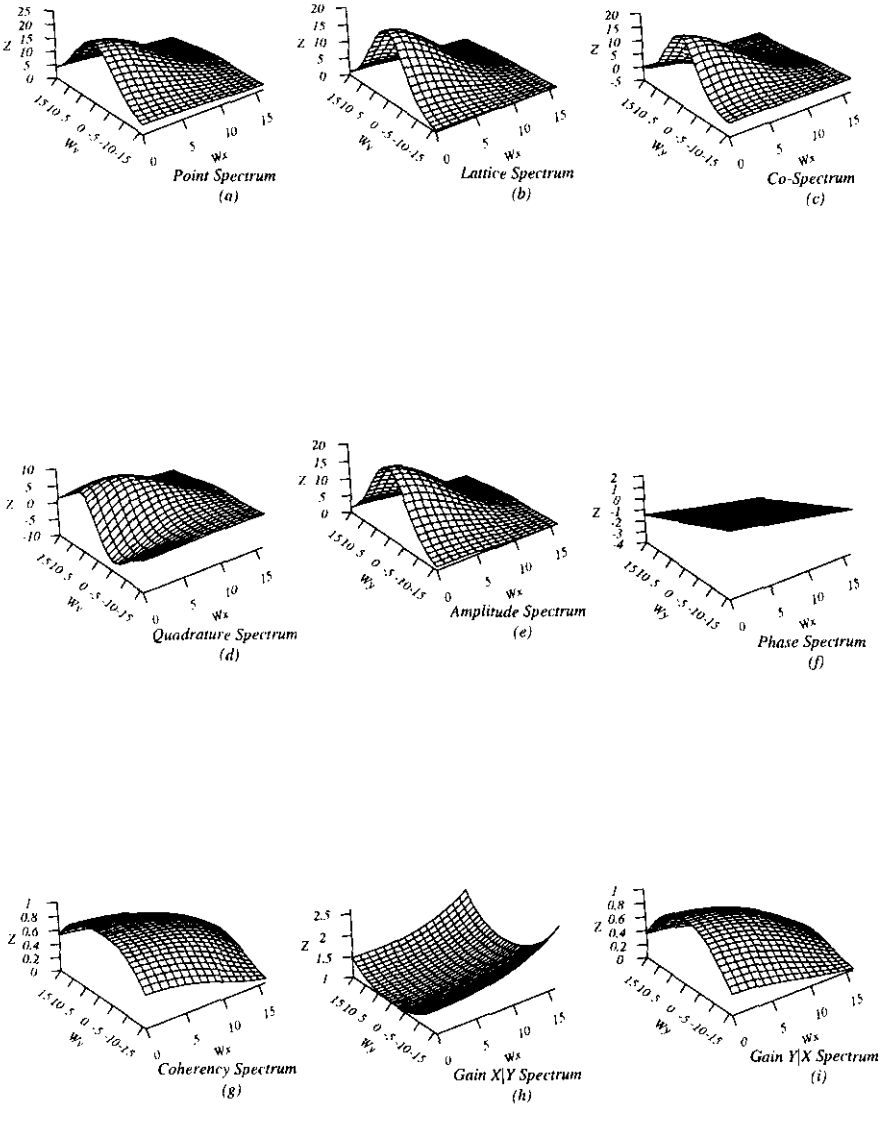

Figure 2.15: Theoretical spectra for the pattern in Figure 2.14 (LINKED): (a) and (b) auto-spectra; (c) and (d) co- and quadrature spectra; (e) to (i) amplitude, phase, coherency and gain spectra.

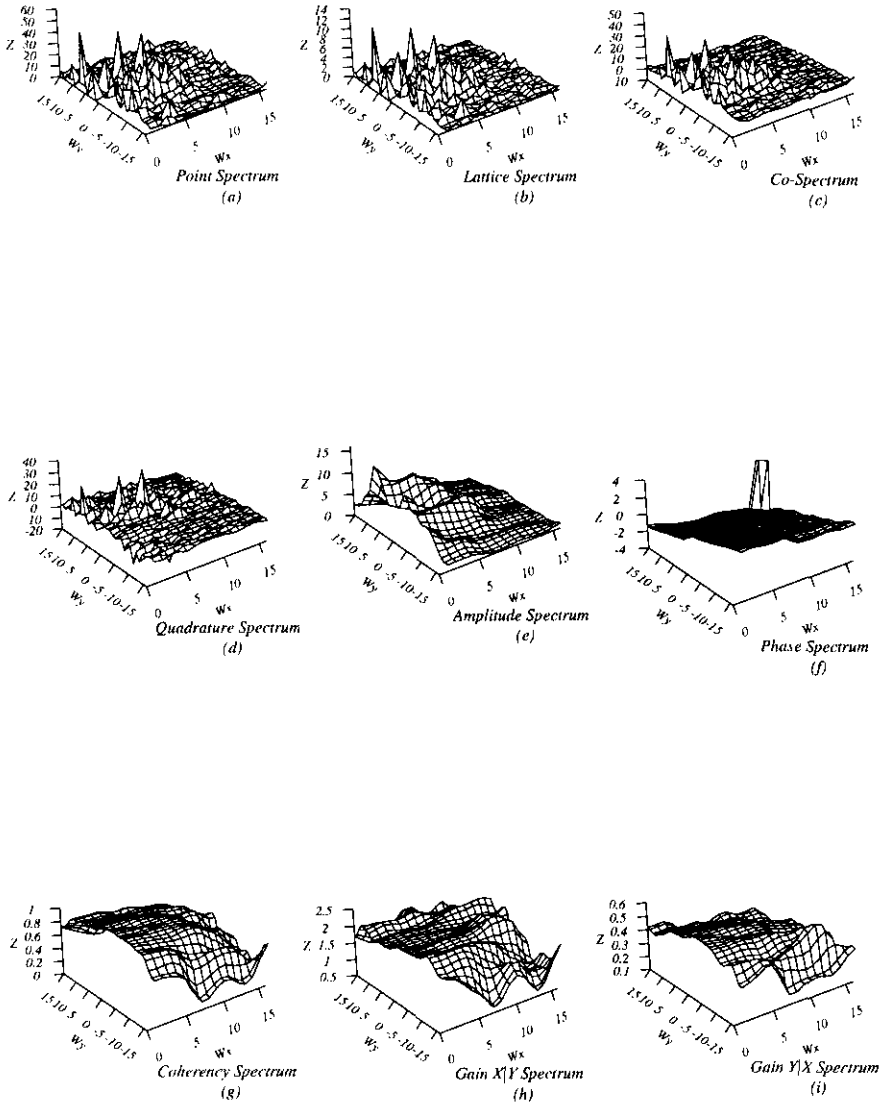

Figure 2.16: Estimated spectra for LINKED (Figure 2.14). (a) and (b) Raw auto-spectra; (c) and (d) raw co- and quadrature spectra; (e) to (i) smoothed amplitude, phase, coherency and gain spectra smoothed using Method A four times.

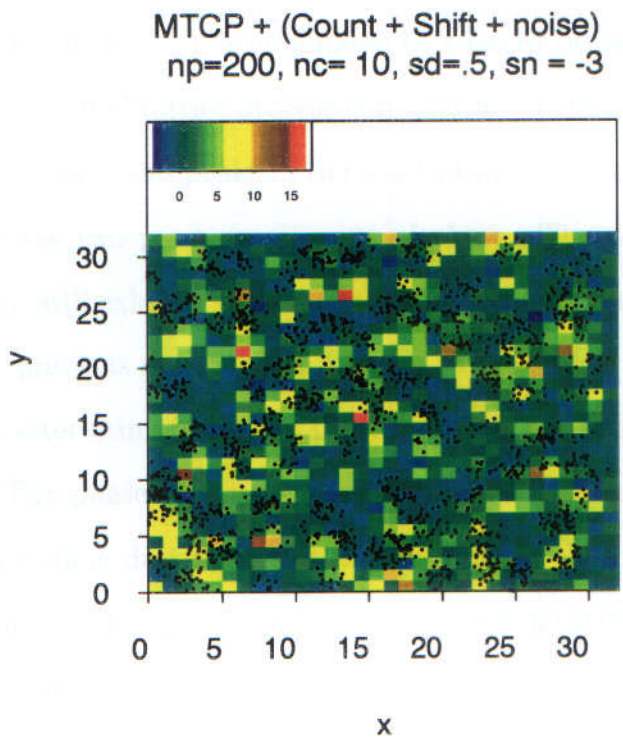

Figure 2.17: LINKEDSHIFTED: modification of the point-lattice pattern of Figure 2.14 (LINKED). The point pattern is as that of LINKED but the lattice pattern has been shifted and Gaussian white noise added to it.

2.5.2.2 Example 5: LINKEDSHIFTED

Figure 2.17 represents the pattern formed by the point pattern component of the previous example LINKED and a transformation of the lattice pattern component of this example. The lattice pattern was obtained by shifting the lattice pattern of LINKED three pixels to the south and adding Gaussian white noise.

The lattice and amplitude sample spectra presented in Figures 2.18(a) and (b), respectively, resemble those of the previous example. Note here

that we have corrected for the -1/2 shift as discussed in Section 2.5.2. The co-spectrum, Figure 2.18(c), is dominated by troughs rather than peaks indicating that the shifted lattice process is negatively correlated with the point pattern. The troughs and peaks in the quadrature spectrum, Figure 2.18(d), indicate that the two processes are out of phase. The squared coherency, Figure 2.18(e), still exhibits power at most frequencies, but it is not as close to one as the previous example. This is due to the added noise.

The most interesting feature of this example is the phase spectrum, Figure 2.18(f). The phase spectrum is seen to be constant across the WE direction despite some discontinuities that are due to the $(-\pi, \pi)$ constraint. In the SN direction the phase spectrum decreases linearly as the ω_y component of the frequency increases. Calculating slopes in the SN direction across bands that contain no discontinuities results in approximately -3. Thus, empirically one can deduce that the lattice process is to the south of the point pattern by 3 pixels.

In principle, one can remove the phase shift to reveal the exact relationship between the two components. In Figure 2.19 we represent the cross-spectra after multiplying the cross-spectrum by $e^{i(0\omega_x - 3\omega_y)}$ where $(0, -3)$ is the detected phase shift. The co-, amplitude and squared coherency spectra in this figure resemble those of LINKED. However, the phase and quadrature spectra are almost zero everywhere.

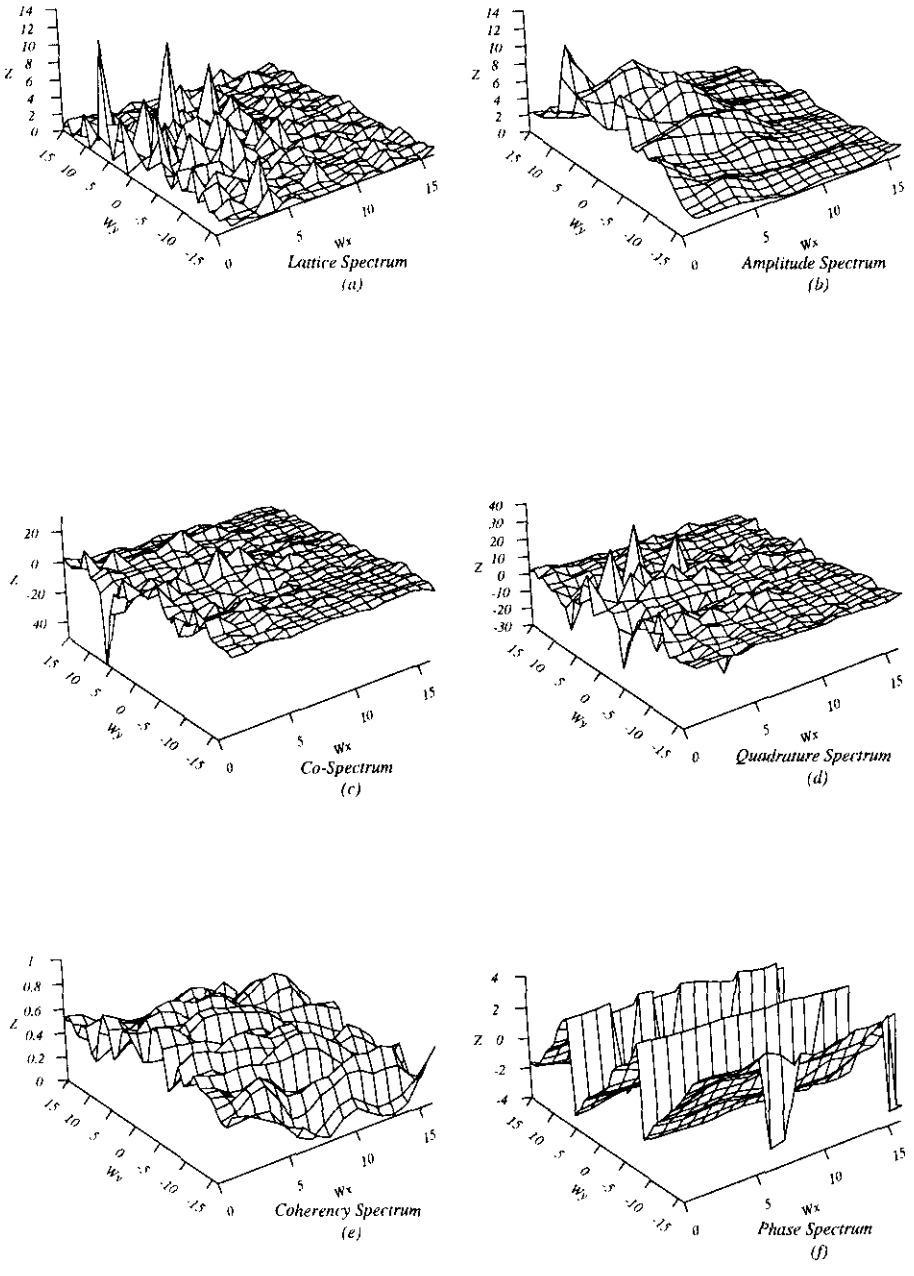

Figure 2.18: Spectra for LINKEDSHIFTED (Figure 2.17). (a) Raw lattice periodogram; (b) smoothed amplitude spectrum; (c) and (d) raw co- and quadrature spectra; (e) and (f) smoothed squared coherency and phase spectra using Method A four times.

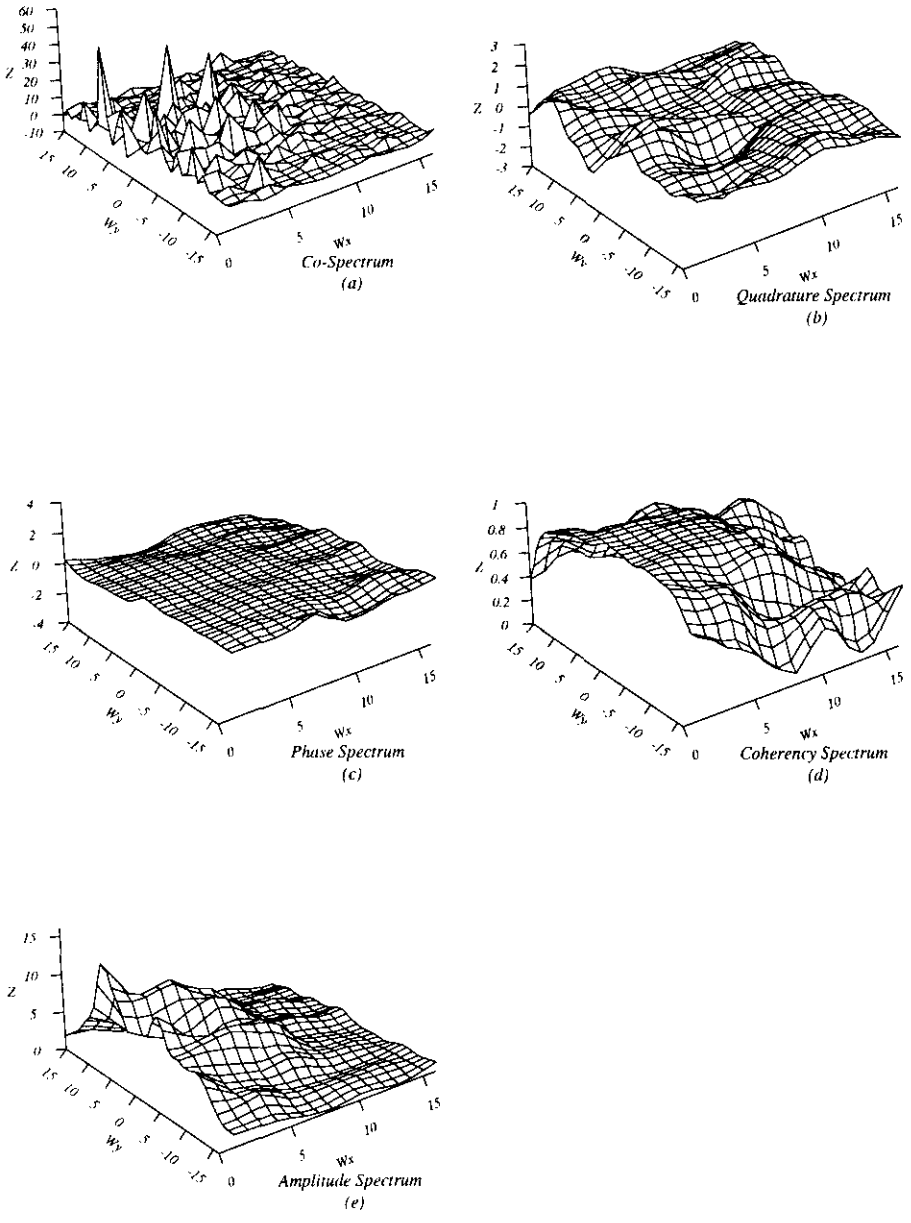

Figure 2.19: Cross-spectra after correcting for the phase shift detected in Figure 2.18(f): (a) raw co-spectrum; (b) to (e) smoothed quadrature, phase, squared coherency and amplitude spectra using Method A four times.

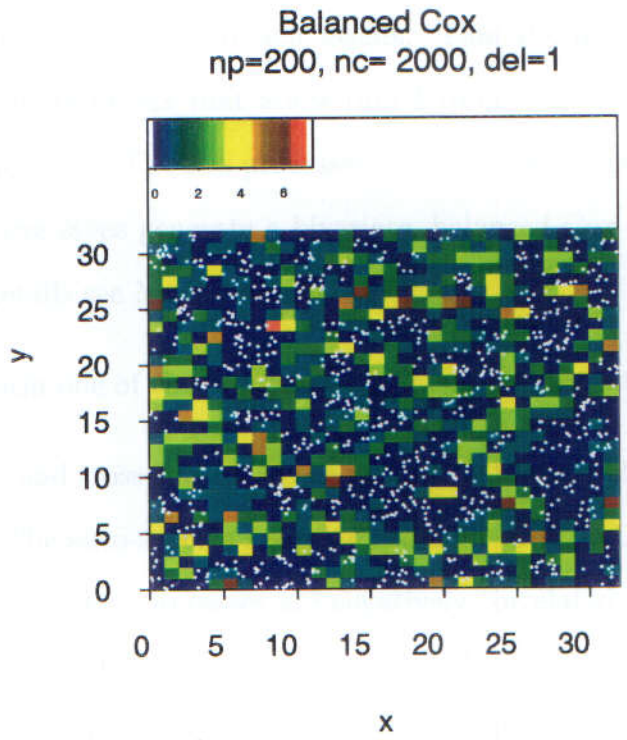

Figure 2.20: BALANCED: a realisation of a balanced DSPLP where the number of parent events is 200, the joint intensity is $2000/32^2$ and the minimal distance is 1.

2.5.2.3 Example 6: BALANCED

Figure 2.20 is a realisation of a balanced DSPLP on a 32×32 lattice. Simulation of balanced DSPLPs is usually carried out using the following steps.

1. Simulate a parent process from the HPP with intensity λ_P, in this example $\lambda_P = 200/(32 \times 32)$.

2. Simulate another two HPP processes X and Y with intensity C, in this example $C = 2000/(32 \times 32)$.

3. Thin one of the processes, say X, by retaining events if they are within a distance δ from the parent events. Thin the other process, say Y, by excluding events that are within δ from the parent events, in this example $\delta = 1$. The two processes are, therefore, negatively correlated. The above steps generate a bivariate, balanced Cox point process, for more details see Mugglestone (1990).

4. Transform one of the processes, say Y, to a count lattice process.

The auto- and cross-spectra of the pattern in Figure 2.20 are presented in Figure 2.21. The auto-spectra resemble those for LINKED. The co-spectrum indicates that the two processes are negatively correlated. The quadrature spectrum indicates that there is a phase shift between the two components. However, the magnitude of this phase shift cannot be determined from the phase spectrum without further adjustments. Techniques of how to adjust the phase spectrum are discussed in Chapter 3. The values of the squared coherency are close to one for low frequencies and are close to zero for high frequencies.

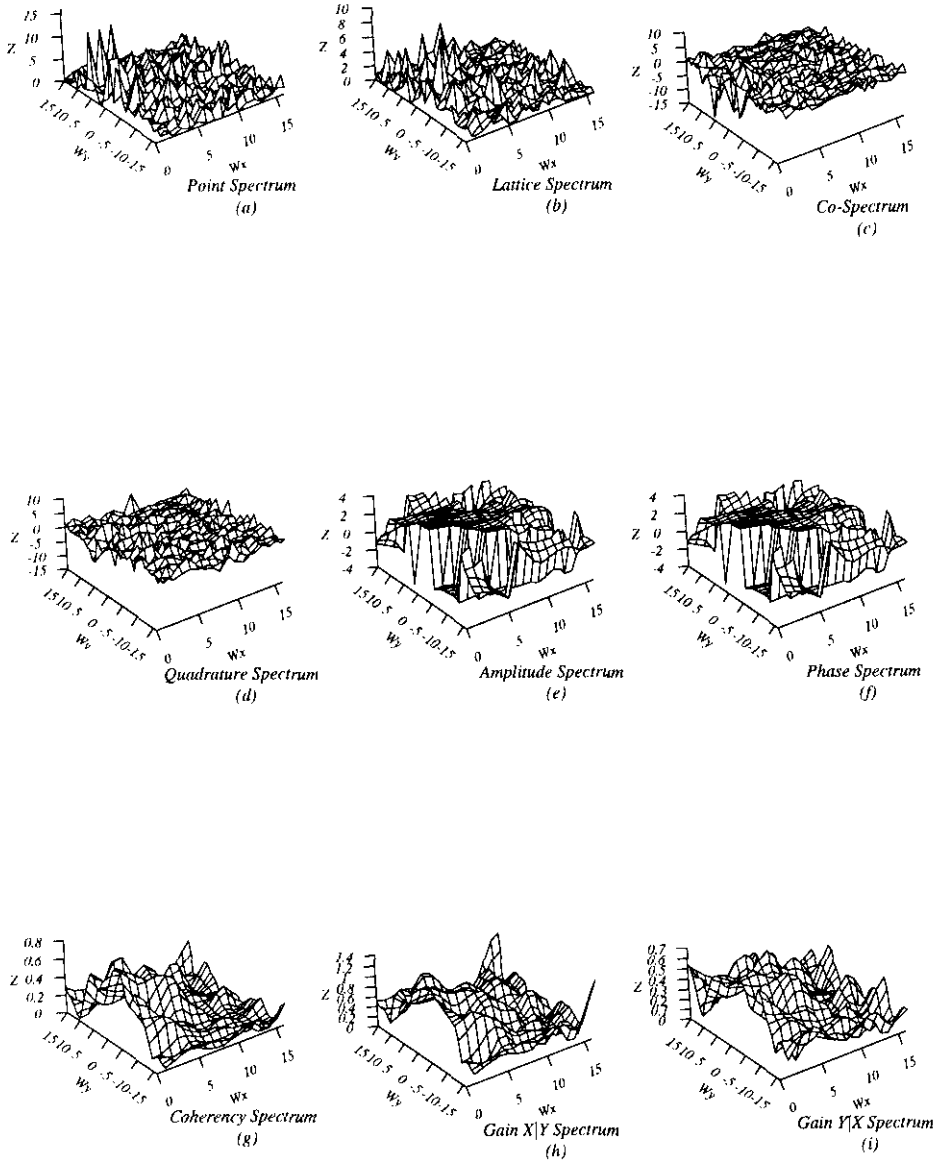

Figure 2.21: Spectra for BALANCED (Figure 2.20). (a) and (b) Raw auto-periodograms; (c) and (d) raw co- and quadrature spectra; (e) to (i) smoothed amplitude, phase, squared coherency and gain spectra using Method A four times.

2.6 Summary

In this chapter, spectral analysis for spatial point-lattice processes was introduced. Different cross-spectral estimates were presented. Several methods to simulate associated point-lattice processes were provided. In addition, theoretical cross-spectra of linked and balanced DSPLPs were derived. Artificial examples were generated in order to demonstrate the potential of cross-spectral estimates as exploratory tools to analyse the correlation between a two-dimensional point process and a lattice process. For these examples not only we were able to determine whether the two components were positively-, negatively-, or un-correlated but we were able to determine if they were out of phase. In some cases, we were able to calculate the magnitude of the phase shift. The examples demonstrated that when the two components were related but where the power in the auto-spectra was concentrated at a couple of frequencies, the co- and quadrature spectra exhibited simple structure. In this case, the phase spectrum was usually unstable, mainly because the squared coherency was close to one only at a couple of frequencies rather than across the whole range of frequencies. However, when the power in the auto-spectra was distributed across a range of frequencies the phase spectrum behaved in a less erratic manner. Furthermore, the constraint on the phase spectrum to lie in the interval $(-\pi, \pi)$ sometimes resulted in a number of discontinuities. Thus, one needs to adjust the phase spectrum. This issue will be discussed in the next chapter together with methods of computing the slopes of the phase spectrum.

Chapter 3

The Phase Spectrum: Practical Considerations

In the previous chapter, we saw that the phase spectrum usually contains a number of discontinuities. Thus, in most cases it is difficult to interpret the phase spectrum as it stands. In this chapter, we will introduce two techniques to estimate the slope of the phase spectrum. In Section 3.1 we introduce a technique which adjusts the phase spectrum in order to calculate its slope, while in Section 3.2 we present a second technique that does not require such an adjustment.

3.1 Adjusting the Phase Spectrum

In the one-dimensional case and for a bivariate time series where one series is a linear shift of another the phase spectrum is theoretically a linear function of the frequency (see Priestley, 1981b, chapter 9). In addition, the slope of the phase spectrum represents the shift between the two series. However, due to the $(-\pi, \pi)$ restriction the phase spectrum might contain a number of dicontinuities, such as those encountered in the two-dimensional case, and

hence it is difficult to calculate the slope. In an ideal situation, the phase spectrum, $\phi_{NY}(\omega)$, should be plotted on a cylinder so that $-\pi$ coincides with π, but this is not practical (see Priestley, 1981b). Hence as suggested by Priestley (1981b), one should plot for each ω three values, one in each of the following ranges $(-3\pi, -\pi), (-\pi, \pi), (\pi, 3\pi)$ and then join the matching entries.

In the two-dimensional case, this adjustment might be done for each ordinate of the frequency $\boldsymbol{\omega}$. This reduces the problem basically to applying a one-dimensional adjustment. For example, adjusting the phase spectrum in the WE direction will require applying the one-dimensional adjustment across the range of frequencies in the WE direction for every frequency in the SN direction. However, we do not have to restrict ourselves to the ranges suggested above. More ranges can be used to attain a coherent graph. The ranges to be used have length 2π and are of the form $(-\pi + 2k\pi, \pi + 2k\pi)$ for $k = 0, \pm 1, \ldots$. For the examples to be presented the total number of ranges using the modified procedure does not exceed five.

To illustrate how the automated version works for the one-dimensional case, a typical example of a one-dimensional phase spectrum, $\{\theta_p\}$, is represented by circles in Figure 3.1. Plots of $\{\theta_p\} \pm 2\pi$ are represented by the rhombuses and crossed rhombuses in Figure 3.1. Whereas it is easy to spot the matching entries by eye, an automated version where the ranges are restricted to only $(-3\pi, -\pi), (-\pi, \pi)$, and $(\pi, 3\pi)$ will require $3^2 \times (\ell_\theta - 2) + 3 \times 2$ operations. Here ℓ_θ is the length of the $\{\theta_p\}$ vector. This automated version also requires that the three vectors which hold the original data and the transformed data are retained throughout the computation. However,

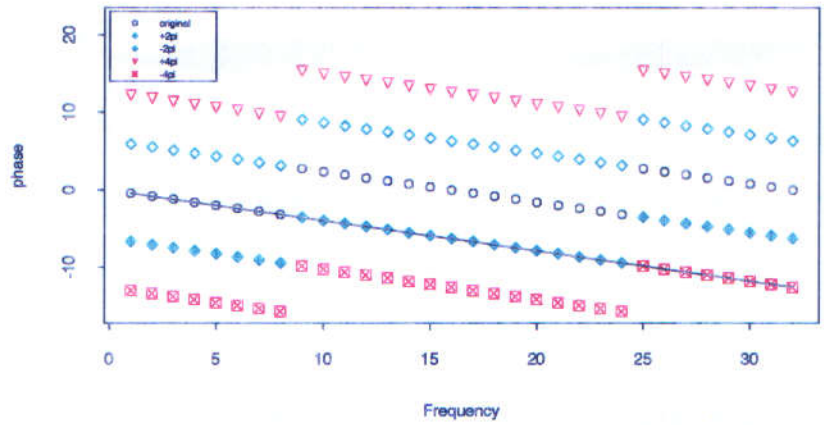

Figure 3.1: The circles are the original values of a hypothetical phase spectrum. The other symbols are the values of the circles mapped to $(-5\pi, -3\pi)$, $(-3\pi, -\pi)$, $(\pi, 3\pi)$, and $(3\pi, 5\pi)$ for a typical frequency band in the WE direction. The line represents how the automated procedure used in this study chooses the appropriate values. The linking criterion is to minimise the distance between consecutive points.

allowing for more ranges to be used and adjusting the vectors as and when a jump is encountered will reduce the number of operations to $3 \times (\ell_\theta - 2) + 2$. In addition, only one copy of the vector is required at any one time in this modified procedure. A jump is observed when the distance separating two consecutive ordinates of the phase spectrum, say $|\theta_2 - \theta_1|$, is greater than one of the distances $|(\theta_2 \pm 2\pi) - \theta_1|$. In this study, we will use the modified approach in computing adjusted phase spectra. Using the modified approach for the $\{\theta_p\}$ example results in the entries joined by the line in Figure 3.1.

To illustrate how the modified approach works in the two-dimensional case we apply it to two of the examples of the previous chapter. Figures 3.2(a) and (b) represent the graphs of the adjusted phase spectra in the WE and SN directions for the example LINKED of Section 2.5.2.1. Adjusting the

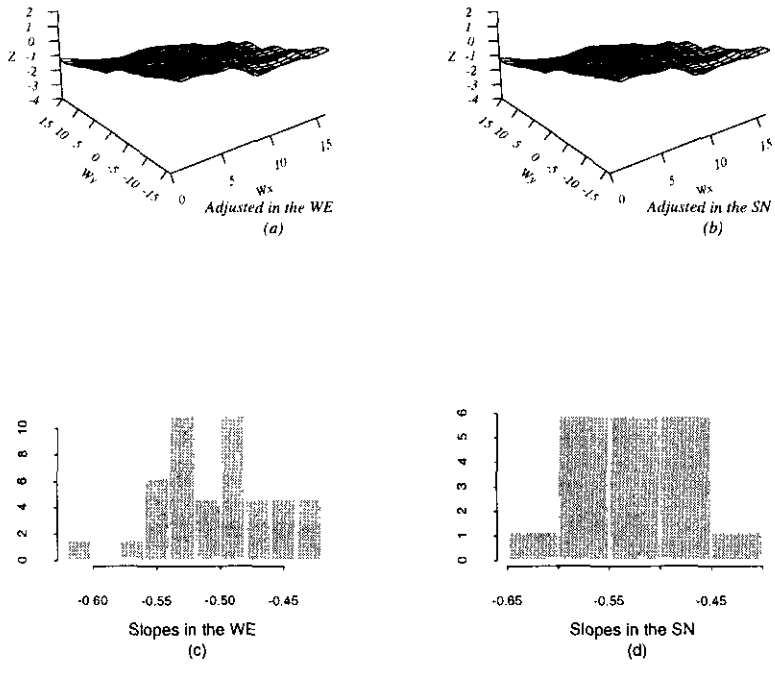

Figure 3.2: (a) and (b) adjusted phase spectra in the WE and SN directions for LINKED; (c) and (d) histograms of the slopes corresponding to (a) and (b), respectively.

phase spectrum of LINKED in both directions results in the same spectrum because the original phase spectrum contained only one discontinuity in each direction. The slopes in each direction are approximately -0.5 as expected (see Figures 3.2(c) and (d)).

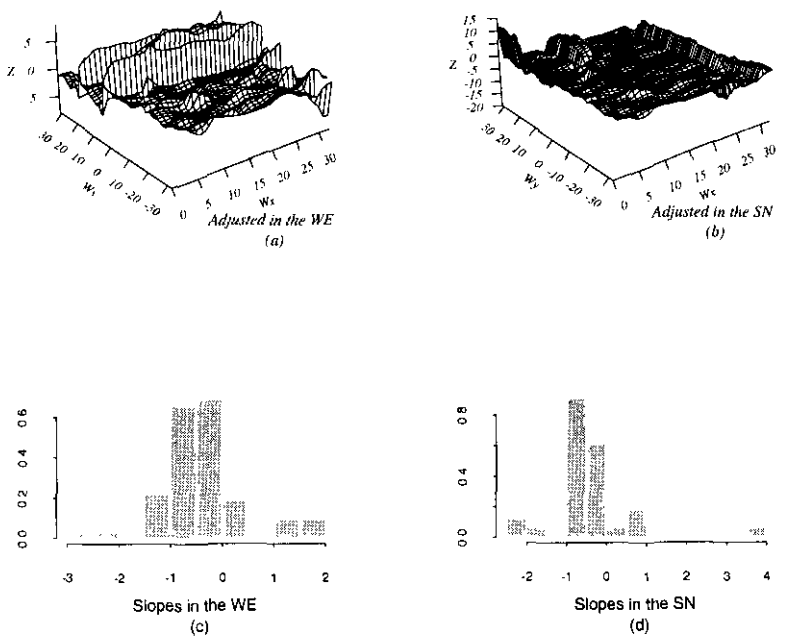

Figure 3.3: (a) and (b) adjusted phase spectra for THRESACOS, Figure 2.7(f), in the WE direction and in the SN direction; (c) and (d) histograms of the slopes corresponding to (a) and (b), respectively.

Next, the adjusted phase spectra for the example THRESACOS of Section 2.5.1.2 are represented in Figures 3.3(a) and (b). The histograms of the slopes for these spectra are given in Figures 3.3(c) and (d). The histograms indicate that the majority of slopes lie between $(-1, 0)$. The range of slopes in the SN direction is $(-2.10, 3.85)$ with mean -0.38 and median -0.51. In the WE direction the range of slopes is $(-2.82, 1.73)$ with mean -0.36 and median -0.46; the minimum is attained at frequency $q = 1$. This extreme value is due to the non-linear behaviour of the adjusted phase spectrum in the WE direction along this frequency. It can be seen from Figure 3.4 that

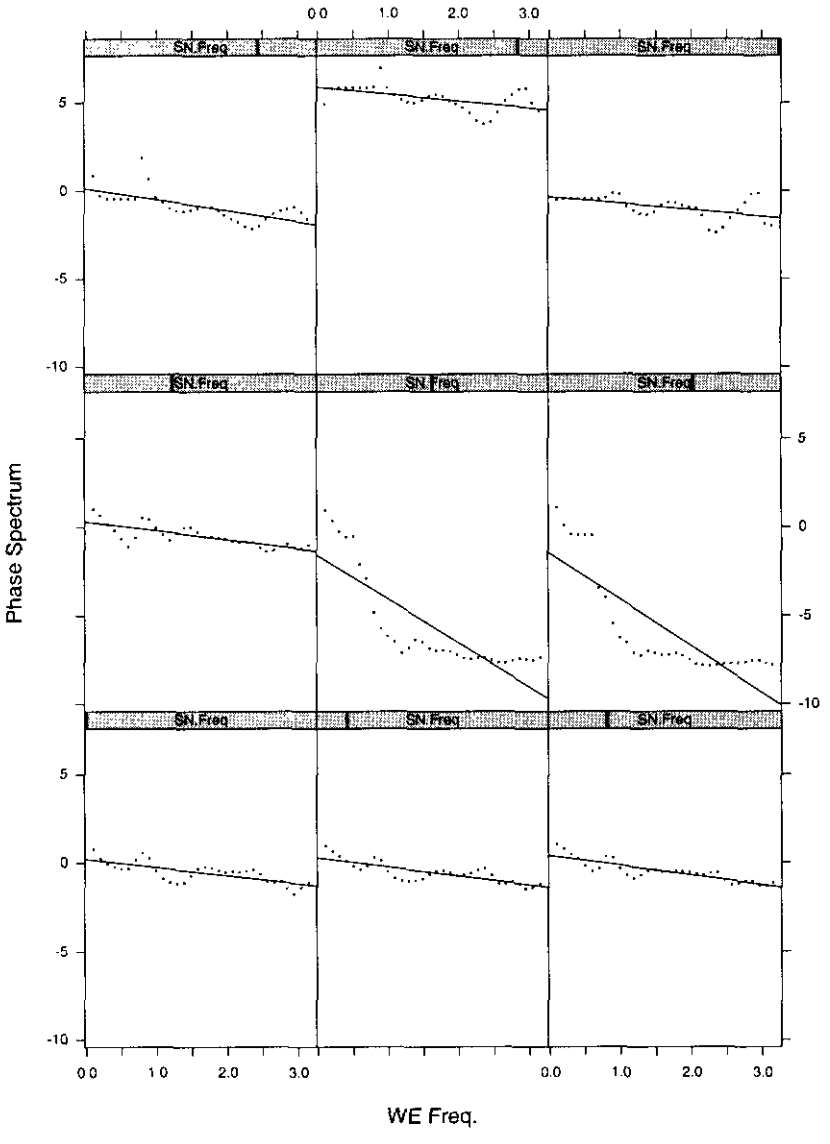

Figure 3.4: Profile of adjusted phase spectrum in the WE direction for THRESACOS, Figure 3.3(a), along the SN frequencies $q = -4, \ldots, 4$. The far left panel of the bottom row corresponds to $q = -4$, the second left panel of the bottom row corresponds to $q = -3$, and so forth such that the far right panel of the top row corresponds to $q = 4$. The dots are the original data, whereas the line is a linear model fitted to the data.

a linear fit to the adjusted phase spectrum in the WE direction along the frequency bands $q = -4, \ldots, 4$ is poor.

In fact, for the panels of Figure 3.4 with $q = 0$ and $q = 1$ a jump of approximately -2π is observed around the WE frequency of 0.6. This jump might be an undesirable outcome of the correction method due to its point by point approach, thus care should be taken when using it. If the jump is removed then a decreasing linear trend might reasonably fit the points in these two panels.

Another problem associated with the adjustment procedure is computational efficiency since the number of adjustments required is of the same order as the dimensions of the study region. Therefore, a method to calculate the slope of the phase spectrum without adjusting it would be desirable. In the next section such a method is presented.

3.2 Phase Correlation Methods

In this section we look at alternative methods to estimate the phase shift between a point process and a lattice process. If the phase spectrum, Φ, of a point-lattice process is a linear function of the frequency, namely $\Phi(\boldsymbol{\omega}) = \boldsymbol{\omega}\mathbf{d}^\top + K$ where $\mathbf{d}$ is the phase shift and K is a constant, then $\mathbf{d}$ can be estimated by:

$$\left(\widehat{d}_1, \widehat{d}_2\right) = \arg\max_{(d_1,d_2)} \sum_{p=-\lfloor \ell_1/2 \rfloor}^{[(\ell_1-1)/2]} \sum_{q=-\lfloor \ell_2/2 \rfloor}^{[(\ell_2-1)/2]} \beta_{p,q} \cos\left[\Phi(p,q) - 2\pi\left(\frac{d_1 p}{\ell_1} + \frac{d_2 q}{\ell_2}\right)\right] \tag{3.1}$$

where β is a given set of weights, and ℓ_1 and ℓ_2 are the dimensions of the study region.

Glasbey and Mardia (2000) derive (3.1) in an attempt to minimise the mean-square-difference between images (a matching criterion) within the framework of image warping. In doing so, they arrive at a set of weights which is given by the amplitude values, $A(p,q)$, of the cross-spectrum; the associated criterion is known as the covariance criterion. However, they point out that these weights can be modified to obtain a range of matching criteria. For example, setting $\beta_{p,q} \equiv 1$ for all p and q gives the phase correlation criterion of Kuglin and Hines (1975). This criterion can be viewed as the correlation after transforming the patterns (images) so that the auto-spectra are flat, see Glasbey and Horgan (1995, chapter 3). Berman et al. (1994) introduce a closely related method to the above, which is Fourier based and accounts for aliasing, in order to estimate band-to-band misregistrations of images within the framework of remote sensing.

Further, Glasbey and Mardia (2000) introduce a new approach by as-

suming that the elements of the phase spectrum are independent von Mises variates with concentration parameters equal to the weights, and term this criterion the *Fourier-von Mises* similarity measure. This assumption is based on asymtpotic properties similar to those derived in Chapter 4 (see Glasbey and Mardia (2000) for more details). Equation (3.1) is then replaced by the log-likelihood:

$$\sum_{p=-[\ell_1/2]}^{[(\ell_1-1)/2]} \sum_{q=-[\ell_2/2]}^{[(\ell_2-1)/2]} \beta_{p,q} \cos\left[\Phi(p,q) - 2\pi\left(\frac{d_1 p}{\ell_1} + \frac{d_2 q}{\ell_2}\right)\right] - \sum_{p=-[\ell_1/2]}^{[(\ell_1-1)/2]} \sum_{q=-[\ell_2/2]}^{[(\ell_2-1)/2]} \log(I_0(\beta_{p,q})), \tag{3.2}$$

where $I_0(\kappa)$ is the modified Bessel function of the first kind and order zero. Glasbey and Mardia (2000) use weights that are modelled by the log-linear function:

$$\beta_{p,q} = \exp\left(\rho_0 + \rho_1 |\omega_{p,q}| + \rho_2 |\omega_{p,q}|^2 + \rho_3 \log(A(p,q))\right), \tag{3.3}$$

with parameters $(\rho_0, \rho_1, \rho_2, \rho_3)$, $\omega_{p,q} = (\omega_p, \omega_q) = \left(\frac{2\pi p}{\ell_1}, \frac{2\pi q}{\ell_2}\right)$, and $|\omega_{p,q}| = \sqrt{\omega_p^2 + \omega_q^2}$. Both the phase correlation and the covariance criteria are special cases of (3.2). Using (3.2) one can also derive the variance of $\left(\widehat{d}_1, \widehat{d}_2\right)$. Note that the density function of the von Mises distribution with mean μ and concentration κ, $VM(\mu, \kappa)$, is given by

$$g(\phi) = \frac{\exp(\kappa \cos(\phi - \mu))}{2\pi I_0(\kappa)}, \tag{3.4}$$

where $0 \leq \phi < 2\pi, \kappa \geq 0, 0 \leq \mu < 2\pi$, and $I_0(\kappa)$ is as above. If $\kappa = 0$ then (3.4) reduces to the circular uniform distribution.

Equation (3.1) extends the one-dimensional spectral estimation of time delay between bivariate time series introduced by Hamon and Hannan (1974)

who derived asymptotic optimal weights. The two-dimensional version of such weights is given by setting $\beta_{p,q} = \frac{\Upsilon(p,q)}{1-\Upsilon(p,q)}$. These weights are thus inversely proportional to the variance of the phase spectrum (see Section 4.1 for derivation). In addition to the simple delay modelled by (3.1) Hamon and Hannan (1974) consider other models for the phase spectrum with several parameters. However, if the ratio $\frac{\Upsilon(p,q)}{1-\Upsilon(p,q)}$ is small, Hannan and Thomson (1988) suggest estimating the phase shift by maximising the one-dimensional version of

$$-\sum_{p=-[\ell_1/2]}^{[(\ell_1-1)/2]}\sum_{q=-[\ell_2/2]}^{[(\ell_2-1)/2]}\log\left(1-\Upsilon\left(p,q\right)\cos^2\left\{\Phi\left(p,q\right)-2\pi\left(\frac{d_1 p}{\ell_1}+\frac{d_2 q}{\ell_2}\right)\right\}\right). \tag{3.5}$$

Based on the simulations they carried out they found that (3.5) performed better than (3.1) in cases where the ratio $\frac{\Upsilon(p,q)}{1-\Upsilon(p,q)}$ is small. Chan et al. (1978) use a weighted least squares approach to estimate the phase shift (time delay) between one-dimensional signals.

The above approaches are closely related to the analysis of circular data. Fisher and Lee (1992) propose regression models for circular data on linear explanatory variables, which generalise the models given by Gould (1969) and Johnson and Wehrly (1978). In particular, Johnson and Wehrly (1978) derive a method of obtaining angular-linear distributions when the marginal distributions are completely specified. Further, Fisher and Lee (1983) define a correlation coefficient between angular variates.

Equation (3.1) can be computed efficiently for all integer values using the Fast Fourier Transform, and then an iterative method, such as the Newton-Raphson method, can be used to determine $\left(\hat{d}_1, \hat{d}_2\right)$ to a finer resolution. For

this reason we will focus on (3.1) to compute the phase shifts for the examples of Chapter 2. The estimates of the phase shifts and their standard deviations are presented in Table 3.1. In Table 3.1 the amplitude weights correspond

Table 3.1: Estimates for the phase shifts of the examples presented in Chapter 2.

Example	Amplitude Weights				Unity Weights			
	Estimate		s.d.		Estimate		s.d.	
	$\widehat{d}_1$	$\widehat{d}_2$	$\widehat{d}_1$	$\widehat{d}_2$	$\widehat{d}_1$	$\widehat{d}_2$	$\widehat{d}_1$	$\widehat{d}_2$
THRESACOS	-0.461	-0.512	0.027	0.029	-0.479	-0.469	0.025	0.025
THRESBMA	2.552	-4.641	0.053	0.125	2.684	-3.961	0.066	0.069
THINCOS	-0.066	0.098	0.029	0.035	-0.053	0.102	0.031	0.042
LINKED	-0.485	-0.558	0.022	0.021	-0.465	-0.606	0.026	0.026
LINKEDSHIFTED	-0.005	-3.047	0.013	0.012	-0.026	-3.043	0.024	0.024
BALANCED	-0.221	-5.122	0.047	0.033	-0.303	-5.003	0.070	0.047

Example	HH Weights			
	Estimate		s.d.	
	$\widehat{d}_1$	$\widehat{d}_2$	$\widehat{d}_1$	$\widehat{d}_2$
THRESACOS	-0.463	-0.498	0.045	0.046
THRESBMA	2.731	-3.985	0.081	0.108
THINCOS	-0.070	0.189	0.063	0.083
LINKED	-0.480	-0.547	0.010	0.010
LINKEDSHIFTED	-0.011	-3.043	0.018	0.018
BALANCED	0.005	-5.135	0.092	0.075

to the weights used in the covariance criterion, the unity weights correspond to the weights used in the phase correlation criterion, and the HH weights correspond to the asymptotic weights derived in Hamon and Hannan (1974). Note that the results for LINKED are similar to the estimates derived in the previous section. For the examples THRESACOS, THRESBMA, THINCOS, and BALANCED where the coherency is concentrated at low frequencies, weights which are band limited will be favourable. In the next chapter, we will discuss a method to determine the range of frequencies where the coherency is non-zero. Then one can use the above methods for the band

limited frequencies in order to determine the phase shift. Nevertheless, the main advantage of using the above methods in comparison to those presented in the previous section is that there is no need to do separate computations and adjustments for each direction. In addition, the bias introduced by smoothing the phase spectrum is avoided.

3.3 Summary

A technique for adjusting the phase spectrum to remove discontinuities due to the $(-\pi, \pi)$ restriction was introduced in this chapter. Using the adjusted phase spectrum slopes in both the WE and SN directions were calculated. In some cases, however, we have seen that this adjustment was inadequate due to the point by point approach of this method. Thus, methods that estimate the phase shift between the components of a point-lattice process without the need to adjust the phase spectrum were discussed. In the next chapter, asymptotic properties of the cross-spectral estimates will be derived.

Chapter 4

Asymptotic Properties of Cross-Spectral Estimates

In this chapter, the asymptotic distributions of cross-spectral estimates for point-lattice processes are derived. These distributions are studied in Section 4.1. Confidence intervals for the cross-spectral estimates based on the asymptotic results are provided in Section 4.2 and a formal test of zero coherency is discussed. In Section 4.3, confidence intervals are derived for some of the examples of Chapter 2 and the test of zero coherency is applied to the coherency spectra of all the examples of Chapter 2.

4.1 Distributional Properties of Cross-Spectral Estimates

In this section, we will discuss the asymptotic properties of the cross-spectral estimates of point-lattice processes. The distributions that will be derived are extensions of those developed by Brillinger (1969) for an r vector-valued time series, Brillinger (1970) for an r vector-valued p-dimensional series, Brillinger (1972) for r vector-valued interval functions, and Rigas (1983) for a hybrid of

a one-dimensional point process and a time series. Priestley (1981b, chapter 9) also studied the distributions of multivariate time series.

Let $Z(\mathbf{a}) = \{N_X(\mathbf{a}), Y_{\mathbf{a}}\}$ be a hybrid process consisting of the process of the number of events, N_X, of a two-dimensional point process, X, and a lattice process, Y, for $\mathbf{a} \in \mathbb{R}^2$, see Section 1.2 for more details. For mathematical convenience we assume that the lattice process is defined for $\mathbf{a} \in \mathbb{R}^2$. Henceforth, we will drop the dependence of N on X in order to simplify notation. A number of assumptions and definitions about the hybrid process will follow.

The point and lattice processes satisfy the assumptions of Chapter 1. In addition, the hybrid process is assumed to be strictly stationary, that is the process $\{N(\mathbf{a}+\mathbf{c}), Y_{\mathbf{a}+\mathbf{c}}\}$ has the same probability distribution as $\{N(\mathbf{a}), Y_{\mathbf{a}}\}$ for any $\mathbf{a}, \mathbf{c} \in \mathbb{R}^2$. Define the *second-order moment* between the components of $Z(\mathbf{a})$ as

$$\mu_{NY}(\mathbf{a})d\mathbf{a} = \mathbb{E}\{dN(\mathbf{a}+\mathbf{c})Y_{\mathbf{c}}\}, \tag{4.1}$$

where $\mathbf{a} = (a_1, a_2)$ and $d\mathbf{a} = da_1 da_2$. The cross-covariance function defined in Section 2.2 is equivalent to the limit of μ_{NY} as $d\mathbf{a} \to 0$. The *cross-cumulant* function is defined by

$$\mathrm{Cum}\{dN(\mathbf{a}+\mathbf{c}), \overline{Y_{\mathbf{c}}}\} = \mathrm{Cov}\{dN(\mathbf{a}+\mathbf{c}), Y_{\mathbf{c}}\} = \gamma_{NY}(\mathbf{a})d\mathbf{a}, \tag{4.2}$$

where $\overline{x}$ denotes the complex conjugate of x. The cross-covariance function satisfies the condition $\int |\mathbf{u}|\,|\gamma_{NY}(\mathbf{u})|d\mathbf{u} < \infty$. Note that the lattice process is assumed to take both complex and real values for reasons of completeness only. More details about the cumulant function are provided in Appendix B.

The hybrid process is also assumed to possess moments of all orders and to satisfy

$$\int \cdots \int \sum_{j=1}^{k-1} |\mathbf{u}^{(j)}| \, |\gamma_{b_1 \cdots b_k}(\mathbf{u}^{(1)}, \ldots, \mathbf{u}^{(k-1)})| d\mathbf{u}^{(1)} \cdots d\mathbf{u}^{(k-1)} < \infty, \text{ where} \tag{4.3}$$

$$\gamma_{b_1 \cdots b_k}(\mathbf{u}^{(1)}, \ldots, \mathbf{u}^{(k-1)}) d\mathbf{u}^{(1)} \cdots d\mathbf{u}^{(k-1)} d\mathbf{t} =$$

$$\text{Cum}\{dZ_{b_1}(\mathbf{u}^{(1)} + \mathbf{t}), \cdots, dZ_{b_{k-1}}(\mathbf{u}^{(k-1)} + \mathbf{t}), dZ_{b_k}(\mathbf{t})\}$$

for $b_1, \ldots, b_k = (Y \text{ or } N)$; $k = 1, 2, \ldots$, and $\mathbf{u}^{(1)}, \ldots, \mathbf{u}^{(k-1)}, \mathbf{t} \in \mathbb{R}^2$. Note that $|\mathbf{u}| = \sqrt{\mathbf{u}\mathbf{u}^\top} = \sqrt{u^2 + v^2}$, where $\mathbf{u} = (u, v)$ and that the process dZ is defined as

$$dZ_j(\mathbf{u}) = \begin{cases} dN(\mathbf{u}) & \text{if } j = N, \\ Y_{\mathbf{u}} d\mathbf{u} & \text{if } j = Y, \end{cases}$$

(see Brillinger, 1970; Brillinger, 1972). Equation (4.3) is a form of a *mixing* condition. The mixing condition implies that the process of increments $\{N(\boldsymbol{\Delta}), Y(\boldsymbol{\Delta})\}$, where $N(\boldsymbol{\Delta}) = \int_{\boldsymbol{\Delta}} dN(\mathbf{a}), Y(\boldsymbol{\Delta}) = \int_{\boldsymbol{\Delta}} Y_{\mathbf{a}} d\mathbf{a}$ and $\boldsymbol{\Delta}$ is a subregion of $\mathbb{R}^2$, has the property that values of the process that are well separated in space become independent.

Next, we define the *k^{th}-order cumulant spectral* density function as

$$\begin{aligned} g_{b_1 \cdots b_k}(\boldsymbol{\omega}^{(1)}, \ldots, \boldsymbol{\omega}^{(k-1)}, \boldsymbol{\omega}^{(k)}) &= g_{b_1 \cdots b_k}(\boldsymbol{\omega}^{(1)}, \ldots, \boldsymbol{\omega}^{(k-1)}) \\ &= (2\pi)^{-2(k-1)} \int \cdots \int \exp\Big\{-i \sum_{j=1}^{k-1} \boldsymbol{\omega}^{(j)} \mathbf{u}^{(j)\top}\Big\} \\ &\quad \times \gamma_{b_1 \cdots b_k}(\mathbf{u}^{(1)}, \ldots, \mathbf{u}^{(k-1)}) d\mathbf{u}^{(1)} \cdots d\mathbf{u}^{(k-1)} \\ &= (2\pi)^{-2(k-1)} f_{b_1 \cdots b_k}(\boldsymbol{\omega}^{(1)}, \ldots, \boldsymbol{\omega}^{(k-1)}), \end{aligned} \tag{4.4}$$

for $\boldsymbol{\omega}^{(1)}, \ldots, \boldsymbol{\omega}^{(k)} \in \mathbb{R}^2$, where $\sum_{j=1}^{k} \boldsymbol{\omega}^{(j)} = \mathbf{0}$, and the other variables are as defined before. Note that the function g_{NY} defined in (2.3) is a special case of (4.4) where $k = 2$, $b_1 = N$, and $b_2 = Y$. The *cross-periodogram* statistic is defined by

$$G_{NY}(\boldsymbol{\omega}) = (2\pi)^{-2} F_{NY}(\boldsymbol{\omega}) = (2\pi)^{-2} |\boldsymbol{\Omega}|^{-1} F_N(\boldsymbol{\omega}) \overline{F_Y(\boldsymbol{\omega})} \tag{4.5}$$

for $\boldsymbol{\omega} \in \mathbb{R}^2$, where $\boldsymbol{\Omega} = [0, \ell_1] \times [0, \ell_2]$, $|\boldsymbol{\Omega}| = \ell_1 \times \ell_2$,

$$F_N(\boldsymbol{\omega}) = \int_{\boldsymbol{\Omega}} \exp\{-i\boldsymbol{\omega}\mathbf{a}^\top\} dN(\mathbf{a}), \tag{4.6}$$

$$\text{and } F_Y(\boldsymbol{\omega}) = \int_{\boldsymbol{\Omega}} \exp\{-i\boldsymbol{\omega}\mathbf{a}^\top\} Y_{\mathbf{a}} d\mathbf{a}. \tag{4.7}$$

F is known as the *finite Fourier transform* of the process. The DFTs defined in Section 1.6 are the estimates of (4.6) and (4.7) for a realisation of a point-lattice process. In practice to avoid bias near $\boldsymbol{\omega} = 0$, we use the modified cross-periodogram statistic

$$\breve{G}_{NY}(\boldsymbol{\omega}) = (2\pi)^{-2} \breve{F}_{NY} \equiv (2\pi)^{-2} |\boldsymbol{\Omega}|^{-1} \breve{F}_N(\boldsymbol{\omega}) \overline{\breve{F}_Y(\boldsymbol{\omega})}, \tag{4.8}$$

$$\text{where } \breve{F}_N(\boldsymbol{\omega}) = F_N(\boldsymbol{\omega}) - \lambda_N \Delta(\boldsymbol{\omega}) = F_N(\boldsymbol{\omega}) - \mathbb{E}[F_N(\boldsymbol{\omega})], \tag{4.9}$$

$$\breve{F}_Y(\boldsymbol{\omega}) = F_Y(\boldsymbol{\omega}) - \mu_Y \Delta(\boldsymbol{\omega}) = F_Y(\boldsymbol{\omega}) - \mathbb{E}[F_Y(\boldsymbol{\omega})], \tag{4.10}$$

and $\Delta(\boldsymbol{\omega}) = \int_{\boldsymbol{\Omega}} \exp\{-i\boldsymbol{\omega}\mathbf{a}^\top\} d\mathbf{a}$.

Next, we state a property that describes the asymptotic behaviour of the cumulant function of several finite Fourier transforms. This property is required to establish the distribution of finite Fourier transforms and some properties of the cross-periodogram. The proof of this and other properties will be provided in Section 4.1.1. Let $Z(\mathbf{a})$, $\mathbf{a} \in \mathbb{R}^2$, be a hybrid process

satisfying (4.3), then as $\ell_1, \ell_2 \to \infty$ we have

$$\mathrm{Cum}\{F_{b_1}(\boldsymbol{\omega}^{(1)}), \cdots, F_{b_k}(\boldsymbol{\omega}^{(k)})\} = (2\pi)^{2(k-1)}\Delta\Big(\sum_{j=1}^{k}\boldsymbol{\omega}^{(j)}\Big) g_{b_1\cdots b_k}(\boldsymbol{\omega}^{(1)}, \cdots, \boldsymbol{\omega}^{(k-1)}) + O(L) \quad (4.11)$$

for $\boldsymbol{\omega}^{(1)}, \ldots, \boldsymbol{\omega}^{(k)} \in \mathbb{R}^2$, where $L = \max(\ell_1, \ell_2)$. Thus asymptotically the cumulant function of finite Fourier transforms of k components tend to a multiple of the k^{th}-order cumulant spectrum.

Using this property, one can prove that for any two frequencies (say $\boldsymbol{\omega}^{(1)}$ and $\boldsymbol{\omega}^{(2)}$ such that $\boldsymbol{\omega}^{(j)} \pm \boldsymbol{\omega}^{(k)} \neq \mathbf{0}$ for $j, k = 1, 2$) as $\ell_1, \ell_2 \to \infty$ the Fourier transforms $\check{F}_Z(\boldsymbol{\omega}^{(j)})$ are asymptotically independent and distributed as

$$N_2^{\mathbb{C}}\big(\mathbf{0}, (2\pi)^2|\boldsymbol{\Omega}|\mathrm{g}_{ZZ}(\boldsymbol{\omega}^{(j)})\big), \text{ where} \quad (4.12)$$

$$\check{F}_Z(\boldsymbol{\omega}) = \begin{bmatrix}\check{F}_N(\boldsymbol{\omega}) \\ \check{F}_Y(\boldsymbol{\omega})\end{bmatrix},$$

$$\mathrm{g}_{ZZ}(\boldsymbol{\omega}) = \begin{bmatrix} g_{NN}(\boldsymbol{\omega}) & g_{NY}(\boldsymbol{\omega}) \\ g_{YN}(\boldsymbol{\omega}) & g_{YY}(\boldsymbol{\omega})\end{bmatrix}.$$

Here $N_2^{\mathbb{C}}$ denotes the bivariate complex normal distribution, see Section A.3. If $\boldsymbol{\omega} = \mathbf{0}$ then $\check{F}_Z(\boldsymbol{\omega})$ is asymptotically $N_2\big(\mathbf{0}, (2\pi)^2|\boldsymbol{\Omega}|\mathrm{g}_{ZZ}(\mathbf{0})\big)$ and independently from the above. Furthermore, if $\boldsymbol{\omega}^{(j)}$ for $j = 1, \ldots, n$ are chosen such that $\boldsymbol{\omega}^{(j)} \to \boldsymbol{\omega}$ as $\ell_1, \ell_2 \to \infty$ then $\check{F}_Z(\boldsymbol{\omega}^{(j)})$ are asymptotically independent

$$\begin{cases} N_2^{\mathbb{C}}\big(\mathbf{0}, (2\pi)^2|\boldsymbol{\Omega}|\mathrm{g}_{ZZ}(\boldsymbol{\omega})\big) & \text{for } \boldsymbol{\omega} \neq \mathbf{0}, \\ N_2\big(\mathbf{0}, (2\pi)^2|\boldsymbol{\Omega}|\mathrm{g}_{ZZ}(\mathbf{0})\big) & \text{for } \boldsymbol{\omega} = \mathbf{0}, \end{cases}$$

variates. Therefore, for most frequencies the mean-corrected finite Fourier transforms of the hybrid process are asymptotically distributed as bivariate complex normal variables with mean zero and covariance matrix a multiple of

the second-order cumulant spectral matrix. In addition, they are independent for different frequencies.

As an immediate consequence of this result and the definition of the (complex) Wishart distribution given in Section A.3, it can be shown that for the periodogram defined by (at frequency $(\boldsymbol{\omega})$)

$$\breve{\mathbf{G}}_{ZZ} = (2\pi)^{-2}\breve{\mathbf{F}}_{ZZ} \equiv (2\pi)^{-2}|\boldsymbol{\Omega}|^{-1}\breve{F}_Z\overline{\breve{F}_Z}^{\top} = \begin{bmatrix} \breve{G}_{NN} & \breve{G}_{NY} \\ \breve{G}_{YN} & \breve{G}_{YY} \end{bmatrix},$$

we have asymptotically that:

$$\breve{\mathbf{G}}_{ZZ}(\boldsymbol{\omega}) \sim \begin{cases} W_2^{\mathbb{C}}\big(1, \mathrm{g}_{ZZ}(\boldsymbol{\omega})\big) & \text{if } \boldsymbol{\omega} \neq \mathbf{0}, \\ W_2\big(1, \mathrm{g}_{ZZ}(\mathbf{0})\big) & \text{if } \boldsymbol{\omega} = \mathbf{0}. \end{cases}$$

Here, $W_2^{\mathbb{C}}$ denotes the complex Wishart distribution defined in Section A.3 of dimension two and one degree of freedom, W_2 denotes the Wishart distribution of dimension two and one degree of freedom. Furthermore,

$$\breve{G}_{ij}(\boldsymbol{\omega}) = (2\pi)^{-2}\breve{F}_{ij}(\boldsymbol{\omega}) \equiv (2\pi)^{-2}|\boldsymbol{\Omega}|^{-1}\breve{F}_i(\boldsymbol{\omega})\overline{\breve{F}_j(\boldsymbol{\omega})}^{\top} \text{ for } i, j = Y, N.$$

Therefore, the periodogram ordinates are distributed as independent (complex) Wishart variates with one degree of freedom and covariance matrix the spectral density. The distributional properties of the auto-spectra provided in Section 1.7 are an immediate consequence of this result and the following property of the (complex) Wishart distribution. For non-zero frequencies, $\breve{\mathbf{G}}$ is distributed as $W_2^{\mathbb{C}}\big(1, \mathrm{g}_{ZZ}(\boldsymbol{\omega})\big)$ which implies that $\breve{G}_{ss}$ for $s = N$ or Y is distributed as $g_{ss}\chi_2^2/2$. This property is a special case of that reported in Brillinger (1981, chapter 4) where the number of degrees of freedom of the complex Wishart distribution is taken to be $n = 1$ and therefore the number of degrees of freedom of the Chi-squared distribution is $2n = 2$. The equiv-

alence for zero frequencies can be established in a similar way. However, as Brillinger (1981) puts it:

> being, a Wishart with just 1 degree of freedom, the distribution is well spread out about $f_{XX}(\lambda)$ $\left[\mathbf{g}_{ZZ}(\boldsymbol{\omega})\right]$. Therefore, $\mathbf{I}_{XX}^{(T)}(\lambda)$ $\left[\breve{\mathbf{G}}_{ZZ}(\boldsymbol{\omega})\right]$, cannot be considered a reasonable estimate.

However, under the above assumptions the spectral density function is a smooth function of frequency (see Brillinger, 1970). Therefore, a *reasonable* estimate at a particular frequency might be constructed by averaging nearby values of the periodogram. Thus, one can consider the uniformly smoothed periodogram,

$$\mathbb{G}_{ZZ}(\boldsymbol{\omega}) \equiv \frac{1}{m}\sum_{k=1}^{m}\breve{\mathbf{G}}_{ZZ}(\boldsymbol{\omega}^{(k)}) = (2\pi)^{-2}\frac{1}{m}\sum_{k=1}^{m}\breve{\mathbf{F}}_{ZZ}(\boldsymbol{\omega}^{(k)}) \equiv (2\pi)^{-2}\mathbb{F}_{ZZ}(\boldsymbol{\omega}),$$

where $\boldsymbol{\omega}^{(k)}$ for $k = 1, \ldots, m$ are nearby frequencies to $\boldsymbol{\omega}$. This smoother is a special case of the smoothers introduced in Section 1.8. Again, using the above results and the properties of the (complex) Wishart distribution the following holds asymptotically:

$$\mathbb{G}_{ZZ}(\boldsymbol{\omega}) \sim \begin{cases} m^{-1}W_2^{\mathbb{C}}\big(m, \mathbf{g}_{ZZ}(\boldsymbol{\omega})\big) & \text{if } \boldsymbol{\omega} \neq \mathbf{0}, \\ m^{-1}W_2\big(m, \mathbf{g}_{ZZ}(\mathbf{0})\big) & \text{if } \boldsymbol{\omega} = \mathbf{0}. \end{cases}$$

Having established the asymptotic joint distribution of the cumulant spectral density function for a point-lattice process, we proceed to give the asymptotic properties of the cross-periodogram statistic. It can be shown that asymptotically $\breve{G}_{NY}(\boldsymbol{\omega})$, which is the cross-periodogram defined in (4.8), has

the following properties:

$$\lim_{\ell_1,\ell_2\to\infty} \mathbb{E}\{\breve{G}_{NY}(\boldsymbol{\omega})\} = g_{NY}(\boldsymbol{\omega}) \quad \text{for } \boldsymbol{\omega} \neq 0, \tag{4.13}$$

$$\text{and } \lim_{\ell_1,\ell_2\to\infty} \mathrm{Cov}\{\breve{G}_{NY}(\mathbf{r}), \breve{G}_{NY}(\mathbf{s})\} = \delta\{\mathbf{r}-\mathbf{s}\} g_{NN}(\mathbf{r}) g_{YY}(-\mathbf{r}) + \delta\{\mathbf{r}+\mathbf{s}\} g_{NY}(\mathbf{r}) g_{YN}(-\mathbf{r}) \tag{4.14}$$

for $\mathbf{r}, \mathbf{s} \neq \mathbf{0}$, where $\delta\{\}$ is the Kronecker delta defined in Section A.2.

Thus asymptotically the cross-periodogram is an unbiased estimator of the second-order cross-cumulant spectral density function. Equations (4.13) and (4.14) can then be used to deduce the asymptotic behaviour of covariances for the co- and the quadrature spectra defined in (2.4). Here the co-spectrum is written as

$$\breve{c}_{NY}(\boldsymbol{\omega}) = \frac{(2\pi)^2}{2}\Big\{\breve{G}_{NY}(\boldsymbol{\omega}) + \overline{\breve{G}_{NY}}(\boldsymbol{\omega})\Big\} = \frac{1}{2}\Big\{\breve{F}_{NY}(\boldsymbol{\omega}) + \overline{\breve{F}_{NY}}(\boldsymbol{\omega})\Big\},$$

and the quadrature spectrum is written as

$$\breve{q}_{NY}(\boldsymbol{\omega}) = \frac{(2\pi)^2}{2i}\Big\{\overline{\breve{G}_{NY}}(\boldsymbol{\omega}) - \breve{G}_{NY}(\boldsymbol{\omega})\Big\} = \frac{1}{2i}\Big\{\overline{\breve{F}_{NY}}(\boldsymbol{\omega}) - \breve{F}_{NY}(\boldsymbol{\omega})\Big\}.$$

Therefore, the covariance matrix of $\breve{F}_{NN}$, $\breve{F}_{YY}$, $\breve{c}_{NY}$, and $\breve{q}_{NY}$ is given by

$$\begin{array}{c|c} & \begin{array}{cccc} \breve{F}_{NN}(\boldsymbol{\omega}) & \breve{F}_{YY}(\boldsymbol{\omega}) & \breve{c}_{NY}(\boldsymbol{\omega}) & \breve{q}_{NY}(\boldsymbol{\omega}) \end{array} \\ \begin{array}{c} \breve{F}_{NN}(\boldsymbol{\omega}) \\ \breve{F}_{YY}(\boldsymbol{\omega}) \\ \breve{c}_{NY}(\boldsymbol{\omega}) \\ \\ \breve{q}_{NY}(\boldsymbol{\omega}) \end{array} & K \begin{bmatrix} f_{NN}^2(\boldsymbol{\omega}) & |f_{NY}(\boldsymbol{\omega})|^2 & f_{NN}(\boldsymbol{\omega})c_{NY}(\boldsymbol{\omega}) & f_{NN}(\boldsymbol{\omega})q_{NY}(\boldsymbol{\omega}) \\ & f_{YY}^2(\boldsymbol{\omega}) & f_{YY}(\boldsymbol{\omega})c_{NY}(\boldsymbol{\omega}) & f_{YY}(\boldsymbol{\omega})q_{NY}(\boldsymbol{\omega}) \\ & & \frac{1}{2}\{f_{NN}(\boldsymbol{\omega})f_{YY}(\boldsymbol{\omega}) & c_{NY}(\boldsymbol{\omega})q_{NY}(\boldsymbol{\omega}) \\ & & +c_{NY}^2(\boldsymbol{\omega}) - q_{NY}^2(\boldsymbol{\omega})\} & \\ & & & \frac{1}{2}\{f_{NN}(\boldsymbol{\omega})f_{YY}(\boldsymbol{\omega}) \\ & & & +q_{NY}^2(\boldsymbol{\omega}) - c_{NY}^2(\boldsymbol{\omega})\} \end{bmatrix} \end{array}. \tag{4.15}$$

Here $K = 1$ but if $\mathbb{G}$ is used instead of $\breve{\mathbf{G}}$ then $K = m$. Only the upper triangle of the covariance matrix is reported; the lower triangle is derived by symmetry. The matrix in (4.15) is similar to that reported in Priestley (1981b, chapter9) for any two components of a one-dimensional multivariate time series.

The asymptotic results for amplitude, phase and squared coherency spectra are derived by expanding these functions around their means using Taylor series expansions, and retaining the first two or three terms. Taylor expansions are needed since the amplitude, phase and squared coherency spectra are non-linear functions of $\breve{c}_{NY}, \breve{q}_{NY}, \breve{F}_{NN}$, and $\breve{F}_{YY}$. In fact, using just the first two terms of Taylor expansion for functions of several variables gives

$$\mathbb{E}\{\breve{\alpha}_{NY}\} = \alpha_{NY},\ \mathbb{E}\{\breve{\phi}_{NY}\} = \phi_{NY},\ \mathbb{E}\{\breve{\upsilon}_{NY}\} = \upsilon_{NY},$$

and

$$\begin{aligned}
\mathrm{Var}(\breve{\alpha}_{NY}) &\sim \frac{K\alpha_{NY}^2}{2}\Big\{\frac{1}{\upsilon_{NY}} + 1\Big\} \\
\mathrm{Var}(\breve{\phi}_{NY}) &\sim \frac{K}{2}\Big\{\frac{1}{\upsilon_{NY}} - 1\Big\} \\
\mathrm{Cov}(\breve{\phi}_{NY}, \breve{\alpha}_{NY}) &\sim 0 \\
\mathrm{Var}(\breve{\upsilon}_{NY}) &\sim 2K\upsilon_{NY}(1 - \upsilon_{NY})^2.
\end{aligned}$$

If the statistics are calculated at frequencies of the form $w_p = \frac{2\pi p}{\ell}$ where p and ℓ are integers then similar results to the above can be established for the equivalent discrete Fourier transforms. Since $w_{p+\ell} \equiv w_p \pmod{2\pi}$ then this should be taken into account when stating conditions in the above results. Moreover, the Kronecker delta in (4.14) should be replaced with the Kronecker comb defined in Section A.2 to account for the equivalence of frequencies modulus 2π.

Next, we establish equivalent properties of those defined above for the estimates defined in Chapter 2. The quantities defined in (2.9) are the sample estimates of the modified cross-periodogram statistic defined by

$$\grave{G}_{NY}(\boldsymbol{\omega}) = (2\pi)^{-2}\grave{F}_{NY} \equiv (2\pi)^{-2}|\boldsymbol{\Omega}|^{-1}F_N(\boldsymbol{\omega})\overline{\breve{F}_Y(\boldsymbol{\omega})}, \tag{4.16}$$

where F_N and $\breve{F}_Y$ are as defined in (4.6) and (4.10). The above definition is required because the lattice pattern in Chapter 2 is assumed to be corrected for its mean which is equivalent to the Fourier transform of the lattice pattern being corrected for its mean. However, no such correction is carried out for the Fourier transform of the point pattern. Defining

$$\grave{F}_Z(\boldsymbol{\omega}) = \begin{bmatrix} F_N(\boldsymbol{\omega}) \\ \breve{F}_Y(\boldsymbol{\omega}) \end{bmatrix},$$

one can establish a similar result to (4.12) with the zero-mean vector being replaced by $\boldsymbol{\eta} = (\lambda_N\Delta(\boldsymbol{\omega}), 0)^\top$. Hence, $\grave{F}_Z(\boldsymbol{\omega})$ are asymptotically independent for different frequencies and distributed as $N_2^{\mathbb{C}}\big(\boldsymbol{\eta}, (2\pi)^2|\boldsymbol{\Omega}|\mathrm{g}_{ZZ}(\boldsymbol{\omega})\big)$, where g_{ZZ} is as defined above. The property $\mathrm{Cov}(X + \mathrm{c}, Y) = \mathrm{Cov}(X, Y)$ for c a constant ensures that the covariance matrices for the distributions of $\grave{F}$ and $\breve{F}$ coincide. Also, one can define $\grave{\mathbf{G}}[\grave{\mathbf{F}}]$ and $\grave{\mathbb{G}}[\grave{\mathbb{F}}]$ in a similar way to $\breve{\mathbf{G}}[\breve{\mathbf{F}}]$ and $\mathbb{G}[\mathbb{F}]$.

Equations (4.13) and (4.14) still hold if $\breve{G}$ is replaced by $\grave{G}$. In addition, the covariance matrix defined in (4.15) also represents the covariance matrix of F_{NN}, $\breve{F}_{YY}$, $\grave{c}\Big(= \frac{1}{2}\big\{\grave{F}_{NY} + \overline{\grave{F}_{NY}}\big\}\Big)$, and $\grave{q}\Big(= \frac{1}{2}\big\{\overline{\grave{F}_{NY}} - \grave{F}_{NY}\big\}\Big)$. Asymptotic properties of the associated amplitude $(\grave{\alpha})$, phase $(\grave{\phi})$ and squared coherency $(\grave{\upsilon})$ coincide with those reported for $\breve{\alpha}$, $\breve{\phi}$, and $\breve{\upsilon}$. Note here that C_{NY}, Q_{NY}, A_{NY}, Φ_{NY}, and Υ_{NY} are the sample estimates of $\grave{c}$, $\grave{q}$, $\grave{\alpha}$, $\grave{\phi}$, and $\grave{\upsilon}$, respectively.

4.1.1 Proofs

In this section, we provide proofs for the asymptotic properties stated in the previous section.

4.1.1.1 Proof of (4.11)

To prove (4.11) let

$$
\begin{aligned}
\mathcal{A} =& \operatorname{Cum}\{F_{b_1}(\boldsymbol{\omega}^{(1)}), \cdots, F_{b_k}(\boldsymbol{\omega}^{(k)})\} \\
=& \operatorname{Cum}\Big\{\int_{\boldsymbol{\Omega}} \exp\{-i\boldsymbol{\omega}^{(1)}\mathbf{a}^{(1)\top}\} dZ_{b_1}(\mathbf{a}^{(1)}), \cdots, \\
& \qquad\qquad \int_{\boldsymbol{\Omega}} \exp\{-i\boldsymbol{\omega}^{(k)}\mathbf{a}^{(k)\top}\} dZ_{b_k}(\mathbf{a}^{(k)})\Big\} \\
=& \int_{\boldsymbol{\Omega}} \cdots \int_{\boldsymbol{\Omega}} \exp\{-i\sum_{j=1}^{k} \boldsymbol{\omega}^{(j)}\mathbf{a}^{(j)\top}\} \operatorname{Cum}\{dZ_{b_1}(\mathbf{a}^{(1)}), \cdots, dZ_{b_k}(\mathbf{a}^{(k)})\} \\
=& \int_{\boldsymbol{\Omega}} \cdots \int_{\boldsymbol{\Omega}} \exp\{-i\sum_{j=1}^{k} \boldsymbol{\omega}^{(j)}\mathbf{a}^{(j)\top}\} \times \\
& \qquad \gamma_{b_1\cdots b_k}(\mathbf{a}^{(1)} - \mathbf{a}^{(k)}, \cdots, \mathbf{a}^{(k-1)} - \mathbf{a}^{(k)})\, d\mathbf{a}^{(1)} \cdots d\mathbf{a}^{(k-1)} d\mathbf{a}^{(k)} \\
=& \int_0^{\ell_2} \int_0^{\ell_1} \cdots \int_0^{\ell_2} \int_0^{\ell_1} \exp\{-i\sum_{j=1}^{k} (\omega_1^{(j)} a_1^{(j)} + \omega_2^{(j)} a_2^{(j)})\} \times \\
& \qquad \gamma_{b_1\cdots b_k}((a_1^{(1)} - a_1^{(k)}, a_2^{(1)} - a_2^{(k)}), \cdots, (a_1^{(k-1)} - a_1^{(k)}, a_2^{(k-1)} - a_2^{(k)})) \\
& \qquad da_1^{(1)} da_2^{(1)} \cdots da_1^{(k-1)} da_2^{(k-1)} da_1^{(k)} da_2^{(k)} \\
=& \int_0^{\ell_2} \cdots \int_0^{\ell_2} \exp\{-i\sum_{j=1}^{k} \omega_2^{(j)} a_2^{(j)}\} \int_0^{\ell_1} \cdots \int_0^{\ell_1} \exp\{-i\sum_{j=1}^{k} \omega_1^{(j)} a_1^{(j)}\} \times \\
& \qquad \gamma_{b_1\cdots b_k}((a_1^{(1)} - a_1^{(k)}, a_2^{(1)} - a_2^{(k)}), \cdots, (a_1^{(k-1)} - a_1^{(k)}, a_2^{(k-1)} - a_2^{(k)})) \\
& \qquad da_1^{(1)} \cdots da_1^{(k)} da_2^{(1)} \cdots da_2^{(k)} \\
=& \int_0^{\ell_2} \cdots \int_0^{\ell_2} \exp\{-i\sum_{j=1}^{k} \omega_2^{(j)} a_2^{(j)}\} (\mathcal{B})\, da_2^{(1)} \cdots da_2^{(k)},
\end{aligned}
$$

$$\text{where} \qquad \mathcal{B} = \int_0^{\ell_1} \cdots \int_0^{\ell_1} \exp\Big\{-i \sum_{j=1}^{k} \omega_1^{(j)} a_1^{(j)}\Big\} \times$$
$$\gamma_{b_1 \cdots b_k}((a_1^{(1)} - a_1^{(k)}, a_2^{(1)} - a_2^{(k)}), \cdots, (a_1^{(k-1)} - a_1^{(k)}, a_2^{(k-1)} - a_2^{(k)}))$$
$$da_1^{(1)} \cdots da_1^{(k)}. \quad (4.17)$$

For the time being we shall drop the dependence of the above equation on the y-ordinate. Set $u_j = a_1^{(j)} - a_1^{(k)}$ for $j = 1, \ldots, k-1$; $a_1^{(k)} = u$ and substitute these values in (4.17) then

$$\mathcal{B} = \int_0^{\ell_1} \int_{-u}^{\ell_1 - u} \cdots \int_{-u}^{\ell_1 - u} \exp\Big\{-i\Big(\sum_{j=1}^{k-1} \omega_1^{(j)} u_j + u \sum_{j=1}^{k} \omega_1^{(j)}\Big)\Big\} \times$$
$$\gamma_{b_1 \cdots b_k}(u_1, \cdots, u_{k-1})\, du_1 \cdots du_{k-1} du.$$

Let $\mathcal{C} = \exp\Big\{-i\big(\sum_{j=1}^{k-1} \omega_1^{(j)} u_j + u \sum_{j=1}^{k} \omega_1^{(j)}\big)\Big\} \gamma_{b_1 \cdots b_k}(u_1, \cdots, u_{k-1})$ and interchange the variables u and u_{k-1} then

$$\mathcal{B} = \int_{-\ell_1}^{0} \int_{-u_{k-1}}^{\ell_1} \int_{-u}^{\ell_1 - u} \cdots \int_{-u}^{\ell_1 - u} \mathcal{C}\, du_1 \cdots du_{k-2}\, du\, du_{k-1}$$
$$+ \int_0^{\ell_1} \int_0^{\ell_1 - u_{k-1}} \int_{-u}^{\ell_1 - u} \cdots \int_{-u}^{\ell_1 - u} \mathcal{C}\, du_1 \cdots du_{k-2}\, du\, du_{k-1}.$$

Next, define the following for $j = 1, \ldots, k-1$

$$M_j = \ell_1 - \max(0, u_j, \cdots, u_{k-1}),$$
$$m_j = -\min(0, u_j, \cdots, u_{k-1}).$$

Then,

$$m_{k-1} = -\min(0, u_{k-1}) = \begin{cases} -u_{k-1} & \text{if } u_{k-1} < 0, \\ 0 & \text{if } u_{k-1} > 0, \text{ and} \end{cases}$$
$$M_{k-1} = \ell_1 - \max(0, u_{k-1}) = \begin{cases} \ell_1 & \text{if } u_{k-1} < 0, \\ \ell_1 - u_{k-1} & \text{if } u_{k-1} > 0. \end{cases}$$

Thus,

$$\mathcal{B} = \int_{-\ell_1}^{0} \int_{m_{k-1}}^{M_{k-1}} \int_{-u}^{\ell_1-u} \cdots \int_{-u}^{\ell_1-u} \mathcal{C}\, du_1 \cdots du_{k-2}\, du\, du_{k-1}$$
$$+ \int_{0}^{\ell_1} \int_{m_{k-1}}^{M_{k-1}} \int_{-u}^{\ell_1-u} \cdots \int_{-u}^{\ell_1-u} \mathcal{C}\, du_1 \cdots du_{k-2}\, du\, du_{k-1}.$$

Therefore, $\mathcal{B} = \int_{-\ell_1}^{\ell_1} \int_{m_{k-1}}^{M_{k-1}} \int_{-u}^{\ell_1-u} \cdots \int_{-u}^{\ell_1-u} \mathcal{C}\, du_1 \cdots du_{k-2}\, du\, du_{k-1}$. Interchanging the variables u_{k-2} and u gives

$$\mathcal{B} = \int_{-\ell_1}^{\ell_1} \left\{ \int_{-M_{k-1}}^{-m_{k-1}} \int_{-u_{k-2}}^{M_{k-1}} + \int_{-m_{k-1}}^{\ell_1-M_{k-1}} \int_{m_{k-1}}^{M_{k-1}} + \int_{\ell_1-M_{k-1}}^{\ell_1-m_{k-1}} \int_{m_{k-1}}^{\ell_1-u_{k-2}} \right\}$$
$$\int_{-u}^{\ell_1-u} \cdots \int_{-u}^{\ell_1-u} \mathcal{C}\, du_1 \cdots du\, du_{k-2}\, du_{k-1}. \quad (4.18)$$

In (4.18) it can be shown that the limits of the variable u are m_{k-2} and M_{k-2} for the lower and upper bounds, respectively, regardless of the limits of the variable u_{k-2}. Therefore,

$$\mathcal{B} = \int_{-\ell_1}^{\ell_1} \int_{-M_{k-1}}^{\ell_1-m_{k-1}} \int_{m_{k-2}}^{M_{k-2}} \int_{-u}^{\ell_1-u} \cdots \int_{-u}^{\ell_1-u} \mathcal{C}\, du_1 \cdots du\, du_{k-2}\, du_{k-1}.$$

Next, interchange the variables u and u_{k-3} by defining the limits of the variable u_{k-3} in the same manner as that of u_{k-2} and repeat the above steps until the last variable u_1 is reached. Figure 4.1 is a graphical representation of how the limits of the integrals involving the variables u and u_j are interchanged. The final step of interchanging variables leads to the following equation

$$\mathcal{B} = \int_{-\ell_1}^{\ell_1} \int_{-M_{k-1}}^{\ell_1-m_{k-1}} \cdots \int_{-M_j}^{\ell_1-m_j} \cdots \int_{-M_2}^{\ell_1-m_2} \int_{m_1}^{M_1} \mathcal{C}\, du\, du_1 \cdots du_j \cdots du_{k-1}$$
$$= \int_{-\ell_1}^{\ell_1} \int_{-M_{k-1}}^{\ell_1-m_{k-1}} \cdots \int_{-M_j}^{\ell_1-m_j} \cdots \int_{-M_2}^{\ell_1-m_2} \mathcal{C}' \int_{m_1}^{M_1} \exp\Big\{-iu \sum_{j=1}^{k} \omega_1^{(j)}\Big\} du$$
$$du_1 \cdots du_j \cdots du_{k-1},$$

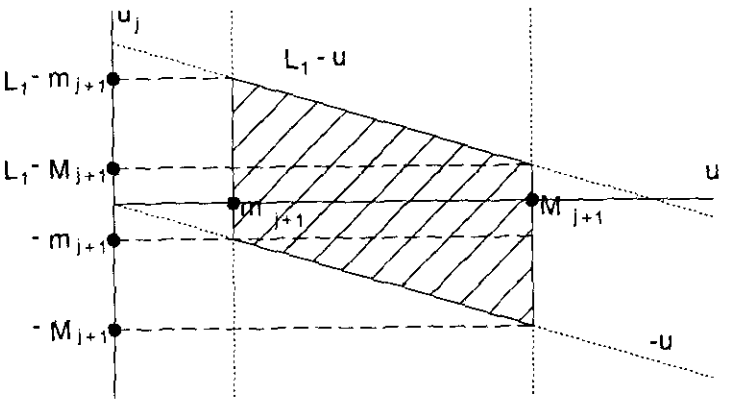

Figure 4.1: Interchanging limits for the variables u and u_j.

where $C' = \exp\Big\{-i\sum_{j=1}^{k-1}\omega_1^{(j)}u_j\Big\}\gamma_{b_1\cdots b_k}(u_1,\cdots,u_{k-1})$. Next, repeat the above for the y-ordinate then (4.1.1) becomes

$$\mathcal{A} = \int_{-\ell_2}^{\ell_2}\int_{-N_{k-1}}^{\ell_2-n_{k-1}}\cdots\int_{-N_j}^{\ell_2-n_j}\cdots\int_{-N_2}^{\ell_2-n_2}\int_{-\ell_1}^{\ell_1}\int_{-M_{k-1}}^{\ell_1-m_{k-1}}\cdots\int_{-M_j}^{\ell_1-m_j}\cdots\int_{-M_2}^{\ell_1-m_2}$$
$$\mathcal{D}\,\mathcal{E}'\,\mathcal{E}''\,\mathcal{H}\,du_1\cdots du_j\cdots du_{k-1}\,dv_1\cdots dv_j\cdots dv_{k-1}.$$

Here, we have for $j = 1,\ldots,k-1$

$$v_j = a_2^{(j)} - a_2^{(k)},$$

$$N_j = \ell_2 - \max(0, v_j, \cdots, v_{k-1}),$$

$$n_j = -\min(0, v_j, \cdots, v_{k-1}),$$

and $a_2^{(k)} = v$. Furthermore,

$$\mathcal{D} = \int_{n_1}^{N_1} \int_{m_1}^{M_1} \exp\Big\{-i \sum_{j=1}^{k} \big(\omega_1^{(j)} u + \omega_2^{(j)} v\big)\Big\} du\, dv,$$

$$\mathcal{E}' = \exp\Big\{-i \sum_{j=1}^{k-1} \omega_1^{(j)} u_j\Big\},$$

$$\mathcal{E}'' = \exp\Big\{-i \sum_{j=1}^{k-1} \omega_2^{(j)} v_j\Big\},$$

$$\mathcal{H} = \gamma_{b_1 \cdots b_k}((u_1, v_1), \cdots, (u_{k-1}, v_{k-1})).$$

Therefore,

$$\mathcal{A} = \int_{-\ell_2}^{\ell_2} \int_{-\ell_1}^{\ell_1} \int_{-N_{k-1}}^{\ell_2 - n_{k-1}} \int_{-M_{k-1}}^{\ell_1 - m_{k-1}} \cdots \int_{-N_j}^{\ell_2 - n_j} \int_{-M_j}^{\ell_1 - m_j} \cdots \int_{-N_2}^{\ell_2 - n_2} \int_{-M_2}^{\ell_1 - m_2}$$
$$\mathcal{D}\, \mathcal{E}'\, \mathcal{E}''\, \mathcal{H}\, du_1\, dv_1 \cdots du_j\, dv_j \cdots du_{k-1}\, dv_{k-1}$$
$$= \int_{\mathbf{\Omega}_k} \int_{\mathbf{\Omega}_{k-1}} \cdots \int_{\mathbf{\Omega}_2} \mathcal{D}\, \mathcal{E}\, d\mathbf{u}^{(1)} \cdots d\mathbf{u}^{(k-2)} d\mathbf{u}^{(k-1)}.$$

Here, we have for $j = 1, \ldots, k-1$,

$$\mathbf{u}^{(j)} = (u_j, v_j),$$

$$d\mathbf{u}^{(j)} = du_j\, dv_j,$$

$$\mathbf{\Omega}_j = [-M_j, \ell_1 - m_j] \times [-N_j, \ell_2 - n_j],$$

and $\mathbf{\Omega}_k = [-\ell_1, \ell_1] \times [-\ell_2, \ell_2]$. Also,

$$\mathcal{E} = \exp\Big\{-i \sum_{j=1}^{k-1} \boldsymbol{\omega}^{(j)} \mathbf{u}^{(j)^\top}\Big\} \gamma_{b_1 \cdots b_k}(\mathbf{u}^{(1)}, \cdots, \mathbf{u}^{(k-1)}).$$

Set $\Delta\big(\sum_{j=1}^{k}\boldsymbol{\omega}^{(j)}\big) = \int_0^{\ell_2}\int_0^{\ell_1}\exp\big\{-i\sum_{j=1}^{k}\big(\omega_1^{(j)}u+\omega_2^{(j)}v\big)\big\}du\,dv$ and consider

$$\begin{aligned}\Big|\mathcal{D}-\Delta\Big(\sum_{j=1}^{k}\boldsymbol{\omega}^{(j)}\Big)\Big| &= \Big|\Big\{\int_0^{\ell_2}\int_0^{m_1}+\int_0^{n_1}\int_{m_1}^{M_1}+\int_{N_1}^{\ell_2}\int_{m_1}^{M_1}+\int_0^{\ell_2}\int_{M_1}^{\ell_1}\Big\}\\ &\qquad \exp\Big\{-i\sum_{j=1}^{k}(\omega_1^{(j)}u+\omega_2^{(j)}v)\Big\}du\,dv\Big|\\ &\le \Big\{\int_0^{\ell_2}\int_0^{m_1}+\int_0^{n_1}\int_{m_1}^{M_1}+\int_{N_1}^{\ell_2}\int_{m_1}^{M_1}+\int_0^{\ell_2}\int_{M_1}^{\ell_1}\Big\}\\ &\qquad \Big|\exp\Big\{-i\sum_{j=1}^{k}(\omega_1^{(j)}u+\omega_2^{(j)}v)\Big\}\Big|du\,dv\end{aligned}$$

$$\begin{aligned}&\le \Big\{\int_0^{\ell_2}\int_0^{m_1}+\int_0^{n_1}\int_{m_1}^{M_1}+\int_{N_1}^{\ell_2}\int_{m_1}^{M_1}+\int_0^{\ell_2}\int_{M_1}^{\ell_1}\Big\}du\,dv\\ &= \ell_2 m_1+n_1(M_1-m_1)+(\ell_2-N_1)(M_1-m_1)+\\ &\qquad \ell_2(\ell_1-M_1).\end{aligned}$$

However,

$$\begin{aligned}|m_1| = |-\min(0,u_1,\ldots,u_{k-1})| &\le \sum_{j=1}^{k-1}|u_j| \le \sum_{j=1}^{k-1}|\mathbf{u}^{(j)}|,\\ |n_1| = |-\min(0,v_1,\ldots,v_{k-1})| &\le \sum_{j=1}^{k-1}|v_j| \le \sum_{j=1}^{k-1}|\mathbf{u}^{(j)}|,\\ |\ell_1-M_1| = |\max(0,u_1,\ldots,u_{k-1})| &\le \sum_{j=1}^{k-1}|u_j| \le \sum_{j=1}^{k-1}|\mathbf{u}^{(j)}|,\\ |\ell_2-N_1| = |\max(0,v_1,\ldots,v_{k-1})| &\le \sum_{j=1}^{k-1}|v_j| \le \sum_{j=1}^{k-1}|\mathbf{u}^{(j)}|,\end{aligned}$$

and $|M_1-m_1| = |\ell_1-\max(0,u_1,\ldots,u_{k-1})+\min(0,u_1,\ldots,u_{k-1})| \le \ell_1$.

Therefore, $\Big|\mathcal{D}-\Delta\big(\sum_{j=1}^{k}\boldsymbol{\omega}^{(j)}\big)\Big| \le 2\big(\ell_2+\ell_1\big)\sum_{j=1}^{k-1}|\mathbf{u}^{(j)}| \le 4L\sum_{j=1}^{k-1}|\mathbf{u}^{(j)}|$ and L is as defined before which implies that $\mathcal{D} = \Delta\big(\sum_{j=1}^{k}\boldsymbol{\omega}^{(j)}\big)+\epsilon$, where

$|\epsilon| \le 4L \sum_{j=1}^{k-1} |\mathbf{u}^{(j)}|$. Thus,

$$\mathcal{A} = \Delta\Big(\sum_{j=1}^{k} \boldsymbol{\omega}^{(j)}\Big) \int_{\Omega_k} \int_{\Omega_{k-1}} \cdots \int_{\Omega_2} \mathcal{E}\, d\mathbf{u}^{(1)} \cdots d\mathbf{u}^{(k-2)}\, d\mathbf{u}^{(k-1)}$$
$$+ \int_{\Omega_k} \int_{\Omega_{k-1}} \cdots \int_{\Omega_2} \epsilon\, \mathcal{E}\, d\mathbf{u}^{(1)} \cdots d\mathbf{u}^{(k-2)}\, d\mathbf{u}^{(k-1)}.$$

However,

$$\Big| \int_{\Omega_k} \cdots \int_{\Omega_2} \epsilon\, \mathcal{E}\, d\mathbf{u}^{(1)} \cdots d\mathbf{u}^{(k-1)} \Big| \le \int_{\Omega_k} \cdots \int_{\Omega_2} 4L \sum_{j=1}^{k-1} |\mathbf{u}^{(j)}| |\mathcal{E}\, | d\mathbf{u}^{(1)} \cdots d\mathbf{u}^{(k-1)}$$
$$= \int_{\Omega_k} \cdots \int_{\Omega_2} 4L \sum_{j=1}^{k-1} |\mathbf{u}^{(j)}| |\gamma_{b_1 \cdots b_k}(\mathbf{u}^{(1)}, \cdots, \mathbf{u}^{(k-1)})| d\mathbf{u}^{(1)} \cdots d\mathbf{u}^{(k-1)}$$
$$\le 4L \int_{\mathbb{R}^2} \cdots \int_{\mathbb{R}^2} \sum_{j=1}^{k-1} |\mathbf{u}^{(j)}| |\gamma_{b_1 \cdots b_k}(\mathbf{u}^{(1)}, \cdots, \mathbf{u}^{(k-1)})| d\mathbf{u}^{(1)} \cdots d\mathbf{u}^{(k-1)}$$
$$\le KL = O(L),$$

since by (4.3)

$$\int_{\mathbb{R}^2} \cdots \int_{\mathbb{R}^2} \sum_{j=1}^{k-1} |\mathbf{u}^{(j)}| |\gamma_{b_1 \cdots b_k}(\mathbf{u}^{(1)}, \cdots, \mathbf{u}^{(k-1)})| d\mathbf{u}^{(1)} \cdots d\mathbf{u}^{(k-1)} \le K/4,$$

and K is a finite number. Therefore,

$$\mathcal{A} = \Delta\Big(\sum_{j=1}^{k} \boldsymbol{\omega}^{(j)}\Big) \int_{\Omega_k} \cdots \int_{\Omega_2} \mathcal{E}\, d\mathbf{u}^{(1)} \cdots d\mathbf{u}^{(k-1)} + O(L)$$
$$= (2\pi)^{2(k-1)} \Delta\Big(\sum_{j=1}^{k} \boldsymbol{\omega}^{(j)}\Big) \times$$
$$(2\pi)^{-2(k-1)} \int_{\Omega_k} \cdots \int_{\Omega_2} \mathcal{E}\, d\mathbf{u}^{(1)} \cdots d\mathbf{u}^{(k-1)} + O(L).$$

Hence, as $\ell_1, \ell_2 \to \infty$

$$\mathcal{A} = (2\pi)^{2(k-1)} \Delta\Big(\sum_{j=1}^{k} \boldsymbol{\omega}^{(j)}\Big) g_{b_1 \cdots b_k}(\mathbf{u}^{(1)}, \cdots, \mathbf{u}^{(k-1)}) + O(L). \tag{4.19}$$

This proves (4.11).

4.1.1.2 Proof of (4.12)

To prove (4.12), first standardise $\breve{F}_Z(\boldsymbol{\omega})$ by multiplying it by $|\boldsymbol{\Omega}|^{-\frac{1}{2}}$. Then,

$$\begin{aligned}\mathbb{E}\Big\{|\boldsymbol{\Omega}|^{-\frac{1}{2}}\breve{F}_Z(\boldsymbol{\omega})\Big\} =&|\boldsymbol{\Omega}|^{-\frac{1}{2}}\begin{bmatrix}\mathbb{E}\{\breve{F}_N(\boldsymbol{\omega})\}\\ \mathbb{E}\{\breve{F}_Y(\boldsymbol{\omega})\}\end{bmatrix}\\ =&|\boldsymbol{\Omega}|^{-\frac{1}{2}}\begin{bmatrix}\mathbb{E}\{F_N(\boldsymbol{\omega})\}-\lambda_N\Delta(\boldsymbol{\omega})\\ \mathbb{E}\{F_Y(\boldsymbol{\omega})\}-\mu_Y\Delta(\boldsymbol{\omega})\end{bmatrix}\\ =&\mathbf{0}.\end{aligned}$$

Next,

$$\begin{aligned}\mathrm{Cov}\Big\{|\boldsymbol{\Omega}|^{-\frac{1}{2}}\breve{F}_Z(\boldsymbol{\omega}^{(1)}),|\boldsymbol{\Omega}|^{-\frac{1}{2}}\breve{F}_Z(\boldsymbol{\omega}^{(2)})\Big\} &= |\boldsymbol{\Omega}|^{-1}\mathbb{E}\Big\{\breve{F}_Z(\boldsymbol{\omega}^{(1)})\overline{\breve{F}_Z(\boldsymbol{\omega}^{(2)})}^{\mathsf{T}}\Big\}\\ &= |\boldsymbol{\Omega}|^{-1}\mathcal{M},\ \text{and}\end{aligned}$$

$$\begin{aligned}\mathcal{M} =&\mathbb{E}\left\{\begin{bmatrix}\breve{F}_N(\boldsymbol{\omega}^{(1)})\\ \breve{F}_Y(\boldsymbol{\omega}^{(1)})\end{bmatrix}\begin{bmatrix}\breve{F}_N(-\boldsymbol{\omega}^{(2)}) & \breve{F}_Y(-\boldsymbol{\omega}^{(2)})\end{bmatrix}\right\}\\ =&\mathbb{E}\left\{\begin{bmatrix}\breve{F}_N(\boldsymbol{\omega}^{(1)})\breve{F}_N(-\boldsymbol{\omega}^{(2)}) & \breve{F}_N(\boldsymbol{\omega}^{(1)})\breve{F}_Y(-\boldsymbol{\omega}^{(2)})\\ \breve{F}_Y(\boldsymbol{\omega}^{(1)})\breve{F}_N(-\boldsymbol{\omega}^{(2)}) & \breve{F}_Y(\boldsymbol{\omega}^{(1)})\breve{F}_Y(-\boldsymbol{\omega}^{(2)})\end{bmatrix}\right\}\\ =&\begin{bmatrix}\mathrm{Cum}\{\breve{F}_N(\boldsymbol{\omega}^{(1)}),\breve{F}_N(-\boldsymbol{\omega}^{(2)})\} & \mathrm{Cum}\{\breve{F}_N(\boldsymbol{\omega}^{(1)}),\breve{F}_Y(-\boldsymbol{\omega}^{(2)})\}\\ \mathrm{Cum}\{\breve{F}_Y(\boldsymbol{\omega}^{(1)}),\breve{F}_N(-\boldsymbol{\omega}^{(2)})\} & \mathrm{Cum}\{\breve{F}_Y(\boldsymbol{\omega}^{(1)}),\breve{F}_Y(-\boldsymbol{\omega}^{(2)})\}\end{bmatrix}\\ =&(2\pi)^2\Delta(\boldsymbol{\omega}^{(1)}-\boldsymbol{\omega}^{(2)})\begin{bmatrix}g_{NN}(\boldsymbol{\omega}^{(1)}) & g_{NY}(\boldsymbol{\omega}^{(1)})\\ g_{YN}(\boldsymbol{\omega}^{(1)}) & g_{YY}(\boldsymbol{\omega}^{(1)})\end{bmatrix}+O(L)\mathbf{1},\end{aligned}$$

where $\mathbf{1}$ is the 2×2 matrix of ones.

If $\boldsymbol{\omega}^{(1)}\neq\boldsymbol{\omega}^{(2)}$ then $|\boldsymbol{\Omega}|^{-1}\mathrm{Cov}\Big\{\breve{F}_Z(\boldsymbol{\omega}^{(1)}),\breve{F}_Z(\boldsymbol{\omega}^{(2)})\Big\}=\mathbf{0}$ as $\ell_1,\ell_2\to\infty$.

If $\boldsymbol{\omega}^{(1)}=\boldsymbol{\omega}^{(2)}$ and $\boldsymbol{\omega}^{(1)}\neq\mathbf{0}$ then $\Delta(\boldsymbol{\omega}^{(1)}-\boldsymbol{\omega}^{(2)})=|\boldsymbol{\Omega}|$.

So $|\boldsymbol{\Omega}|^{-1}\mathrm{Cov}\Big\{\breve{F}_Z(\boldsymbol{\omega}^{(1)}),\breve{F}_Z(\boldsymbol{\omega}^{(1)})\Big\}=(2\pi)^2\mathbf{g}_{ZZ}(\boldsymbol{\omega}^{(1)})$. For higher order moments/cumulants this will involve calculating cumulants of order greater than two such as

$$\begin{aligned}|\boldsymbol{\Omega}|^{-\frac{k}{2}}\mathrm{Cum}\Big\{\breve{F}_{b_1}(\boldsymbol{\omega}^{(1)}),\cdots,\breve{F}_{b_k}(\boldsymbol{\omega}^{(k)})\Big\} = |\boldsymbol{\Omega}|^{-\frac{k}{2}}\Big\{&(2\pi)^{2(k-1)}\Delta\Big(\sum_{j=1}^{k}\boldsymbol{\omega}^{(j)}\Big)\times\\ &g_{b_1\ldots b_k}(\boldsymbol{\omega}^{(1)},\ldots,\boldsymbol{\omega}^{(k-1)})+O(L)\Big\}.\end{aligned}$$

Now $O\big(\Delta\big(\sum_{j=1}^{k}\boldsymbol{\omega}^{(j)}\big)\big) = O(|\boldsymbol{\Omega}|)$ so for $k > 2$ the above equation tends to zero asymptotically. This proves (4.12) for the case $\boldsymbol{\omega} \neq \mathbf{0}$ by using the remark on cumulants of normal variables given in Result 2 of Appendix B. A similar proof holds for the other case.

4.1.1.3 Proofs of (4.13) and (4.14)

The proofs of (4.13) and (4.14) are provided in what follows.

Consider $\mathbb{E}\Big\{\check{G}_{NY}(\boldsymbol{\omega})\Big\} = \frac{1}{(2\pi)^2|\boldsymbol{\Omega}|}\mathbb{E}\Big\{\check{F}_N(\boldsymbol{\omega})\overline{\check{F}_Y(\boldsymbol{\omega})}\Big\}$ but

$$\begin{aligned}\mathbb{E}\Big\{\check{F}_N(\boldsymbol{\omega})\overline{\check{F}_Y(\boldsymbol{\omega})}\Big\} &= \mathbb{E}\Big\{\big(F_N(\boldsymbol{\omega}) - \lambda_N\Delta(\boldsymbol{\omega})\big)\overline{\big(F_Y(\boldsymbol{\omega}) - \mu_Y\Delta(\boldsymbol{\omega})\big)}\Big\}\\ &= \mathrm{Cov}\big\{F_N(\boldsymbol{\omega}), F_Y(\boldsymbol{\omega})\big\}\\ &= \mathrm{Cum}\big\{F_N(\boldsymbol{\omega}), F_Y(-\boldsymbol{\omega})\big\},\end{aligned}$$

because $\mathbb{E}\big\{F_N(\boldsymbol{\omega})\big\} = \lambda_N\Delta(\boldsymbol{\omega})$, $\mathbb{E}\big\{F_Y(\boldsymbol{\omega})\big\} = \mu_Y\Delta(\boldsymbol{\omega})$ and $\mathrm{Cov}(Y, Z) = \mathbb{E}\big\{Y\overline{Z}\big\} - \mathbb{E}\big\{Y\big\}\mathbb{E}\big\{\overline{Z}\big\}$ for complex variables Y and Z. So

$$\begin{aligned}\mathbb{E}\big\{\check{G}_{NY}(\boldsymbol{\omega})\big\} &= \frac{1}{(2\pi)^2|\boldsymbol{\Omega}|}\mathrm{Cum}\big\{F_N(\boldsymbol{\omega}), F_Y(-\boldsymbol{\omega})\big\}\\ &= \frac{1}{(2\pi)^2|\boldsymbol{\Omega}|}\Big\{(2\pi)^2\Delta\big(\boldsymbol{\omega}-\boldsymbol{\omega}\big)g_{NY}(\boldsymbol{\omega}) + O(L)\Big\}\\ &= g_{NY}(\boldsymbol{\omega}),\end{aligned}$$

as $\ell_1, \ell_2 \to \infty$ since $\Delta(\boldsymbol{\omega} - \boldsymbol{\omega}) = \Delta(\mathbf{0}) = \ell_1\ell_2 = |\boldsymbol{\Omega}|$, and $O(L)/|\boldsymbol{\Omega}| \to 0$. This proves (4.13). Equation (4.14) is proved as follows. Consider

$$\begin{aligned}\mathrm{Cov}\Big\{\check{G}_{NY}(\mathbf{r}), \check{G}_{NY}(\mathbf{s})\Big\} &= \mathrm{Cov}\Big\{\frac{1}{(2\pi)^2|\boldsymbol{\Omega}|}\check{F}_N(\mathbf{r})\check{F}_Y(-\mathbf{r}), \frac{1}{(2\pi)^2|\boldsymbol{\Omega}|}\check{F}_N(\mathbf{s})\check{F}_Y(-\mathbf{s})\Big\}\\ &= \frac{1}{(2\pi)^4|\boldsymbol{\Omega}|^2}\mathrm{Cov}\Big\{\check{F}_N(\mathbf{r})\check{F}_Y(-\mathbf{r}), \check{F}_N(\mathbf{s})\check{F}_Y(-\mathbf{s})\Big\}\\ &= \frac{1}{(2\pi)^4|\boldsymbol{\Omega}|^2}\mathrm{Cum}\Big\{\check{F}_N(\mathbf{r})\check{F}_Y(-\mathbf{r}), \check{F}_N(-\mathbf{s})\check{F}_Y(\mathbf{s})\Big\}\\ &= \frac{1}{(2\pi)^4|\boldsymbol{\Omega}|^2}\mathcal{G}.\end{aligned}$$

Using Lemma B.2.1 and the properties of cumulants, $\mathcal{G}$ can be written as

$$
\begin{aligned}
\mathcal{G} &= \mathrm{Cum}\big\{(F_N(\mathbf{r}) - \lambda_N\Delta(\mathbf{r}))(F_Y(-\mathbf{r}) - \mu_Y\Delta(-\mathbf{r})), \\
&\qquad (F_N(-\mathbf{s}) - \lambda_N\Delta(-\mathbf{s}))(F_Y(\mathbf{s}) - \mu_Y\Delta(\mathbf{s}))\big\} \\
&= \mathrm{Cum}\big\{F_N(\mathbf{r})F_Y(-\mathbf{r}) - \lambda_N\Delta(\mathbf{r})F_Y(-\mathbf{r}) \\
&\qquad - \mu_Y\Delta(-\mathbf{r})F_N(\mathbf{r}) + \lambda_N\Delta(\mathbf{r})\mu_Y\Delta(-\mathbf{r}), \\
&\qquad F_N(-\mathbf{s})F_Y(\mathbf{s}) - \lambda_N\Delta(-\mathbf{s})F_Y(\mathbf{s}) \\
&\qquad - \mu_Y\Delta(\mathbf{s})F_N(-\mathbf{s}) + \lambda_N\Delta(-\mathbf{s})\mu_Y\Delta(\mathbf{s})\big\} \\
&= \mathrm{Cum}\big\{F_N(\mathbf{r})F_Y(-\mathbf{r}), F_N(-\mathbf{s})F_Y(\mathbf{s})\big\} \\
&\quad - \mu_Y\Delta(\mathbf{s})\mathrm{Cum}\big\{F_N(\mathbf{r})F_Y(-\mathbf{r}), F_N(-\mathbf{s})\big\} \\
&\quad - \lambda_N\Delta(-\mathbf{s})\mathrm{Cum}\big\{F_N(\mathbf{r})F_Y(-\mathbf{r}), F_Y(\mathbf{s})\big\} \\
&\quad - \mu_Y\Delta(-\mathbf{r})\mathrm{Cum}\big\{F_N(\mathbf{r}), F_N(-\mathbf{s})F_Y(\mathbf{s})\big\} \\
&\quad - \lambda_N\Delta(\mathbf{r})\mathrm{Cum}\big\{F_Y(-\mathbf{r}), F_N(-\mathbf{s})F_Y(\mathbf{s})\big\} \\
&\quad + \lambda_N\mu_Y\Delta(-\mathbf{r})\Delta(-\mathbf{s})\mathrm{Cum}\big\{F_N(\mathbf{r}), F_Y(\mathbf{s})\big\} \\
&\quad + \lambda_N\mu_Y\Delta(\mathbf{r})\Delta(\mathbf{s})\mathrm{Cum}\big\{F_Y(-\mathbf{r}), F_N(-\mathbf{s})\big\} \\
&\quad + \lambda_N^2\Delta(\mathbf{r})\Delta(-\mathbf{s})\mathrm{Cum}\big\{F_Y(-\mathbf{r}), F_Y(\mathbf{s})\big\} \\
&\quad + \mu_Y^2\Delta(-\mathbf{r})\Delta(\mathbf{s})\mathrm{Cum}\big\{F_N(\mathbf{r}), F_N(-\mathbf{s})\big\} \\
&= \mathcal{O} + \mathcal{P} + \mathcal{Q} + \mathcal{R} + \mathcal{S} + \mathcal{T} + \mathcal{U} + \mathcal{V} + \mathcal{W}.
\end{aligned}
$$

Again using Lemma B.2.1, the components of the above equation can be expanded to

$$
\begin{aligned}
\mathcal{O} = {} & \mathrm{Cum}\{F_N(\mathbf{r}), F_Y(-\mathbf{r}), F_N(-\mathbf{s}), F_Y(\mathbf{s})\} \\
& + \mathrm{Cum}\{F_N(\mathbf{r})\}\mathrm{Cum}\{F_Y(-\mathbf{r}), F_N(-\mathbf{s}), F_Y(\mathbf{s})\} \\
& + \mathrm{Cum}\{F_Y(-\mathbf{r})\}\mathrm{Cum}\{F_N(\mathbf{r}), F_N(-\mathbf{s}), F_Y(\mathbf{s})\} \\
& + \mathrm{Cum}\{F_N(-\mathbf{s})\}\mathrm{Cum}\{F_N(\mathbf{r}), F_Y(-\mathbf{r}), F_Y(\mathbf{s})\} \\
& + \mathrm{Cum}\{F_Y(\mathbf{s})\}\mathrm{Cum}\{F_N(\mathbf{r}), F_Y(-\mathbf{r}), F_N(-\mathbf{s})\} \\
& + \mathrm{Cum}\{F_N(\mathbf{r})\}\mathrm{Cum}\{F_N(-\mathbf{s})\}\mathrm{Cum}\{F_Y(-\mathbf{r}), F_Y(\mathbf{s})\} \\
& + \mathrm{Cum}\{F_N(\mathbf{r})\}\mathrm{Cum}\{F_Y(\mathbf{s})\}\mathrm{Cum}\{F_Y(-\mathbf{r}), F_N(-\mathbf{s})\} \\
& + \mathrm{Cum}\{F_Y(-\mathbf{r})\}\mathrm{Cum}\{F_N(-\mathbf{s})\}\mathrm{Cum}\{F_N(\mathbf{r}), F_Y(\mathbf{s})\} \\
& + \mathrm{Cum}\{F_Y(-\mathbf{r})\}\mathrm{Cum}\{F_Y(\mathbf{s})\}\mathrm{Cum}\{F_N(\mathbf{r}), F_N(-\mathbf{s})\} \\
& + \mathrm{Cum}\{F_N(\mathbf{r}), F_N(-\mathbf{s})\}\mathrm{Cum}\{F_Y(-\mathbf{r}), F_Y(\mathbf{s})\} \\
& + \mathrm{Cum}\{F_N(\mathbf{r}), F_Y(-\mathbf{r})\}\mathrm{Cum}\{F_Y(-\mathbf{r}), F_N(-\mathbf{s})\}, \\
\mathcal{P} = {} & -\mu_Y \Delta(\mathbf{s})\Big\{\mathrm{Cum}\{F_N(\mathbf{r}), F_Y(-\mathbf{r}), F_N(-\mathbf{s})\} \\
& \quad + \mathrm{Cum}\{F_N(\mathbf{r})\}\mathrm{Cum}\{F_Y(-\mathbf{r}), F_N(-\mathbf{s})\} \\
& \quad + \mathrm{Cum}\{F_Y(-\mathbf{r})\}\mathrm{Cum}\{F_N(\mathbf{r}), F_N(-\mathbf{s})\}\Big\}, \\
\mathcal{Q} = {} & -\lambda_N \Delta(-\mathbf{s})\Big\{\mathrm{Cum}\{F_N(\mathbf{r}), F_Y(-\mathbf{r}), F_Y(\mathbf{s})\} \\
& \quad + \mathrm{Cum}\{F_N(\mathbf{r})\}\mathrm{Cum}\{F_Y(-\mathbf{r}), F_Y(\mathbf{s})\} \\
& \quad + \mathrm{Cum}\{F_Y(-\mathbf{r})\}\mathrm{Cum}\{F_N(\mathbf{r}), F_Y(\mathbf{s})\}\Big\}
\end{aligned}
$$

$$\begin{aligned}\mathcal{R} = -\mu_Y \Delta(-\mathbf{r})\Big\{ & \mathrm{Cum}\big\{F_N(\mathbf{r}), F_N(-\mathbf{s}), F_Y(\mathbf{s})\big\} \\ & + \mathrm{Cum}\big\{F_N(-\mathbf{s})\big\}\mathrm{Cum}\big\{F_N(\mathbf{r}), F_Y(\mathbf{s})\big\} \\ & + \mathrm{Cum}\big\{F_Y(\mathbf{s})\big\}\mathrm{Cum}\big\{F_N(\mathbf{r}), F_N(-\mathbf{s})\big\}\Big\},\end{aligned}$$

$$\begin{aligned}\mathcal{S} = -\lambda_N \Delta(\mathbf{r})\Big\{ & \mathrm{Cum}\big\{F_Y(-\mathbf{r}), F_N(-\mathbf{s}), F_Y(\mathbf{s})\big\} \\ & + \mathrm{Cum}\big\{F_N(-\mathbf{s})\big\}\mathrm{Cum}\big\{F_Y(-\mathbf{r}), F_Y(\mathbf{s})\big\} \\ & + \mathrm{Cum}\big\{F_Y(\mathbf{s})\big\}\mathrm{Cum}\big\{F_Y(-\mathbf{r}), F_N(-\mathbf{s})\big\}\Big\}.\end{aligned}$$

With the aid of some algebra, it can be shown that

$$\begin{aligned}\mathcal{G} = & \mathrm{Cum}\big\{F_N(\mathbf{r}), F_Y(-\mathbf{r}), F_N(-\mathbf{s}), F_Y(\mathbf{s})\big\} \\ & + \mathrm{Cum}\big\{F_N(\mathbf{r}), F_N(-\mathbf{s})\big\}\mathrm{Cum}\big\{F_Y(-\mathbf{r}), F_Y(\mathbf{s})\big\} \\ & + \mathrm{Cum}\big\{F_N(\mathbf{r}), F_Y(-\mathbf{r})\big\}\mathrm{Cum}\big\{F_Y(-\mathbf{r}), F_N(-\mathbf{s})\big\}.\end{aligned}$$

Hence,

$$\begin{aligned}\mathcal{G} = & (2\pi)^{2(3)}\Delta(\mathbf{0})g_{NYNY}(\mathbf{r}, -\mathbf{r}, -\mathbf{s}) + O(L) \\ & + \big\{(2\pi)^2\Delta(\mathbf{r}-\mathbf{s})g_{NN}(\mathbf{r}) + O(L)\big\} \times \big\{(2\pi)^2\Delta(-\mathbf{r}+\mathbf{s})g_{YY}(-\mathbf{r}) + O(L)\big\} \\ & + \big\{(2\pi)^2\Delta(\mathbf{r}+\mathbf{s})g_{NY}(\mathbf{r}) + O(L)\big\} \times \big\{(2\pi)^2\Delta(-\mathbf{r}-\mathbf{s})g_{YN}(-\mathbf{r}) + O(L)\big\}.\end{aligned}$$

Rearranging and simplifying the above entries give

$$\begin{aligned}\mathcal{G} = & (2\pi)^6|\boldsymbol{\Omega}|g_{NYNY}(\mathbf{r}, -\mathbf{r}, -\mathbf{s}) + (2\pi)^4|\Delta(\mathbf{r}-\mathbf{s})|^2 g_{NN}(\mathbf{r})g_{YY}(-\mathbf{r}) \\ & + (2\pi)^4|\Delta(\mathbf{r}+\mathbf{s})|^2 g_{NY}(\mathbf{r})g_{YN}(-\mathbf{r}) \\ & + O(L)\big\{\Delta(\mathbf{r}-\mathbf{s})g_{NN}(\mathbf{r}) + \Delta(-\mathbf{r}+\mathbf{s})g_{YY}(-\mathbf{r}) \\ & \qquad \Delta(\mathbf{r}+\mathbf{s})g_{NY}(\mathbf{r}) + \Delta(-\mathbf{r}-\mathbf{s})g_{YN}(-\mathbf{r}) + O(L)\big\}.\end{aligned}$$

Note that

$$|\Delta(\mathbf{a})| = \Big|\int_0^{\ell_2}\int_0^{\ell_1} \exp\big\{-i(a_1t_1 + a_2t_2)\big\}dt_1dt_2\Big| \leq \int_0^{\ell_2}\int_0^{\ell_1} dt_1dt_2 = \ell_1\ell_2 = |\boldsymbol{\Omega}|.$$

Hence,

$$\mathcal{G} = (2\pi)^6|\boldsymbol{\Omega}|g_{NYNY}(\mathbf{r},-\mathbf{r},-\mathbf{s}) + (2\pi)^4|\Delta(\mathbf{r}-\mathbf{s})|^2 g_{NN}(\mathbf{r})g_{YY}(-\mathbf{r}) + (2\pi)^4|\Delta(\mathbf{r}+\mathbf{s})|^2 g_{NY}(\mathbf{r})g_{YN}(-\mathbf{r}) + O(L^3),$$

since $O(|\boldsymbol{\Omega}|) = O(L^2)$. As $\ell_1, \ell_2 \to \infty$ we have

$$\begin{aligned}\mathrm{Cov}\left\{\breve{G}_{NY}(\mathbf{r}), \breve{G}_{NY}(\mathbf{s})\right\} &= \frac{1}{(2\pi)^4|\boldsymbol{\Omega}|^2}\Big\{(2\pi)^6|\boldsymbol{\Omega}|g_{NYNY}(\mathbf{r},-\mathbf{r},-\mathbf{s}) \\ &\quad + (2\pi)^4|\Delta(\mathbf{r}-\mathbf{s})|^2 g_{NN}(\mathbf{r})g_{YY}(-\mathbf{r}) \\ &\quad + (2\pi)^4|\Delta(\mathbf{r}+\mathbf{s})|^2 g_{NY}(\mathbf{r})g_{YN}(-\mathbf{r}) \\ &\quad + O(L^3)\Big\} \\ &\to \delta\{\mathbf{r}-\mathbf{s}\}g_{NN}(\mathbf{r})g_{YY}(-\mathbf{r}) \\ &\quad + \delta\{\mathbf{r}+\mathbf{s}\}g_{NY}(\mathbf{r})g_{YN}(-\mathbf{r})\end{aligned}$$

for $\mathbf{r}, \mathbf{s} \neq \mathbf{0}$. Note that $\frac{|\Delta(\mathbf{a})|^2}{|\boldsymbol{\Omega}|^2} \to \delta\{\mathbf{a}\}$ as $\ell_1, \ell_2 \to \infty$, where δ is the Kronecker delta defined in Section A.2. Hence, equations (4.13) and (4.14) are proved.

4.2 Confidence Intervals

By analogy with Brillinger (1981) and Priestley (1981a, chapter 9) methods to construct confidence intervals for spectral estimates are discussed in this section. In Section 1.7 the standardised auto-spectra were stated to be independently distributed as Chi-squared variables with two degrees of freedom, χ^2_2, for $\boldsymbol{\omega} \neq \mathbf{0}$. Thus, confidence intervals can be constructed for the auto-spectra based on this distribution. However, these estimates are unstable being based on the χ^2_2 distribution, hence smoothed estimates are used.

The asymptotic independence of scaled periodogram ordinates together

with (1.14) and (1.15) imply that smoothed periodogram ordinates are asymptotically distributed as

$$\sum_{\imath=-u}^{u}\sum_{\jmath=-v}^{v} w_{(\imath,\jmath)}\chi_2^2 \equiv \sum_{k=1}^{m} w_k\chi_2^2. \tag{4.20}$$

In practice the distribution of such a variate is usually approximated by the $K\chi_n^2$ distribution. The degrees of freedom, n, and the multiplier, K, of $K\chi_n^2$ are determined by equating the first and second moments of $K\chi_n^2$ to those of (4.20) Brillinger (1981)see. Hence,

$$nK = 2\sum_{k=1}^{m} w_k = 2\sum_{\imath=-u}^{u}\sum_{\jmath=-v}^{v} w_{(\imath,\jmath)} = 2,$$

$$\text{and } 2nK^2 = 4\sum_{k=1}^{m} w_k^2 = 4\sum_{\imath=-u}^{u}\sum_{\jmath=-v}^{v} w_{(\imath,\jmath)}^2.$$

Therefore, $n = 2/(\sum_{k=1}^{m} w_k^2)$ and $K = 2/n$. In the case where the weights are uniform, that is $w_k = 1/m$ for $k = 1, \ldots, m$, the distribution of (4.20) is exactly $\frac{1}{m}\chi_{2m}^2$. For computational convenience, uniform weighting will be used when constructing confidence intervals, unless otherwise specified. Thus, a $100(1-\alpha)\%$ confidence interval for $f_{ss}(\boldsymbol{\omega})$ is

$$\left[\frac{mF_{ss}(\boldsymbol{\omega})}{\chi_{2m}^2(1-\alpha/2)}, \frac{mF_{ss}(\boldsymbol{\omega})}{\chi_{2m}^2(\alpha/2)}\right], \tag{4.21}$$

where $\chi_n^2(\alpha)$ is the 100α percentile of the Chi-squared distribution with n degrees of freedom, $s = Y$ or N and F_{ss} is the uniformly smoothed non-scaled auto-spectrum. As the sample size increases the normal approximation to the above distribution can be used to construct confidence intervals.

In Section 4.1 an estimate of the cross-spectral density was provided via $\hat{\mathbb{F}}_{NY}(\boldsymbol{\omega}) = m^{-1}\sum_{k=1}^{m}\hat{F}_{NY}(\boldsymbol{\omega}^{(k)})$. Furthermore, it was shown that $\hat{F}_{NY}(\boldsymbol{\omega}^{(k)})$

for $k = 1, \ldots, m$ can be considered as m independent estimates of $\hat{F}_{NY}(\boldsymbol{\omega})$ for $\boldsymbol{\omega}^{(k)}$ near $\boldsymbol{\omega}$. Thus, one can construct a confidence interval for the co-spectrum, $c_{NY}(\boldsymbol{\omega}) = \mathrm{Re}\{f_{NY}(\boldsymbol{\omega})\}$, based on the estimate

$$C \equiv C_{NY}(\boldsymbol{\omega}) = m^{-1} \sum_{k=1}^{m} \mathrm{Re}\{F_{NY}(\boldsymbol{\omega}^{(k)})\} \equiv m^{-1} \sum_{k=1}^{m} C_k.$$

Let $\hat{\sigma}^2 = (m-1)^{-1} \sum_{k=1}^{m} (C_k - C)^2$ then, by analogy with Brillinger (1981), the Student's t distribution can be used to approximate the distribution of the variate $\frac{C-c}{\hat{\sigma}/\sqrt{m}}$. Hence, a $100(1-\alpha)\%$ confidence interval for c is given by $C \pm \frac{\hat{\sigma}}{\sqrt{m}} t_{m-1}(1-\alpha/2)$, where $t_n(\beta)$ denotes the 100β percentile of Student's t distribution with n degrees of freedom. Alternatively, the normal distribution $N\big(c, \frac{K}{2}\{f_{NN} f_{YY} + c^2 - q^2\}\big)$ can be used to find an approximate confidence interval.

The confidence interval constructed for the co-spectrum can be used to test whether the two in-phase components of the hybrid process are correlated at a particular frequency. If the two components are uncorrelated then one expects the co-spectrum to be zero. The same procedure can be used to obtain confidence limits for the quadrature spectrum by replacing c by q where $q = q_{NY}(\boldsymbol{\omega}) = \mathrm{Im}\{f_{NY}(\boldsymbol{\omega})\}$.

The other cross-spectral estimate for which one might be interested in calculating a confidence interval is the phase spectrum. A confidence interval for the phase spectrum may be derived by approximating $\tan\{\Phi\} = -Q/C$ by a normal distribution with mean $\tan\{\phi\}$ and variance $\frac{K}{2} \sec^4\{\phi\}(\upsilon^{-1} - 1)$. The mean and variance are derived by using Taylor expansion (see Priestley, 1981b).

Note that if $\upsilon = 0$ then one can show that ϕ is uniformly distributed

on $(-\pi/2, \pi/2)$. This can be done by noting that when $\upsilon = 0$ then C and Q are uncorrelated. Further, if C and Q are assumed to be bivariate normal, then in this case they are independent with zero means and common variance $\frac{K}{2}\{f_{NN}f_{YY}\}$. This implies that their ratio is Cauchy. Hence, the $\tan^{-1}$ transformation results in a uniformly distributed random variable on $(-\pi/2, \pi/2)$ as stated in Section 2.4.

Hannan (1970, chapter 5) gives the following confidence interval for the phase spectrum

$$|\sin\{\Phi - \phi\}| \leq t_{2(m-1)}(\beta)\sqrt{\frac{1-\Upsilon}{2(m-1)\Upsilon}},$$

where t and β are as before. This confidence interval is derived from the distribution of the complex regression coefficient, $\Gamma(\omega) = \frac{f_{NY}(\omega)}{f_{NN}(\omega)}$, of Y on N (see Section 4.2.1 for more details). For computational convenience we will use the earlier approach to find a confidence interval for the phase spectrum because we compute the phase spectrum based on the $\tan^{-1}$ function.

4.2.1 Test for Zero Squared Coherency

In this section, a test for zero squared coherency is discussed. This test is an adaptation of a test for the one-dimensional multivariate case discussed by Priestley (1981b, chapter 9). The two-dimensional version follows immediately. Hence, we will only summarise the one-dimensional test statistic.

Under the null hypothesis that the coherency, $\sqrt{\upsilon}$, is zero we have

$$\frac{(m-1)(\sqrt{\Upsilon})^2}{1-(\sqrt{\Upsilon})^2} = \frac{(m-1)\Upsilon}{1-\Upsilon} = \mathrm{F}_{2,2(m-1)}\,, \tag{4.22}$$

where $\mathrm{F}_{p,q}$ is the F-distribution with p and q degrees of freedom, and m is the number of ordinates used in smoothing the periodogram at a particular

frequency. An insight into this result can be gained by investigating a linear relationship between the two components X and Y of a bivariate process as outlined below. Consider

$$Y(t) = \sum_{u=-\infty}^{\infty} h(u)X(t-u) + \epsilon(t),$$

where ϵ is added noise and uncorrelated with X and h is a function. In addition, ϵ and X have zero means.

However, the spectral representation theorem implies that

$$dZ_Y(\omega) = \Gamma(\omega)dZ_X(\omega) + dZ_\epsilon(\omega), \tag{4.23}$$

where $M = \int_{-\infty}^{\infty} \exp\{it\omega\}dZ_M(\omega), M = Y, X, \epsilon$ and $\Gamma(\omega) = \sum_{u=-\infty}^{\infty} h(u)\exp\{-iu\omega\}$, (see Priestley, 1981a, chapter 4). Note that the process dZ_M has the following properties:

$$\mathbb{E}\{dZ_M(\omega)\} = 0 \qquad \text{for all } \omega,$$

$$\mathbb{E}\{|dZ_M(\omega)|^2\} = f_{MM}(\omega)d\omega \text{ for all } \omega,$$

$$\mathbb{E}\{dZ_M(\omega)\overline{dZ_M(\omega')}\} = 0 \qquad \text{for } \omega \neq \omega',$$

where $f_{MM}(\omega)$ is the non-normalised auto-spectrum. For the case where ϵ and X are zero mean complex Gaussian, Goodman (1963) proves that the increments dZ_ϵ, dZ_X and dZ_Y are also zero mean complex Gaussian. In addition, he concludes that even for non-Gaussian processes the increments can *still* be regarded as complex Gaussian. Therefore, treating (4.23) as an ordinary linear regression problem yields the following quantities:

1. *residual sum of squares* (RSS):

$$\mathbb{E}\{|dZ_\epsilon(\omega)|^2\} = f_{YY}(\omega)\Big(1 - \frac{|\Gamma(\omega)|^2 f_{XX}(\omega)}{f_{YY}(\omega)}\Big)d\omega,$$

2. *explained sum of squares* (ESS):

$$\mathbb{E}\{|\Gamma(\omega)dZ_X(\omega)|^2\} = |\Gamma(\omega)|^2 f_{XX}(\omega)d\omega.$$

Since $\Gamma(\omega) = \frac{f_{XY}(\omega)}{f_{XX}(\omega)}$ then RSS $= f_{YY}(\omega)[1 - \upsilon(\omega)]d\omega$ and ESS $= \upsilon(\omega)f_{YY}(\omega)d\omega$. Therefore, $\frac{\text{ESS}}{\text{RSS}} = \frac{\upsilon(\omega)}{1-\upsilon(\omega)}$ as required.

Hannan (1970, chapter 5) gives a detailed derivation of the density function for the coherency spectrum, $\sqrt{\Upsilon(\omega)} = \frac{|F_{XY}(\omega)|}{\sqrt{F_{XX}(\omega)F_{YY}(\omega)}}$. The derived density yields (4.22) under the null hypothesis.

Note that for the two-dimensional point-lattice process and under the null hypothesis of CSR, where the point process is an HPP and the lattice process is white noise, the individual DFTs are distributed as Gaussian random variables. Thus, one can extend the above arguments in an obvious way to derive a zero coherency test for the two-dimensional case. In the next section, we will apply the results of this section to some of the examples of Chapter 2.

4.3 Application

In this section, we will construct confidence intervals for auto- and cross-spectra of the examples LINKED and CSRPLE of Chapter 2. In addition, we will provide the figures for the zero test statistic for the other examples of Chapter 2.

Figures 4.2 and 4.3 represent the profiles of the auto-spectra of LINKED together with 95% confidence bands at each frequency. The profiles are obtained by conditioning on the WE frequencies since this results in fewer panels per plot. For most frequencies the auto-spectra lie close to the upper bound of the confidence bands. This is because the upper bound for most ordinates is calculated as $(9F_{ss}(\omega)/\chi^2_{18}(0.05/2)) \approx 1.1\, F_{ss}(\omega)$ since most ordinates have eight neighbours. In addition, the spectral power is concentrated mainly around low frequencies. The similarity between the point and lattice spectra is attributed to the method that generated them. For comparison Figures 4.4 and 4.5 give the 95% confidence bands for the auto-spectra based on using Method A once and the approximation $K\chi^2_n$. This approach results in wider confidence bands.

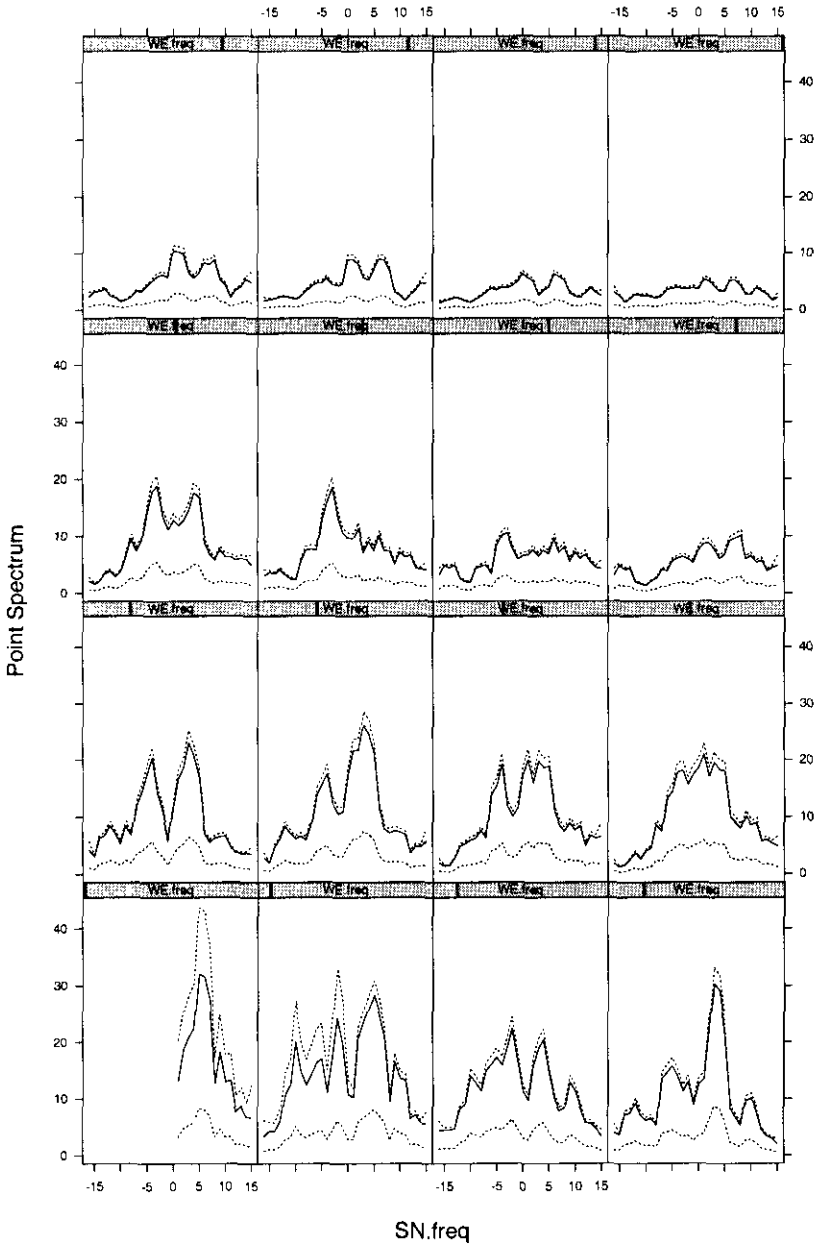

Figure 4.2: Profile of the point spectrum of LINKED using uniform smoothing, solid line, and the 95% confidence band around each frequency, dotted lines. The far left panel of the bottom row corresponds to $p = 0$, the second left panel of the bottom row corresponds to $p = 1$, and so forth such that the far right panel of the top row corresponds to $p = 15$.

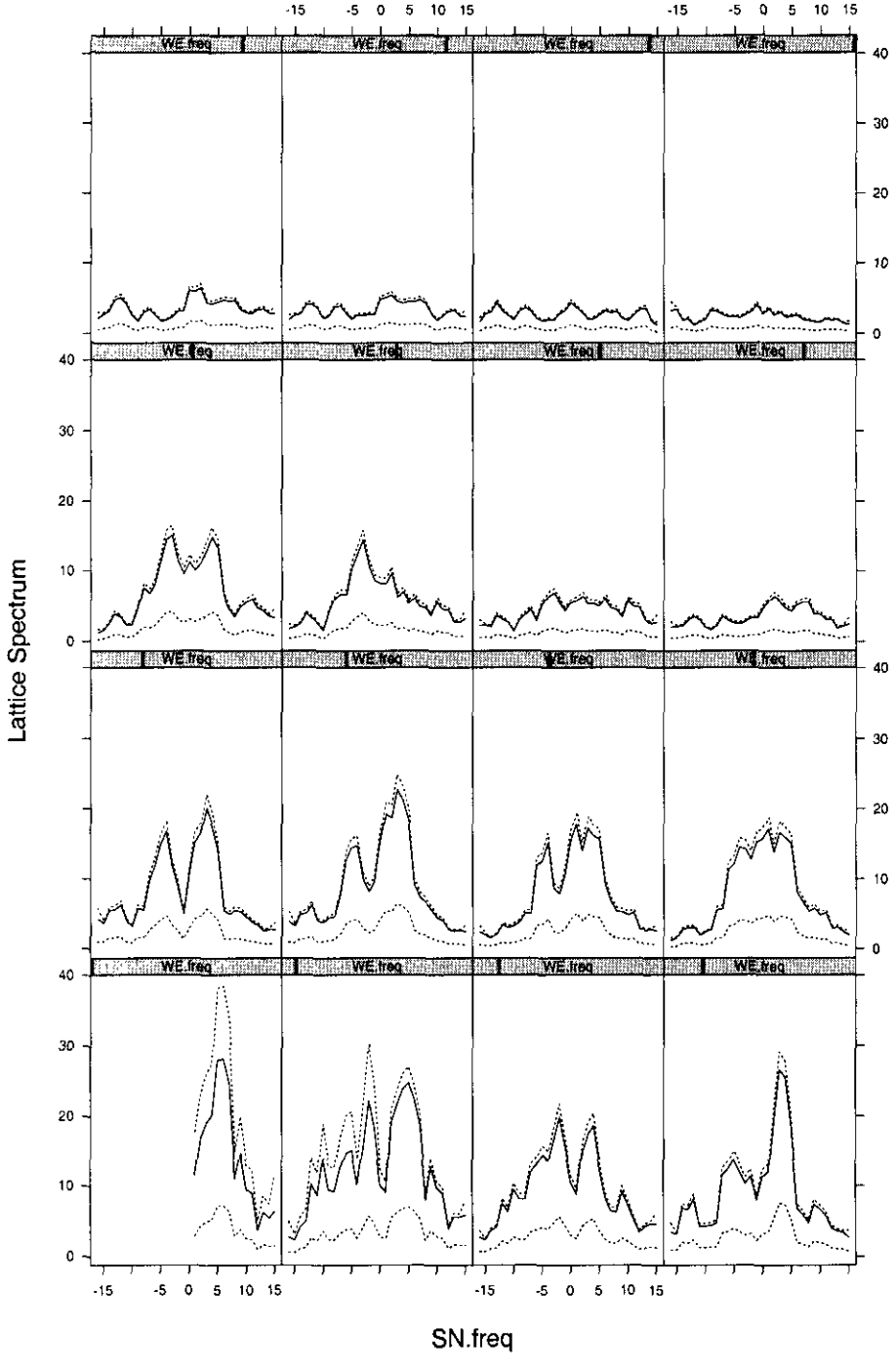

Figure 4.3: Profile of the lattice spectrum of LINKED, solid line, and the 95% confidence band around each frequency, dotted lines.

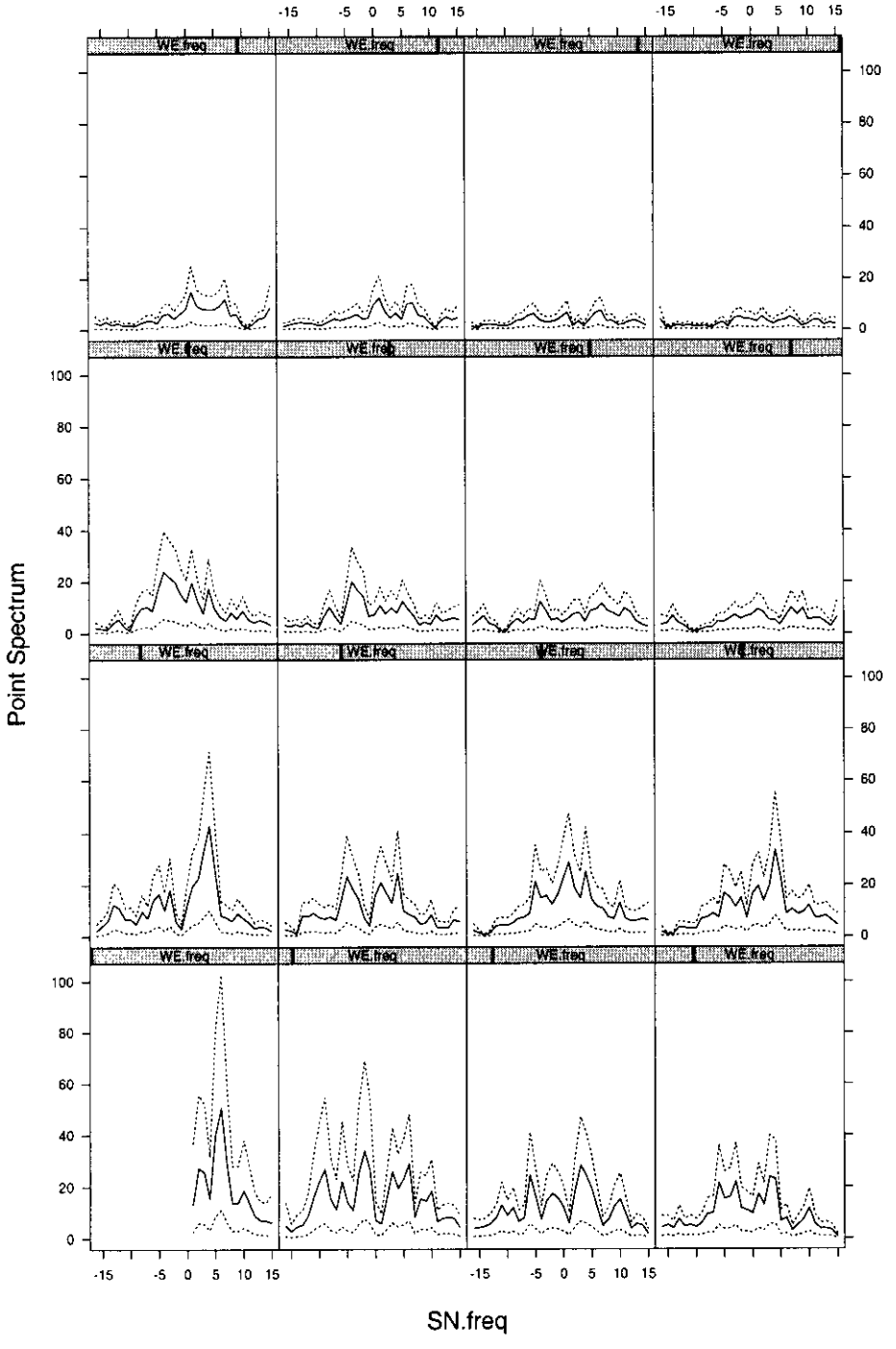

Figure 4.4: Profile of the point spectrum of LINKED, solid line, using Method A once and the 95% confidence band around each frequency, dotted lines.

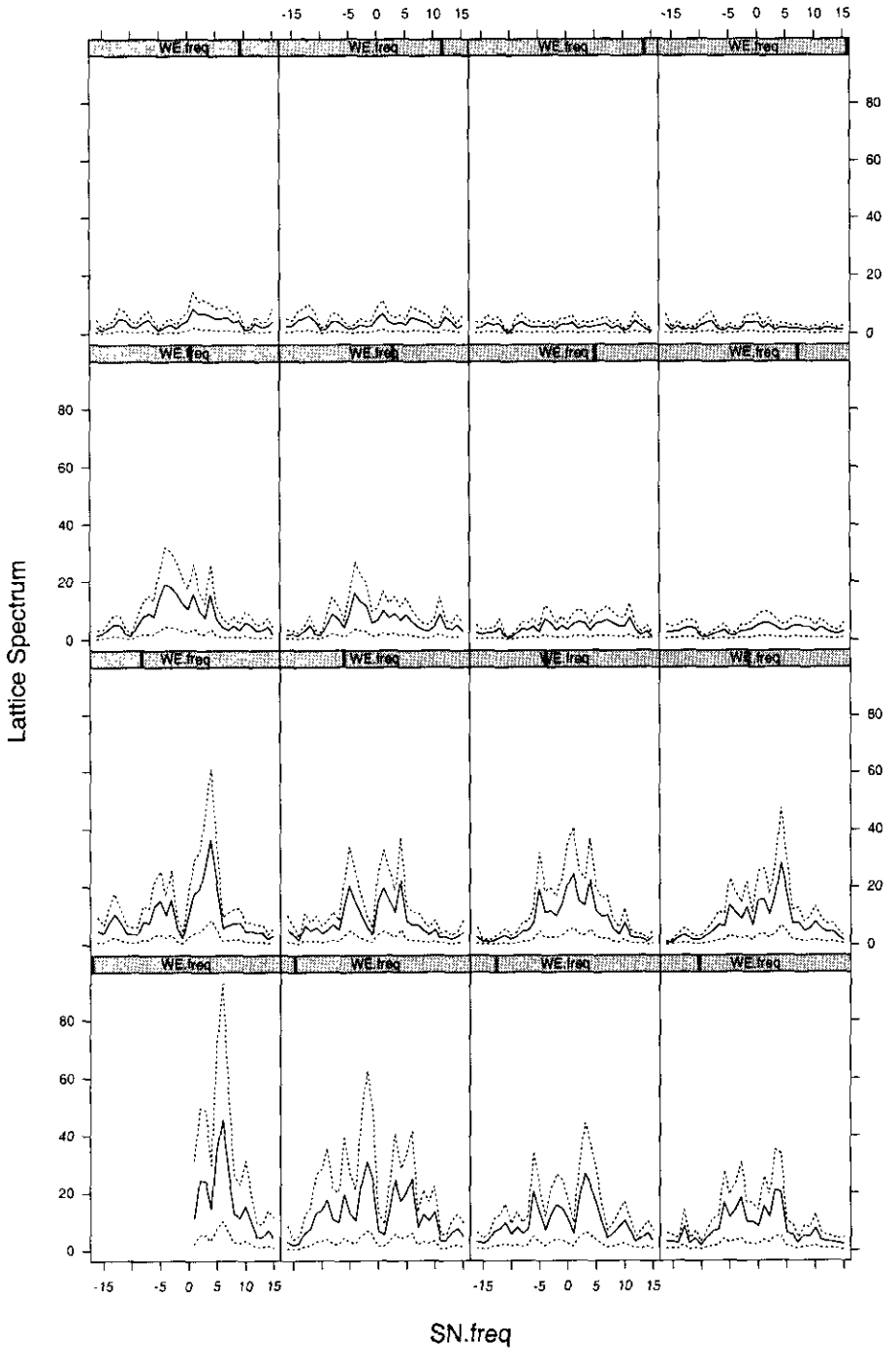

Figure 4.5: Profile of the lattice spectrum of LINKED, solid line, using Method A once and the 95% confidence band around each frequency, dotted lines.

The co-spectrum plots reveal that the two components are positively correlated for frequencies in the range $p = 0, \ldots, 9$ and $q = -10, \ldots, 10$, see Figure 4.6. It is worth noting here that the confidence bands around most frequencies in the above range exclude zero. Furthermore, the co-spectrum is almost zero outside this range, thus, the in-phase components are uncorrelated for high frequencies. For low WE frequencies the quadrature spectrum resembles a sine wave, see Figure 4.7. This feature fades out as the WE frequency increases. In fact, for large WE frequencies the quadrature spectrum is almost zero.

Figure 4.8 represents the profile of the zero coherency test statistic together with the corresponding upper 5% critical point of the F distribution. The figure implies that the two components are correlated at almost all frequencies. However, this correlation is pronounced for the frequency range $p = 0, \ldots, 9$ and $q = -10, \ldots, 10$. Having established the range for which the squared coherency is non-zero, one can construct confidence intervals for the phase spectrum in this range. Figures 4.9 and 4.10 represent the tangent of the phase spectrum together with the corresponding 95% confidence bands for the frequency band $p = 0, \ldots, 5$ and $q = -5, \ldots, 5$. The first of the two figures is conditioned on the WE frequencies, while the other is conditioned on the SN frequencies. The figures reveal that the tangent of the phase spectrum decreases linearly along these frequencies. Hence, one can conclude that the two components of the hybrid pattern are positively correlated in the frequency range $p = 0, \ldots, 9$ and $q = -10, \ldots, 10$. In addition, as implied by the quadrature spectrum and the tangent of the phase graphs there exists a phase shift between the two components.

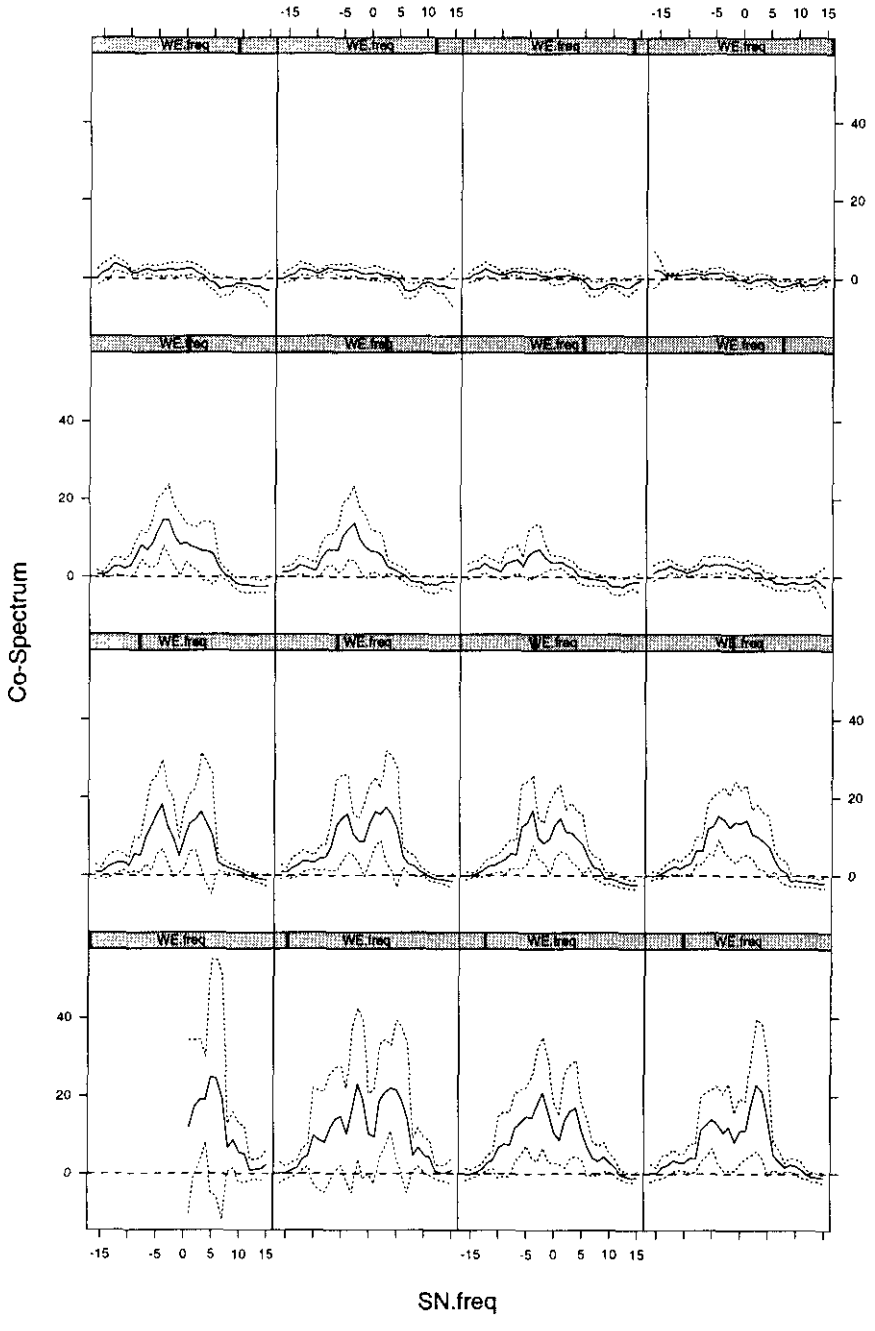

Figure 4.6: Profile of the co-spectrum of LINKED, solid line, and the 95% confidence band around each frequency, dotted lines. Dashed line represents the zero value.

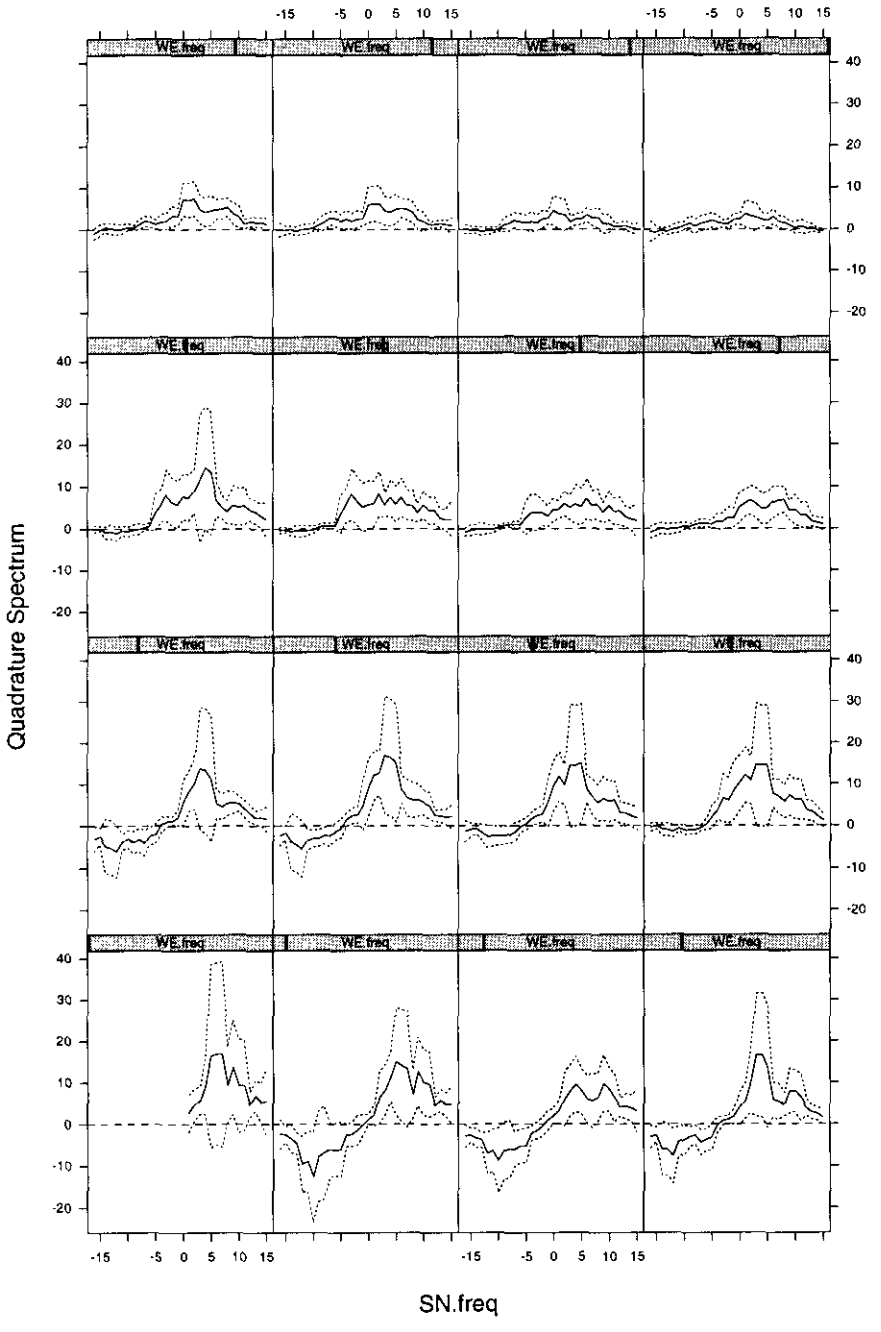

Figure 4.7: Profile of the quadrature spectrum of LINKED, solid line, and the 95% confidence band around each frequency, dotted lines. Dashed line represents the zero value.

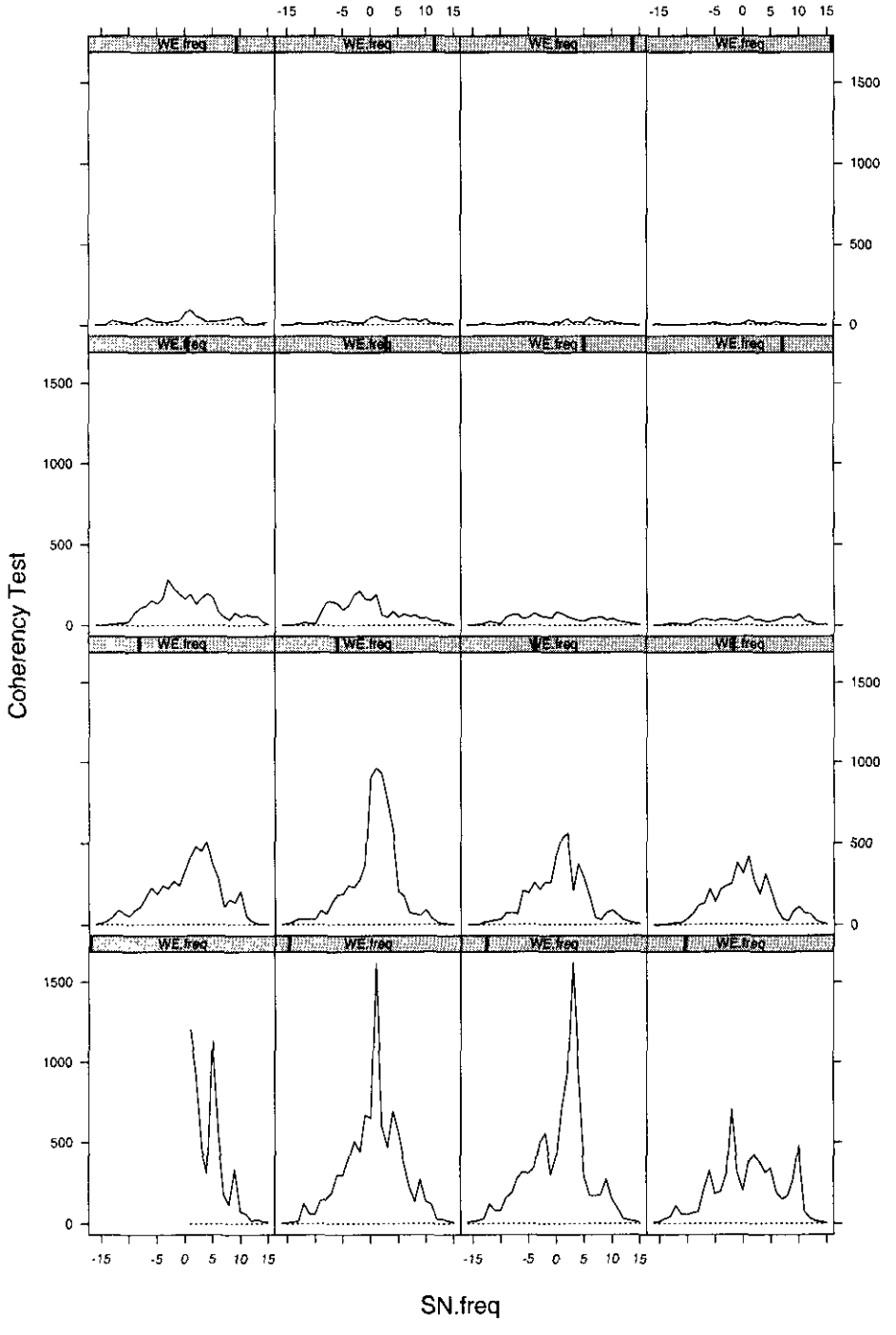

Figure 4.8: Profile of the zero coherency test statistic spectrum for LINKED, solid line, and the corresponding upper 5% critical point of the F distribution, dotted line.

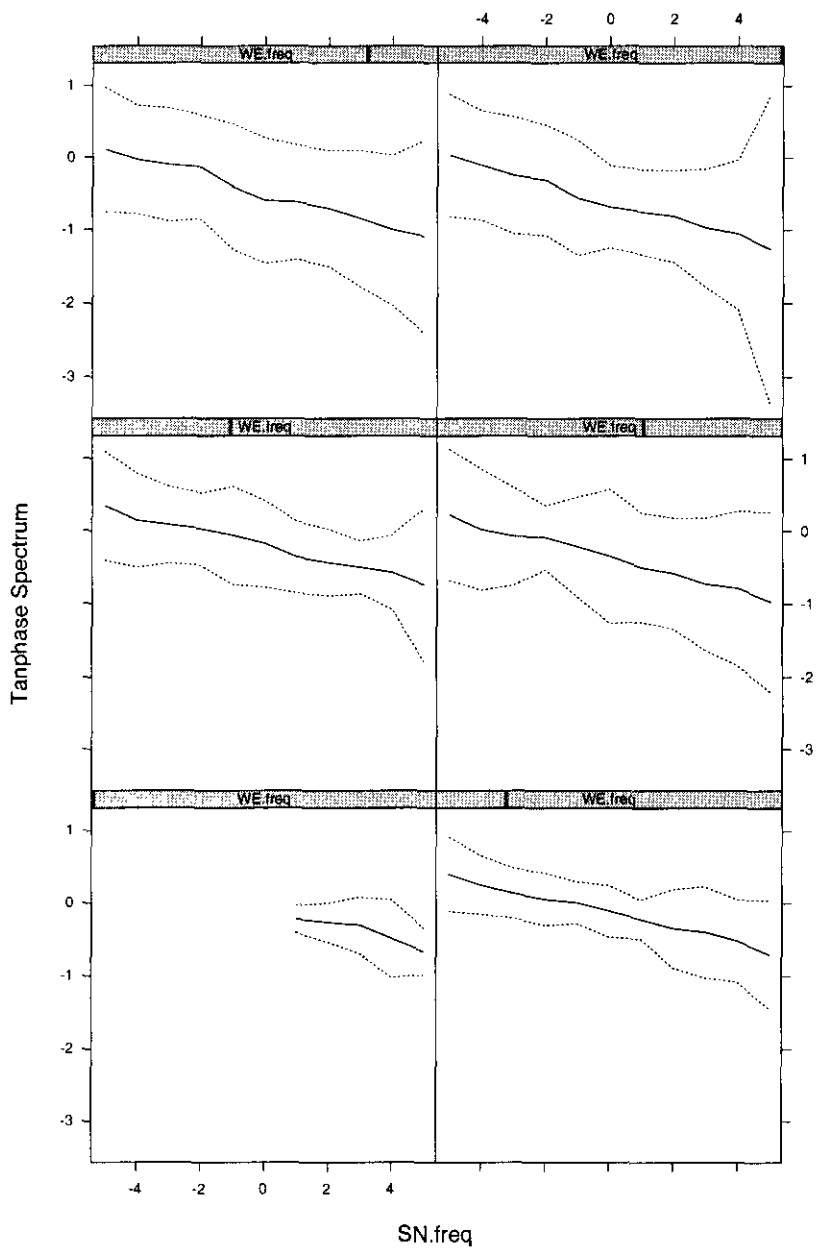

Figure 4.9: Profile of the tangent of the phase spectrum of LINKED, solid line, for $p = 0, \ldots, 5$ and $q = -5, \ldots, 5$, conditioning here is on the WE frequencies, and the 95% confidence band around each frequency, dotted lines.

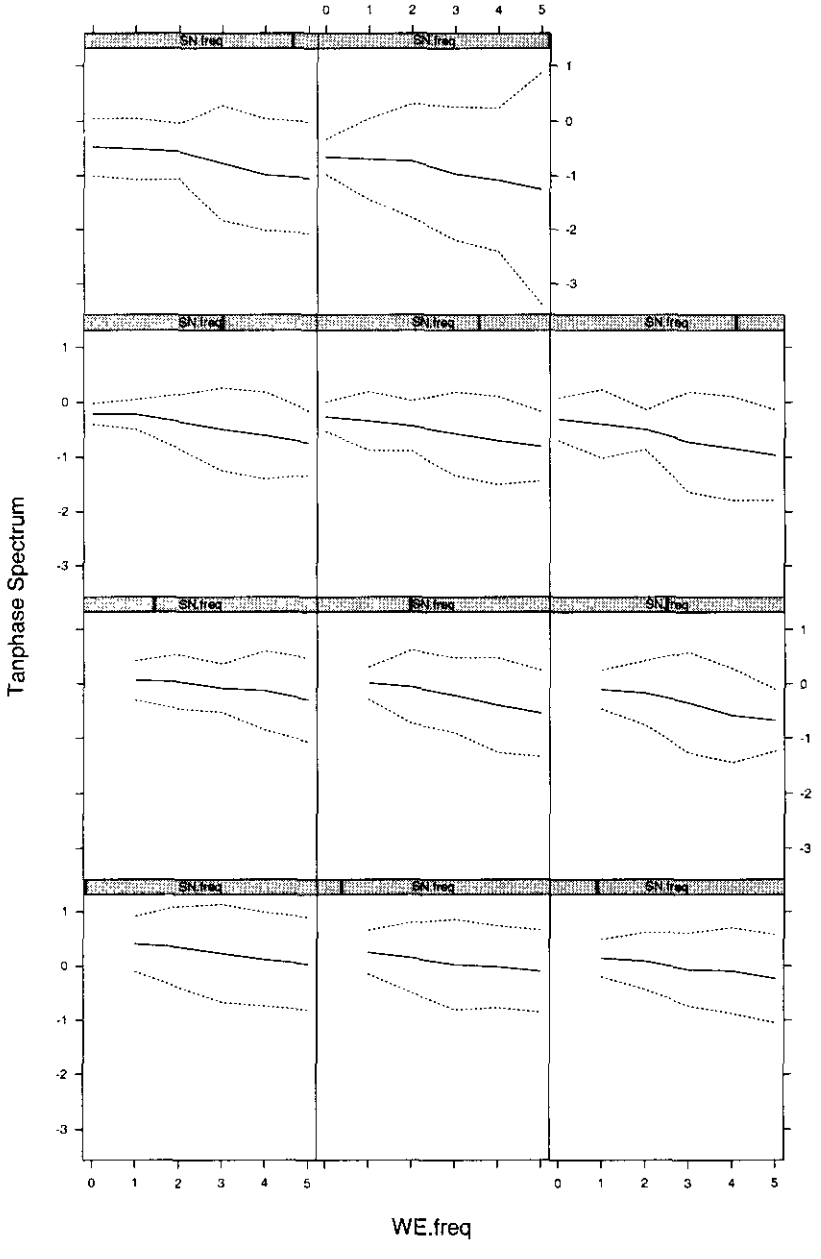

Figure 4.10: Profile of the tangent of the phase spectrum of *LINKED*, solid line, for $p = 0, \ldots, 5$ and $q = -5, \ldots, 5$, conditioning here is on the SN frequencies, and the 95% confidence band around each frequency, dotted lines.

Figures 4.11, 4.12, 4.13, 4.14 and 4.15 represent the profiles of the auto-, co-, quadrature and zero coherency spectra, respectively, for CSRPLE. The confidence bands are calculated at the 99% confidence level. The auto-spectral power is spread across all frequencies as expected for a completely spatially random process. The co- and quadrature spectra oscillate around zero. Note that all the confidence bands include zero. The zero coherency statistic is well below the upper 1% critical point of the F distribution for almost all frequencies. As expected, one can conclude that the two processes are uncorrelated.

For the examples THRESACOS, THINCOS, THRESBMA and BALANCED of Chapter 2 graphs of the zero coherency statistic are presented in Figures 4.16, 4.17, 4.18, and 4.19, respectively. The plots for THRESACOS and THINCOS reveal that the two components are correlated in the neighbourhood of the frequencies where the lattice spectra have their power concentrated, see Figures 2.7 and 2.12. However, the plots for THRESBMA and BALANCED imply that the two components are correlated at low frequencies. The zero coherency figures for LINKEDSHIFTED are not shown because they closely resemble those for LINKED. Thus, using the zero coherency test we are able to determine the range where the two components are correlated formally. Having done so, we are then able to find confidence intervals for the tangent of the phase spectrum. In addition, this test plays an important role when studying the phase spectrum, since the variance of the phase spectrum is inversely proportional to the squared coherency, see Section 4.1. So if the coherency is zero then the phase spectrum is expected to behave in an erratic manner because its variance will tend to infinity.

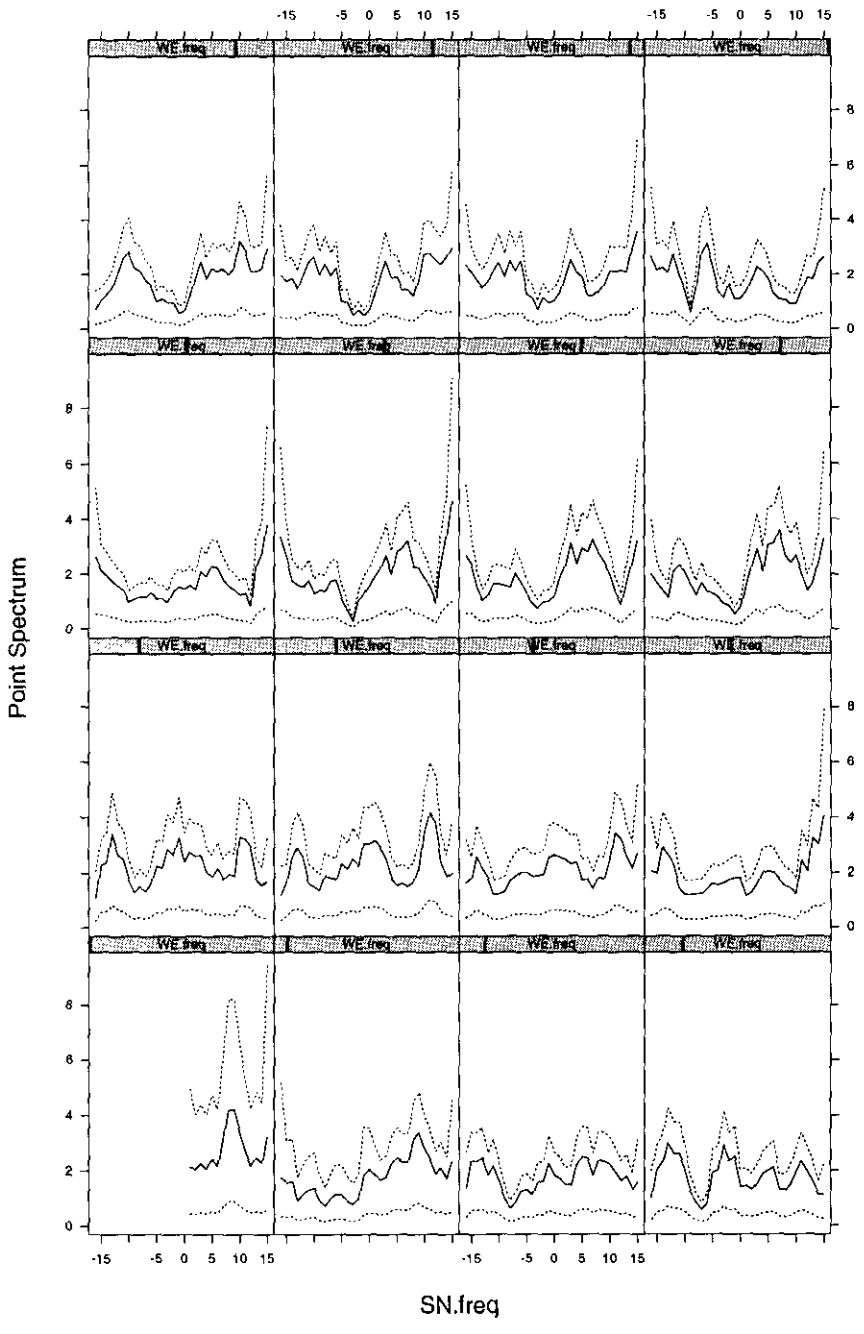

Figure 4.11: Profile of the point spectrum for CSRPLE, solid line, using uniform smoothing and the 99% confidence band around each frequency, dotted lines.

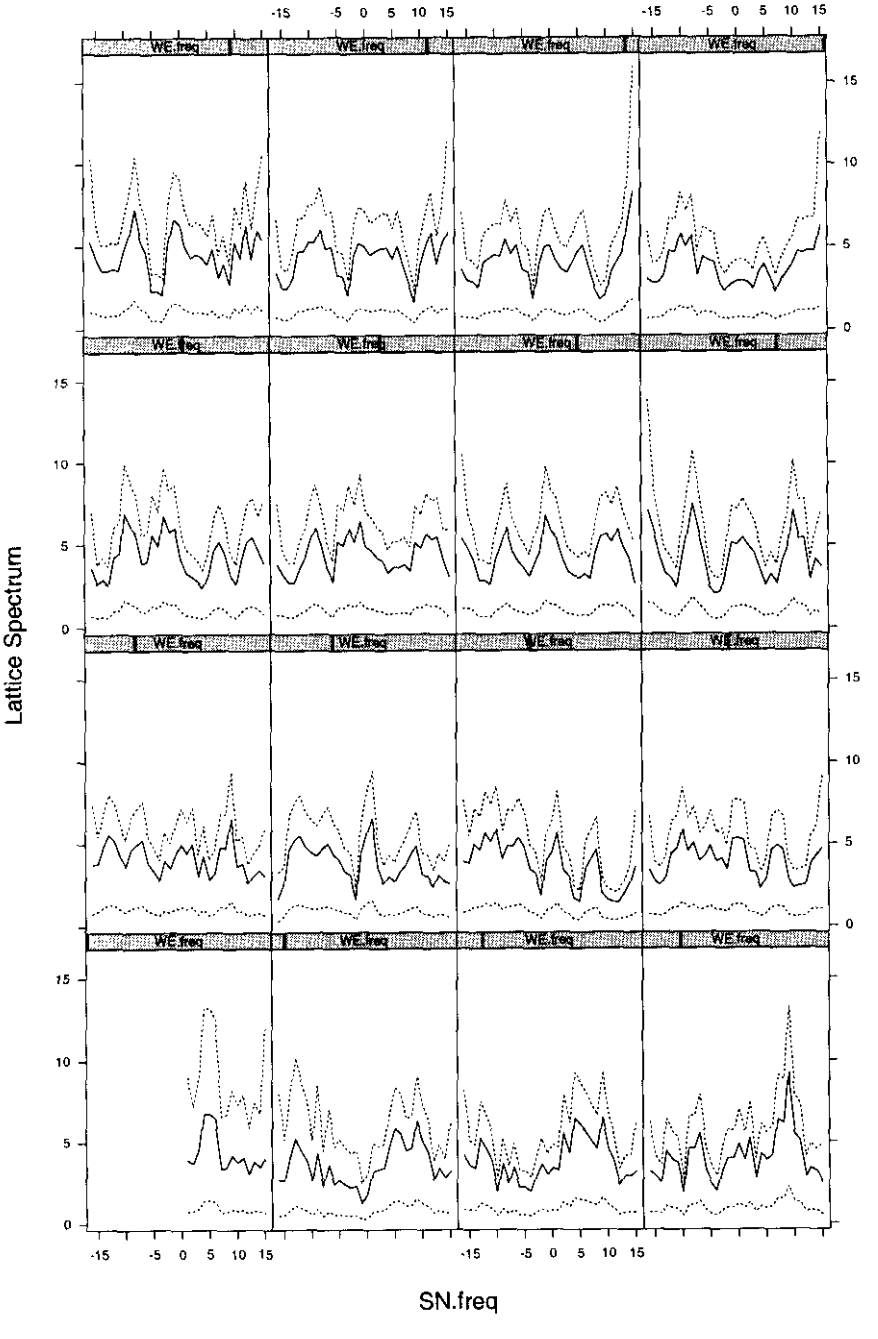

Figure 4.12: Profile of the lattice spectrum for CSRPLE, solid line, and the 99% confidence band around each frequency, dotted lines.

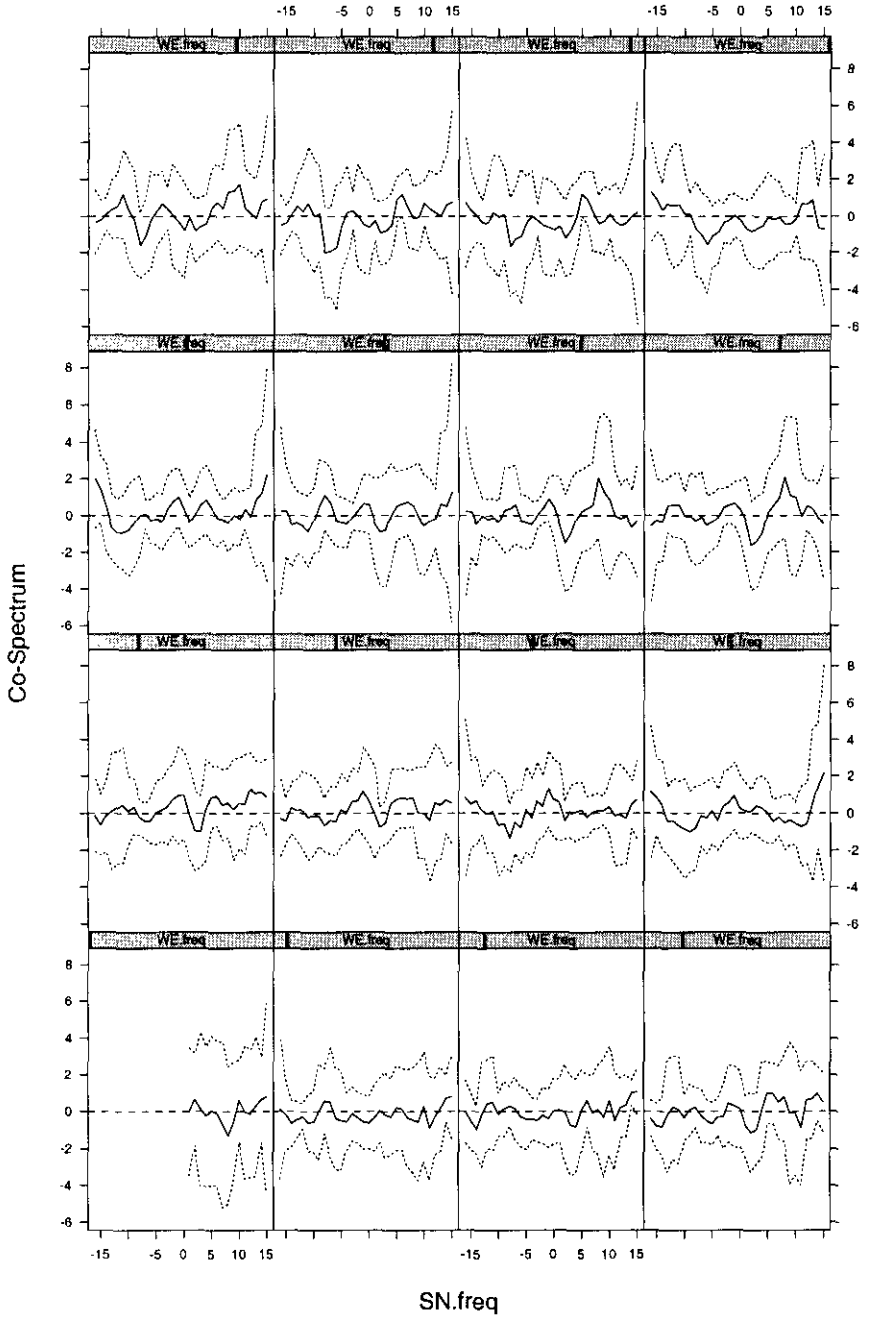

Figure 4.13: Profile of the co-spectrum for CSRPLE, solid line, and the 99% confidence band around each frequency, dotted lines. Dashed line is the zero line.

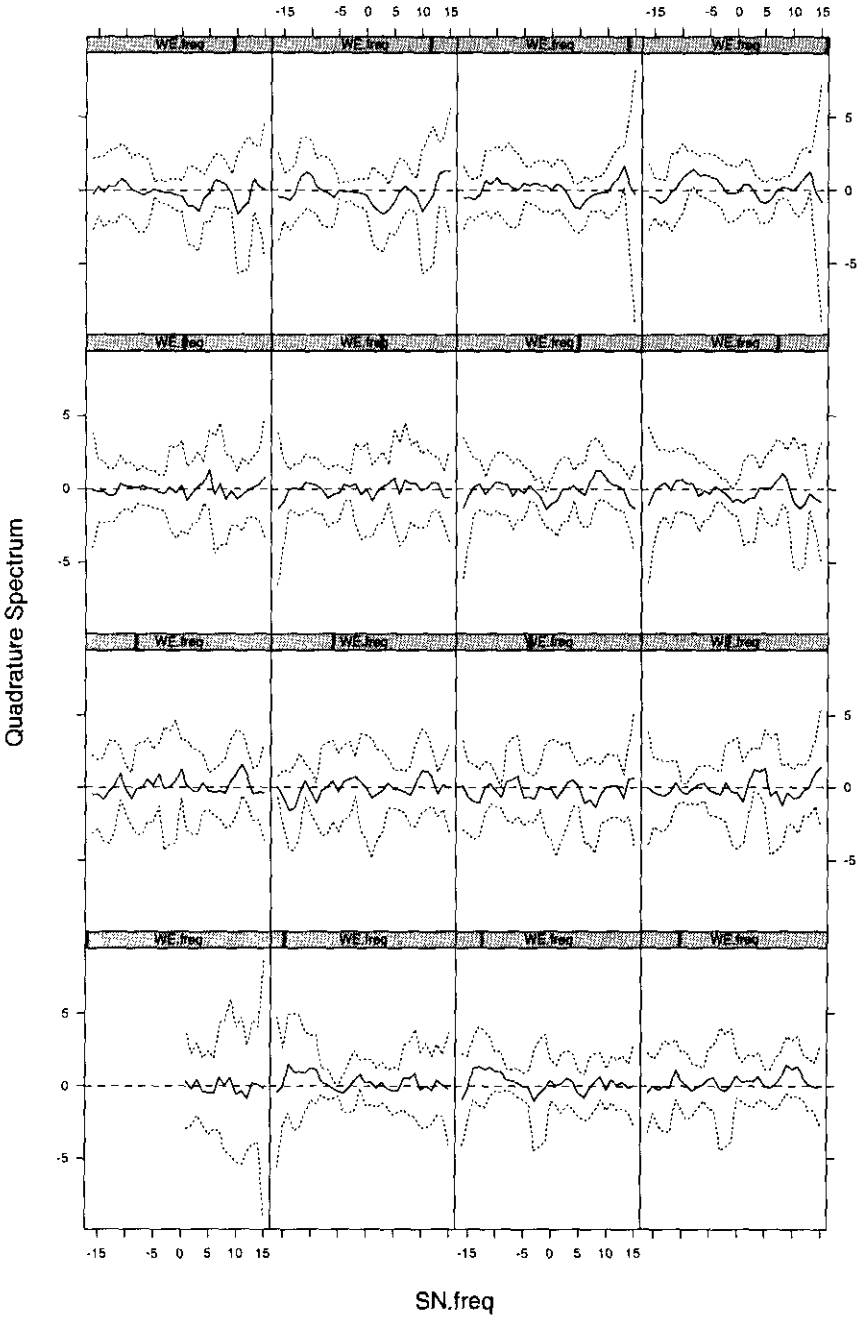

Figure 4.14: Profile of the quadrature spectrum for CSRPLE, solid line, and the 99% confidence band around each frequency, dotted lines. Dashed line is the zero line.

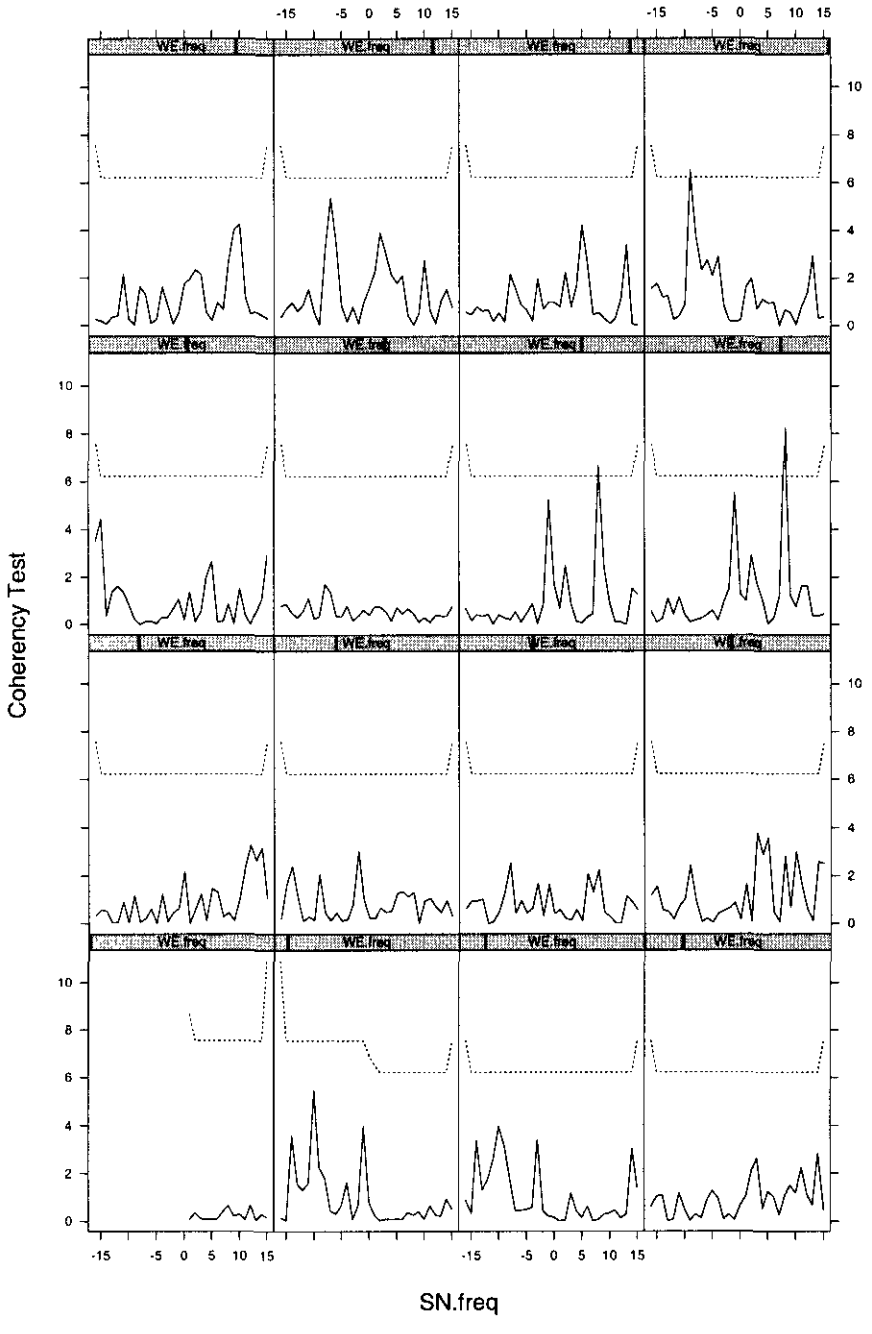

Figure 4.15: Profile of the zero coherency test statistic spectrum for CSRPLE, solid line, and the dotted line represents the upper 1% critical point of the F-distribution.

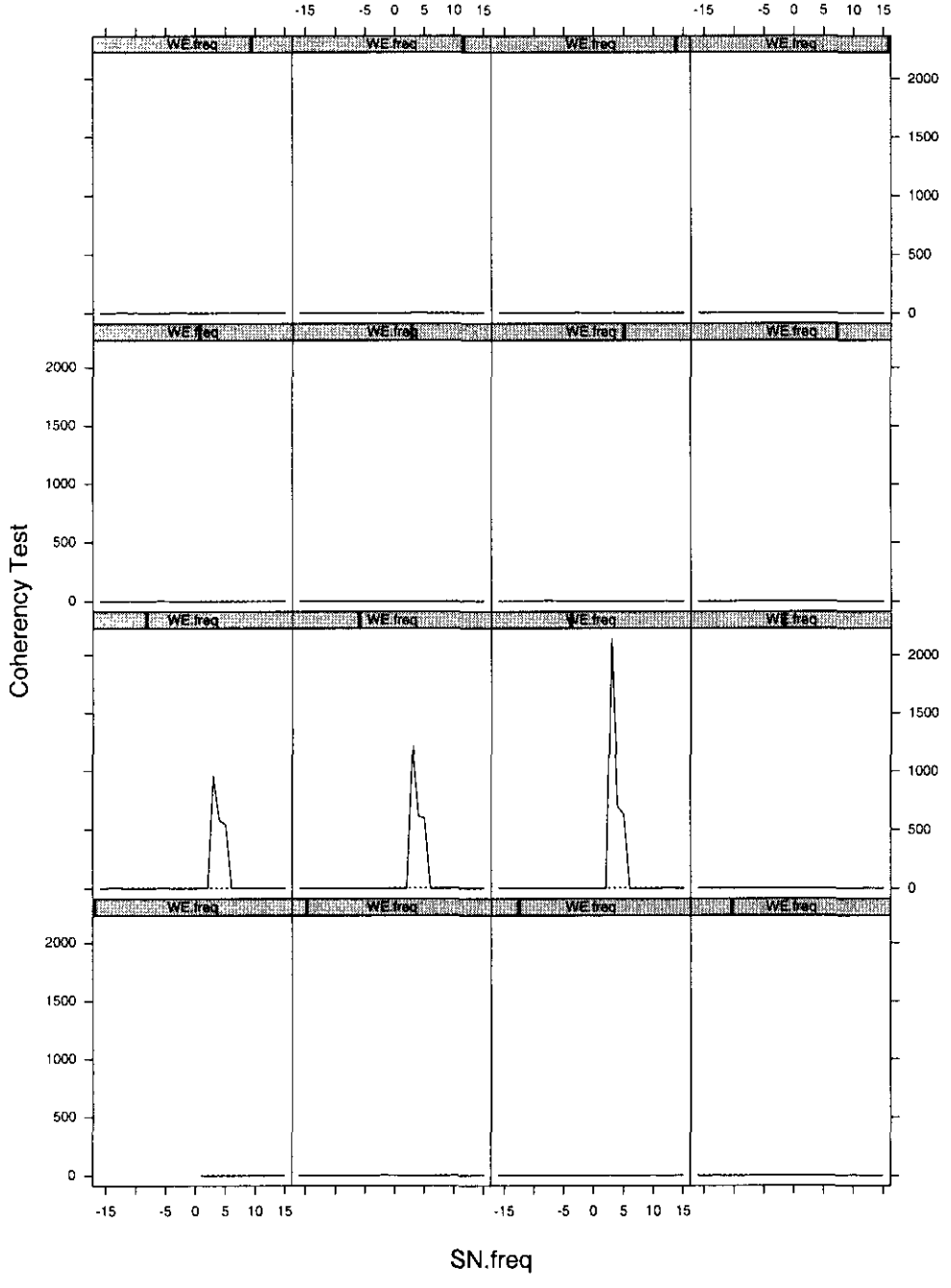

Figure 4.16: Profile of the zero coherency test statistic spectrum for THRESACOS, solid line, and the corresponding upper 5% critical point of the F distribution, dotted line.

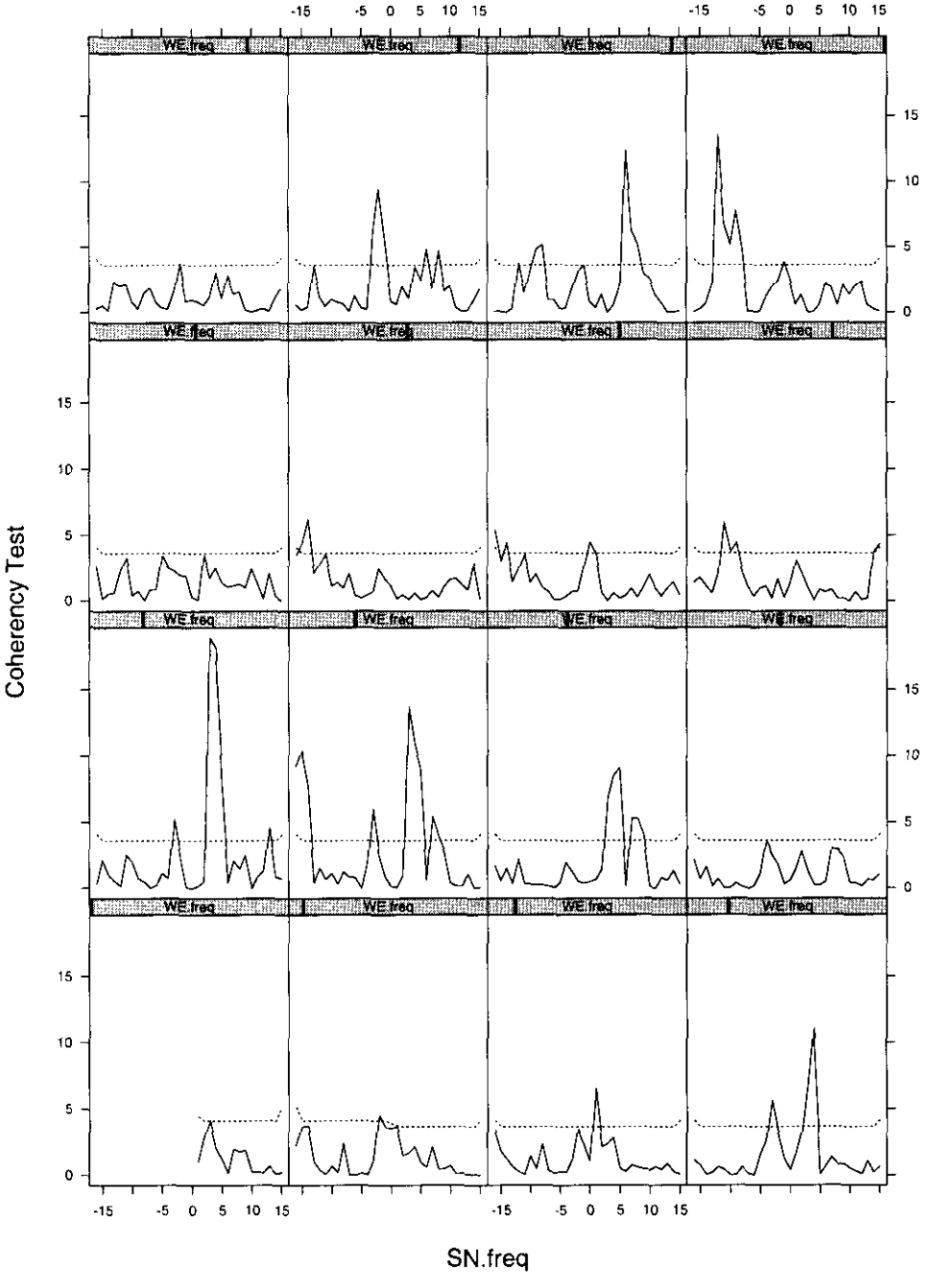

Figure 4.17: Profile of the zero coherency test statistic spectrum for THINCOS, solid line, and the corresponding upper 5% critical point of the F distribution, dotted line.

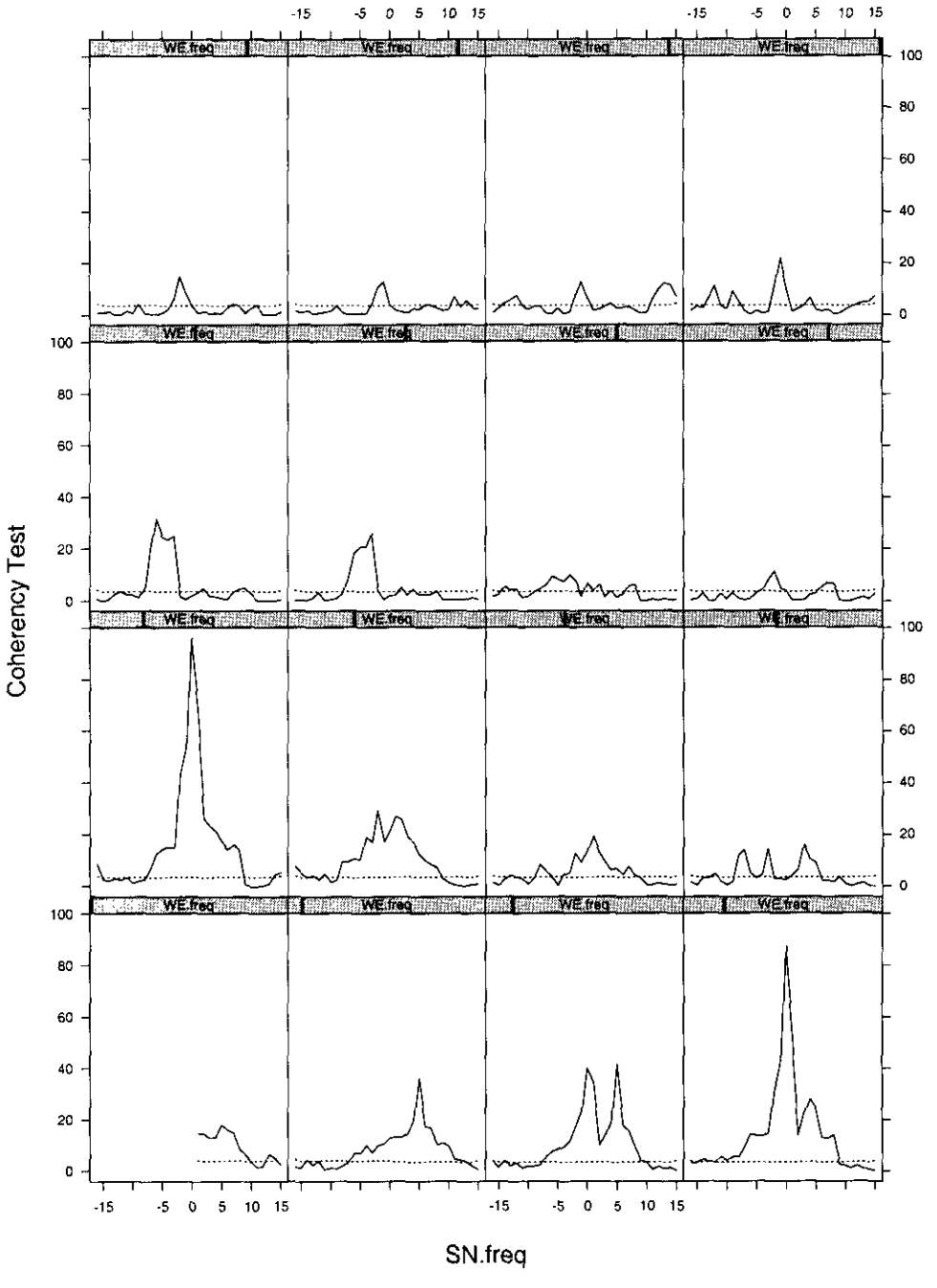

Figure 4.18: Profile of the zero coherency test statistic spectrum for THRESBMA, solid line, and the corresponding upper 5% critical point of the F distribution, dotted line.

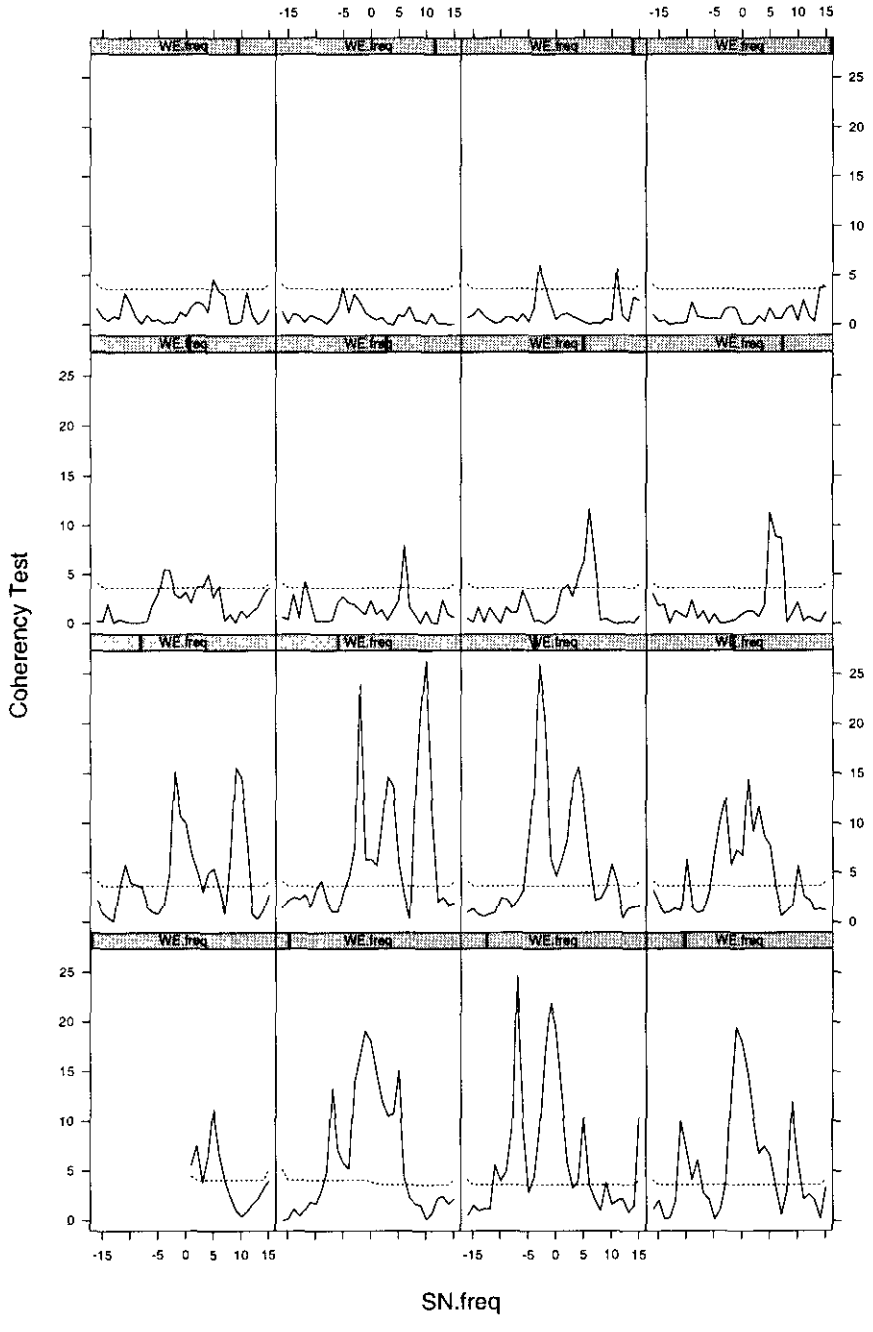

Figure 4.19: Profile of the zero coherency test statistic spectrum for BALANCED, solid line, and the corresponding upper 5% critical point of the F distribution, dotted line.

4.4 Summary

In this chapter, the asymptotic distribution of the cross-spectral statistic matrix $\check{\mathbf{G}}_{ZZ}(\boldsymbol{\omega})$ was established to be a complex Wishart distribution of dimension two with one degree of freedom for $\boldsymbol{\omega} \neq \mathbf{0}$, and to be a Wishart distribution of dimension two with one degree of freedom for $\boldsymbol{\omega} = \mathbf{0}$. The cross-periodogram statistic was found to be an unbiased estimator of the cross-spectral statistic $\check{G}_{NY}(\boldsymbol{\omega})$. The cross-spectral estimates at different frequencies were shown to be asymptotically independent of each other. Having established the asymptotic properties of the cross-spectral statistic, confidence intervals were obtained for the auto-, co-, quadrature and phase spectra. In addition, a test for zero coherency was discussed. It was verified that the test statistic followed an F distribution. Furthermore, confidence intervals were provided for some of the examples of Chapter 2, and the test for zero coherency was used to determine whether the two components of the examples were correlated. In the next chapter we will discuss another tool that one might use in an attempt to uncover patterns of correlation in point-lattice processes. This tool is based on discretising the point pattern and studying the joint properties of the resulting pattern and the lattice pattern using spectral analysis.

Chapter 5

Lattice-Lattice Processes

Lattice processes are observed at regular grid points. However, this property is not shared by point processes that can be observed anywhere in the study region. This situation might lead to some complications in the estimates of the cross-spectra, especially the phase spectrum. So one might consider discretising the point process in order to eliminate any discrepancies attributed to the above fact. Lattice-lattice processes, their properties and their estimates are discussed briefly in Section 5.1. In Section 5.2 methods to discretise the point pattern are discussed and some examples are considered.

5.1 Estimates

A lattice-lattice process is a process with two components where each component is a lattice process. Both components are observed in the same study region. Thus the matrices that represent both processes have the same dimension. Analysis of such processes can be carried out in the same manner as point-lattice processes by replacing estimates of the point process with those of a lattice process.

Let $\{Y_1, Y_2\}$ be a lattice-lattice process where Y_1 and Y_2 are observed on the rectangular region $[0, \ell_1] \times [0, \ell_2]$. Then in accordance with previous chapters one can estimate the auto-spectra via (1.11) and the cross-spectra via

$$\begin{aligned} F_{Y_1Y_2}(p,q) &= F_{Y_1}(p,q)\overline{F}_{Y_2}(p,q) \\ &= \left(\frac{1}{\sqrt{\ell_1\ell_2}}\sum_{b_1=0}^{\ell_1-1}\sum_{b_2=0}^{\ell_2-1} Y_{1(b_1,b_2)} \exp\left\{-2\pi i\left(\frac{pb_1}{\ell_1}+\frac{qb_2}{\ell_2}\right)\right\}\right) \times \\ &\quad \left(\frac{1}{\sqrt{\ell_1\ell_2}}\sum_{b_1=0}^{\ell_1-1}\sum_{b_2=0}^{\ell_2-1} Y_{2(b_1,b_2)} \exp\left\{2\pi i\left(\frac{pb_1}{\ell_1}+\frac{qb_2}{\ell_2}\right)\right\}\right), \end{aligned} \tag{5.1}$$

where F is the DFT of a process, (b_1, b_2) denote the grid points where the processes are observed, and p, q are integers that index frequency (ω_p, ω_q), compare (5.1) to (2.9). Equation (5.1) can then be decomposed either into its real and imaginary parts or into its amplitude and phase spectra. In addition, the squared coherency and gain spectra may be estimated.

Asymptotic properties can be derived in the same manner as for point-lattice processes. These properties are a special case of the properties derived by Brillinger (1970) for an r vector-valued p-dimensional series where $r = p = 2$ (see also Priestley, 1981b, chapter 9). Therefore, as seen from (5.1) one can adjust the spectral techniques discussed so far to accommodate lattice-lattice processes.

5.2 Point Processes into Lattice Processes

In this section, methods to discretise a point pattern are investigated. A point pattern can be transformed to a lattice pattern via simple binning, linear binning, fitting a fine lattice or using a kernel intensity estimator.

Details of these methods are given below. Note that if the number of events is large and the dimensions of the region are composite then discretising the point pattern results in computational gains because we are able to use the FFT.

5.2.1 Simple Binning

In this study, simple binning constitutes discretising a point pattern using either a binary or a count operation. Let X be the point process component of a point-lattice process in the region $[0, \ell_1] \times [0, \ell_2]$. The associated binary lattice (BL) or presence/absence lattice, X^{BL}, is defined as follows: let $X^{BL}(b_1, b_2)$ denote the value of the lattice in the quadrat $\Delta_{\mathbf{b}} = \Delta_{(b_1,b_2)}$, where $\Delta_{(b_1,b_2)} = [b_1, b_1 + 1] \times [b_2, b_2 + 1]$, then

$$X^{BL}(b_1, b_2) = \begin{cases} 1 & \text{if at least one event occurs in } \Delta_{\mathbf{b}}, \\ 0 & \text{if no events are present in } \Delta_{\mathbf{b}}, \end{cases}$$

where $b_1 = 0, \ldots, \ell_1 - 1$, $b_2 = 0, \ldots, \ell_2 - 1$. The count lattice (CL), X^{CL}, is obtained by assigning the number of events in the quadrat $\Delta_{\mathbf{b}}$ to $X^{CL}(b_1, b_2)$.

5.2.2 Linear Binning

As discussed by Wand and Jones (1995) linear binning assigns weights to the nearest neighbouring grid points of an event. Let the rectangle formed by the nearest neighbours be partitioned into subrectangles according to the position of the event within the rectangle, see Figure 5.1 for illustration. Then the weight at a given neighbour is calculated as the proportion of the area of the opposite subrectangle to the total area. For example, the point X_1 in Figure 5.1 is assigned the weight a_1 where a_1 is the proportion of the

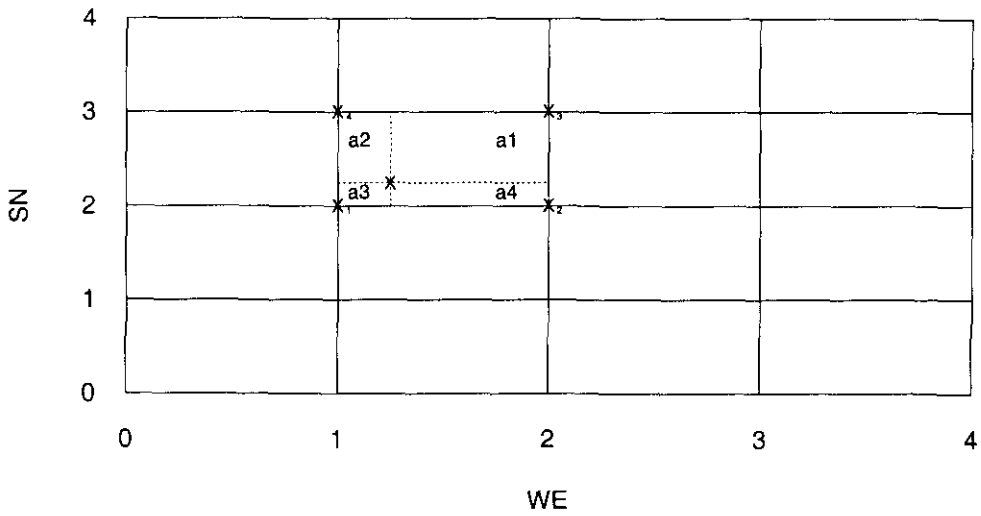

Figure 5.1: An example illustrating how weights are assigned to neighbouring grid points of an event X using linear binning. Points X_1, X_2, X_3 and X_4 are assigned the weights a_1, a_2, a_3 and a_4 respectively, see main text for more details.

area of the subrectangle determined by the event at X and the point X_3 to the area determined by the points X_1, X_2, X_3 and X_4. For examples in this study the area of the rectangle determined by the neighbouring grid points is always one because the grid is sampled at unit intervals. The lattice resulting from using linear binning will be denoted by LBL.

5.2.3 Fitting a Fine Lattice

Let $\{X^{FL}\}$ denote the class of lattices fitted to the point process X such that no more than one event is present in a given quadrat. Each member of this class is termed a fine lattice (FL). Let X_{sm}^{FL} be a member of this class such that the dimensions of X_{sm}^{FL} are the smallest integer multiples of ℓ_1 and ℓ_2.

Let the dimensions of X_{sm}^{FL} be $m\ell_1$ and $n\ell_2$. If m or n is greater than one then the lattice component Y of the hybrid process should be enlarged to have the same dimension as X_{sm}^{FL}. The enlarged process Y^{enl} can be obtained from the process Y by assigning to the quadrats

$$[mb_1, mb_1 + 1] \times [nb_2, nb_2 + 1], \ldots\ldots\ldots,$$
$$[m(b_1 + 1) - 1, m(b_1 + 1)] \times [n(b_2 + 1) - 1, n(b_2 + 1)]$$

of the enlarged process the same value as the quadrat $\Delta_{\mathbf{b}}$ of the process Y. Alternatively, the lattice pattern can be interpolated to fit the finer grid.

Computationally X_{sm}^{FL} is determined as follows.

1. Let X^{CL} be the count lattice for the process X. If all the entries in X^{CL} are either zeros or ones then set $X_{sm}^{FL} = X^{CL}$ and stop, otherwise go to step 2.

2. For $X^{CL} > 1$ determine the minimal distance between events in the corresponding quadrat. Let $\Delta_{\min}$ be the quadrat where the (global) minimal distance is detected.

3. Determine the minimal integers m and n such that if $\Delta_{\min}$ is divided into $m \times n$ subquadrats then no two events within Δ belong to the same subquadrat.

4. Let X_{sm}^{FL} be the lattice with dimensions $m\ell_1 \times n\ell_2$ and entries zero if no event is present in a quadrat and one otherwise.

Note that fitting an FL is computationally expensive especially if the minimum distance is relatively small. In practice, the point processes are usually

recorded to a certain number of decimal places, so one can use this number to define the minimal distance. However, this might lead to heavy computations if the locations of points are given to great precision due to the size of the lattices required.

5.2.4 Kernel Intensity Estimator

The kernel intensity lattice (KIL), X^{KIL}, is obtained by finding estimates of the number of events at the grid points (b_1, b_2) using the kernel intensity estimator. The kernel intensity estimator is defined as

$$X^{KIL}(\mathbf{b}; \mathbf{H}) = \sum_{j=1}^{N_X} K_{\mathbf{H}}(\mathbf{b} - \mathbf{a}_j), \tag{5.2}$$

where $\mathbf{a}_j$ $(j = 1, \ldots, N_X)$ are the locations of the events of the point process X in the study region, N_X is the number of events of the point pattern and $\mathbf{H}$ is a symmetric positive definite 2×2 matrix known as the *bandwidth matrix.* In addition, $K_{\mathbf{H}}(\mathbf{b}) = \big(\det(\mathbf{H})\big)^{-1/2} K(\mathbf{H}^{-1/2}\mathbf{b}^{\top})$ where K is a bivariate function satisfying $\int K(\mathbf{b}) d\mathbf{b} = 1$ and is known as the *kernel function.* Usually the kernel function is taken to be a bivariate symmetric probability density function, for example, the bivariate standard normal distribution (see Wand and Jones , 1995).

Conditional on the number of events $\frac{1}{N_X} X^{KIL} \equiv \hat{h}(\mathbf{b}; \mathbf{H})$ can be treated as a kernel density estimation problem. This enables us to use existing techniques addressing the different issues related to the choice of the bandwidth matrix and the kernel function, the former being the most important of the two (see Wand and Jones , 1995). Several bandwidth selectors have been studied in the literature including least squares cross-validation (LSCV) and

plug-in methods, see Wand and Jones (1994) and Wand and Jones (1995, chapter 4) for more details. The usual criterion for selecting a bandwidth when using the two selectors mentioned above involves minimising the mean integrated square error (MISE) function of $\hat{h}$, namely

$$\text{MISE}\{\hat{h}(\mathbf{H})\} = \int \mathbb{E}\{\hat{h}(\mathbf{b}, \mathbf{H}) - h(\mathbf{b})\}^2 d\mathbf{b},$$

where h is the true process. The LSCV method is based on minimising the quantity

$$\text{LSCV}(\mathbf{H}) = \int \hat{h}(\mathbf{b}, \mathbf{H})^2 d\mathbf{b} - 2N_X^{-1} \sum_{j=1}^{N_X} \hat{h}_{-j}(\mathbf{a}_j, \mathbf{H}),$$

where $\hat{h}_{-j}$ is the kernel estimator based on the sample less the point $\mathbf{a}_j$. As the name suggests plug-in methods are based on inserting estimates of the unknown parameters that are encountered in the formulae of the asymptotic MISE optimal bandwidth.

Diggle (1985) has proposed a kernel estimator for the one-dimensional DSPP that does not require conditioning on the observed number of events. Diggle and Marron (1988) have proved the equivalence between bandwidth selectors for Diggle's (1985) intensity estimator and LSCV bandwidth selectors for the one-dimensional kernel density. In the light of this equivalence further studies might be carried out to investigate the possibility of an equivalence between bandwidth selectors for kernel density and intensity estimators for the one- and two-dimensional cases using plug-in methods.

In this study, we will use the plug-in approach within the conditional framework. The reason for this choice is the availability of computer code that calculates the two-dimensional kernel density estimator and uses the

plug-in method for bandwidth selection. The computer code is available from wanddensity library of Splus functions.

Another issue related to the kernel intensity estimator is the boundary effect, whereby the intensity function is extended beyond the study region by setting it equal to zero, and where the intensity is positive at the boundaries, for more details see Diggle and Marron (1988). This situation will result in the kernel intensity having discontinuties at the boundaries. Diggle (1985) has addressed this problem for the one-dimensional point process. He suggested that the one-dimensional version of (5.2) can be modified to correct for boundary problems by dividing the estimator by the convolution of the kernel function with one over the study area. This correction can be easily extended to the two-dimensional case. However, we will overlook this problem due to the illustrative role the kernel intensity estimator plays in this study.

5.2.5 Application

The point pattern of the example LINKED of Chapter 2 is discretised as an illustration of the above methods. Figures 5.2(a) to (e) represent the graphs of the point pattern of LINKED, and the discretised point pattern using BL, CL, LBL and KIL, respectively. The discretised pattern using FL is not included in Figure 5.2 due to graphical resolution limitations. The size of the resulting lattice using FL is 3040×3040 corresponding to a minimal inter-event distance of $1/95$. This lattice has 1965 unit entries; all the other entries are zero. The number of unit entries corresponds to the number of events of the point pattern of LINKED. The size of the original lattice was

extended to 3040×3040 using Section 5.2.3 method to enlarge the original lattice (component Y of the process) where $m = n = 95$.

The auto- and cross-spectra of the resulting lattice-lattice patterns are presented in Figures 5.3, 5.4, 5.5, 5.6 and 5.7. The kernel intensity estimator calculations have been carried out using wanddensity library of functions.

The discretised point pattern, component Y_1 of the process, auto-spectra using BL, CL and LBL resemble the auto-spectrum of the original lattice pattern. However, using KIL results in a slightly different auto-spectrum that has most of its power concentrated at low frequencies. In fact when using the CL the two auto-spectra are identical. This is due to the way the lattice pattern was generated in LINKED. The fact that the auto-spectra are identical results in the co-spectrum being identical to them. The quadrature and phase spectra are identically zero, and the squared coherency is identically one, see Figure 5.3.

The auto-spectrum of the discretised point pattern using FL, Figure 5.7(a), also resembles that of the original lattice pattern for the range of frequencies $p = 0, \ldots, 16$ and $q = -16 \ldots, 15$. Outside this range the spectrum of the discretised point pattern fluctuates around zero. The same is true for the original lattice but the FL auto-spectrum fluctuates more wildly. The range of frequencies presented in Figure 5.7 is restricted to $p = 0, \ldots, 32$ and $q = -32 \ldots, 32$. This is a subset of the frequency range $p = 0, \ldots, 1520$ and $q = -1520, \ldots, 1519$ that can be investigated using the FL method. The reason for only displaying the restricted subset of frequencies is that and as mentioned above the values outside the range $p = 0, \ldots, 16$ and $q = -16 \ldots, 15$ fluctuate around zero.

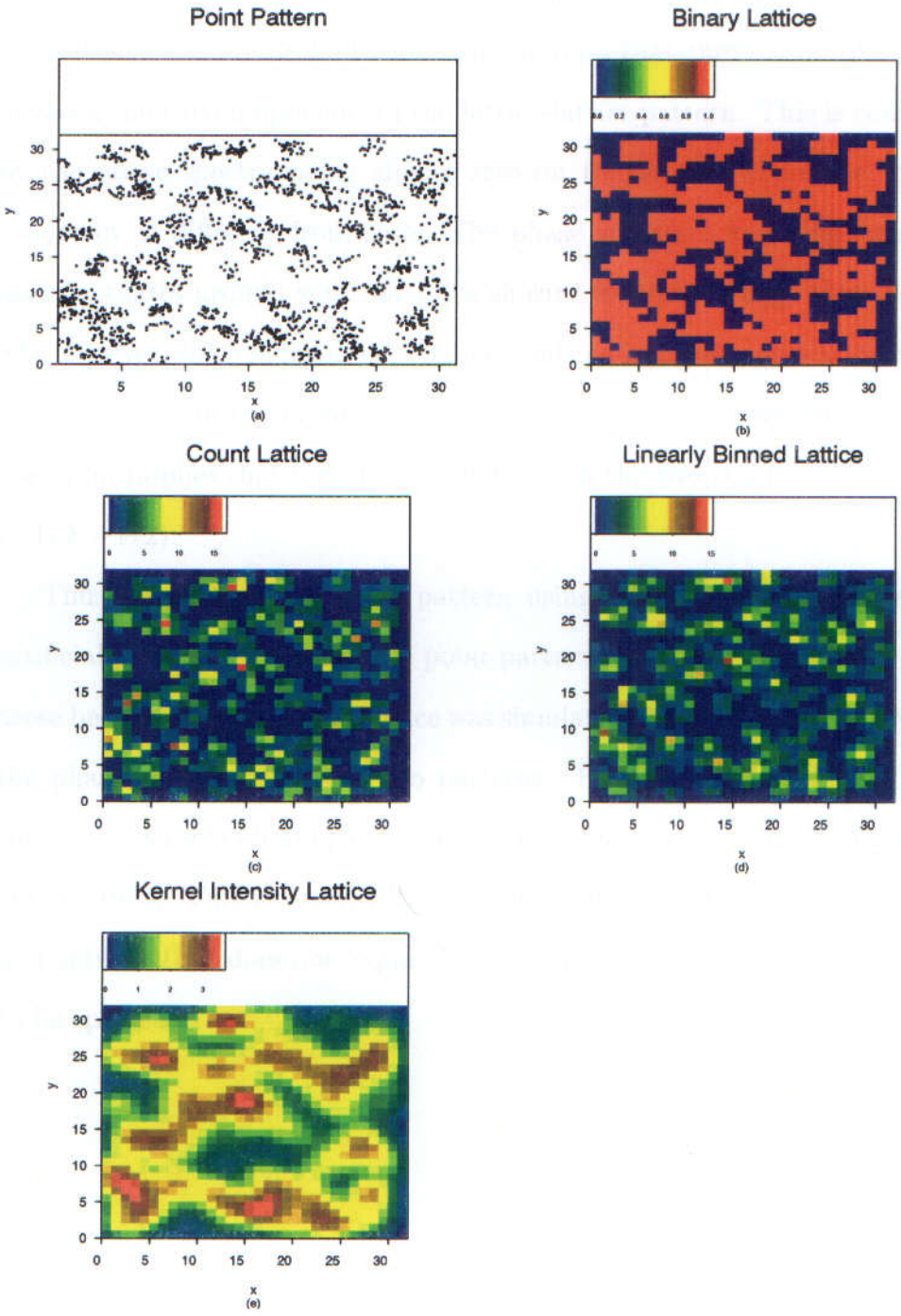

Figure 5.2: (a) Point Pattern of LINKED; (b) to (e) discretised patterns using BL, CL, LBL and KIL, respectively.

The quadrature spectra that result from the BL and FL methods of discretisation fluctuate around zero. This implies that there is no phase shift between the two components of the lattice-lattice pattern. This is confirmed by the phase spectra being almost zero for frequencies where the squared coherency is different from zero. The phase spectrum resulting from KIL also fluctuates around zero but for a shorter frequency range than BL and FL. However, the quadrature spectrum resulting from the application of LBL resembles that of the original point-lattice process. Furthermore, the phase spectrum implies that the phase shift between the two components is $(-1/2, -1/2)$.

Thus discretising the point pattern using BL, CL or FL removed the artificial phase shift between the point pattern and the lattice pattern which arose because of the way the lattice was simulated. Using LBL did not remove the phase shift between the two patterns. However, LBL is known to be superior to simple binning in estimating the true distribution (see Wand and Jones , 1995). Furthermore, LBL is computationally less expensive than FL and unlike KIL it does not require bandwidth selectors and density functions to be specified.

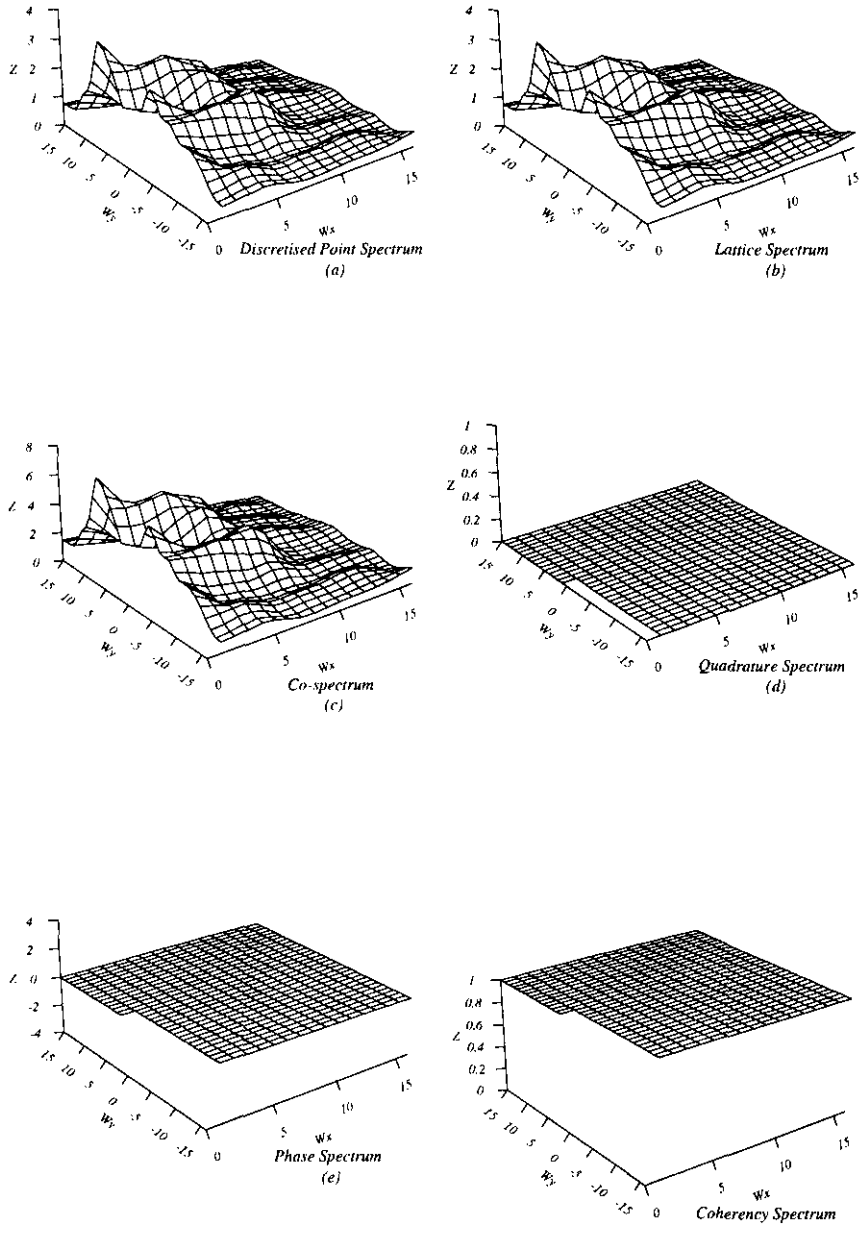

Figure 5.3: (a) Auto-spectrum of the count lattice corresponding to Figure 5.2(c); (b) auto-spectrum of the original lattice Figure 2.14; (c) to (f) co-, quadrature, phase, and squared coherency spectra of the lattice-lattice pattern.

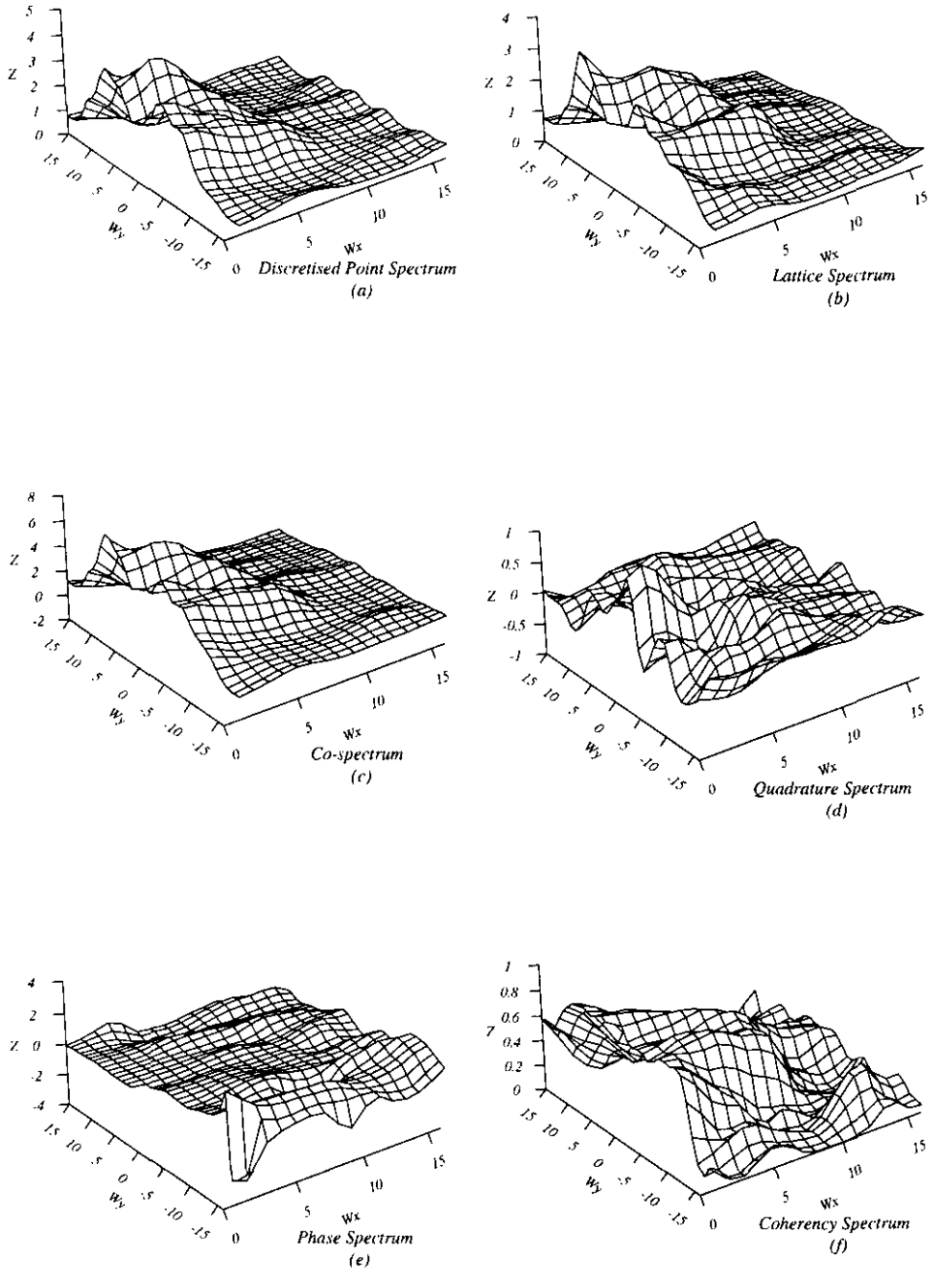

Figure 5.4: Auto- and cross-spectra using the Binary Lattice.

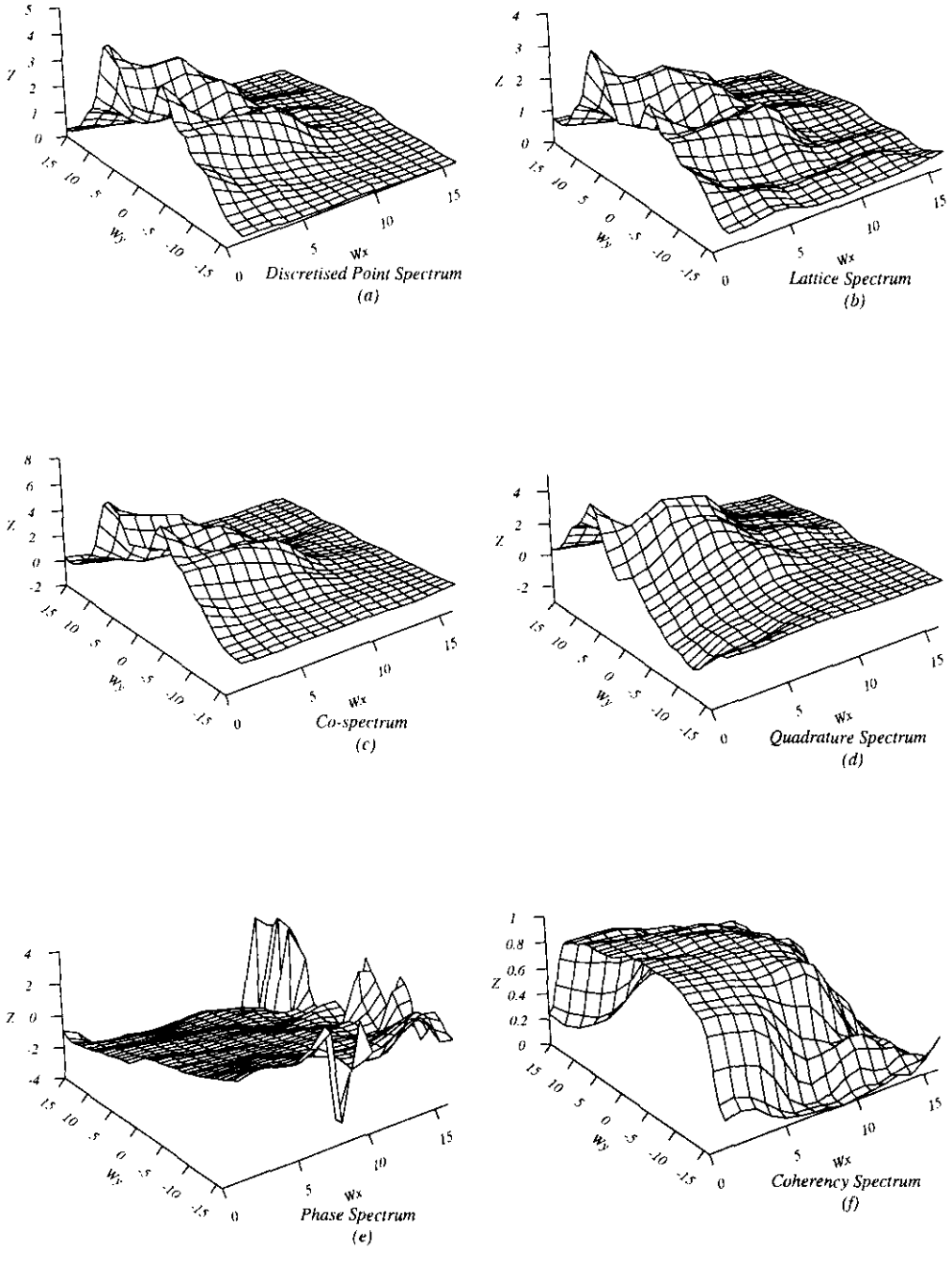

Figure 5.5: Auto- and cross-spectra using the Linearly Binned Lattice.

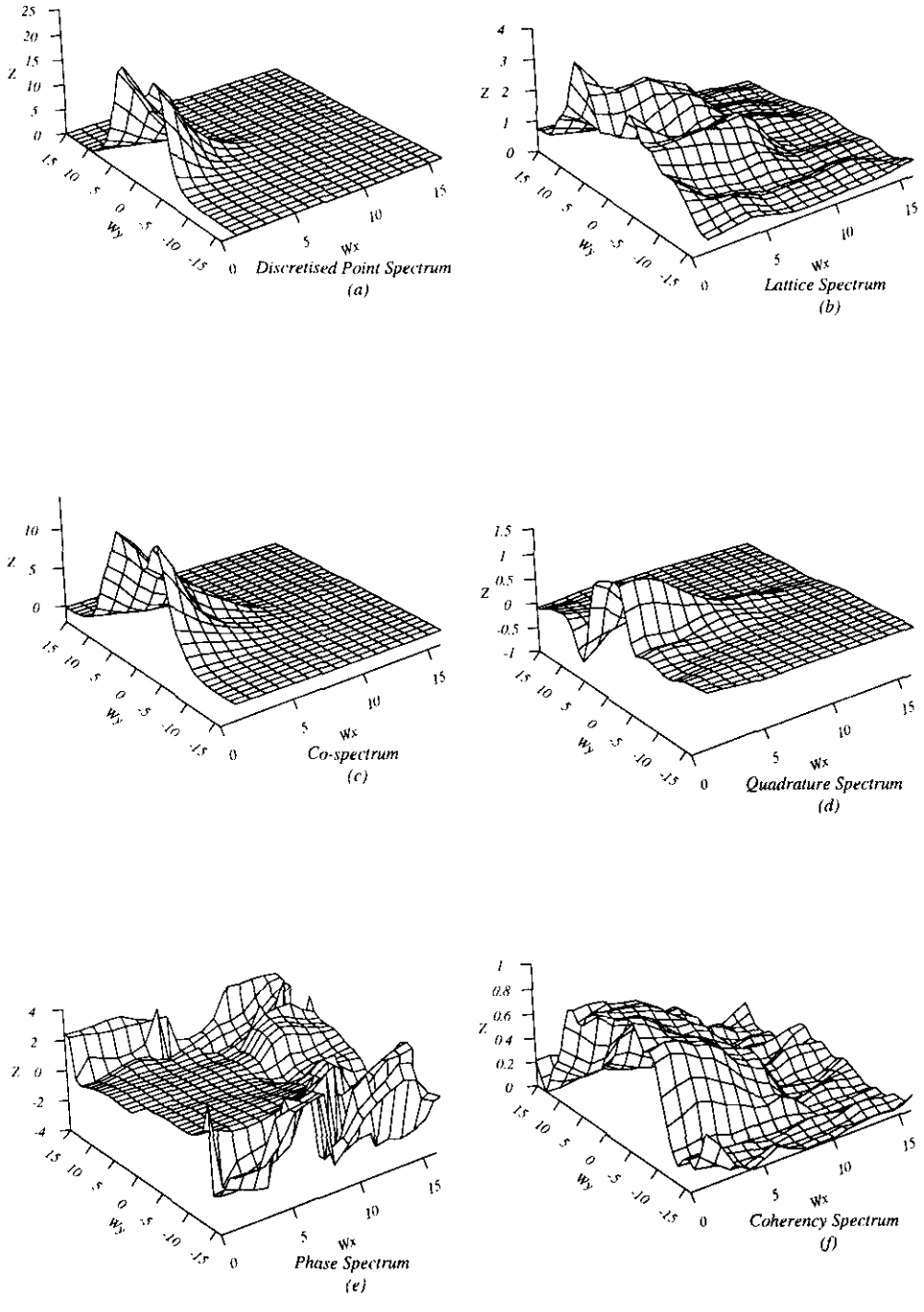

Figure 5.6: Auto- and cross-spectra using the Kernel Intensity Lattice.

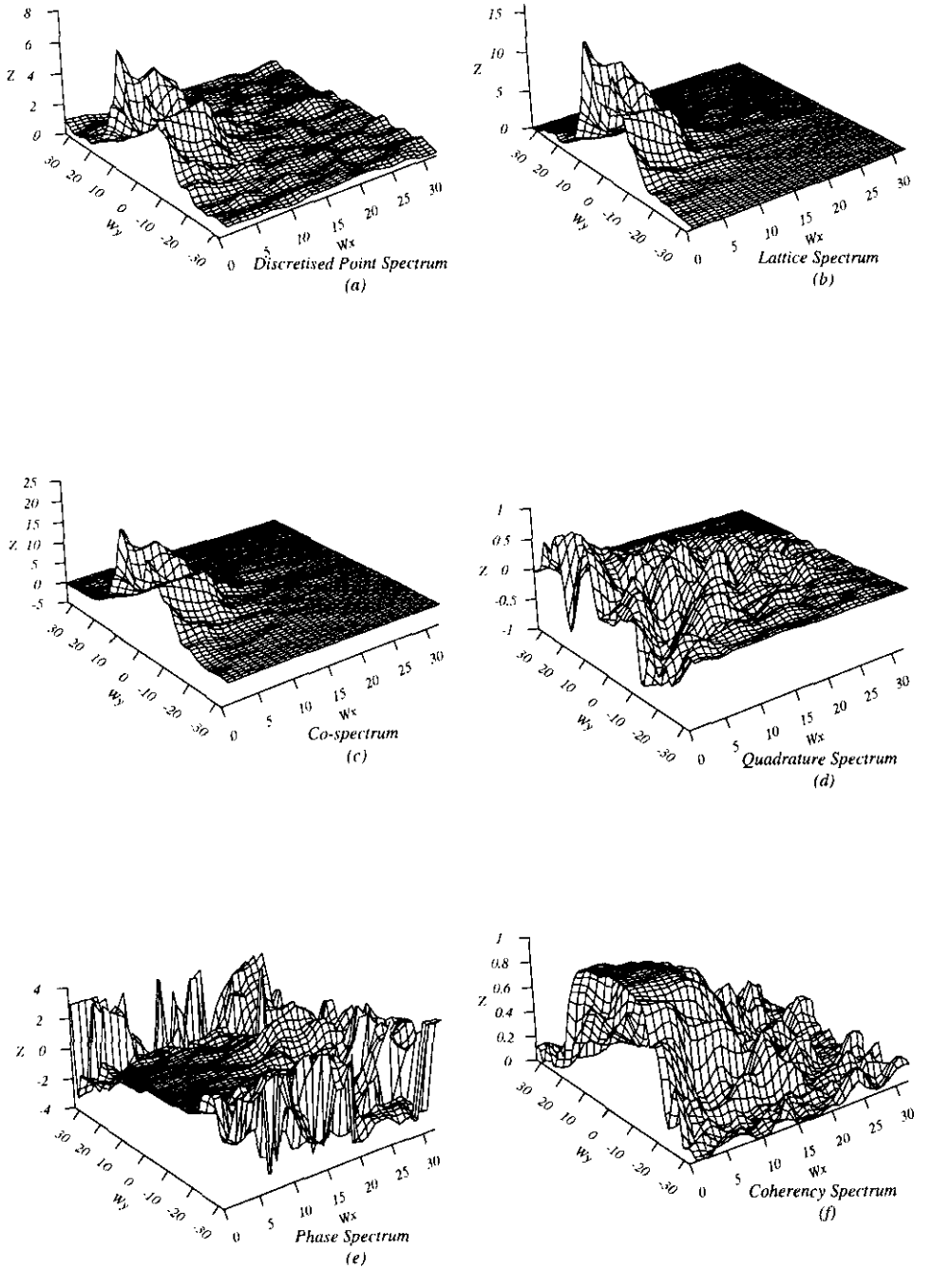

Figure 5.7: Auto- and cross-spectra using the Fine Lattice.

5.3 Summary

Analyses of point-lattice patterns through discretisation of the point pattern to form lattice-lattice patterns have been investigated. The main advantage of such an approach is that it eliminates problems that are due to lattice processes being observed on a grid whereas point processes are not. Several methods to discretise the point pattern have been discussed. These include linear binning which has been recommended by Wand and Jones (1995) as a better alternative to simple binning. Kernel intensity estimators have also been studied. In addition, using a fine lattice has been investigated. It is computationally expensive to use this method, especially when the minimum distance between events is relatively small. In the next chapter we will use the techniques discussed so far to explore the relationship between the components of a point-lattice pattern for a real data set.

Chapter 6

Cross-Spectral Analysis of Tree Species in a Rain Forest in French Guyana

In this chapter, we explore the relationship between the components of a real point-lattice pattern using cross-spectral analysis techniques. The data set consists of the locations of fifty-one tree species in a rain forest at Paracou in French Guyana; altitude values of the study area are also provided. This data set has been supplied by Dr. Michel Goulard of *Le Centre INRA de Toulouse*, France, and Dr. Hélène Dessard of *CIRAD-Forêt*, France. In Section 6.1 the tree species data are briefly discussed. In Sections 6.2 to 6.5 cross-spectral analyses for some species are provided.

6.1 The Data

The data set consists of locations of fifty-one groups of tree species in a plot of land of dimensions 250m $\times$ 250m. For convenience we will use the term species to mean a group of one or more species. In addition, altitude values are provided on a 50×50 square grid with spacings of 5m between consecutive

grid points in each direction. Altitude values, which are relatively easy to measure, are of interest to foresters due to the information they hold about soil characteristics, in particular, the type of drainage. The data were collected at an experimental site at Paracou ($5°18N, 52°53W$) near Sinnamary, French Guyana. Figure 6.1 is a map of French Guyana. This map was downloaded from the University of Texas library website. The website address is http://www.lib.utexas.edu and the map can be obtained by following links to the Perry-Castañeda Library Map collection. Figure 6.2 gives the location of the experimental site where the current data set was collected at plot number one. This map is an extract from a map downloaded from the website of Silvolab Guyana which is a research group interested in studying the ecosystem of tropical forests in French Guyana. The website address for Silvolab Guyana is http://kourou.cirad.fr/silvolab. For more details about the data set see Dessard (1996) and Forget et al. (1999).

For species two to fourteen Table 6.1 gives the species number, botanical family, scientific name, and local names used in French Guyana and (British) Guyana. The number of trees of each species and the status of the species are also given. The status is a classification of the species as either an active timber tree (a) or a potential timber tree (p). The classification was extracted from the appendix of Hammond et al. (1996). Any missing information is indicated as NA. Table 6.1 indicates that potential timber trees are relatively abundant compared to active timber trees.

We do not possess detailed information for species one and species fifteen to fifty-one. However, the number of events for species one is 1543 whereas species fifteen to fifty-one consist of thirty-three events or less. Species one

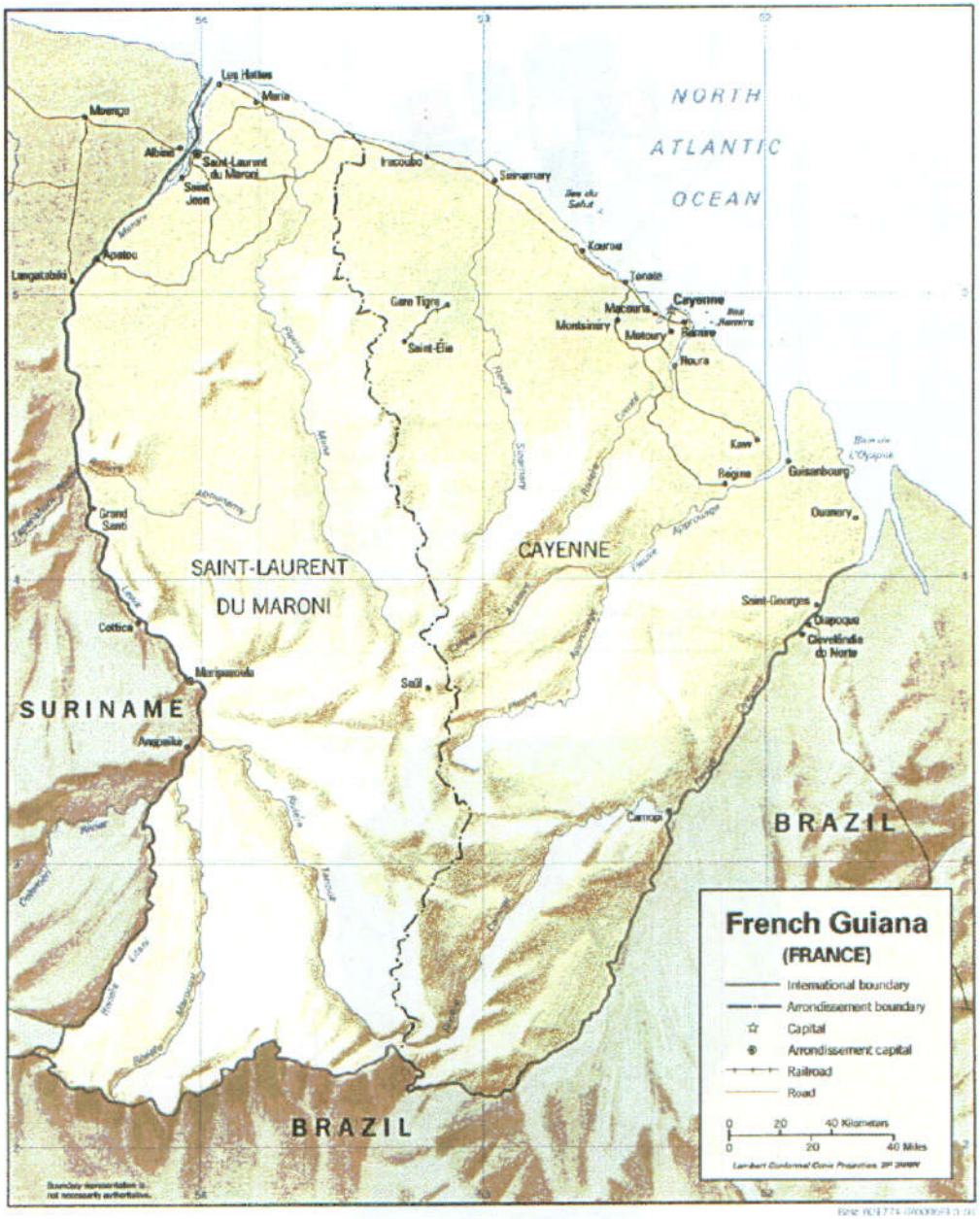

Figure 6.1: Map of French Guyana.

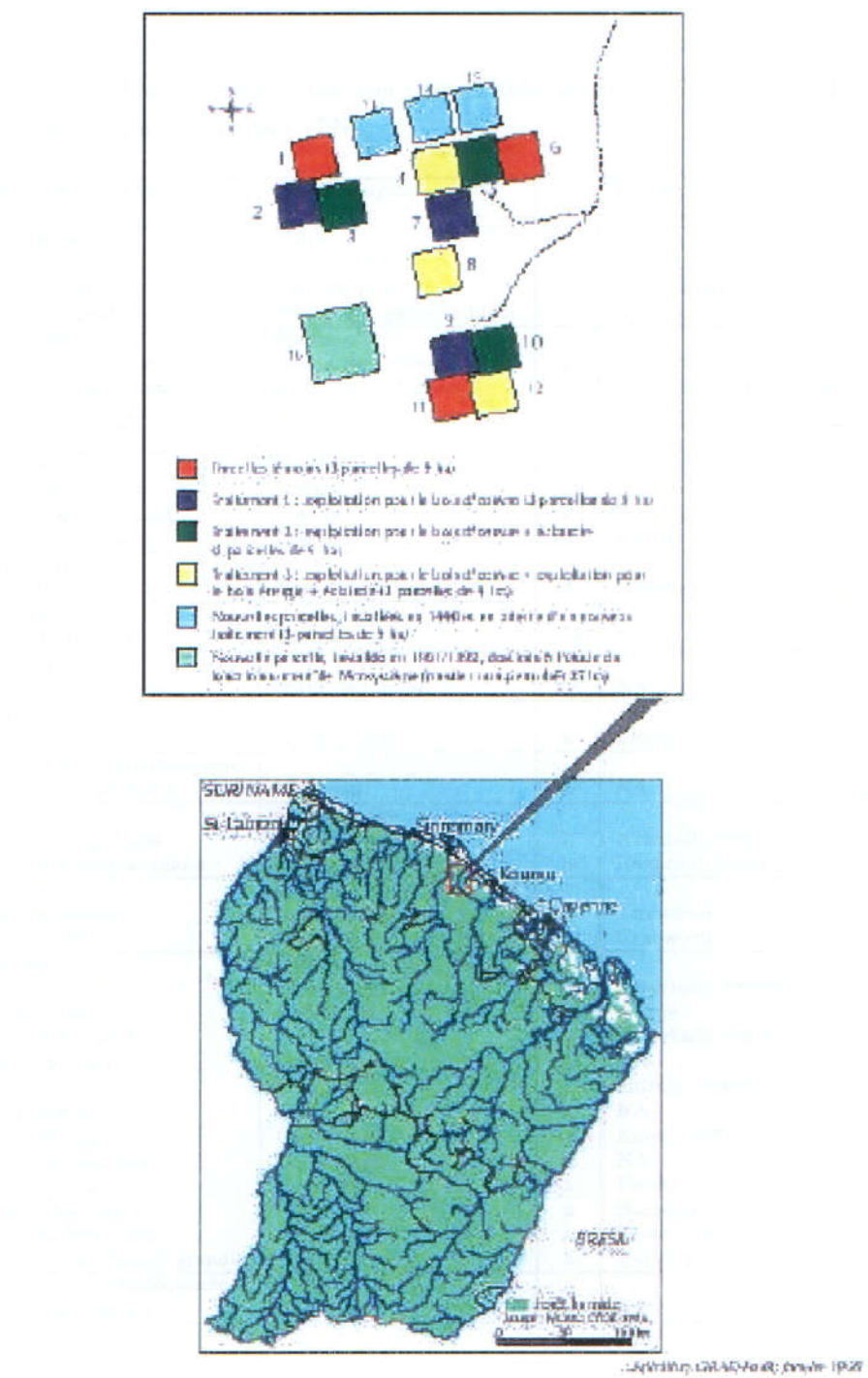

Figure 6.2: Map of experimental site at Paracou. The current data set was collected at plot one.

Table 6.1: Scientific/local names of thirteen species, their number (SN), status (ST) as active/potential and number of trees (TN).

SN	*Family*/Scientific name	French Guyana local name	ST	British Guyana local name	TN
2	*Chrysobalanaceae*	Gaulette			637
	Licania majuscula	Bois, gaulette	p	Kautaballi	
	Licania micrantha	Pali, gaulette	p	Marishiballi	
	Parinari campestris	Foungouti, gaulette blanc	p	Burada, broad-leaved	
3	*Lecythidaceae*	Mahot noir			572
	Eschweilera chartacea	Mahot noir, rouge	p	Kakaralli, Toko	
	Eschweilera pedicellata	Mahot noir, Baikaaki	p	Kakaralli, swamp wina	
	Eschweilera poiteaui	Mahot noir, rouge	p	NA	
4	NA	Palmiers	NA	NA	145
5	*Burseraceae*	Encens			131
	Protium decandrum	Encens	a	Kurokai	
	Protium heptaphyllum	Encens	a	Haiawa, Incense tree	
	Protium sagotianum	Encens	a	Kurohi	
6	*Myristicaceae*				
	Iryanthera sagotiana	Tosso Passa	p	Kirikaua	130
7	*Papilionaceae*				
	Bocoa prouacensis	Boco	NA	NA	100
8	*Clusiacees*				
	Symphonia globulifera	Manil Marecage	NA	NA	96
9	*Vochysiaceae*				
	Qualea rosea	Gonfolo rose	a	Yakopi	84
10	*Leguminosae-Caesalpineaceae*				
	Vouacapoua americana	Wacapou	a	NA	81
11	*Lecythidaceae*	Mahot rouge			69
	Eschweilera sagotiana	Mahot rouge	a	Kakaralli, common black	
	Eschweilera subglandulosa	Mahot rouge	p	Kakaralli, black	
12	*Meliaceae*	Carapa			61
	Carapa guianesis	Carapa rouge	a	Crabwood	
	Carapa procera	Carapa	a	Crabwood	
13	*Lauraceae*	Cedres			52
	Licania cannella	Cedre carlelle	a	Silverballi, brown	
	Nectandra pisi	Cedre noir	a	Shirua	
	Ocotea canaliculata	Cedre canelle	a	Silverballi, white	
	Ocotea globifera	Cedre apicic	a	NA	
	Ocotea guianensis	Cedre	a	Shirua, Tokowe	
	Ocotea neesiana	Cedre	a	NA	
	Ocotea oblonga	Cedre apici	a	Kereti, soft	
	Ocotea petalanthera	Cedre apici	a	NA	
	Ocotea puberla	Cedre gris	a	Kereti	
	Ocotea tomentella	Cedre	a	Baradan	
	Ocotea wachenheimii	Cedre gris	a	Kereti, hard	
	Rhodostemonodaphne grandis	Cedre jaune	a	Buradiye	
14	*Leguminosae-Caesalpineaceae*				
	Dicorynia guianensis	Angelique	a	NA	35

consists of trees that were not identified botanically and are of least importance for the foresters.

In the next sections preliminary exploratory analyses of Species 3, 10, 11 and 12 are provided. Species 3 and 11 were chosen because they belong to the same family. It is therefore of interest to compare Species 3 and 11 because Species 3 is a potential timber tree while Species 11, according to Table 6.1, can be either a potential or an active timber tree. We suspect that in the current data set Species 11 contains only the subgroup that is an active timber tree. The number of events of Species 3 is 572 while that of Species 11 is 69. Species 10 and 12 were chosen since they are important commercial trees (see Forget et al., 1999). Analyses of the remaining tree species are provided in Appendix C.

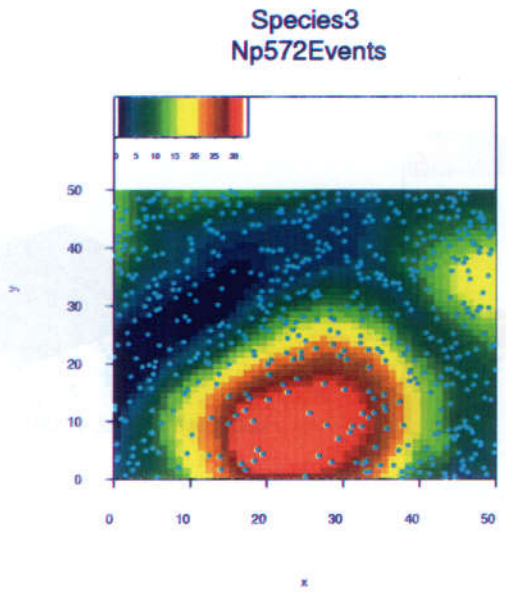

Figure 6.3: The lattice pattern represents the altitude data; the point pattern represents the locations of Mahot Noir (Species 3) trees.

6.2 Species 3: Mahot Noir

The point-lattice pattern presented in Figure 6.3 consists of the locations of Mahot Noir trees within the study region (the point pattern) and the altitude values of the study region (the lattice pattern).

A graphical representation of the auto-periodogram for the lattice pattern is provided in Figure 6.4(a). Peaks are observed at frequencies $(0, 1)$, $(1, -1), (1, 0)$, and $(1, 1)$ in decreasing order of their magnitude. Henceforth, when peaks/troughs are reported they will be arranged in decreasing/increasing order according to their magnitudes. Collectively these frequencies contribute approximately 87% of the power present in the periodogram. Hence one can infer that the lattice pattern is composed of sinu-

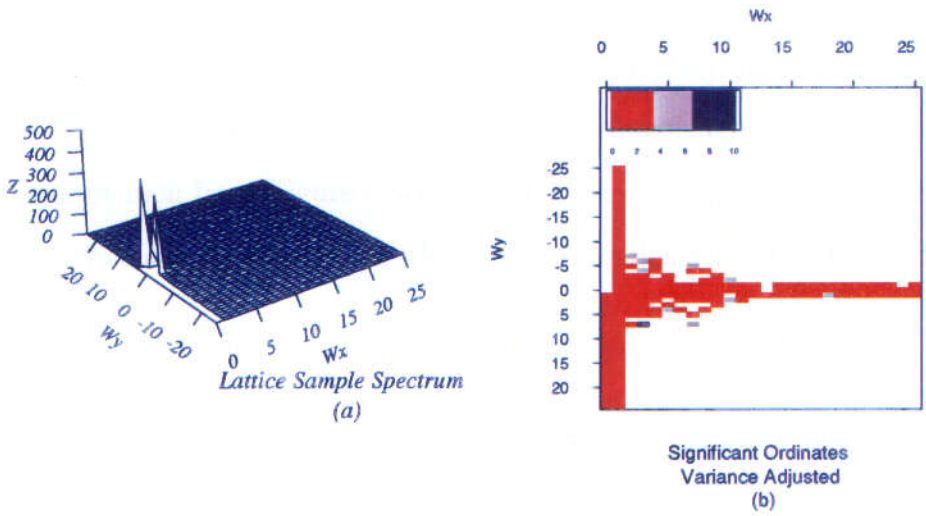

Figure 6.4: (a) Raw auto-periodogram of the altitude pattern; (b) significant ordinates of (a) using Fisher's test with adjusted variance at the 1%, 5%, and 10% levels, the value of the ordinate indicates the percentage level of significance.

soidal waves repeating once in the WE and SN directions, diagonally at an angle of 45° and also at an angle of 135° from the x-axis. The diagonal patterns correspond to waves travelling from the south-west to the north-east and from the south-east to the north-west of the study region. Note that the magnitude of the pattern repeating across the SN direction is relatively greater than the other patterns detected.

The significance of the different periodogram ordinates using the 1%, 5%, and 10% critical values of Fisher's test (as described in Section 1.12) is provided in Figure 6.4(b). From this figure one can conclude that all the peaks mentioned above are significant at the 1% level. However, other ordinates mostly across the frequency bands $p = 0, 1, 2$ and $q = -2, \ldots, 2$

are detected as significant at this level (see the comment in Section 2.5.1.3 about tapering).

The magnitude of the (scaled) periodogram (defined in Section 1.9.2) ordinates does not exceed one for most of the additional significant frequencies. This can be seen from Figure 6.5(a) which gives a categorised representation of the lattice auto-periodogram where the categories are defined as follows.

1. Values exceeding 100 are assigned to category 1.
2. Values between 10 and 100 are assigned to category 2.
3. Values of the lattice periodogram between 1 and 10 are assigned to category 3.
4. Values less than 1 are set to be not available on the graph.

The importance of the value one is that under the null hypothesis of CSR the expected value of the (scaled) periodogram is unity. Furthermore, the total power contributed by all the frequencies with value less than one is approximately 2.3%. Therefore, the detection of frequencies with magnitude less than one is spurious and might be due to the repeated use of Fisher's test.

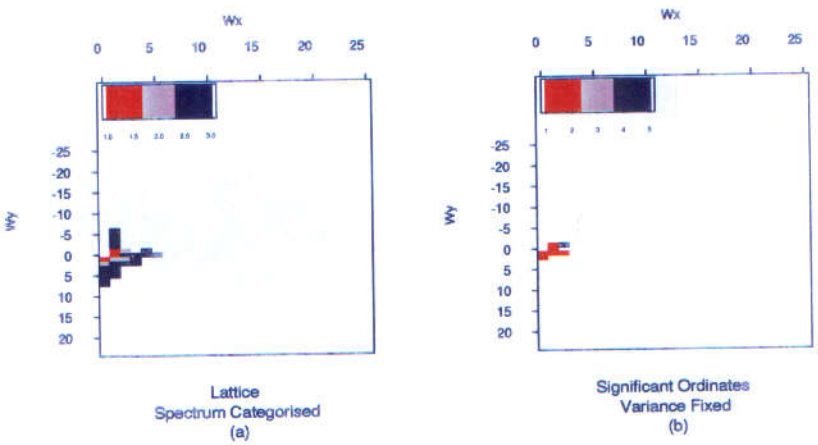

Figure 6.5: (a) Altitude lattice spectrum, Figure 6.4(a), divided into three categories, where 1 corresponds to the periodogram values greater than 100, 2 corresponds to those between 10 and 100 and 3 corresponds to those between 1 and 10; (b) significant ordinates of the auto-periodogram for altitude using Fisher's test with fixed variance at the $1, 5, 10\%$ levels.

In Whittle's extension of Fisher's test when testing for the significance of the maximum ordinate, the second greatest ordinate, and so forth the variance is adjusted according to the sample available after discarding the maximum-significant ordinate. However, under the null hypothesis of white noise all the periodogram ordinates contribute the same power and are equal to the variance. Thus, one might estimate the variance from all the periodogram ordinates, and use this estimate as the variance throughout the repeated application of Fisher's test rather than adjusting the variance for each application of the test. Figure 6.5(b) gives the significant ordinates at the 1%, 5%, and 10% levels using the same variance for all the ordinates being tested. From this figure we note that the spurious ordinates are no

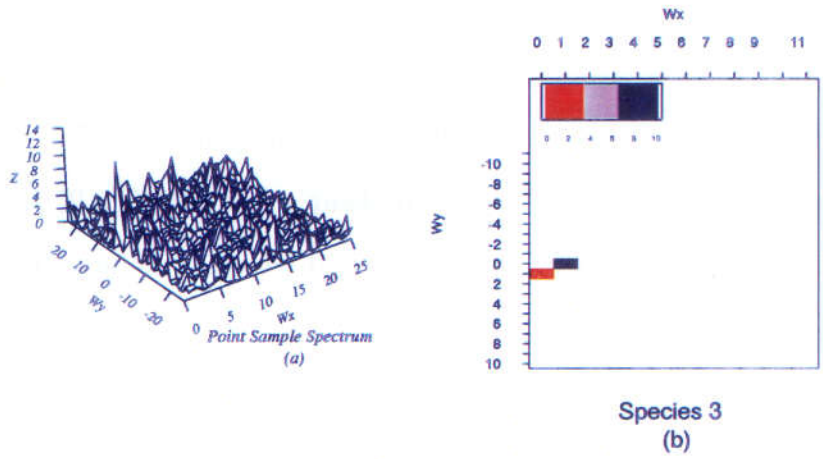

Figure 6.6: (a) Raw auto-periodogram of the point pattern; (b) significant ordinates for the point spectrum of Mahot Noir.

longer detected as significant at the levels investigated. In fact, the significant peaks detected at the 1% level are $(0,1)$, $(1,-1)$, $(1,0)$, $(1,1)$, $(0,2)$ and $(2,1)$.

Figure 6.6(a) represents the sample spectrum of the point pattern. This graph exhibits peaks at the frequencies $(0,1)$ and $(1,0)$. The former peak is significant at the 1% level whereas the latter is significant at the 10% level, see Figure 6.6(b). Therefore, one might conclude that Mahot Noir trees tend to form one big cluster along the SN direction. Note that the number of frequencies investigated is restricted by the number of events of the species.

The co-spectrum for the point-lattice pattern is presented in Figure 6.7(a). It is almost zero everywhere except for troughs at the frequencies $(0,1)$, $(1,-1)$ and $(1,0)$. The troughs indicate that the in-phase components of the pattern

are negatively correlated. Therefore, the intensity of the trees is negatively correlated with altitude with fewer trees at higher altitudes. This coincides with the pattern visible in Figure 6.3.

Figure 6.7(b) is the graph of the quadrature spectrum. This figure has troughs at $(0,1),(1,0)$ and a peak at $(1,0)$. Thus the two components are out of phase and one expects that a phase shift exists between the two components.

No specific information can be extracted from the full phase spectrum, Figure 6.7(c), due to its erratic behaviour. This behaviour is a result of the coherency spectrum, Figure 6.7(d), being almost zero except at low frequencies. Figures 6.8 and 6.9 represent the profiles of the coherency spectrum together with the corresponding upper 1% and 5% critical points of the F distribution. These figures confirm that the coherency is zero for almost all frequencies except for $p = 0, 1, 2$ and $q = 0, 1, 2$ and some sparse higher frequencies. However, we will focus only on the lower frequencies since both lattice and point spectra have their power concentrated at low frequencies.

Having established the range where the point and lattice patterns are correlated, we investigate the phase spectrum across this range. Figures 6.10(a) and (b) represent the profiles for the adjusted phase spectra in the WE and SN directions, respectively, for the frequency band $p = 0, 1, 2$ and $q = 1, 2, 3$. The profiles indicate that there is a phase shift between the two components of the point-lattice pattern. The mean value of the slope in the WE direction is 2.2 and in the SN direction is -0.83. Thus the point pattern is to the west of the lattice pattern by 2.2 pixels ($2.2 \times 5\text{m} = 11\text{m}$ on the original scale) and to its north by 0.83 pixels ($0.83 \times 5\text{m} = 4.15\text{m}$ on the original scale).

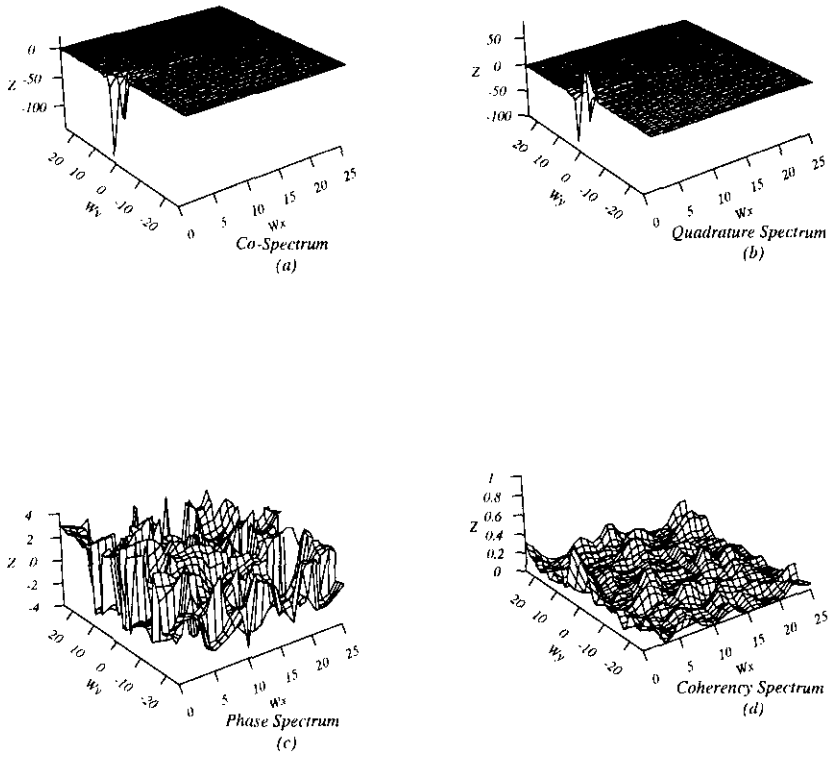

Figure 6.7: Cross-spectra for Mahot Noir versus altitude pattern: (a) and (b) raw co- and quadrature spectra; (c) and (d) smoothed phase and coherency spectra using Method A four times.

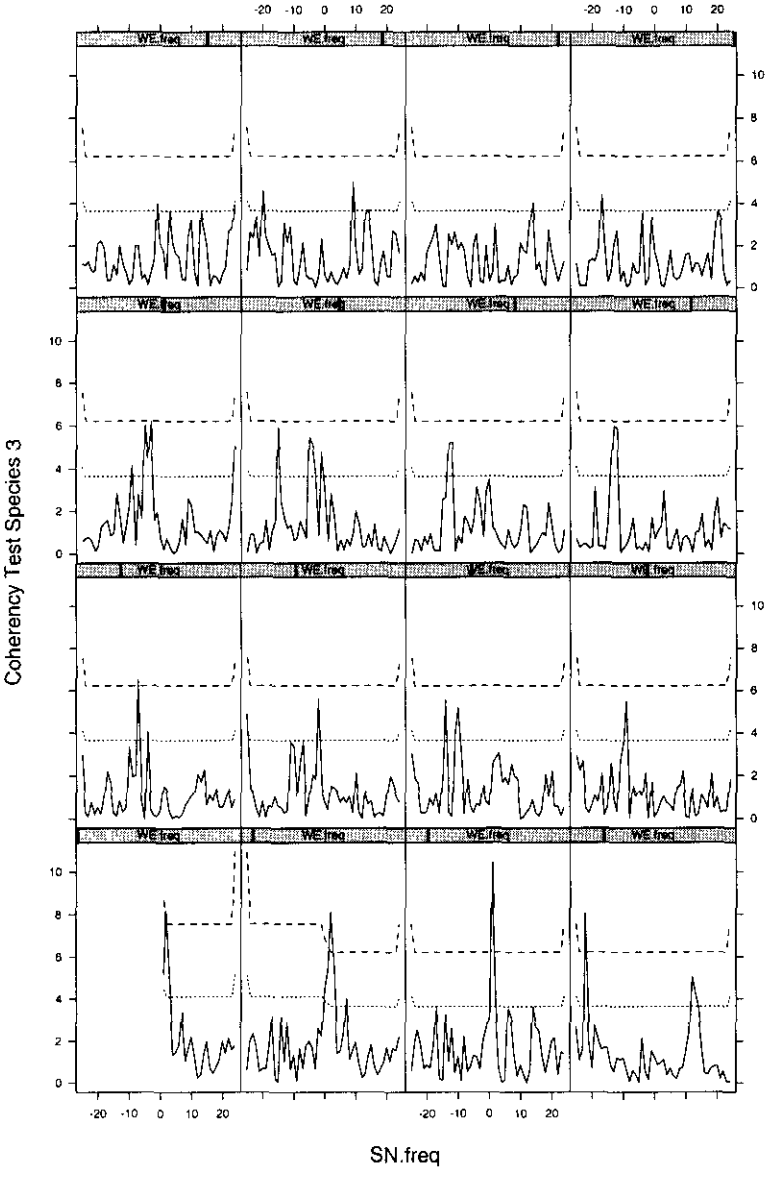

Figure 6.8: Profile of the zero coherency test statistic spectrum for Mahot Noir versus altitude, solid line, and the corresponding upper 1% and 5% critical points of the F distribution, dashed and dotted line. The far left panel of the bottom row corresponds to $p = 0$, the second left panel of the bottom row corresponds to $p = 1$, and so forth so that the far right panel of the top row corresponds to $p = 15$.

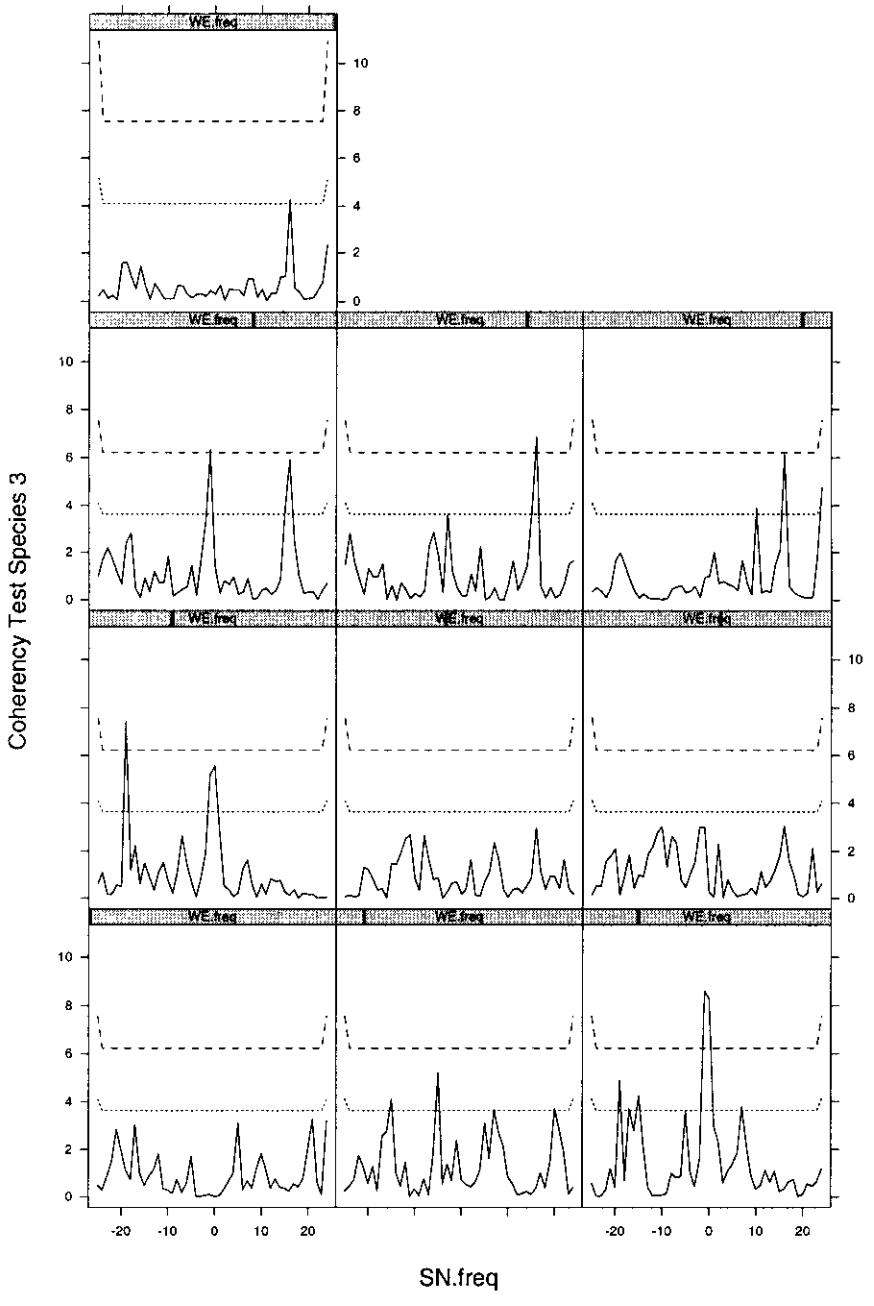

Figure 6.9: Profile of the zero coherency test statistic spectrum for Mahot Noir versus altitude, solid line, and the corresponding upper 1% and 5% critical points of the F distribution, dashed and dotted line, for $p = 16, \ldots, 25$. The far left panel of the bottom row corresponds to $p = 16$.

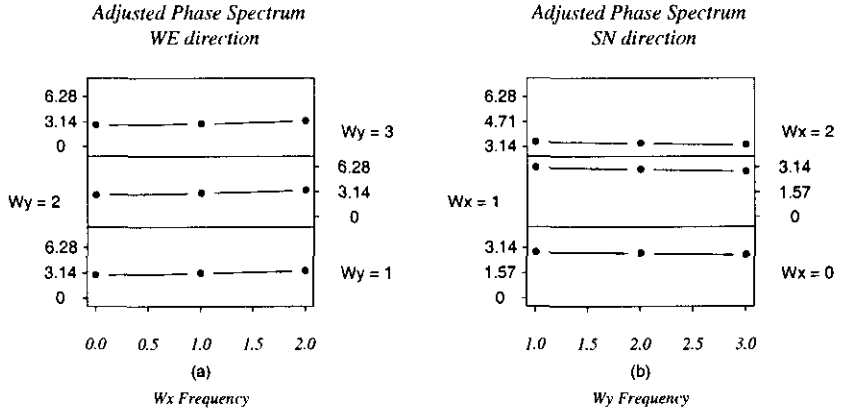

Figure 6.10: (a) and (b) Profiles of the adjusted phase spectra in the WE and SN directions for the frequency band $p = 0, 1, 2$ and $q = 1, 2, 3$, respectively.

Using the techniques of Section 3.2, the phase shift estimate is approximately 0.86 in the WE direction and -0.65 in the SN direction. These estimates were based on using the Hamon and Hannan weights. The difference between the two sets of estimates is attributed to the fact that the first set of estimates is based on the smoothed and adjusted phase spectrum, whereas the second set is based on the unsmoothed phase spectrum. Henceforth, we will use the Hamon and Hannan weights (see Section 3.2), unless otherwise stated. The reason for this choice is that the frequency bands of interest within the phase spectrum are chosen according to the zero-coherency test statistic which is equivalent to the Hamon and Hannan weights.

For illustration puposes, we discretise the pattern of Mahot Noir using LBL, see Figure 6.11(a), and study the cross-spectral properties of the discretised pattern and altitude. The auto-periodogram of the discretised pattern is

shown in Figure 6.11(b). The associated cross-spectra of the discretised pattern and altitude (a lattice-lattice pattern) are presented in Figures 6.11(c) to (f). These figures resemble those of the point-lattice pattern. No significant features are detected in these figures that were not detected using the point-lattice pattern. For this reason and in order not to overload the reader with too many figures, thereafter, we will not attempt to produce similar analyses of discretised patterns for the other species.

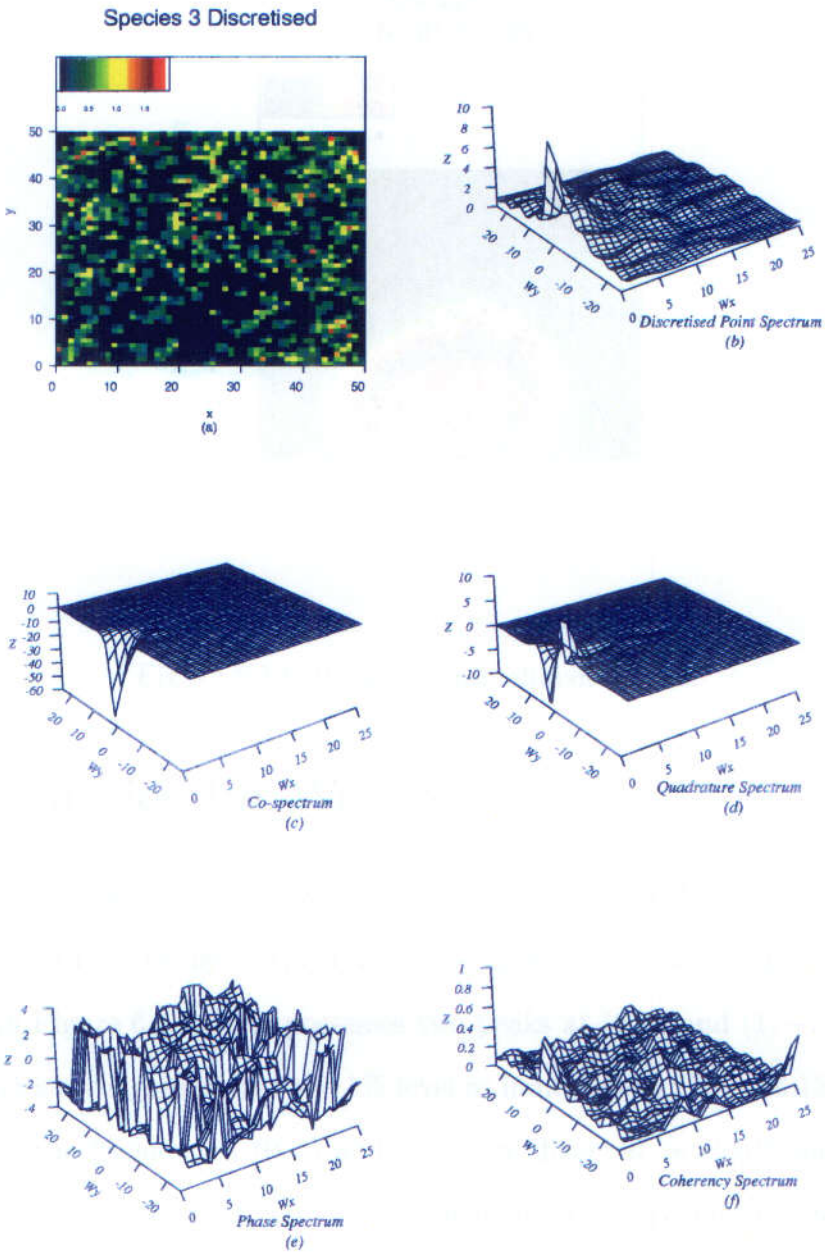

Figure 6.11: (a) Discretised pattern of Mahot Noir using LBL; (b) auto-periodogram of the discretised pattern; (c) to (f) co-, quadrature, phase and coherency spectra for the discretised pattern and altitude.

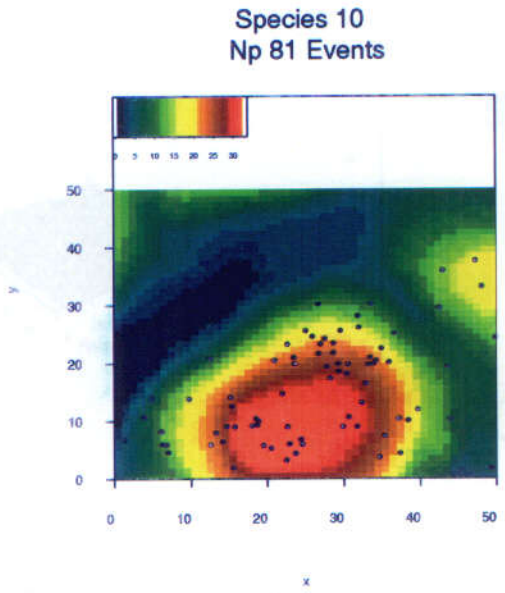

Figure 6.12: Wacapou versus altitude pattern.

6.3 Species 10: Wacapou

Figure 6.12 gives the locations of the active timber tree Wacapou superimposed on altitude values. The auto-periodogram of the point pattern is presented in Figure 6.13(a). It possesses two peaks at $(0, 1)$ and $(1, -1)$. These frequencies are significant at the 1% level as indicated by Figure 6.13(b). In addition, the frequencies $(0, 3)$ and $(1, 0)$ are detected as significant at the 1% and 5% levels, respectively. Thus Wacapou trees aggregate in one cluster along the SN direction which in turn is formed by smaller clusters as suggested by the significance of the frequency $(0, 3)$. The trees are also clustered diagonally along the south-west to north-east direction.

The peaks in the co-spectrum, Figure 6.14(a), occur at $(0, 1), (1, -1)$ and

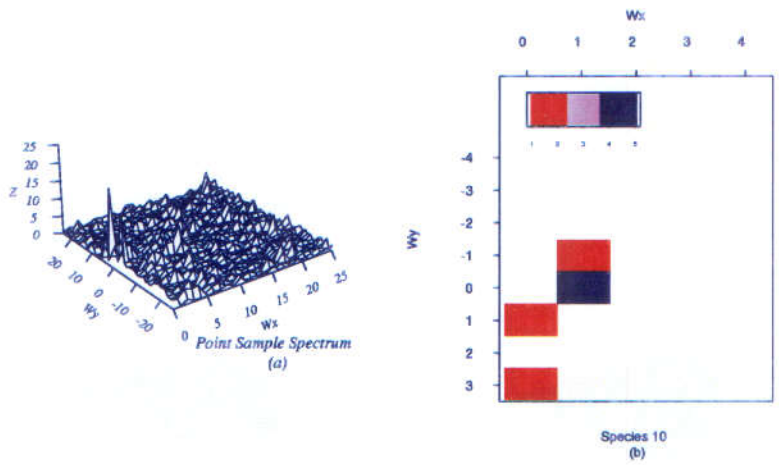

Figure 6.13: (a) raw auto-periodogram of the point pattern; (b) significant ordinates for the point spectrum of Wacapou.

$(1, 0)$. The quadrature spectrum, Figure 6.14(b), exhibits a major peak at $(0, 1)$ and a trough at $(1, -1)$. Thus Wacapou trees favour high altitudes and the two components are out of phase.

Figure 6.14(d) represents the coherency spectrum. The profile of the zero coherency test statistic is provided in Figures 6.15 and 6.16. These figures indicate that the coherency spectrum is significantly different from zero for the frequencies $(p = 0, q = \{1, 2\})$, $(p = 1, q = \{-2, \ldots, 2\})$ and $(p = 2, q = \{-2, -1, 0\})$. However, for most of the other frequencies the coherency spectrum is almost zero. This explains the erratic behaviour of the phase spectrum in Figure 6.14(c).

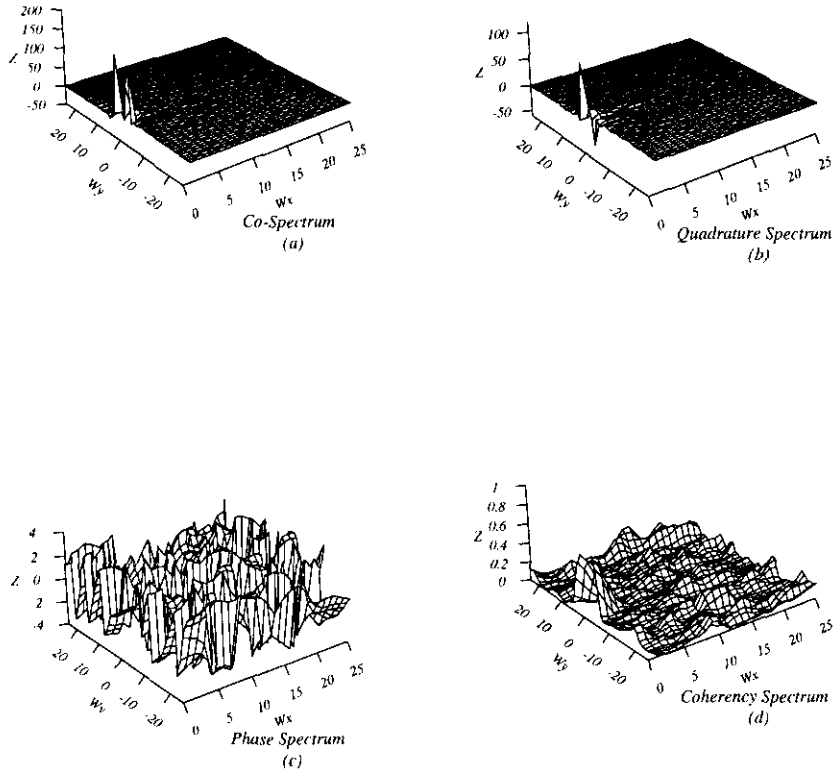

Figure 6.14: Cross-spectra for Wacapou versus altitude pattern: (a) and (b) raw co- and quadrature spectra; (c) and (d) smoothed phase and coherency spectra using method A four times.

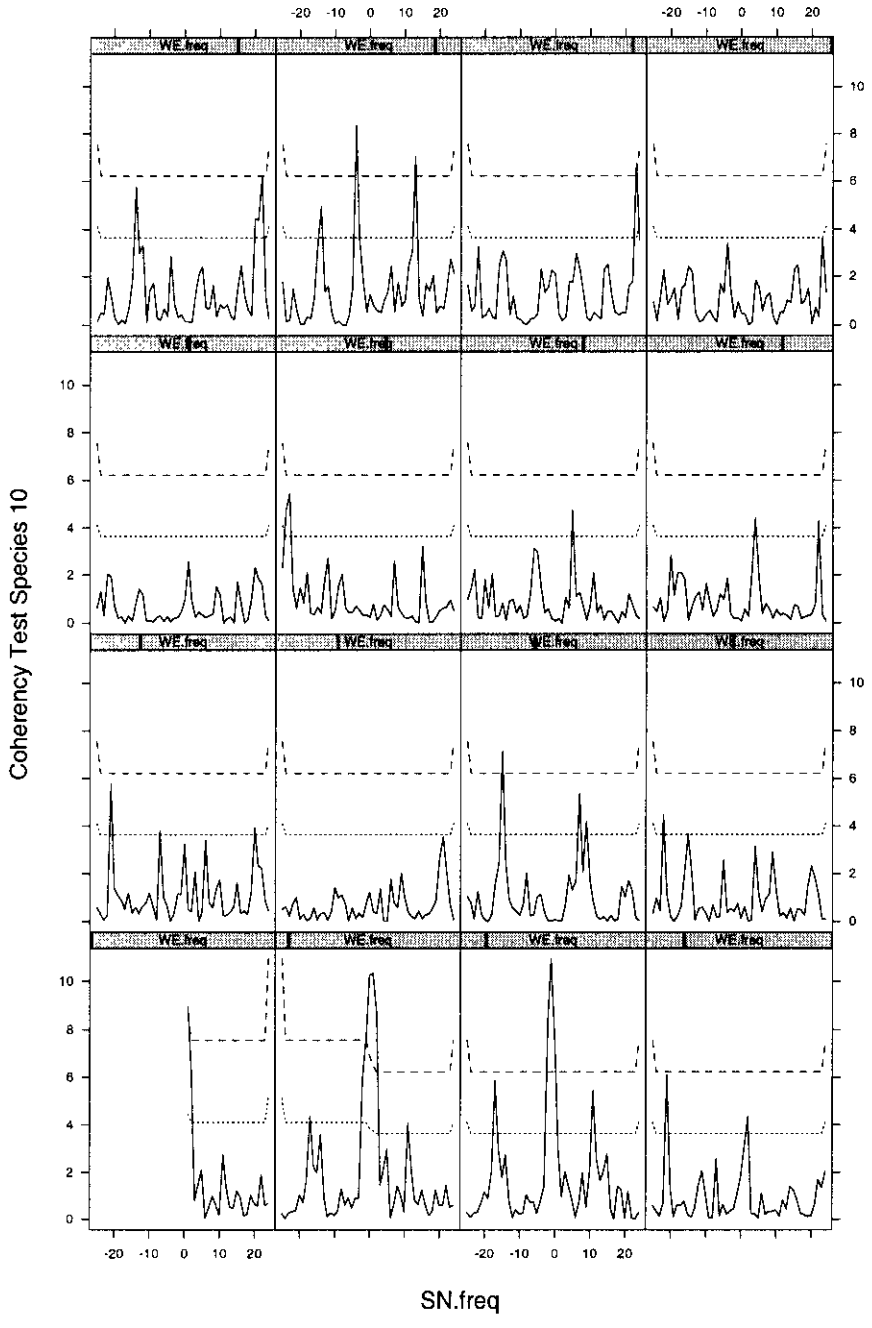

Figure 6.15: Profile of the zero coherency test statistic spectrum for Wacapou versus altitude pattern, solid line, and the corresponding upper 1% and 5% critical points of the F distribution, dashed and dotted line, for $p = 0, \ldots, 15$. The far left panel of the bottom row corresponds to $p = 0$.

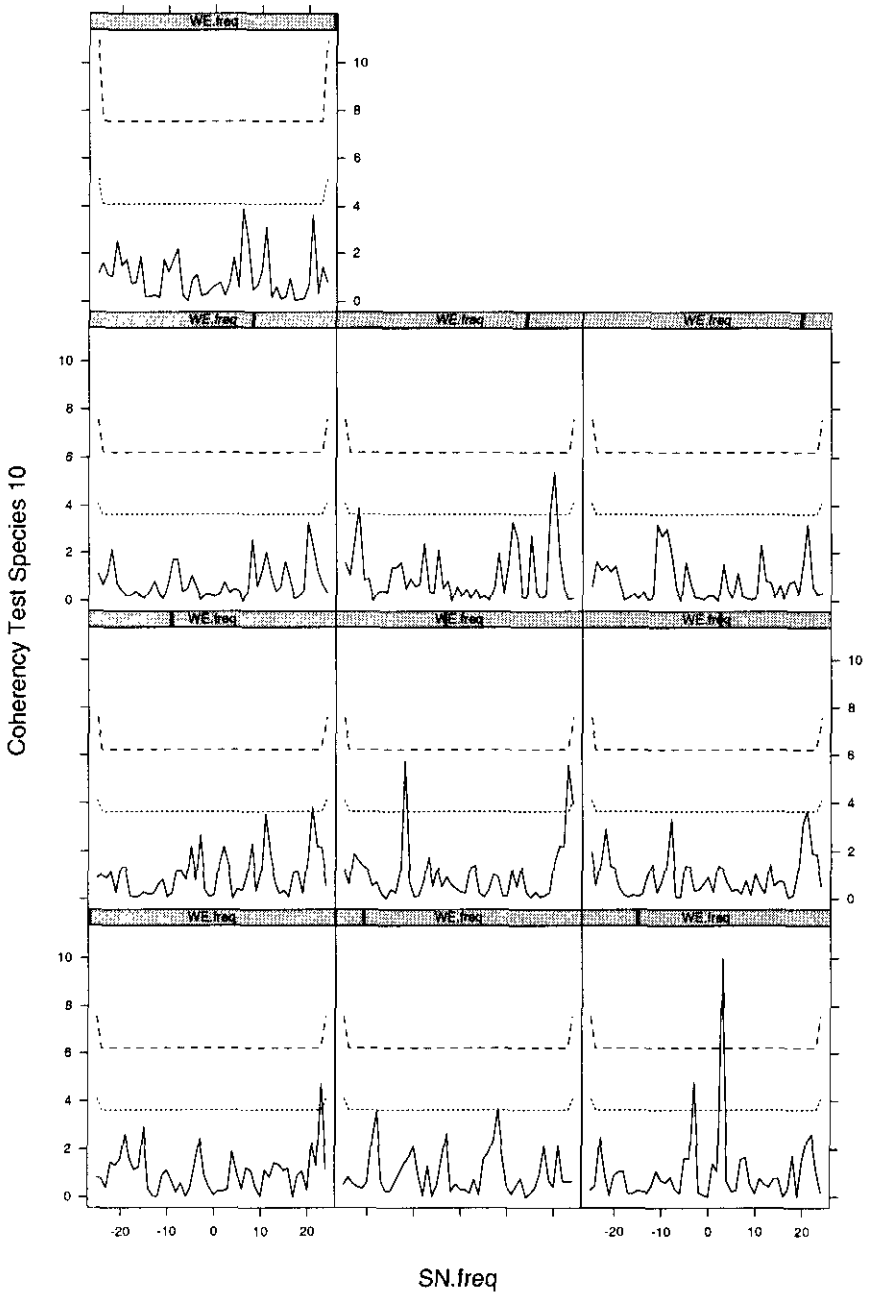

Figure 6.16: Profile of the zero coherency test statistic spectrum for Wacapou versus altitude pattern, solid line, and the corresponding upper 1% and 5% critical points of the F distribution, dashed and dotted line, for $p = 16, \ldots, 25$. The far left panel of the bottom row corresponds to $p = 16$.

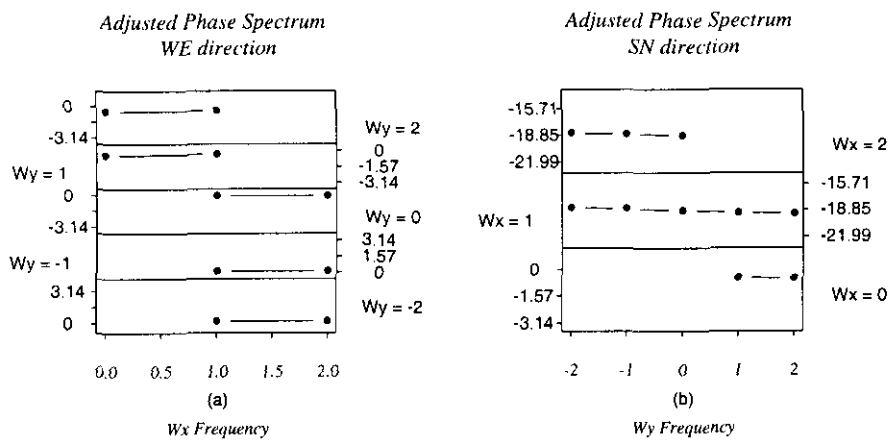

Figure 6.17: (a) and (b) Profiles of the adjusted phase spectra for Wacapou versus altitude pattern in the WE and SN directions for the frequencies $(p = 0, q = \{1, 2\})$, $(p = 1, q = \{-2, \ldots, 2\})$ and $(p = 2, q = \{-2, -1, 0\})$.

Figures 6.17(a) and (b) represent the profiles of the adjusted phase spectra for Wacapou versus altitude pattern in the WE and SN directions for the frequencies $(p = 0, q = \{1, 2\})$, $(p = 1, q = \{-2, \ldots, 2\})$ and $(p = 2, q = \{-2, -1, 0\})$. The magnitudes of the slopes in the WE direction for the frequencies with $q = -2, \ldots, 2$, are approximately 0, 0.04, 0.12, 1.1, and 0.55, respectively. The slopes in the SN direction are approximately -0.28, -1.51 and -1.14 for the frequencies with $p = 0, 1, 2$, respectively. Thus, the Wacapou pattern is to the west of the altitude pattern by an average of 1.81m for low significant frequencies, and to the north of the altitude pattern with a mean phase shift of approximately 6.6m for frequencies with $p = 1, 2$. The estimates based on phase correlation techniques are 0.216 pixels in the WE direction and -0.525 in the SN direction.

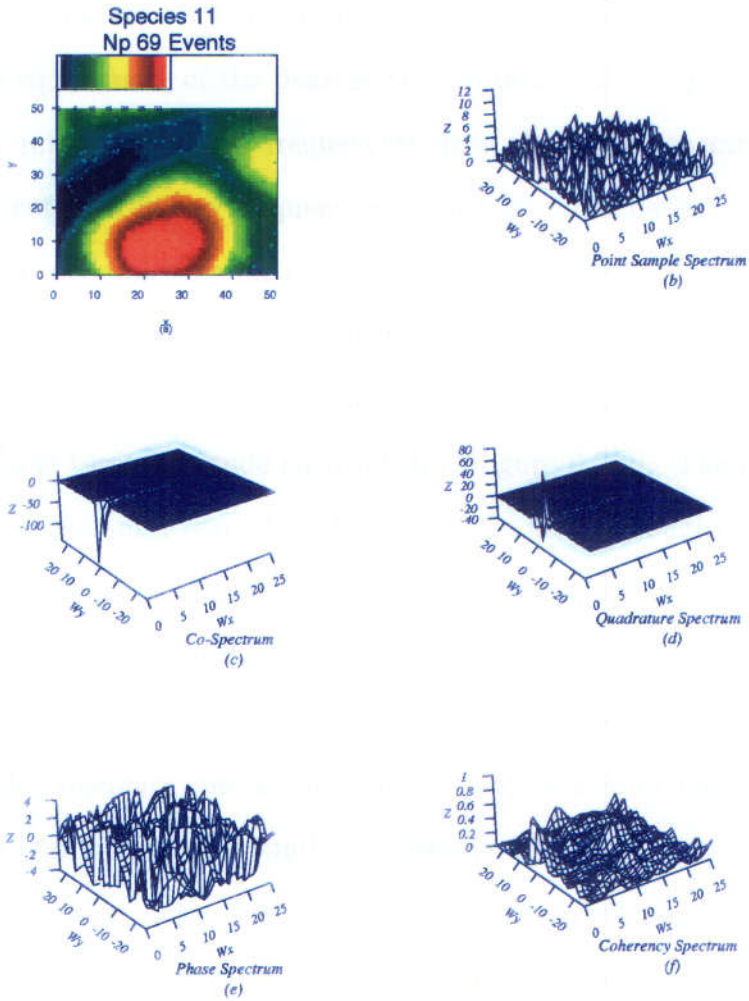

Figure 6.18: (a) Mahot Rouge versus altitude pattern; (b) raw auto-periodogram of the point pattern; (c) and (d) raw co- and quadrature spectra, (e) and (f) smoothed phase and coherency spectra using Method A four times.

6.4 Species 11: Mahot Rouge

The graph of Mahot Rouge versus altitude pattern is presented in Figure 6.18(a). The sample auto-spectrum for the point pattern, Figure 6.18(b), has peaks at $(2, -21), (0, 1)$ and $(1, 0)$. The frequency at $(0, 1)$ is significant at the 1% level whereas that at $(1, 0)$ is significant at the 5% level. However,

the number of events of Mahot Rouge is 69 which hinders the possibility of testing the significance of the peak at the frequency $(2, -21)$. Moreover, we are mainly interested in low frequencies since the lattice spectrum has its power concentrated at low frequencies. Thus the point pattern resembles a cluster process completing one cycle in both the SN and WE directions.

The troughs at $(0, 1)$ and $(1, 0)$ in the co-spectrum, Figure 6.18(c), imply that the trees favour low altitude values. These troughs coincide with those of Mahot Noir versus altitude co-spectrum, Figure 6.7(c). The peak in the quadrature spectrum, Figure 6.18(d), at $(1, -1)$ and the troughs at $(1, 0)$ and $(0, 1)$ indicate that the two components are out of phase.

Despite the discontinuities in the phase spectrum, Figure 6.18(e), a positive slope is observed along the SN direction for frequencies with low p values. Note that the coherency spectrum, Figure 6.18(f), is close to one around these frequencies and fluctuates around zero elsewhere.

The profile of the zero coherency test and the corresponding upper 1% and 5% critical points of the F distribution for the frequencies $p = 0, \ldots, 15$ and $q = -25, \ldots, 24$ conditional on the WE frequencies are presented in Figure 6.19. This figure indicates that for low frequencies the coherency is significantly different from zero at the 5% significance level around $(p = \{0, \ldots, 4\}, q = \{0, 1\})$ and $(p = \{0, 1\}, q = 2)$.

The adjusted phase spectra in the WE and SN directions for the frequencies $(p = \{0, \ldots, 4\}, q = \{0, 1\})$ and $(p = \{0, 1\}, q = 2)$ are given in Figure 6.20. A positive slope is detected in the WE direction for the frequencies $q = 0, 1$, and its mean value is 0.21. The slope in the SN direction has a mean value of approximately -1.41 for the frequencies $p = 1, \ldots, 4$. Thus

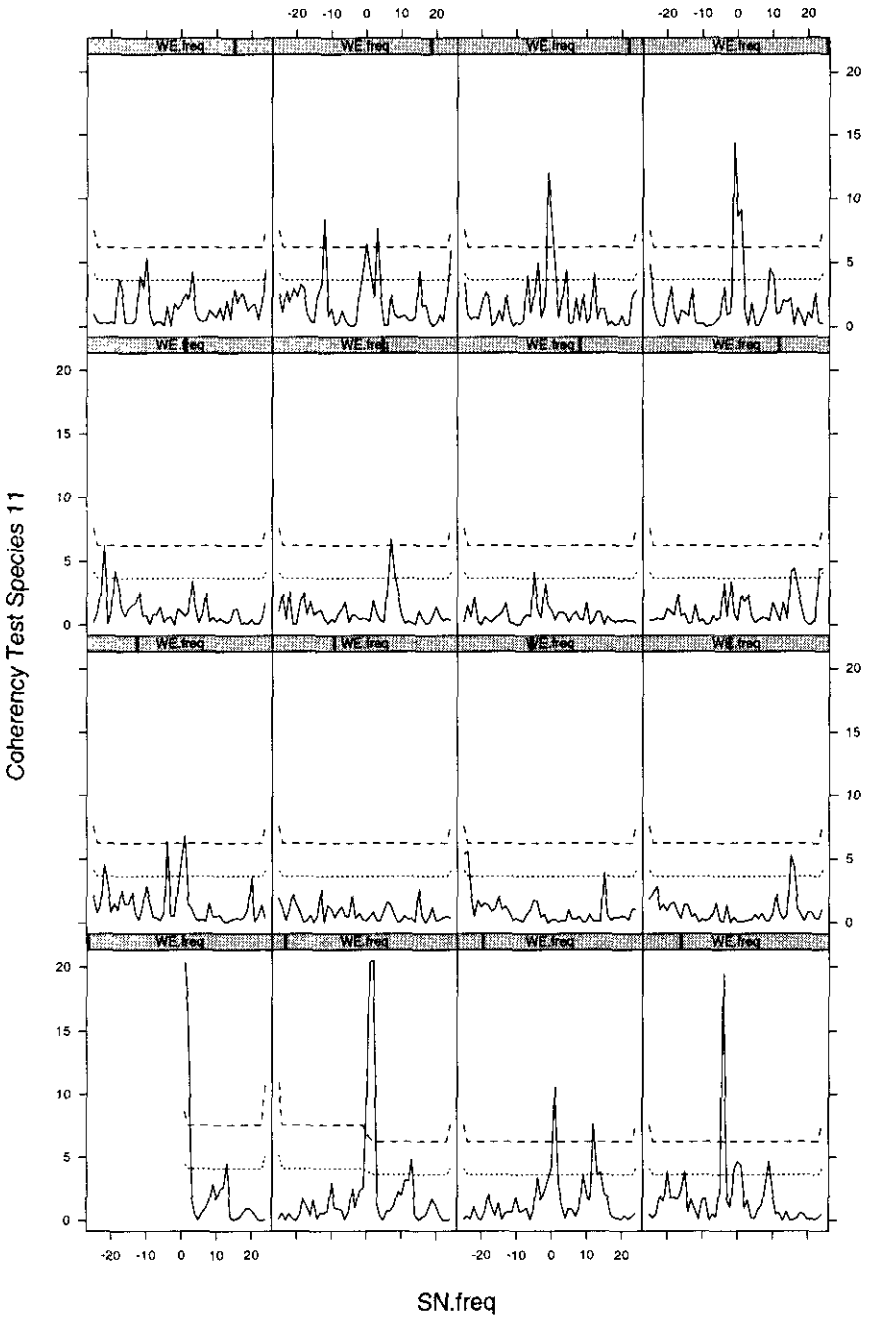

Figure 6.19: Profile of the zero coherency test statistic spectrum for Mahot Rouge versus altitude pattern, solid line, and the corresponding upper 1% and 5% critical points of the F distribution, dashed and dotted line, for $p = 0, \ldots, 15$. The far left panel of the bottom row corresponds to $p = 0$.

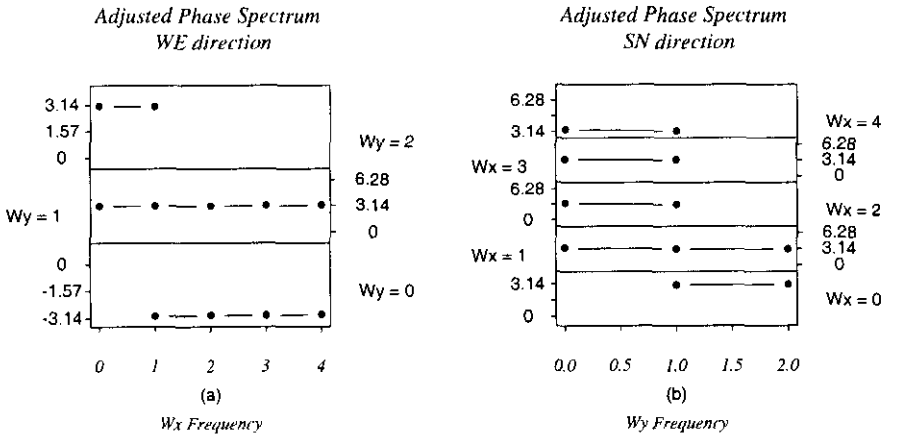

Figure 6.20: (a) and (b) Profiles of the adjusted phase spectra for Mahot Rouge versus altitude pattern in the WE and SN directions for the frequencies ($p = \{0, \ldots, 4\}, q = \{0, 1\}$) and ($p = \{0, 1\}, q = 2$).

on average the Mahot Rouge pattern is to the west of the altitude pattern by 1.05m and to its north by 7.05m. The estimates of the slopes in the WE and SN directions based on the phase correlation techniques are 0.855 and -1.206, respectively.

6.5 Species 12: Carapa

The graph of Carapa versus altitude pattern is presented in Figure 6.21(a). Peaks of the auto-periodogram of the point pattern, Figure 6.21(b), are detected at $(18, -12)$ and $(1, -1)$. The number of Carapa trees is 61 which implies that one can test the significance of the frequencies $(p = \{0, \ldots, 3\}, q = \{-3, \ldots, 2\})$. The frequency $(1, -1)$ is the only significant peak at the 1% level. The test was also carried out at the 10% level of significance but no other frequency was detected as significant. Therefore, the Carapa pattern completes 1.41 cycles in the unit square along the direction of the 135° angle from the x-axis.

The troughs at $(1, -1)$ and $(0, 1)$ in the co-spectrum, Figure 6.21(c), indicate that the intensity of the trees and altitude values are negatively correlated. Hence Carapa trees favour relatively low altitude. The two components are out of phase as indicated by the peaks in the quadrature spectrum, Figure 6.21(d), at $(0, 1)$ and $(1, -1)$. The troughs of the co-spectrum coincide with the peaks of the quadrature spectrum. The phase spectrum for the ordinates where the quadrature spectrum has its peaks and the co-spectrum has its troughs therefore lies between $-\pi$ and $-\pi/2$.

The phase and coherency spectra are given in Figures 6.21(e) and (f), respectively. The coherency spectrum fluctuates around zero for most frequencies except for frequencies with low p and q. However, the profile of the zero coherency test statistic, Figure 6.22, indicates that none of these frequencies is significant at the 1% level and only a few number of low frequencies are significant at the 5% level. Thus the negative correlation between the two

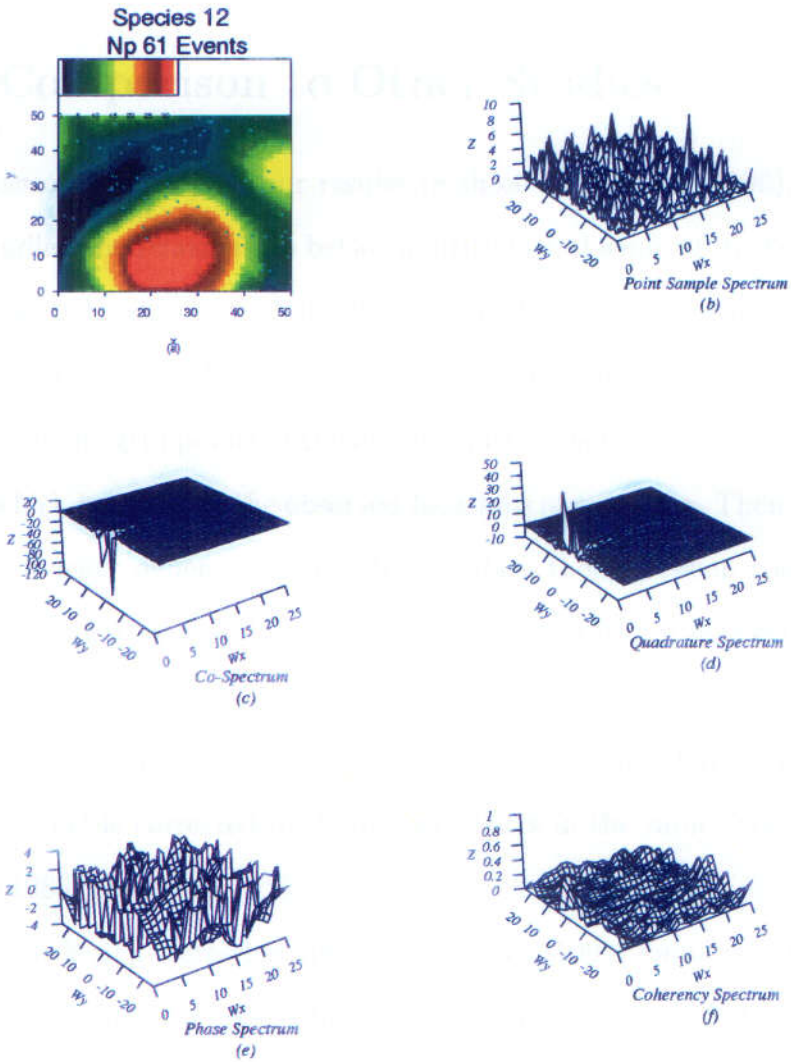

Figure 6.21: (a) Carapa versus altitude pattern; (b) raw point periodogram; (c) and (d) raw co-and quadrature spectra; (e) and (f) smoothed phase and coherency spectra using Method A four times.

components which is detected by the co-spectrum is weak. No further analysis of the phase spectrum will be carried out due to the lack of significant frequencies in the coherency spectrum.

6.6 Comparison to Other Studies

In this section we compare our results to those of Dessard (1996). Dessard (1996) studied the relationship between altitude and some of the tree species based on kernel regression of the intensity of the tree species on the grid of altitude values. In brief, Dessard (1996) proceeds by first estimating local intensities at the grid points of the altitude lattice using a kernel intensity estimator which is based on the observed locations of a species. Then assuming that the intensity depends on the altitude data the regression coefficient is calculated using a weighted kernel intensity estimator, not necessarily equal to the one used in the first step, where the weights are taken to be equal to the estimated intensities calculated in the first step. Furthermore, this weighted kernel is corrected for boundary effects in the same way as that of Diggle's (1985) correction.

Using the kernel regression approach Dessard (1996) found that the intensity of Mahot Rouge decreases quite rapidly with altitude, and that Wacapou prefers dry soils which is a characteristic of high altitude. These results agree with the results of our spectral approach with regard to the relationships between both species and altitude. In Section 6.3 and Section 6.4 we found that Wacapou favoured high altitudes whereas Mahot Rouge favoured relatively low altitudes. These conclusions are mainly based on the information provided by the co-spectrum of each species and altitude. Further information

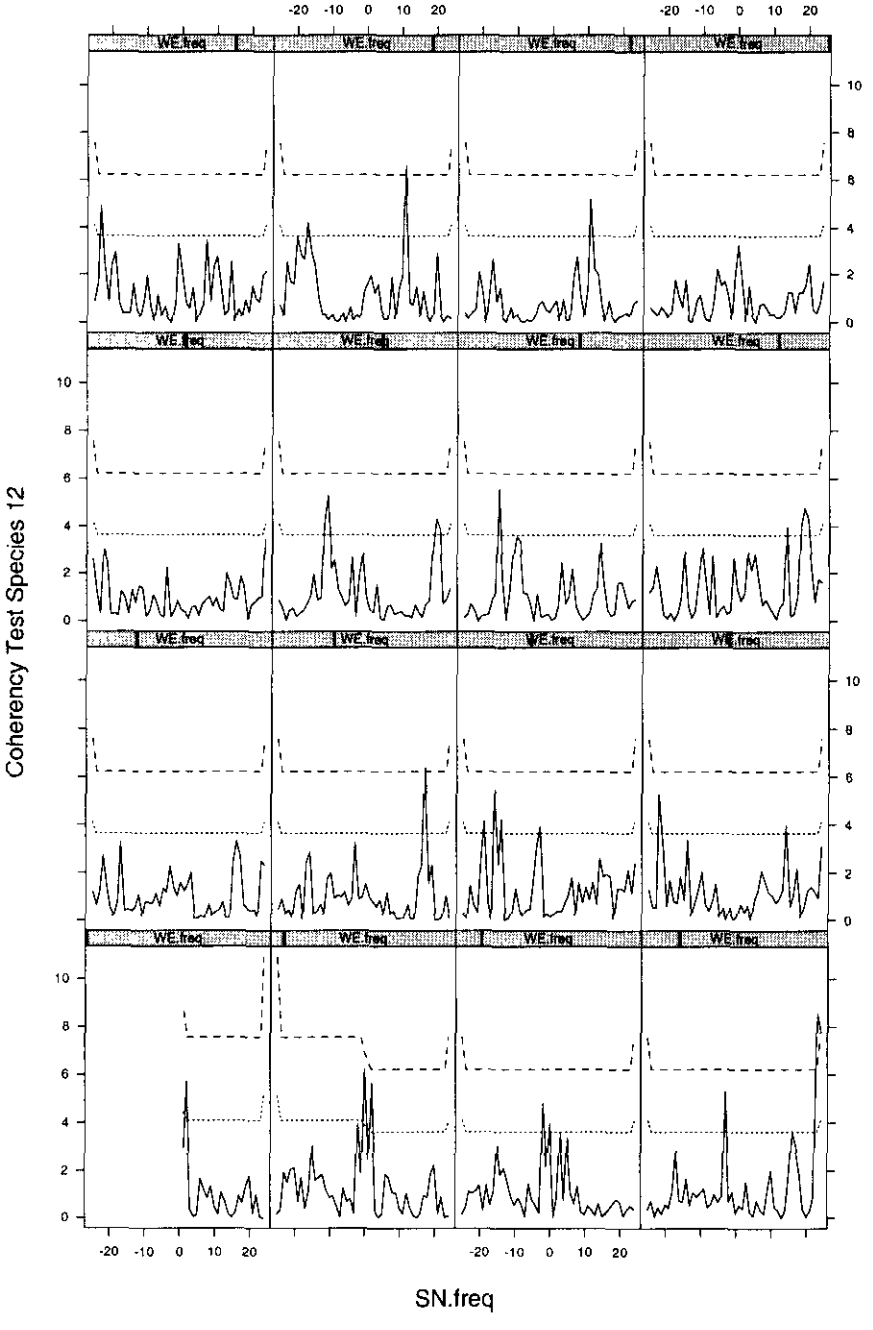

Figure 6.22: *Profile of the zero coherency test statistic spectrum for Carapa versus* altitude pattern, solid line, and the corresponding upper 1% and 5% critical points of the F distribution, dashed and dotted line, for $p = 0, \ldots, 15$. The far left panel of the bottom row corresponds to $p = 0$.

about the relationship between the species and altitude has been extracted using the other spectra. Using the phase and coherency specrta we found that the two species are to the north-west of the altitude pattern but with different magnitudes. However, no such information could be extracted using the kernel regression approach. In addition, Dessard (1996) assumes that the intensity depends on altitude in order to proceed with the analysis of the two processes. No such assumption is needed in our approach.

6.7 Summary

In this chapter we have demonstrated the ability to explore the relationship between the components of a real point-lattice pattern using cross-spectral techniques. The relationships between a number of tree species and altitude were investigated. Cross-spectral analyses revealed whether or not the tree patterns were related to altitude. For Species 3, 10 and 11 we found that the point pattern is to the north-west of the lattice pattern. In addition, it was revealed that Species 3, 11, and 12 favoured relatively low altitudes whereas Species 10 favoured high altitude. In the next chapter, we will investigate another data set and discuss how to extend the techniques discussed so far in order to unveil the relationship, if any, between marked point processes and lattice processes.

Chapter 7

Cross-Spectral Analysis of African Storms

In this chapter, we will investigate a data set consisting of locations of storms in the Sahel region of Africa together with elevation values of the region. In Section 7.1 we describe the data set in more detail. In Section 7.2 marked point-lattice processes will be introduced and spectral techniques for analysing such processes will be discussed. These techniques are extensions of those used for point-lattice processes. Analysis of the storm data set using spectral tools will be provided in Section 7.3.

7.1 The Data

The Sahel region of Africa lies south of the Sahara desert. The region extends in the WE direction from the Atlantic ocean to Ethiopia and in the SN direction from 5°N to 20°N. The storm data set was collected in order to identify and understand the characteristics of convective storms, which are the sources of most of the rain in this region. The need for studying storm characteristics was highlighted by the severe droughts that devastated the

Sahel area during the early seventies and eighties. Haile (1994) collected spatial location and time of storm initiation, maximum size and dissipation from meteorological satellite imagery of the Sahel region for the month of July 1989. In addition, the data set provides duration and speed of the observed storms. Dr. Menghestab Haile of the Ethiopian Disaster Preparedness and Prevention Commission made the storm data available for this project.

Topography is thought to be one of the parameters that affect the storm life cycle. This assumption is mainly based on visual inspection of the storm location and characteristics such as the storm duration and topographical features of the region, specifically elevation from the sea surface (altitude). The mountains in the eastern side of the Sahel region are believed to affect storm duration thus giving rise to short- or long-lived storms. In the western side, which consists mainly of river plains, it is thought that no such segregation exists (see Mugglestone and Taylor, 1994). (The eastern side of the Sahel region stretches from 7.5°E to 40°E while the western side stretches between 18°W and 7.5°E.) In Mugglestone and Taylor (1994), short-lived storms are defined to be storms that lasted between six and fifteen hours and the long-lived storms are those that lasted more than fifteen hours.

Elevation data were downloaded from the GTOPO30 website. These data are derived from a global digital elevation model that is based on data from eight sources. The sources that are listed in decreasing order of percentage of the global data derived from each are: Digital Terrain Elevation Data (50%), Digital Chart of the World (29.9%), Antarctic Digital Database (8.3%), United States Geographical Survey 1-degree digital elevation model (6.7%), International Map of the World (3.7%), (American) Army Map Ser-

vice (1.1%), New Zealand digital elevation model (0.2%), and Peru Map (0.1%). The website address is http://edcwww.cr.usgs.gov/landdaac/gtopo30. The data available from this website are in the form of 16-bit binary-signed integer data. After downloading they were converted to a format acceptable to S-plus.

The elevation data in this study come from two files which collectively range from 10°S to 40°N and from 20°W to 60°E. However, in our analysis we will investigate the study region stretching from 6.446°N to 19.937°N and from 10.704°W to 36.787°E. Henceforth, this region will be referred to as Region A. Elevation data in Region A range from 35m to 3398m with mean value of 449.7m and median of 401m. Elevation in GTOPO30 is measured regularly at 30-arc seconds spacing which is approximately equivalent to one kilometre. Note that the ground distance in the WE direction (longitude) of a quadrat decreases with increasing latitude while in the SN direction it increases. For example, the WE distance of a quadrat at 10°N is equivalent to 914m and the SN distance equates to 922m, whereas at 20°N the WE distance corresponds to 872m and the SN distance to 923m. The size of the lattice corresponding to the Region A elevation data is 5700×1620. Figure 7.1 is a map of elevation data for Africa where the spacing is as before. The superimposed box defines Region A. The map was downloaded from the website of the Africa Data Dissemination Service. The address of the website is http://edcintl.cr.usgs.gov/adds.

Using spectral analysis we will explore the relationships between storm characteristics and elevation. Thus we will be able to establish the validity of the above claims regarding these relationships. However we still need to

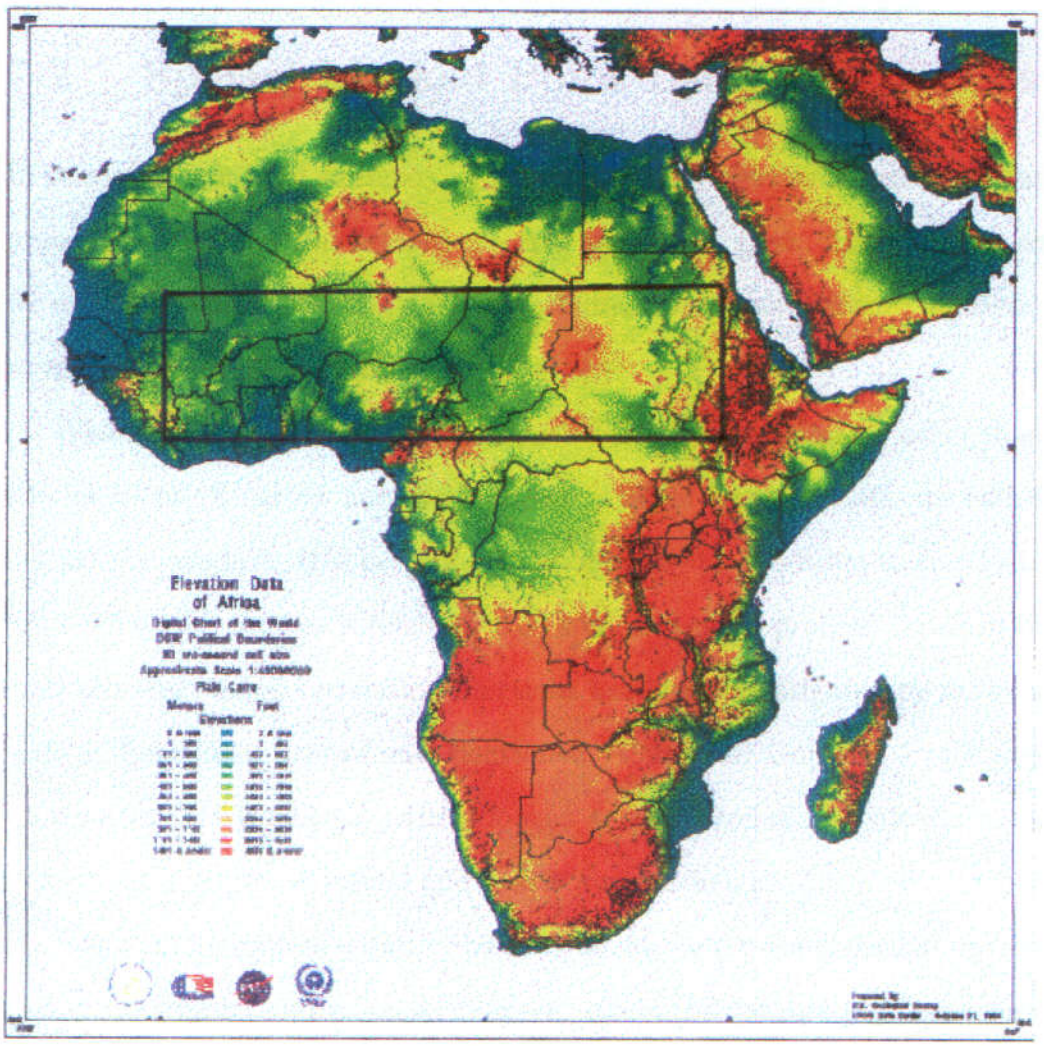

Figure 7.1: Elevation map of Africa from Africa Data Dissemination Service, see main text for details. The superimposed box defines the boundaries of our study region. Note that the high elevations correspond to bright red colours whereas low elevations correspond to dim green colours.

develop techniques to explore the relationships between point processes and their characteristics and lattice processes. In an attempt to achieve this goal, we will discuss marked point-lattice processes in the next section.

7.2 Spatial Marked Point-Lattice Processes

In this section, a brief summary of how to study properties of marked point processes using two-dimensional spectral analysis is given. Having done so we will extend cross-spectral analysis techniques from point-lattice processes to marked point-lattice processes.

When spatial point processes are investigated, measurements other than the locations of events may be recorded. Such measurements are called marks. For example, tree heights may be measured in addition to tree locations. The joint process is referred to as a marked point process. Analysis of such processes using correlation functions has been investigated by authors such as Penttinen, Stoyan and Henttonen (1992) and Goulard, Pagès and Cabanettes (1995). These articles looked at the correlations between locations of trees in forest stands and marks such as height, diameter, number of sprouts and length of crown. The analyses of the data sets carried out assumed stationarity and isotropy, however, within their theoretical framework Goulard, Pagès and Cabanettes (1995) assumed only stationarity. Renshaw (1999) used two-dimensional spectral analysis to study stationary spatial marked point processes.

Formally a marked point process is denoted by $\{M(\mathbf{a})\}$ where $\mathbf{a}$ is an event of the point process. It will be assumed that this process is stationary and that the marks are nonnegative. By analogy with point processes one

can define the first-order intensity function of this process as

$$\lambda_M(\mathbf{a}) = \lim_{|d\mathbf{a}|\to 0}\left\{\frac{\mathbb{E}(dM(\mathbf{a}))}{|d\mathbf{a}|}\right\}, \tag{7.1}$$

where $dM(\mathbf{a})$ is the sum of marks within a small neighbourhood of the event $\mathbf{a}$, and the second-order intensity function is defined as

$$\lambda_{MM}(\mathbf{a}_1, \mathbf{a}_2) = \lim_{|d\mathbf{a}_1|,|d\mathbf{a}_2|\to 0}\left\{\frac{\mathbb{E}(dM(\mathbf{a}_1)\, dM(\mathbf{a}_2))}{|d\mathbf{a}_1||d\mathbf{a}_2|}\right\}, \tag{7.2}$$

(see Cressie, 1991, chapter 8). Since the process is assumed to be stationary then λ_{MM} depends on $\mathbf{a}_1$ and $\mathbf{a}_2$ only through their difference $\mathbf{a}_1 - \mathbf{a}_2$. The mark spectral density function, $f_{MM}(\boldsymbol{\omega})$, can be defined in a similar way to the point process spectral density function. Estimates of the mark spectral density function are provided via

$$F_{MM}(\boldsymbol{\omega}) \equiv F_{MM}(\omega_p, \omega_q) = \frac{1}{N_X} F_M(p,q)\overline{F}_M(p,q). \tag{7.3}$$

Here

$$F_M(p,q) = \sum_{j=1}^{N_X} M(a_{1j}, a_{2j}) \exp\{-2\pi i(\frac{pa_{1j}}{\ell_1} + \frac{qa_{2j}}{\ell_2})\}, \tag{7.4}$$

where $(a_{1j}, a_{2j}) = \mathbf{a}_j$, $j = 1, \ldots, N_X$, are the events of the point pattern observed in the study region $[0, \ell_1] \times [0, \ell_2]$, $M(a_{1j}, a_{2j})$ is the mark associated with event $\mathbf{a}_j$, N_X is the total number of events within the study region and $(\omega_p, \omega_q) = (\frac{2\pi p}{\ell_1}, \frac{2\pi q}{\ell_2})$, (see Renshaw, 1999). The marked point process is assumed to be corrected for its mean $\overline{M} = \sum_{j=1}^{N_X} M(a_{1j}, a_{2j})/N_X$. As for the point process the marked point process has no Nyquist frequency. Likewise, the number of independent periodogram ordinates is limited by the number of events.

Note that the DFTs of point and lattice processes are special cases of (7.3). The point process can be obtained by substituting one in place of the mark, M. The lattice process is a marked point process with events occurring at the grid points of the lattice and marks the value of the lattice process at these events.

A model for a marked point process that exhibits CSR would have marks that are IID random variables and are independent of the associated point process. An example of such a process is provided by considering the *compound Poisson process* that has IID marks that are positive integers and events that form an HPP (see Cressie, 1991). Alternative models to CSR are also given in Cressie (1991). Renshaw (1999) simulates some models in order to study the spectral properties of marked point processes.

A *spatial marked point-lattice process* is a process with three components, namely, the marks associated with the point process, the point process itself and the lattice process. We denote such a process by $Z(\mathbf{a}) = \{M(\mathbf{a}), N_X(\mathbf{a}), Y(\mathbf{a})\}$. To study the second-order spectral properties of this process we need to extend the functions defined for the point-lattice processes from two to three components.

The spectral matrix for a spatial marked point-lattice process, $\mathbf{F}_{ZZ}$, is defined as

$$\mathbf{F}_{ZZ}(\boldsymbol{\omega}) = F_Z(\boldsymbol{\omega})\overline{F_Z(\boldsymbol{\omega})}^{\top} = \begin{bmatrix} F_{MM}(\boldsymbol{\omega}) & F_{MN}(\boldsymbol{\omega}) & F_{MY}(\boldsymbol{\omega}) \\ F_{NM}(\boldsymbol{\omega}) & F_{NN}(\boldsymbol{\omega}) & F_{NY}(\boldsymbol{\omega}) \\ F_{YM}(\boldsymbol{\omega}) & F_{YN}(\boldsymbol{\omega}) & F_{YY}(\boldsymbol{\omega}) \end{bmatrix},$$

where $F_Z(\boldsymbol{\omega}) = (F_M(\boldsymbol{\omega}), F_N(\boldsymbol{\omega}), F_Y(\boldsymbol{\omega}))$, and $F_{AB}(\boldsymbol{\omega}) = F_A(\boldsymbol{\omega})\overline{F_B(\boldsymbol{\omega})}$ for $A, B = M, N, Y$. Here F_M, F_N, F_Y are the DFTs of the mark, point and lattice processes, respectively. Note that the above matrix is symmetric in the sense

that $F_{AB}(\omega) = F_{BA}(-\omega)$. Thus one needs only to study the elements of the matrix that are on and above the diagonal. Initially the range of frequencies investigated will depend on the size of the lattice process, as is the case for point-lattice processes.

Asymptotic properties for marked point-lattice processes may be derived by analogy with point-lattice processes, see Chapter 4. Defining the process of increments for the marks process as

$$M(\Delta) = \int_{\Delta} dM(\mathbf{a}),$$

where Δ is a subregion of $\mathbb{R}^2$, one can extend the results of Chapter 4 to three components rather than two.

Figure 7.2 represents a realisation of a marked point-lattice process that exhibits CSR. The lattice pattern is a realisation of white noise on a 32×32 study region. The point pattern is a realisation of an HPP. The number of events of this pattern is 1024. The marks are a realisation of a Poisson process with mean 5 and are independent from the point pattern.

The auto-spectra of the individual processes are presented in Figure 7.3. As expected power is distributed across the range of frequencies for all these spectra. None of these frequencies for the different patterns was found to be significant at the 10% level using Fisher's test.

Figure 7.4 represents the co-, quadrature and coherency spectra for the point versus lattice, mark versus lattice and mark versus point patterns. All these spectra are seen to fluctuate around zero indicating that the components of the marked point-lattice pattern are not correlated. In the next section we will analyse the storm data using spectral tools.

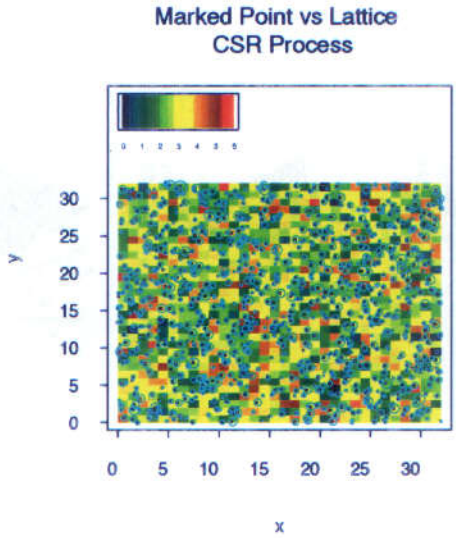

Figure 7.2: A realisation of a CSR marked point-lattice process. The circles represent the marks. The size of the circle reflects the magnitude of the mark.

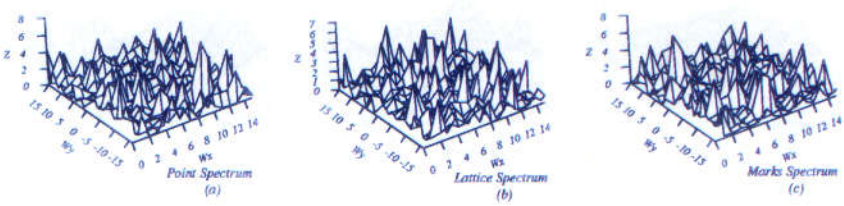

Figure 7.3: Auto-spectra for the point pattern (a), lattice pattern (b) and marks pattern (c).

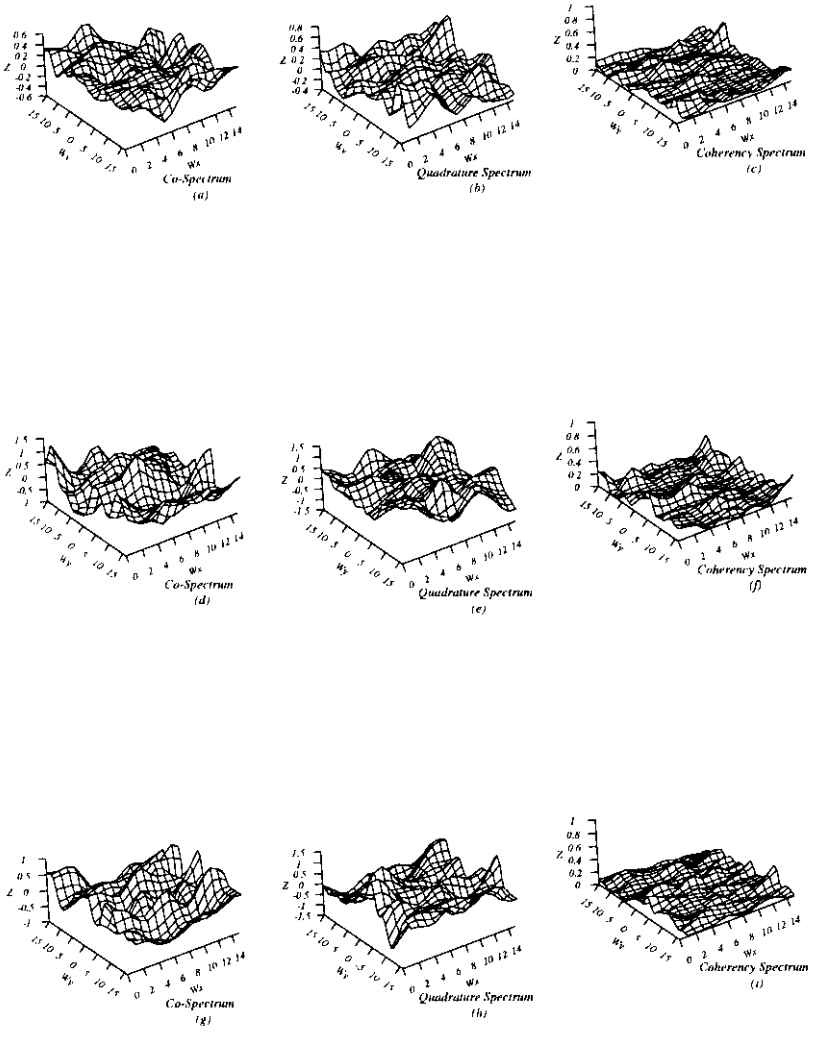

Figure 7.4: Cross-spectra for point versus lattice, first row, mark versus lattice, second row, and mark versus point, third row. Column 1 figures (a), (d) and (g) are the co-spectra; column 2 figures (b), (e) and (h) are the quadrature spectra; and column 3 figures (c), (f) and (i) are coherency spectra. All the spectra were smoothed using Method A four times.

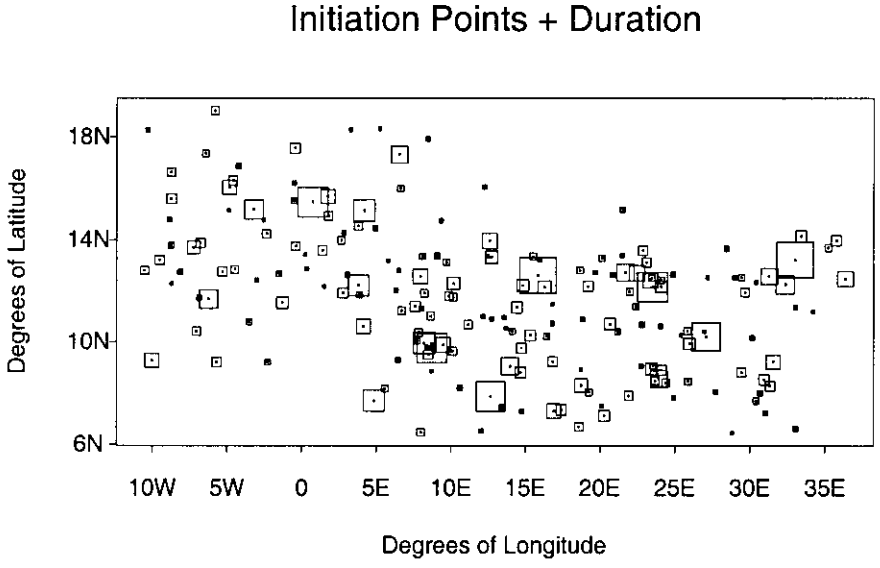

Figure 7.5: Initiation points in Region A represented as centres of the squares together with storm duration represented as size of squares. The size of the square reflects the storm duration where larger sizes imply longer durations. Storm duration ranges from 4 to 44 hours.

7.3 Cross-spectral Analysis of the Storm Data

In this section, we will investigate the relationships between storm initiation points and duration and elevation in Region A. Figure 7.5 represents initiation points in Region A as centres of squares and associated storm duration as the relative size of the squares. Storm initiation points superimposed on elevation data of this region are presented in Figure 7.6. There are 190 events of initiation within this region and the storm duration varies between 4 and 44 hours with a mean value of 10.59 and median 8. In what follows, using spectral analysis we will investigate the auto- and joint-properties of elevation data, initiation points and their duration.

Since the elevation data matrix is of dimension 5700×1620 (see Sec-

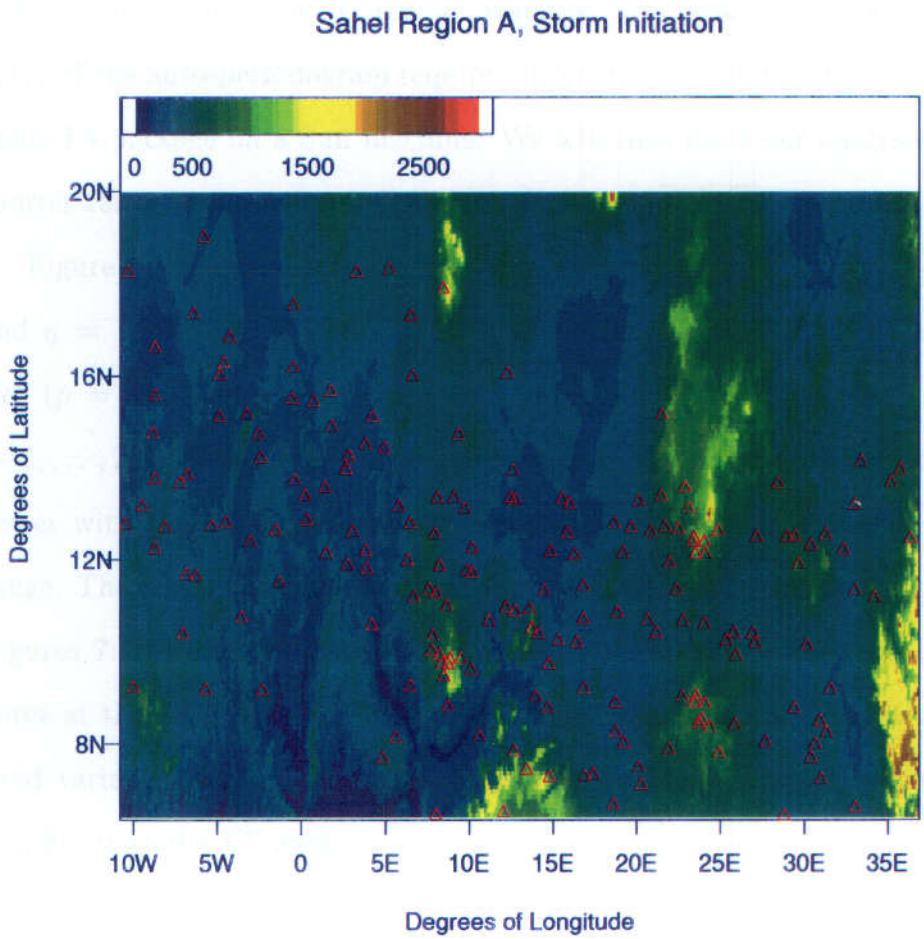

Figure 7.6: Elevation data of Region A together with storms that initiated in this region.

tion 7.1) then the range of frequencies for the elevation auto-periodogram is $p = 0, \ldots, 2850$ and $q = -810, \ldots, 809$. However, 84% of the power in this periodogram is explained by the frequencies with $p = 0, \ldots, 15$ and $q = -16, \ldots, 15$. Furthermore, using the full range of frequencies requires heavy computations and is time-consuming. For example, to get a summary of the auto-periodogram requires approximately half an hour using the Splus 3.4 package on a Sun machine. We will thus limit our analysis to the shorter range.

Figure 7.7(a) is the auto-periodogram of elevation data for $p = 0, \ldots, 15$ and $q = -16, \ldots, 15$. Concentration of power is observed along frequencies $(p = \{1, \ldots, 7\}, q = 0)$, $(p = 1, q = \{-3, \ldots, 1\})$ and $(p = 2, q = \{-2, \ldots, 2\})$. These frequencies contribute 51% of the auto-periodogram power with the full range of frequencies and 61% of that with the shorter range. The dominant peaks occur at $(p = \{1, 3, 4\}, q = 0)$ and $(p = 2, q = 1)$. Figures 7.7(b) and (c) give the significance of elevation-periodogram ordinates at the 1%, 5%, and 10% levels using Fisher's test with adjusted and fixed variance, respectively. Most of the above frequencies are detected as significant at the 1% level.

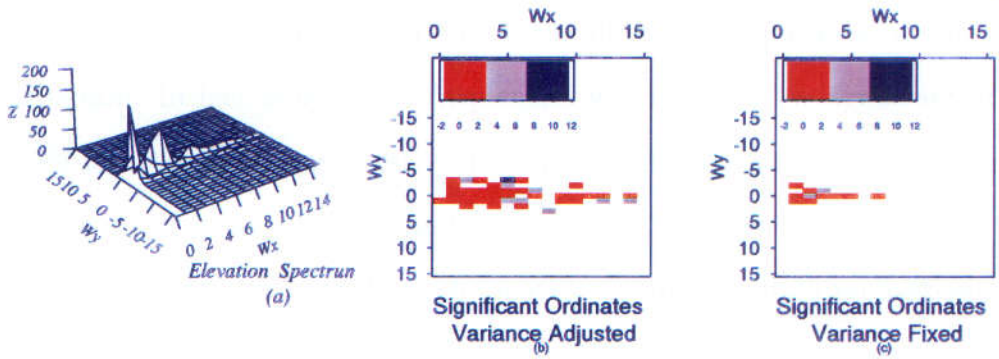

Figure 7.7: (a) Auto-periodogram of elevation data for $p = 0, \ldots, 16$ and $q = -16, \ldots, 15$; (b) and (c) significant ordinates of (a) using Fisher's test with adjusted and fixed variance, respectively, the values indicate significance level.

Therefore, in the WE direction elevation data are composed of several sinusoidal patterns, but the magnitudes of the patterns repeating one-, three- and four-times are greater than the others. Other patterns are detected in the direction of the angles $\pm 60.39°$ corresponding to the frequencies $(2, \pm 1)$ and $-81.91°$ corresponding to $(1, -2)$. Thus elevation data are generated by a number of different sinusoidal waves, this is an indication of the complexity of this pattern.

The auto-periodogram of initiation points is presented in Figure 7.8(a). Peaks are observed at $(p = \{0, 1\}, q = 1)$. These are the only frequencies detected at the 1% level of significance within the frequency range $p = 0, \ldots, 6 = [\sqrt{190}/2]$ and $q = -6, \ldots, 5$. Thus the pattern of initia-

tion points repeats once in the SN direction and once in the direction of the vector with angle 74.13°.

Figure 7.8(b) represents the auto-periodogram of the duration pattern. Power seems to be distributed over the different frequencies of this periodogram. In fact none of the frequencies was found to be significant at the 10% level using Fisher's test. The range of frequencies investigated using Fisher's test is $p = 0, \ldots, 6$ and $q = -6, \ldots, 5$. In another attempt to test the null hypothesis of CSR of the marks, we simulated 99 realisations of a Poisson process with mean equal to that of the mean mark and used a Monte Carlo approach to test the null hypothesis. Approximately 40% of the auto-periodogram ordinates, 194 out of 495, were found to be significant at the 1% level, see Figure 7.8(c). Thus storm duration pattern is composed of many sinusoidal waves.

Figures 7.9(a) to (c) represent the co-, quadrature and coherency spectra for initiation versus elevation, respectively. A trough is observed in the co-spectrum at the frequency $(1, 1)$ and a peak at the frequency $(3, 0)$. Thus for patterns travelling in the direction of the 74.13° angle initiation points are negatively correlated with elevation values. However for patterns repeating three times in the WE direction the two components are positively correlated. The troughs and peaks in the quadrature spectrum indicate that the two components are out of phase.

The significant values of the zero coherency test at the 1%, 5%, and 10% levels are given in Figure 7.9(d). Concentration of coherency is detected along the frequencies $(p = \{6, 7, 8\}, q = -10)$, $(p = \{2, \ldots, 7\}, q = \{-4, -3\})$, $(p = \{5, 6, 7\}, q = 9\})$, and $(p = 8, q = \{2, \ldots, 6\})$. Ordinates of the adjusted

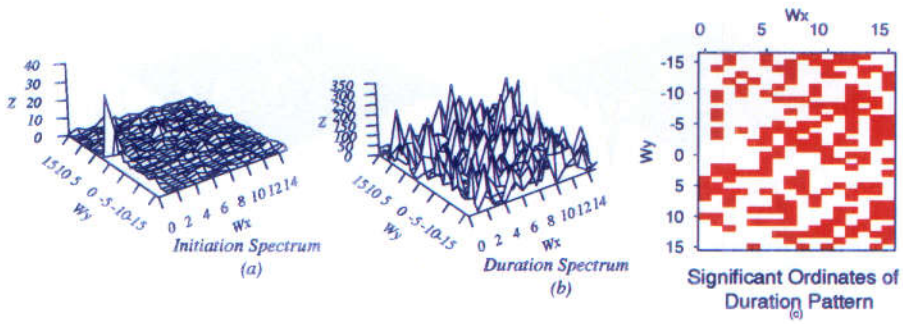

Figure 7.8: (a) and (b) Auto-periodograms of initiation points and duration; (c) significant ordinates at the 1% level of the auto-periodogram for storm duration using Monte Carlo test are the blacked entries.

phase spectrum in the WE direction for the above frequencies with $q = -10, -4, -3, 9$ are shown in Figure 7.9(e). The slopes in the WE direction for $q = -10, -4, -3, 9$ are 2.13, 1.60, 1.01 and 0.00, respectively. Figure 7.9(f) represents the profile of the adjusted phase spectrum in the SN direction for $p = 8$; the slope for this frequency band is -0.13. Thus for waves with $q = -4, -3$ the lattice pattern is to the east of the point pattern with a mean shift of 1.3 pixels, and for $p = 8$ it is to the south of the point pattern. Using the phase correlation techniques for the frequency band $p = 1, \ldots, 7$ and $q = -10, \ldots, 0$, the estimates of the slopes are 0.17 in the WE direction and -0.01 in the SN direction.

Peaks and troughs are observed in both the co- and quadrature spectra of duration versus elevation, Figures 7.10(a) and (b), respectively. However,

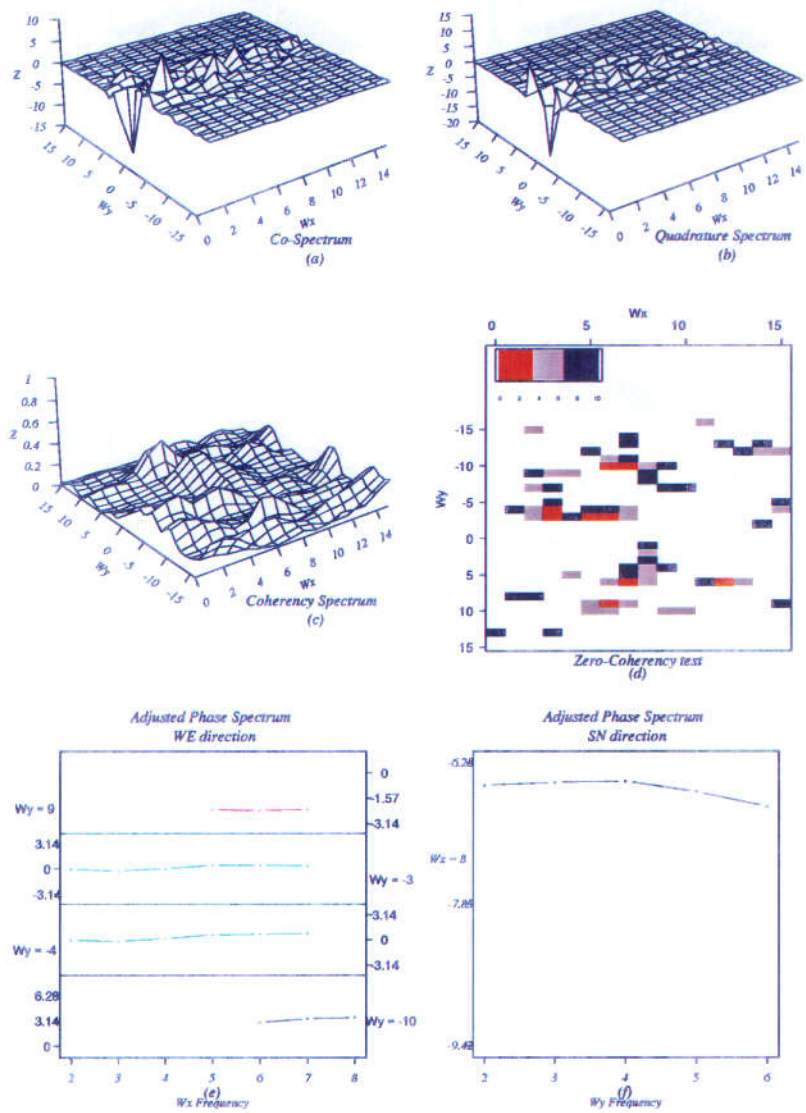

Figure 7.9: Cross-spectra of initiation points versus elevation: (a) and (b) raw co- and quadrature spectra; (c) coherency spectrum smoothed using Method A four times; (d) significant ordinates of the zero coherency test at the 1%, 5% and 10% levels the value represents the significance level; (e) and (f) profiles of adjusted phase spectra in the WE direction for $(p = \{6,7,8\}, q = -10)$, $(p = \{2,\ldots,7\}, q = \{-4,-3\})$, $(p = \{5,6,7\}, q = 9\})$, and SN direction for $(p = 8, q = \{2,\ldots,6\})$.

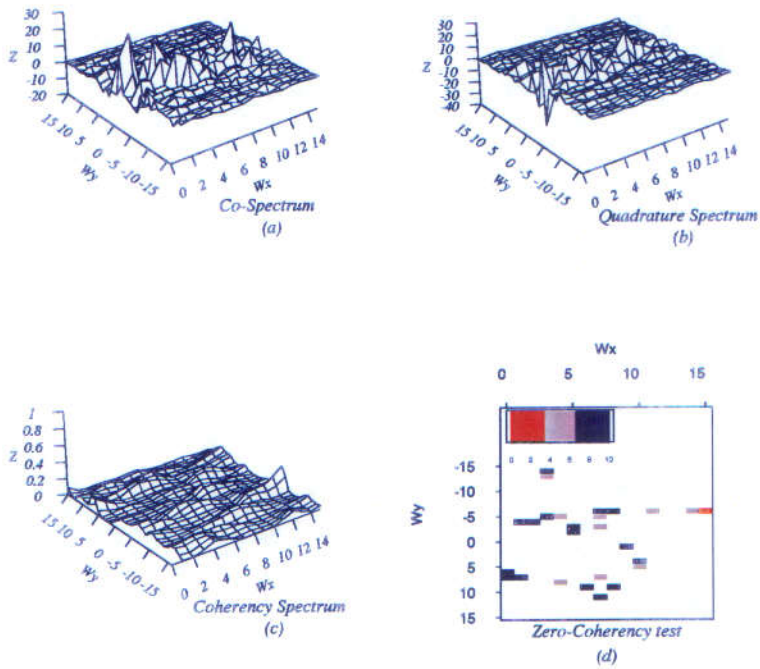

Figure 7.10: Cross-spectra of duration versus elevation: (a) and (b) raw co- and quadrature spectra; (c) smoothed four times coherency spectrum; (d) significant ordinates of the zero coherency test at the 1%, 5% and 10% levels, the value represents the significance level.

only the ordinate of the coherency spectrum, Figure 7.10(c), at $(15, -6)$ is significant at the 1% level as indicated by Figure 7.10(d). Nine other ordinates are significant at the 5% level, however no concentration of coherency is detected. Thus despite the correlation suggested by peaks and troughs in the co-, quadrature and amplitude spectra, the lack of concentration of coherency indicates that duration and lattice patterns are not strongly correlated.

Figures 7.11(a) and (b) represent the co- and quadrature spectra for du-

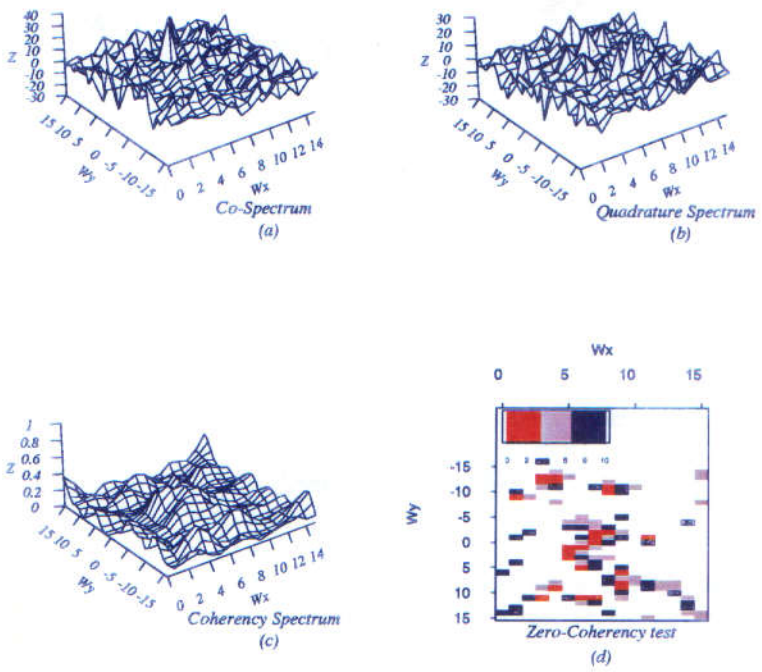

Figure 7.11: Cross-spectra of duration versus initiation: (a) and (b) raw co- and quadrature spectra; (c) smoothed four times coherency spectrum; (d) significant ordinates of the zero coherency test at the 1%, 5% and 10% levels, the value represents the significance level.

ration versus initiation. Some peaks are observed at high frequencies in both periodograms. The significant ordinates of the coherency spectrum, Figure 7.11(c), are presented in Figure 7.11(d). Concentration of significant ordinates of coherency at the 5% level is detected around relatively high frequencies. Therefore duration and initiation are mainly correlated around relatively high frequencies.

In summary storms tend to initiate to the north-west of the lattice pattern

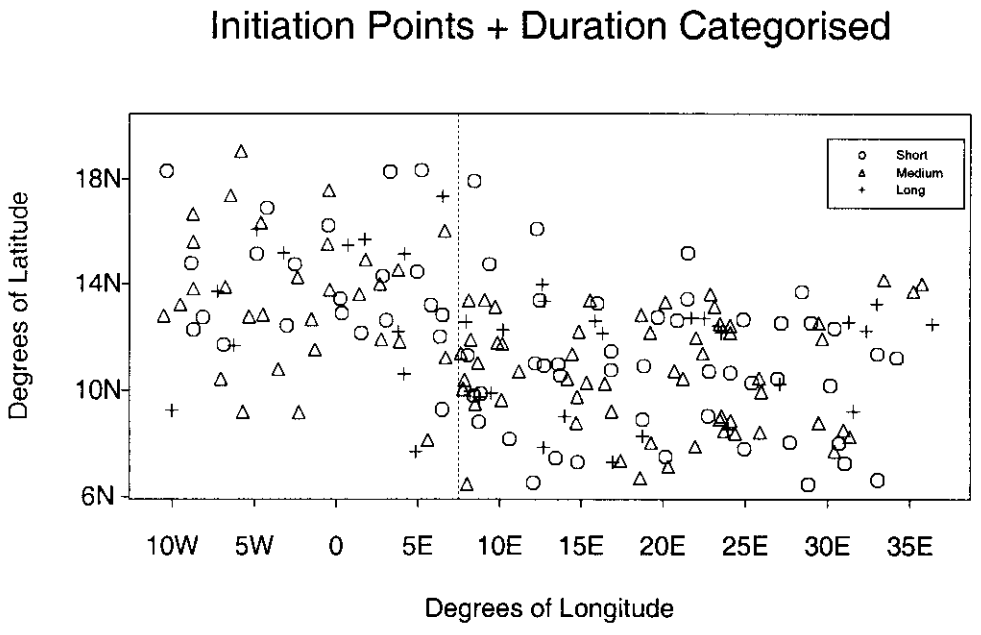

Figure 7.12: Storms that initiated in Region A classified as short- (circles), medium- (triangles), or long-lived (crosses). The vertical dotted line at 7.5°E divides the region into eastern and western subregions.

in Region A. However, evidence that storm duration is correlated with global features of elevation or the storm initiation patterns is not strong.

In order to investigate the present data set further, we will study the properties of storm initiation versus elevation conditional on storm duration. In this study, storms will be classified as: short-lived if they lasted less than six hours, medium-lived if they lasted strictly more than 6 hours and strictly less than 15 hours, or long-lived if they lasted more than 15 hours. There are 67 short-lived storms, 87 medium-lived and 36 long-lived. A graphical representation of Region A storms classified as short-, medium-, or long-lived is provided in Figure 7.12. Conditional on the storm being short-, medium-, or long-lived Figures 7.13, 7.14 and 7.15 represent the auto-periodograms

for initiation, co-, quadrature, amplitude, and coherency spectra, and the zero-coherency test statistic for initiation and elevation.

Fisher's test applied to the auto-periodogram ordinates of short-lived initiation points indicates that $(0, 1)$ is significant at the 5% level. For medium-lived storms significant ordinates are detected at the 1% level at $(0, 1)$ and at the 5% level at $(1, 1)$. None of the investigated frequencies for the long-lived storms was found to be significant at the 10% level. Thus short- and medium-lived storms cluster in one big clump in the SN direction, in addition medium-lived storms cluster in the direction of the vector with angle 74.13°. However, for long-lived storms the null hypothesis of CSR cannot be rejected based on Fisher's test. Note that significant peaks of the auto-periodogram for medium-lived storms coincide with those of the unclassified storms.

Troughs are observed at $(1, 1)$ in all the co-spectra of the classified storms, but the magnitude of the medium-lived storms is the largest. Furthermore, for medium-lived storms a peak is noticed at $(3, 0)$ and for long-lived at $(2, 1)$. Thus in broad terms storms tend to initiate from relatively low land rather than high. This can be easily seen by visual inspection of Figure 7.6. The quadrature spectra of all three categories have peaks and troughs indicating that storms and elevation are out of phase. The amplitude spectra indicate that all types of storms are correlated to elevation. However, the extent of such correlation is not strong as seen from the coherency spectra and the zero coherency test statistic.

Concentration of significant coherency ordinates at the 5% level is detected for short-lived storms and elevation at $(p = \{2, 3, 4\}, q = -4)$ and $(p = \{11, 12, 13\}, q = -13)$. The slope in the WE direction of the phase

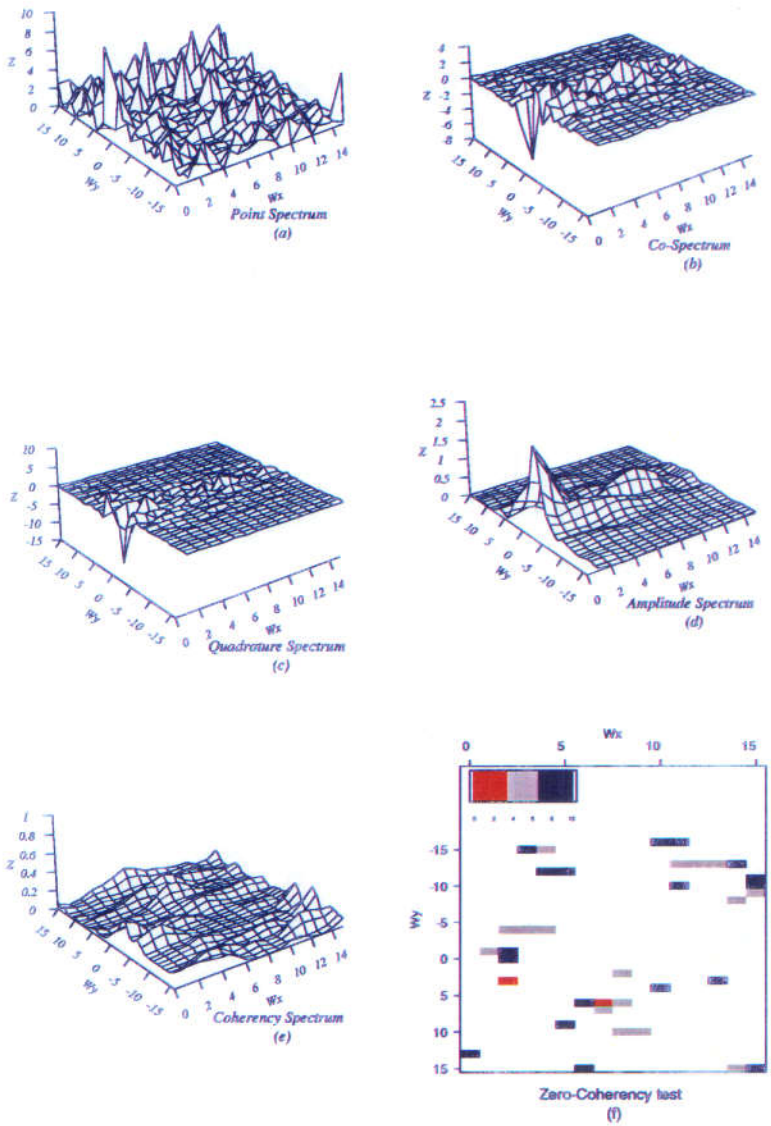

Figure 7.13: Spectra of initiation versus elevation for short-lived storms: (a) auto-periodogram of initiation points; (b) and (c) raw co-, quadrature spectra; (d) and (e) amplitude and coherency spectra smoothed using Method A four times; (f) significant ordinates of the zero coherency test at the 1%, 5% and 10% levels, the value represents the significance level.

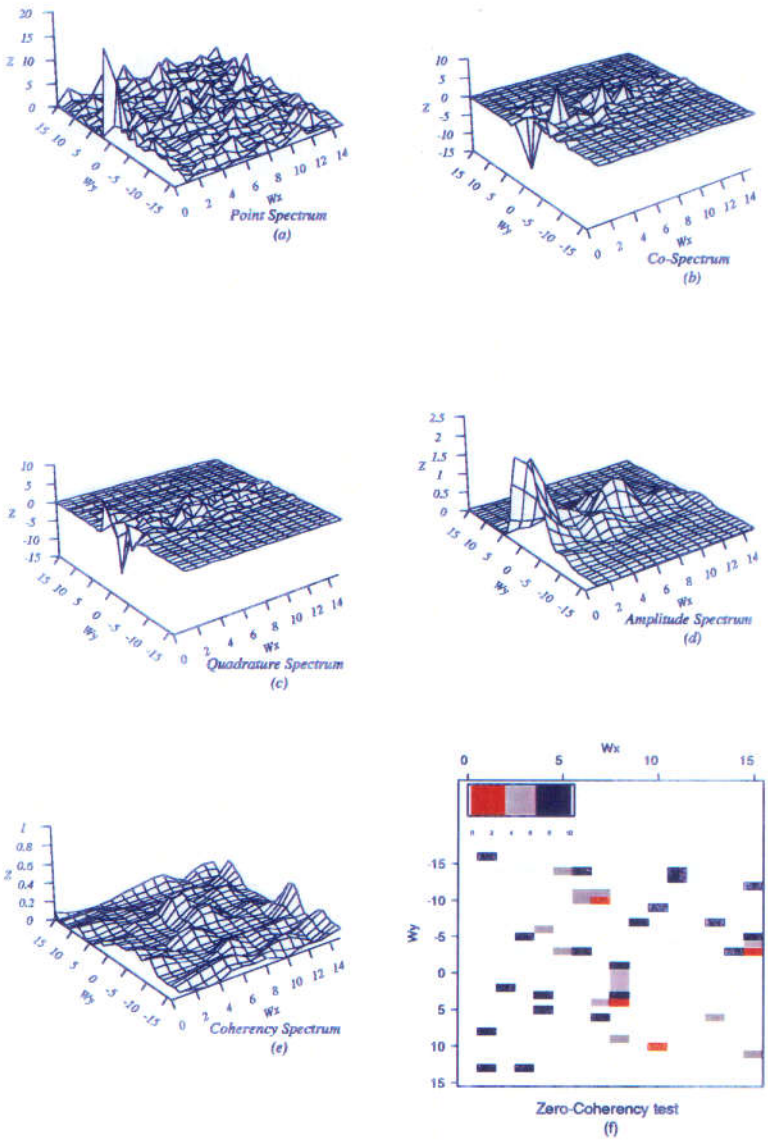

Figure 7.14: Spectra of initiation versus elevation for medium-lived storms: (a) auto-periodogram of initiation points; (b) and (c) raw co- and quadrature spectra; (d) and (e) amplitude and coherency spectra smoothed using Method A four times; (f) significant ordinates of the zero coherency test at the 1%, 5% and 10% levels, the value represents the significance level.

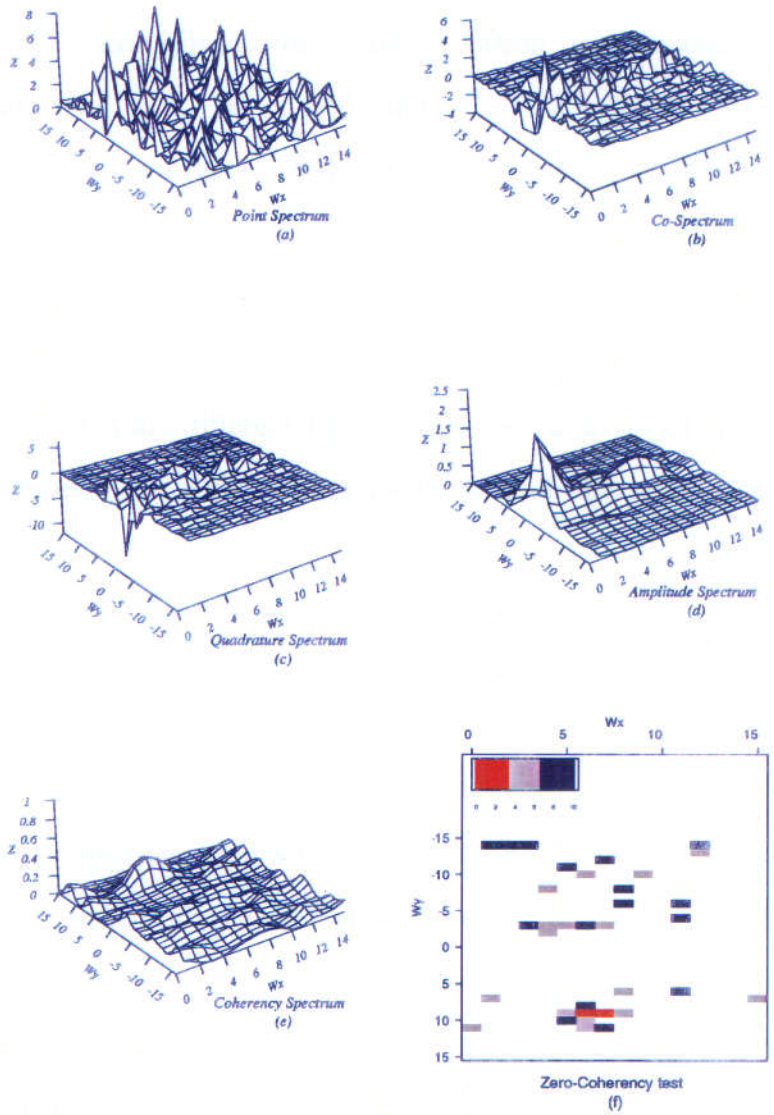

Figure 7.15: Spectra of initiation versus elevation for long-lived storms: (a) auto-periodogram of initiation points; (b) and (c) raw co- and quadrature spectra; (d) and (e) amplitude and coherency spectra smoothed using Method A four times; (f) significant ordinates of the zero coherency test at the 1%, 5% and 10% levels, the value represents the significance level.

spectrum along the first frequency band is 1.1 and along the second band is -0.55. For medium-lived storms and elevation, concentration is detected along $(p = 8, q = \{0, 1, 2\})$. The slope in the SN direction for this frequency band is -0.16. Long-lived storms and elevation have concentration of coherency at $(p = \{5, \ldots, 8\}, q = 9)$ and $(p = 6, q = \{9, 10, 11\})$; the slope in the WE direction along the first frequency band is 1.19 and in the SN direction along the second is -0.27. Thus in general storm initiation points are negatively correlated with elevation irrespective of storm duration.

Next, we note that the topographical features in the western and eastern parts of Region A are different (see Mugglestone and Taylor, 1994) and that the differences might affect storm locations and characteristics. We will, therefore, divide Region A into the two subregions studied by Mugglestone and Taylor (1994) and provide separate analyses for each subregion in the next sections.

7.3.1 Eastern Subregion

The eastern subregion extends from 7.5°E to 36.787°E. There are 126 storms that initiated in the eastern subregion. Figure 7.16 gives the graphical representation of auto-periodograms of elevation, initiation points, and duration of the eastern subregion, in addition to the significant ordinates of the elevation data using Fisher's test. In the elevation auto-periodogram peaks occur at $(2, 0)$ and $(1, 1)$, in addition to other minor peaks around low frequencies. These peaks are detected as significant at the 1% level using Fisher's test. The frequency $(0, 1)$ is detected as significant at the 1% level in the initiation auto-periodogram. Using Fisher's test none of the frequencies in the duration

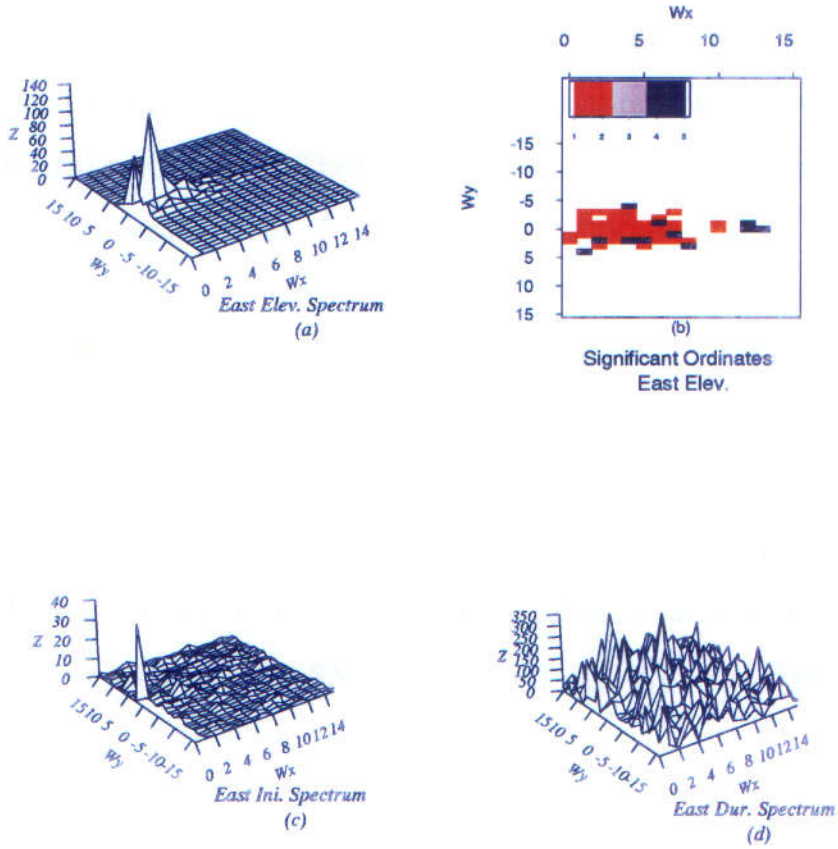

Figure 7.16: Eastern subregion auto-periodograms: (a) elevation data, (c) initiation points and (d) duration; (b) significant ordinates of (a) using Fisher's test with adjusted variance, the values indicate significance level.

auto-periodogram has been found to be significant at the 10% level.

Figures 7.17(a) and (b) represent the co- and quadrature spectra of initiation versus elevation in the east subregion. A peak is observed at $(2, 0)$ in the co-spectrum implying that for patterns repeating twice in the WE direction elevation and initiation are positively correlated. Thus storms tend to initiate on relatively high land. However, the trough at $(1, 1)$ indicates

that the two components are negatively correlated along the vector with angle 65.25°. Note that the magnitudes of the trough and peak are inversely proportional to the trough and peak of the initiation versus elevation co-spectrum of the whole area. The peaks in the quadrature spectrum indicate that the components are out of phase.

Concentration of significant coherency, Figure 7.17(c), at the 5% level is observed in the zero coherency test statistic image, Figure 7.17(d), along the frequency bands $(p = 1, q = \{-5, \ldots, -2\})$, $(p = 2, q = \{-4, -3, -2\})$, $(p = 5, q = \{-2, -1, 0\})$, $(p = \{6, 7, 8\}, q = \{-14, 3\})$, $(p = \{7, 8, 9\}, q = -13)$, and $(p = \{1, 2, 3\}, q = -3)$. Figures 7.17(e) and (f) represent the profiles of adjusted phase spectra of the above frequency bands in the WE direction for $q = -14, -13, \pm 3$ and in the SN direction for $p = 1, 2, 5$. The slopes in the WE direction are 1.12, 0.09, 0.61, and 0.01 for $q = -14, -13, -3, 3$, and in the SN direction are -0.14, -0.3, and -0.58 for $p = 1, 2, 5$, respectively. The estimates of the corresponding slopes using phase correlation techniques are 0.285 in the WE direction and -0.143 in the SN direction.

Figures 7.18 and 7.19 represent the co-, quadrature, coherency spectra and zero coherency test statistic for duration versus elevation and initiation within the eastern subregion. In general, these spectra exhibit similar characteristics to their equivalents for the entire region. As before it can be seen that duration is not highly correlated with elevation or initiation.

Next, we will explore the relationship between initiation and elevation within the eastern subregion conditional on the storm duration. Storms initiating in the eastern subregion and classified according to their storm duration are presented to the east of the dashed line in Figure 7.12. There are

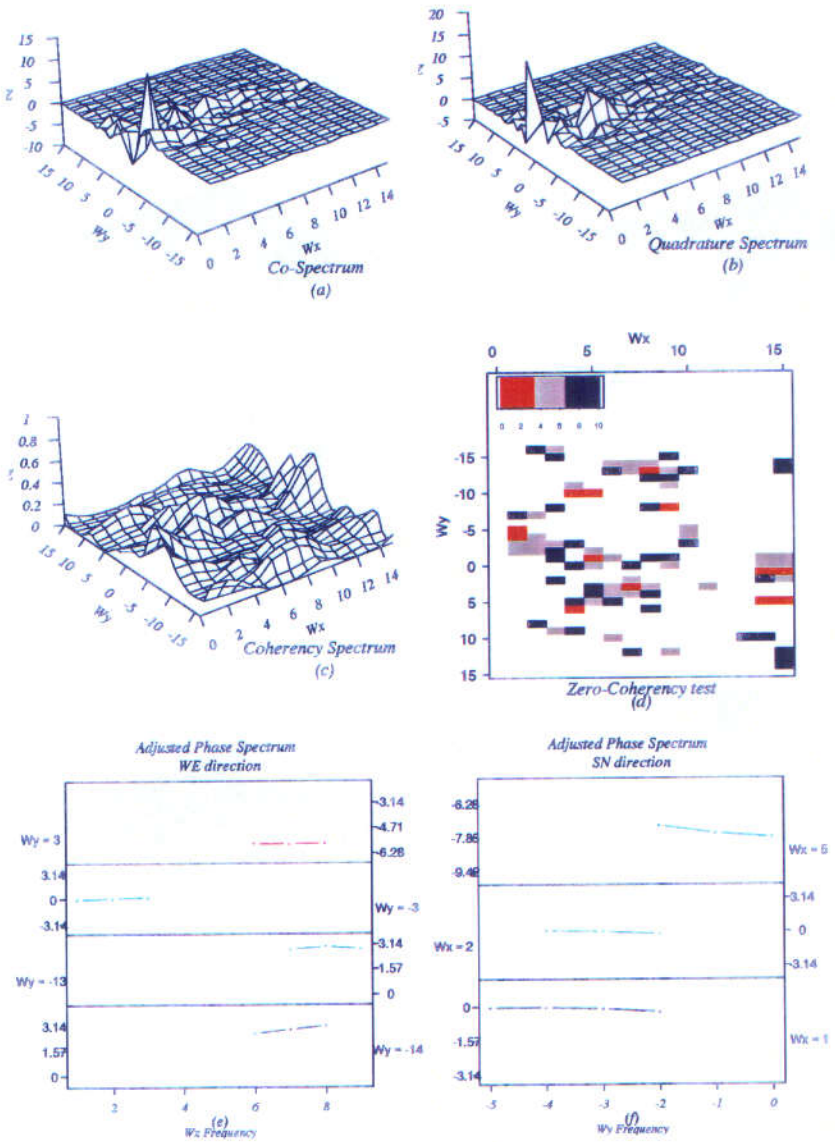

Figure 7.17: Cross-spectra of initiation versus elevation in the eastern subregion: (a) and (b) raw co- and quadrature spectra; (c) coherency spectrum smoothed using Method A four times; (d) significant ordinates of the zero coherency test at the 1%, 5% and 10% levels, the value represents the significance level; (e) and (f) profiles of adjusted phase spectra in the WE and SN directions for the frequency bands mentioned in the main text.

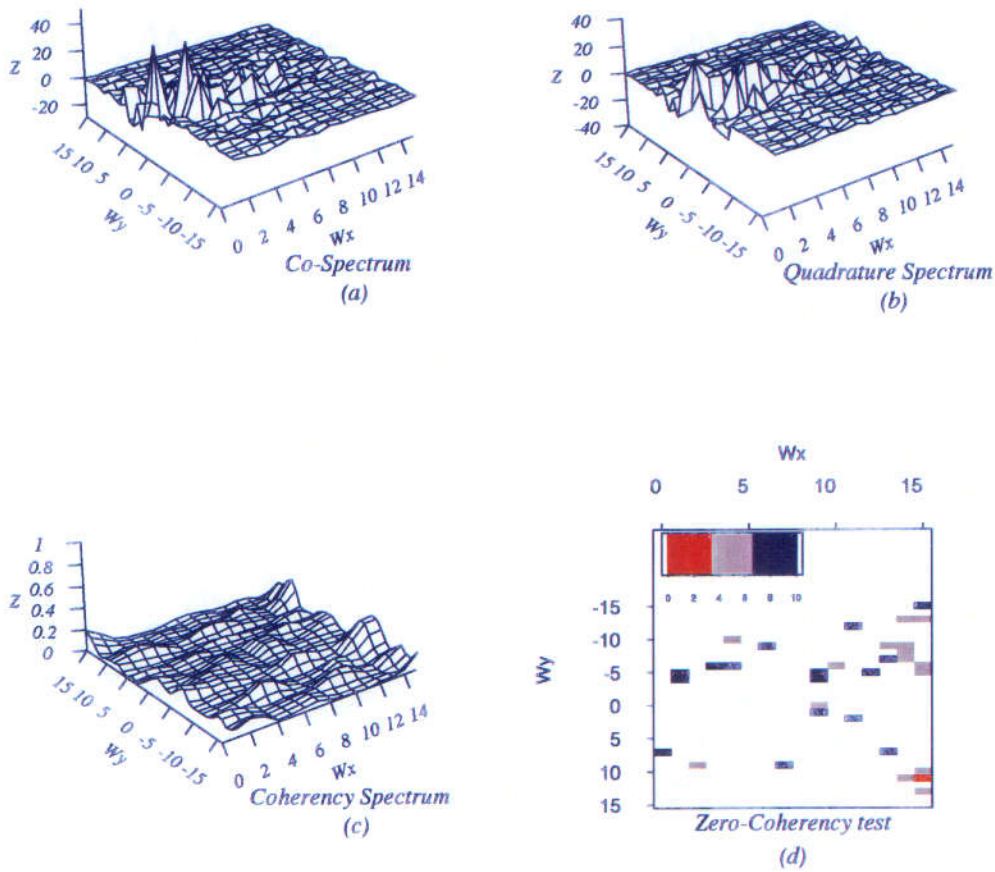

Figure 7.18: Cross-spectra of duration versus elevation in the eastern subregion: (a) and (b) raw co- and quadrature spectra; (c) coherency spectrum smoothed using Method A four times; (d) significant ordinates of the zero coherency test at the 1%, 5% and 10% levels, the value represents the significance level.

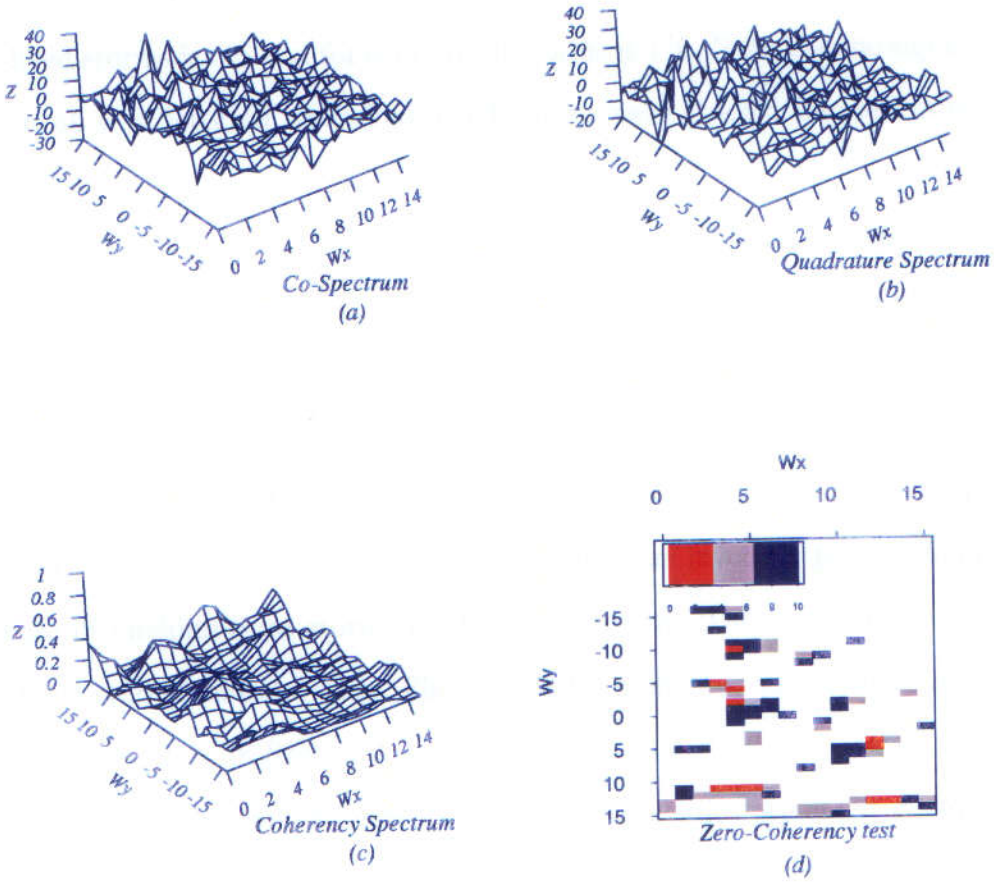

Figure 7.19: Cross-spectra of duration versus initiation in the eastern subregion: (a) and (b) raw co- and quadrature spectra; (c) coherency spectrum smoothed using Method A four times; (d) significant ordinates of the zero coherency test at the 1%, 5% and 10% levels, the value represents the significance level.

45 short-, 57 medium-, and 24 long-lived storms within the eastern subregion.

The auto-periodograms for short-, medium-, and long-lived storm initiation points in the eastern subregion are given in sub-figures (a) of Figures 7.20, 7.21, and 7.22, respectively. All these periodograms exhibit one significant peak at $(0,1)$ where the level of significance for the medium- and long-lived storms is 5% and for short-lived storms is 1%. Note that no significant peak was detected when long-lived storms were studied for the entire region.

The short-lived storms and elevation co-spectrum, Figure 7.20(b), has a peak at $(7,1)$. Note that the major trough observed in the co-spectrum for short-lived storms at $(1,1)$ for the entire region is not visible for this subregion. The co-spectrum for elevation versus medium-lived storms, Figure 7.21(b), resembles the corresponding co-spectrum of the entire region. However, the magnitudes of the peaks and troughs are inversely proportional to those of medium-lived storms in the entire region. The co-spectrum for long-lived storms and elevation, Figure 7.22(b), is similar to the long-lived storms co-spectrum in Region A.

The quadrature spectra for all the duration categories presented in sub-figures (c) of Figures 7.20, 7.21 and 7.22 exhibit major peaks and minor troughs. This is an indication that the two components are out of phase.

The amplitude spectra, sub-figures (d) of Figures 7.20, 7.21 and 7.22, emphasise that the two components are correlated. Sparsely spread significant coherency ordinates are detected at the 5% level, as seen from sub-figures (e) and (f) of Figures 7.20, 7.21 and 7.22.

In summary, initiation points in the eastern subregion are correlated with

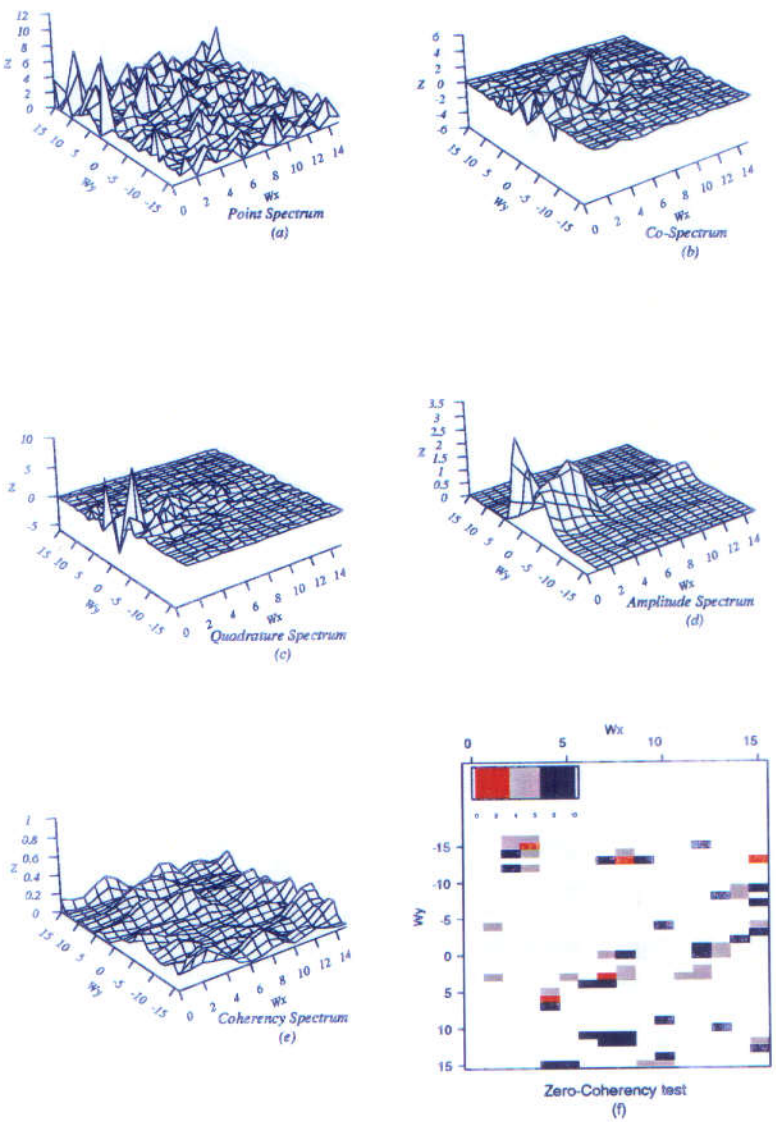

Figure 7.20: Spectra of initiation versus elevation for short-lived storms in the eastern subregion: (a) auto-periodogram of initiation points; (b) and (c) raw co- and quadrature spectra; (d) and (e) amplitude and coherency spectra smoothed using Method A four times; (f) significant ordinates of the zero coherency test at the 1%, 5% and 10% levels, the value represents the significance level.

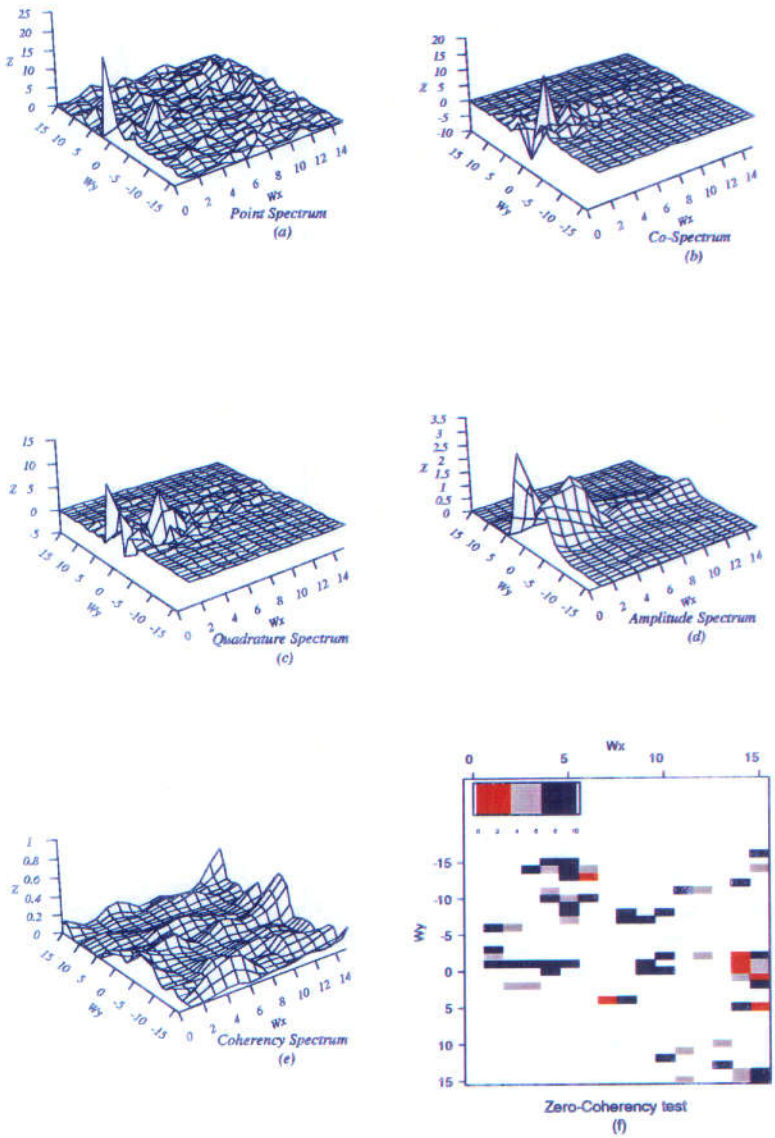

Figure 7.21: Spectra of initiation versus elevation for medium-lived storms in the eastern subregion: (a) auto-periodogram of initiation points; (b) and (c) raw co- and quadrature spectra; (d) and (e) smoothed four times amplitude and coherency spectra; (f) significant ordinates of the zero coherency test at the 1%, 5% and 10% levels, the value represents the significance level.

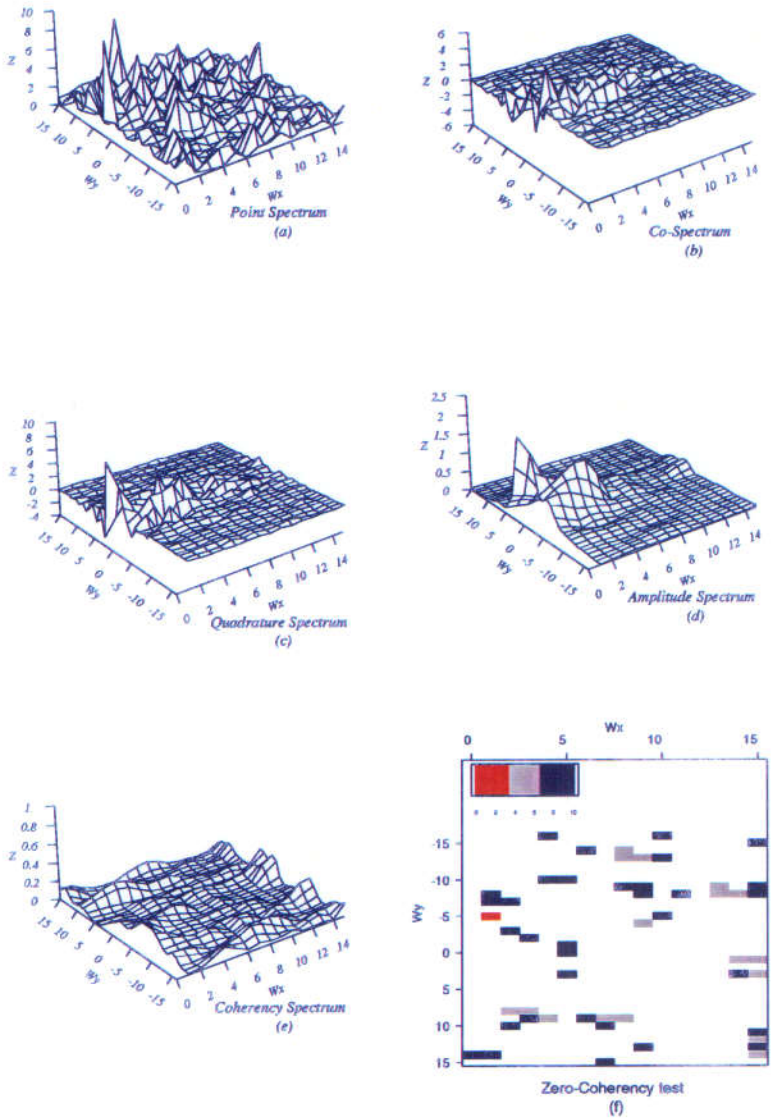

Figure 7.22: Spectra of initiation versus elevation for long-lived storms in the eastern subregion: (a) auto-periodogram of initiation points; (b) and (c) raw co- and quadrature spectra; (d) and (e) amplitude and coherency spectra smoothed using Method A four times; (f) significant ordinates of the zero coherency test at the 1%, 5% and 10% levels, the value represents the significance level.

elevation data, however the nature of the correlation depends on the direction of travel of the patterns. When storms are classified by duration such correlation is mainly observed for medium-lived storms.

7.3.2 Western Subregion

The western subregion extends from 10.704°W to 7.5°E. The initiation points and their durations are presented in Figure 7.12 west of the dashed line. There are 64 events of initiation within this subregion out of which there are 12 long-lived, 30 medium-lived and 22 short-lived storms.

Figures 7.23(a) and (b) represent the auto-periodogram of elevation data within this subregion and the significant ordinates using Fisher's test. Peaks are observed at $(1, 0)$ and $(1, -1)$. These peaks are significant at the 1% level. Other significant ordinates are detected within the frequency range with $p = 0, \ldots, 5$ and $q = -5, \ldots, 5$. The initiation points auto-periodogram, Figure 7.23(c), possesses a peak at $(0, 1)$ which is significant at the 1% level. As in the entire region and the eastern subregion the duration auto-periodogram, Figure 7.23(d), does not possess any significant ordinates at the 10% level using Fisher's test.

A major trough is observed in the co-spectrum for initiation versus elevation at $(2, 1)$. In addition, two minor peaks occur at $(1, -1)$ and $(0, 4)$, see Figure 7.24(a). The trough in the quadrature spectrum, Figure 7.24(b), indicates that the two components are out of phase. The significant ordinates of the coherency spectrum, Figure 7.24(c), using the zero coherency test statistic are presented in Figure 7.24(d). No concentration of coherency is detected for relatively low frequencies. However, concentration at the 5% level is detected along $(p = \{12, 13, 14\}, q = 6)$ and $(p = 13, q = \{4, 5, 6\})$. The slope in the WE direction for the first frequency band is -0.41 and the slope in the SN direction along the second frequency band is -0.26. The esti-

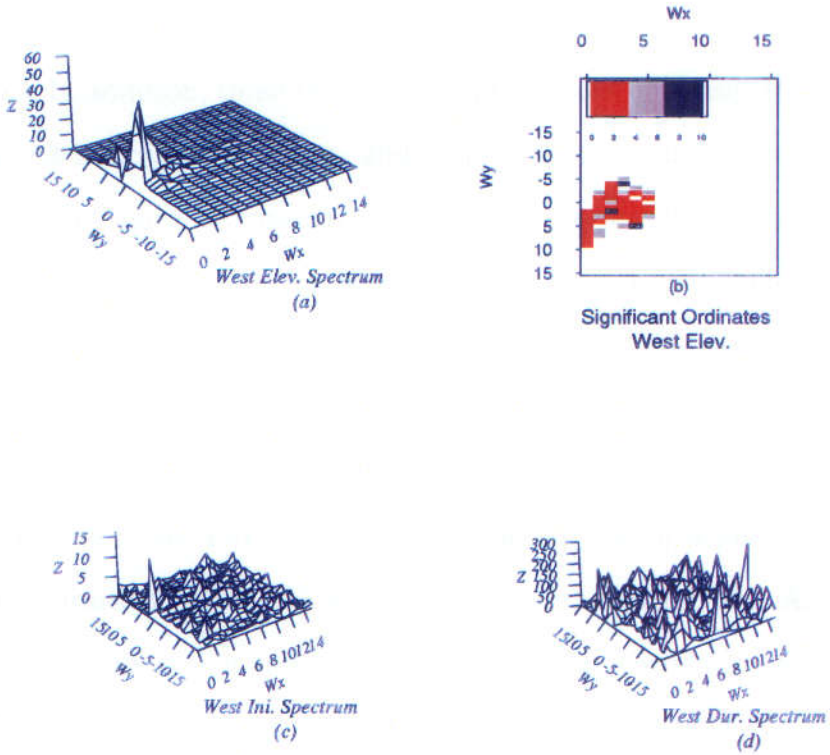

Figure 7.23: Western subregion auto-periodograms: (a) elevation data, (c) initiation points and (d) duration; (b) significant ordinates of (a) using Fisher's test with adjusted variance, the values indicate significance level.

mates of the slopes along the frequency band $p = 11, \ldots, 14$ and $q = 3, \ldots, 7$ using the phase correlation techniques are 0.29 and -0.18 for the WE and SN directions, respectively.

Therefore, initiation points and elevation are negatively correlated along the vector with angle 34°. Moreover, they are positively correlated along the vector with angle $-53.45°$ and for the pattern repeating four times in the SN direction. In addition, these two components are out of phase. However, the correlations indicated by the co- and quadrature spectra at low frequencies are not strong, since no concentration of coherency is detected around these frequencies. Furthermore, for relatively high frequencies where coherency is concentrated the elevation pattern is to the west of initiation points by approximately half a pixel and to the south by one third of a pixel.

Figures 7.25 and 7.26 represent the co-, quadrature, and coherency spectra in addition to the zero coherency test statistic for duration versus elevation and initiation within the western subregion, respectively. As it is the case for the entire region and the eastern subregion, correlation between the marks and lattice pattern is suggested by the peaks and troughs in the co- and quadrature spectra. However, there is insufficient evidence to suggest that such correlation is strong due to the lack of concentration of coherency for duration versus elevation. Note here that the peaks and troughs in the co-spectrum are mainly concentrated around frequencies with low p, whereas the co-spectra for the entire region and the eastern subregion have theirs concentrated around frequencies with low q.

The co- and quadrature spectra for the marks and initiation exhibit a similar structure to those of the entire region and the eastern subregion.

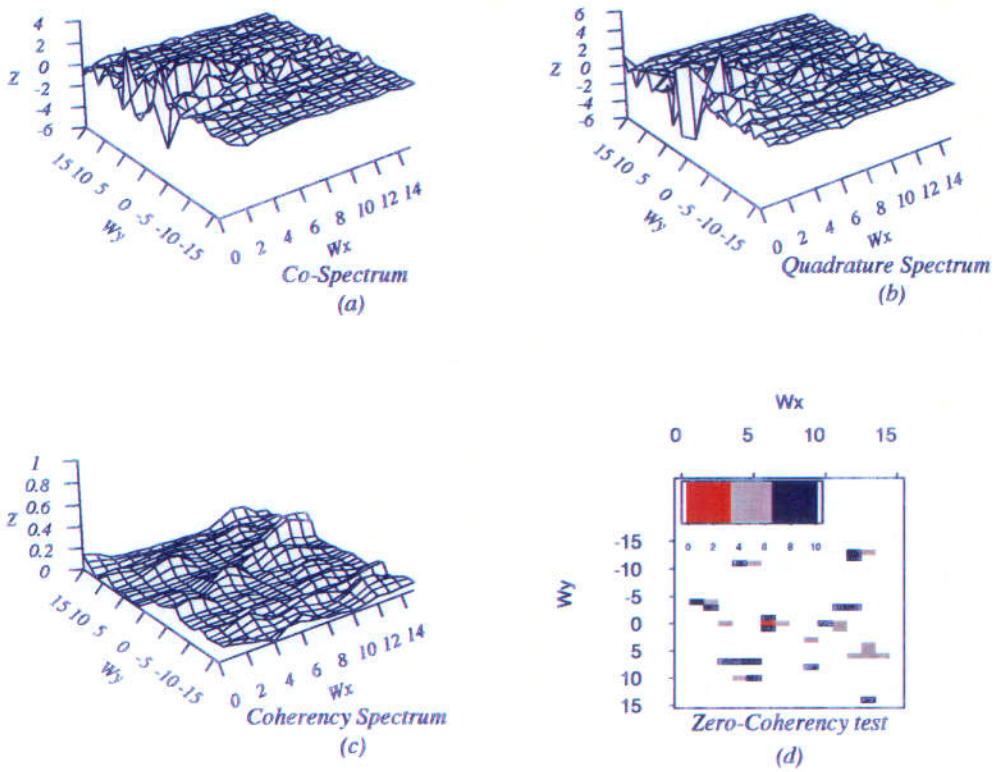

Figure 7.24: Cross-spectra of initiation versus elevation in the western subregion: (a) and (b) raw co-, quadrature spectra; (c) coherency spectrum smoothed using Method A four times; (d) significant ordinates of the zero coherency test at the 1%, 5% and 10% levels, the value represents the significance level.

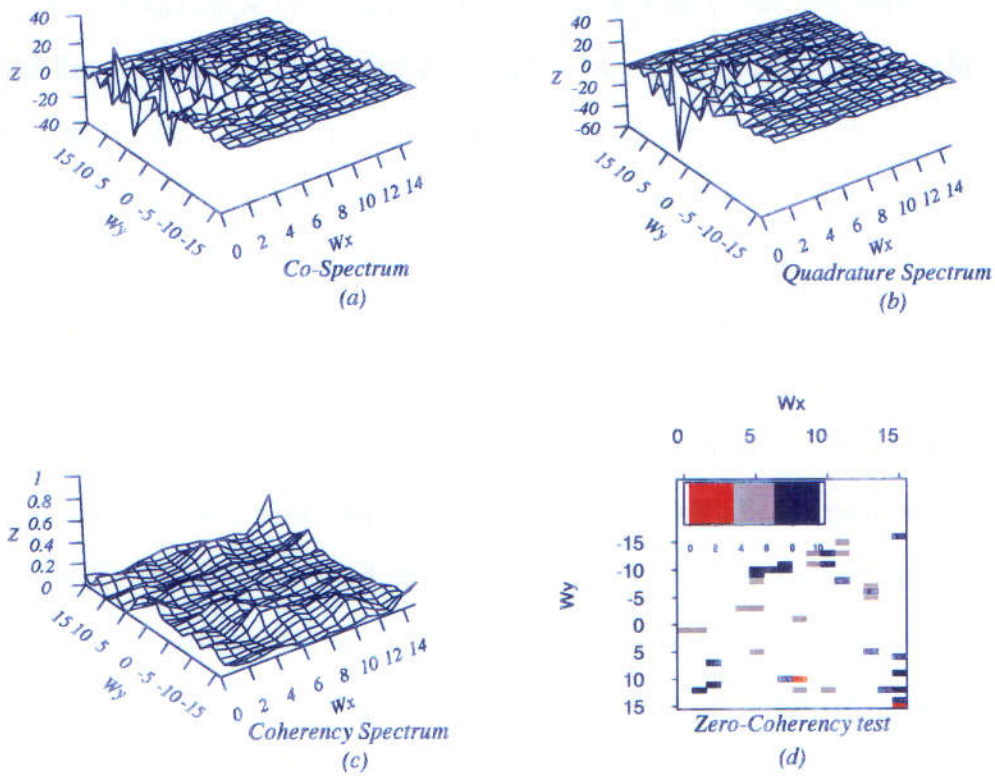

Figure 7.25: Cross-spectra of duration versus elevation in the western subregion: (a) and (b) raw co- and quadrature spectra; (c) coherency spectrum smoothed using Method A four times; (d) significant ordinates of the zero coherency test at the 1%, 5% and 10% levels, the value represents the significance level.

None of the spectra for the entire region and its subregions are characterised by distinctive features but peaks and troughs are observed over the whole investigated range. Concentration of coherency at the 5% level is detected around the frequencies $(p = \{1, \ldots, 4\}, q = \{-15, -14, -13\})$, $(p = 6, q = \{-4, -3, -2\})$, $(p = 8, q = \{-2, -1, 0\})$, and $(p = \{8, 9, 10\}, q = 0)$. The mean value of the slope of the adjusted phase spectrum in the WE direction for the first frequency band with $q = -15, -14, -13$ is -0.83, whereas the mean shift in the SN direction for frequencies with $p = 2, 3, 4$ is 0.33. The slopes in the SN direction for the frequency bands with $p = 6, 8$ are 0.54 and 0.32, respectively. The slope in the WE direction for $q = 0$ is 0.14.

Figures 7.27(a), 7.28(a) and 7.29(a) represent the auto-periodograms of the short-, medium-, and long-lived storm initiation points. A significant peak of the auto-periodogram of short-lived initiation points is detected at $(0, 1)$ at the 5% level. This frequency is also the only significant peak at the 10% level for the medium-lived storms. Note that for long-lived storms we were not able to use Fisher's test since $[\sqrt{12}/2] = 1$ where 12 is the number of events of long-lived storms in the western subregion. However, visual inspection of the auto-periodogram for long-lived storms does not suggest any specific structure. In order to assess the hypothesis of CSR for this point pattern we simulated 99 realisations of the HPP process on the western subregion. Only 3% of these ordinates were found to be significant at the 5% level. None of the frequencies in the range $p = 0, \ldots, 12$ and $q = -4, \ldots, 4$ were found to be significant at this level.

The co- and quadrature spectra for the initiation points classified by duration and the elevation surface are presented in sub-figures (b) and (c) of

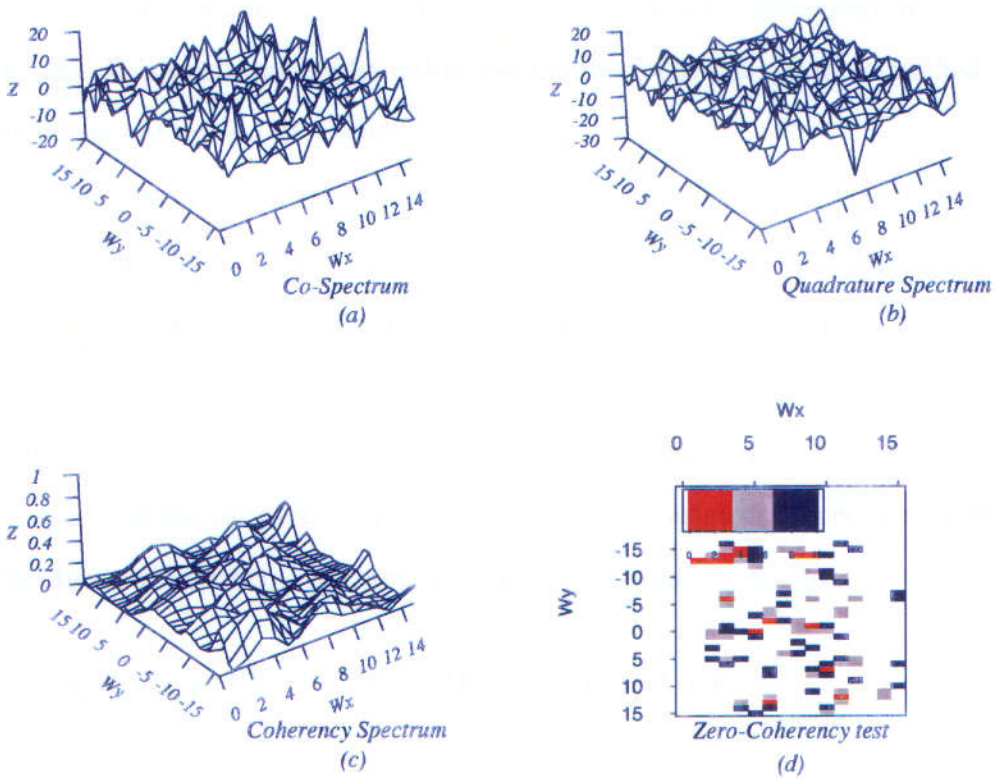

Figure 7.26: Cross-spectra of duration versus initiation in the western subregion: (a) and (b) raw co- and quadrature spectra; (c) coherency spectrum smoothed using Method A four times; (d) significant ordinates of the zero coherency test at the 1%, 5% and 10% levels, the value represents the significance level.

Figures 7.27, 7.28 and 7.29 for the short-, medium-, and long-lived storms, respectively. The peaks and troughs in both spectra and the peaks in the amplitude spectra, sub-figures (d), indicate that initiation points are correlated with elevation. However, the sparsity of significant coherency ordinates implies that such correlation is not strong. Coherency spectra are presented in sub-figures (e), while the zero coherency test images are presented in sub-figures (f). It is worth noting here that the number of events for the classified storms does not exceed 30 events in each case.

In summary, storm initiation is correlated with elevation within the western subregion. However, the nature of this correlation varies with the direction of travel of the waves. For duration versus the elevation surface there is no strong evidence to suggest that the global patterns in the two components are correlated. The same holds true for duration versus initiation. Furthermore, studying the properties of initiation points versus elevation conditional on the duration of storms has not revealed any distinctive features.

7.4 Comparison to Other Studies

In this section we compare our findings about the storm data and those of Mugglestone and Taylor (1994). Mugglestone and Taylor (1994) used random labelling to determine if there is any difference between the spatial distributions of medium- and long-lived storms in the eastern and western subregions. They found out that there is a slight difference between the two types of storms in the eastern subregion where the medium-lived storms are more strongly aggregated than the long-lived storms. However, they had insufficient evidence to claim that such a link exists in the western subregion.

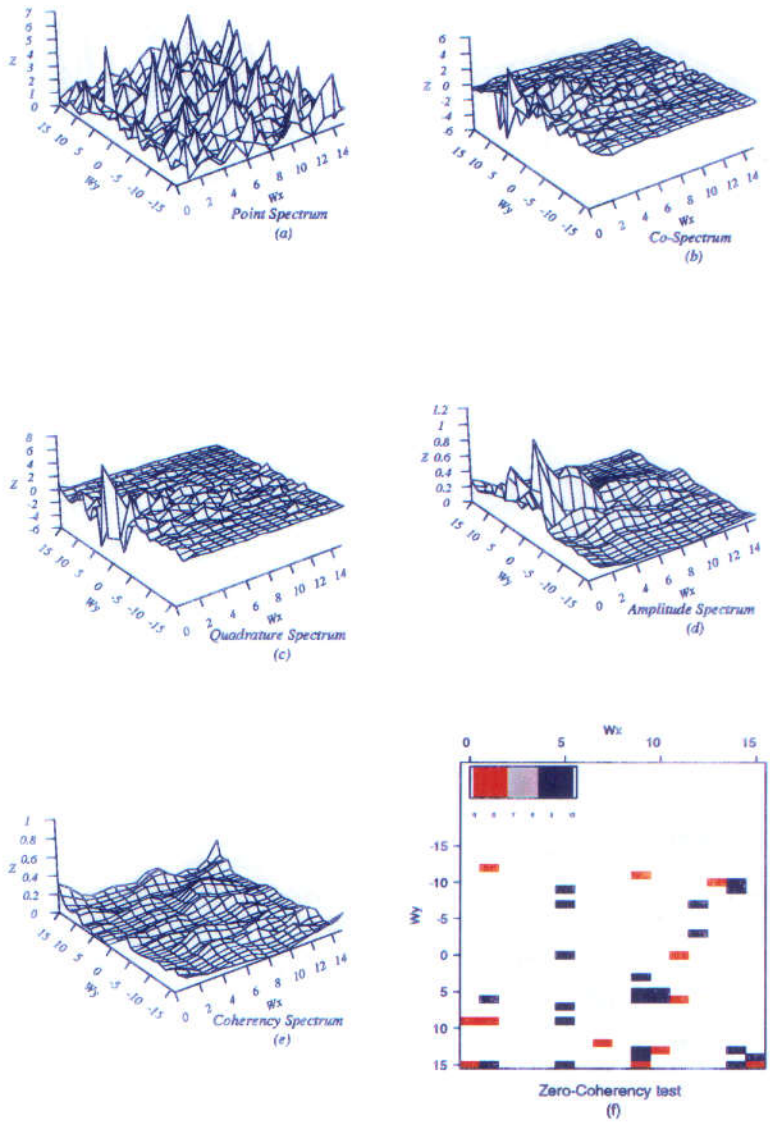

Figure 7.27: Spectra of initiation versus elevation for short-lived storms in the western subregion:(a) auto-periodogram of initiation points; (b) and (c) raw co- and quadrature spectra; (d) and (e) amplitude and coherency spectra smoothed using Method A four times; (f) significant ordinates of the zero coherency test at the 1%, 5% and 10% levels, the value represents the significance level.

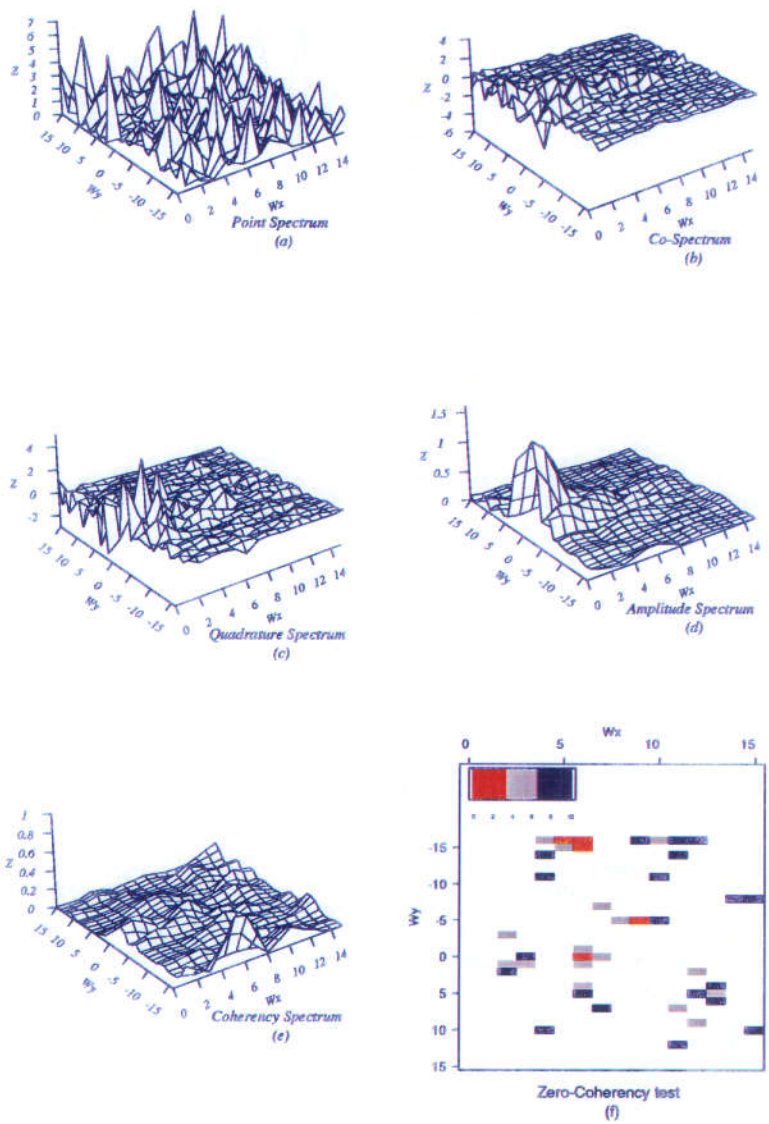

Figure 7.28: Spectra of initiation versus elevation for medium-lived storms in the western subregion:(a) auto-periodogram of initiation points; (b) and (c) raw co- and quadrature spectra; (d) and (e) amplitude and coherency spectra smoothed using Method A four times; (f) significant ordinates of the zero coherency test at the 1%, 5% and 10% levels, the value represents the significance level.

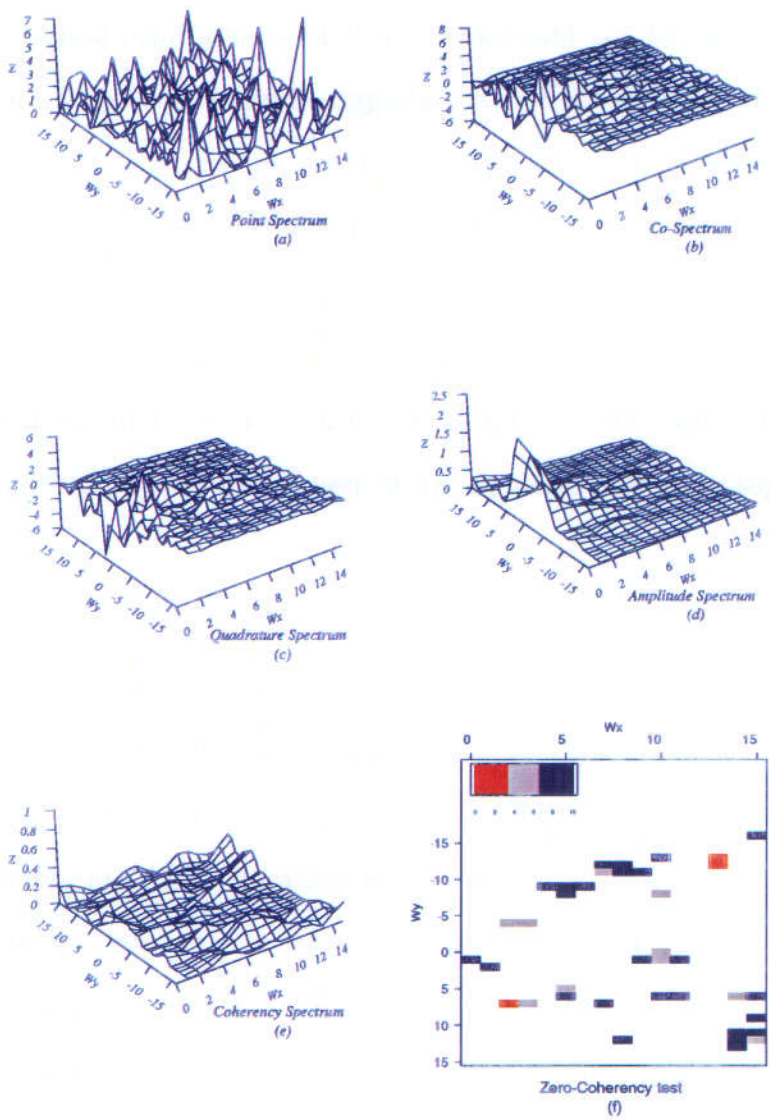

Figure 7.29: Spectra of initiation versus elevation for long-lived storms in the western subregion:(a) auto-periodogram of initiation points; (b) and (c) raw co- and quadrature spectra; (d) and (e) amplitude and coherency spectra smoothed using Method A four times; (f) significant ordinates of the zero coherency test at the 1%, 5% and 10% levels, the value represents the significance level.

They also reported that visual comparison of the maps of storm initiation points and elevation suggests that there is a link between the storm duration and the proximity of mountains to the points where the storms initiate. However, formal confirmation of such a link could not be established using random labelling. Our analysis suggests that for the data set at hand there is insufficient evidence to support the claim that storm duration is in general related to the elevation data, except for medium-lived storms in the eastern subregion where there is some evidence that such a link exists. Nevertheless, storm initiation was found to be correlated with elevation. Further studies can be carried out to see if such relationships hold for similar data and to investigate if there is a link between storm duration and other topographical features.

7.5 Summary

Using cross-spectral analysis techniques for processes with two and three components, we explored the relationship between elevation data, storm initiation points and their duration within the Sahel region of Africa. The analysis of this data set was carried out using several scenarios.

First, the data set was studied within the entire region. It was shown that initiation points and elevation data are correlated, however the type of correlation is dependent on the direction of travel of the main waves underlying the processes. Furthermore, evidence of correlation between duration and either elevation or initiation was not strong.

Second, conditional on duration being classified as short-, medium-, or long-lived, the properties of initiation points and elevation were explored.

The spectra between initiation and elevation for the different categories exhibited similar features, mainly within the co-spectrum, but the magnitudes of these features varied from one category to another. Again it was not evident that correlation between initiation points and elevation differed according to storm duration.

Third, the above two approaches were used to study the properties of two subsets of the data. The two subsets were derived by splitting Region A into eastern and western subregions. Initiation points in the eastern subregion were found to be correlated with elevation data. However, in the western subregion correlation between these two components was to a lesser extent. Furthermore, there was insufficient evidence to suggest duration and the other two components were correlated within the subregions. Classifying the storms by duration in the eastern subregion revealed that correlation between initiation and elevation differed between the duration categories. Visual inspection of the different spectra revealed that the correlation between the medium-lived storms and elevation was relatively stronger than for the other duration categories. However, no such phenomenon was detected in the western subregion.

Chapter 8

Conclusions and Directions for Further Research

In this chapter, we summarise the main results of this study and propose directions for further research in this area.

8.1 Conclusions

In this section, we recap the major contributions of this study. In general, we have established that two-dimensional spectral analysis techniques can be used to explore the relationship between the components of a hybrid process consisting of a spatial point process and a lattice process. Thus, the basis for nonparametric analysis of such processes was laid down. In addition, we have derived asymptotic distributions of the spectral density matrix of the hybrid process. These distributions are analogous to results from studies of one-dimensional processes. We have also provided analyses of two real data sets. In more detail, this thesis contains the following achievements.

- The potential of cross-spectral estimates to unveil the nature of correlation between a two-dimensional point process and a lattice process

was demonstrated using simulated examples.

- Models that extend two-dimensional linked and balanced doubly stochastic point processes introduced by Diggle and Milne (1983) to the case of linked and balanced point-lattice processes were provided. In addition, for simulated examples of these models we have shown that the spectral estimates were in agreement with the theoretical results.

- A method to adjust the phase spectrum for jumps that are due to the constraint of the phase belonging to the interval $(-\pi, \pi)$ was provided. The importance of these adjustments for extracting information about the phase shift between the two components of the hybrid process was manifested through simulated examples.

- Techniques to calculate slopes of the phase spectrum locally were suggested. The need for these techniques arises mainly for two reasons:

    1. in some situations, the two components are only related at a subset of the frequencies investigated; and

    2. the phase spectrum is not necessarily linear in all cases.

- For non-zero frequencies, the asymptotic distribution of the cross-spectral matrix was established to be a complex Wishart distribution of dimension two with one degree of freedom. For zero frequencies, the distribution was established to be a Wishart distribution of dimension two with one degree of freedom. In addition, the cross-periodogram statistic was shown to be an unbiased estimator of the cross-spectral statistic

and cross-spectral estimates at different frequencies were shown to be asymptotically independent of each other.

- Confidence intervals were obtained for the auto-, co-, quadrature and phase spectra using the asymptotic properties.

- A test for zero coherency was discussed. The test statistic followed an F distribution. The motivation for applying the test is to determine formally the range of frequencies where the two components are correlated.

- Several methods for discretising point patterns to form lattice patterns were considered, and the joint properties of the resulting lattice-lattice patterns were studied. We examined the extent to which such an approach eliminates problems that can be attributed to lattice patterns being observed on grid points whereas point patterns being observed anywhere in the study region.

- We established spectral tools for analysing hybrid processes including marked point processes.

- For the trees of the rain forest of French Guyana, we found that Species 3, 10 and 11 were to the north-west of the altitude pattern. In addition, Species 3, 11, and 12 favoured relatively low altitudes, whereas Species 10 favoured high altitude.

- In analysing the storm data of the Sahel region of Africa, we considered several scenarios. The main findings in each case are listed below.

- For the entire region, we showed that initiation points and elevation data were correlated. However, the nature of correlation depended on the direction of travel of the main waves underlying the two components. Furthermore, evidence of correlation between duration and either elevation or initiation was not strong.
- The relationships between initiation points and elevation were explored conditional on duration being classified as short-, medium-, or long-lived. Similar features were observed in the cross-spectra of initiation and elevation for the different duration categories. This similarity was mainly manifested in the co-spectrum.
- The study region was divided into eastern and western subregions, and the relationships between initiation points, their durations, and elevation were studied using the previous scenarios. In the eastern subregion, initiation points were found to be correlated with elevation data, whereas in the western subregion this correlation was not as strong. Again, correlation between duration and the other two components was not evident within the subregions. Analyses of storm initiation and elevation conditional on the classified duration revealed that the extent of correlation between medium-lived storms and elevation was relatively stronger than for the other duration categories. No such phenomenon was observed in the western subregion.

8.2 Future Work

This thesis has not exhausted all the possible methods one can use to study the relationship between a spatial point process and a lattice process. In what follows, we list some suggestions for extending this study.

- Throughout this thesis analysis of hybrid processes has been based on second-order cumulant functions. As an immediate extension one can consider studying the properties of hybrid processes using *third-* and *higher-order cumulants* and their Fourier transforms. This approach might be particularly useful for the hybrid process consisting of a marked spatial point process and a lattice process because it would enable us to study quantities such as

$$\mathrm{Cum}\{dM_X(\mathbf{a}), dN_X(\mathbf{a}), Y_{\mathbf{a}}\},$$

where M_X and N_X represent the cumulative mark process and cumulative number of events of the point process X, and Y is the lattice process. The importance of third- and higher-order cumulant functions is due mainly to the fact that for Gaussian processes cumulants that are of order greater than two vanish (see Brillinger, 1994). This is relevant to our case because under the null hypothesis of CSR it was found that the individual DFTs of point and lattice processes were Gaussian. In addition, studying higher-order spectra would enable the detection of processes that have their first- and second-order equivalent to those of a completely spatially random process but are not themselves completely spatially random.

- Spectral analysis techniques are based on transformations of the process using Fourier functions. As an alternative approach one might investigate the joint properties of the (marked) point processes and lattice processes using *wavelets*. Wavelets are transformations of a process composed of translations and scalings of a single function called the *mother* function (see Nason and Silverman, 1994). In time series analysis wavelets offer a more efficient representation for non-smooth and/or discontinuous functions than do Fourier transforms, although for smooth functions the converse is true (see Nason and Silverman, 1994).

- In this study, when the joint properties of marked spatial point processes and lattice processes were examined the mark process was assumed to possess one component. An obvious extension would be to consider several components of this process. For example, the marks process for the Sahel storms may consist of the storm speed in addition to the storm duration.

- Further studies to investigate the possibility of an equivalence between bandwidth selectors for kernel density and intensity estimators for the one- and two-dimensional cases using plug-in methods could be carried out, see Chapter 5 for more details. This equivalence might be based on the equivalence between bandwidth selectors for this intensity estimator and kernel density for the one-dimensional case using the LSCV criterion proved by Diggle and Marron (1988).

- In connection with the study of the storms data set, it would be of interest to study the joint spectral properties of storm tracks and the

elevation data. The storm tracks are defined as the line segments joining the points where the storms initiated, reached their maximum size and dissipated, see Figure 8.1. In Figure 8.1 the dots represent initiation points, the triangles represent the positions where the storms reached their maximum size, and the crosses represent the positions where the storms dissipated. Thus one might consider an extension of Bartlett's (1967) work on the spectral analysis of line segments.

- Both data sets that were used in this study are extracts from a larger data base. An interesting extension would be to carry out similar analyses on the other parts of the data and compare and contrast results with the findings of this study.

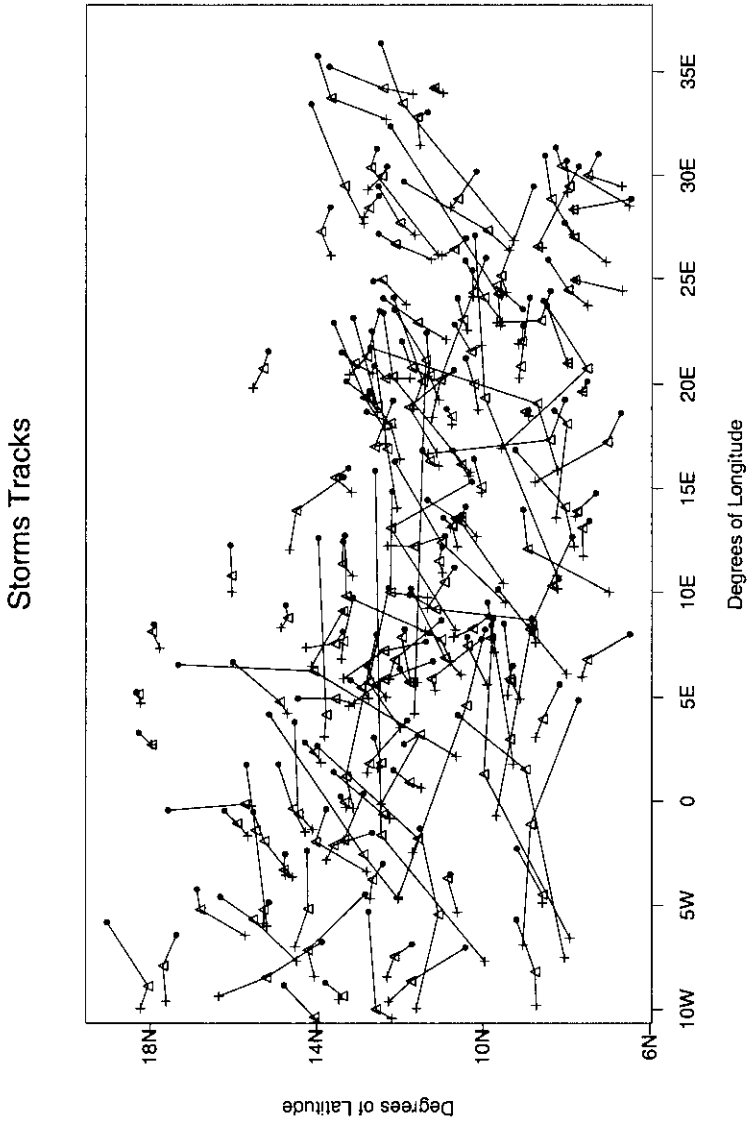

Figure 8.1: The dots represent initiation points, the triangles represent the positions where the storms reached their maximum size, and the crosses represent the positions where the storms dissipated. The storm tracks are defined as the line segments joining the points.

Appendix A

Mathematical Tools

A.1 Useful Identities

The following are a set of well known trigonometric relations. Let p_1 and p_2 be two integers such that $0 \leq p_1, p_2 \leq [N/2]$, then

$$\sum_{t=1}^{N} \cos\left(\frac{2\pi p_1 t}{N}\right) \cos\left(\frac{2\pi p_2 t}{N}\right) = \begin{cases} 0 & \text{if } 0 \leq p_1 \neq p_2 \leq [N/2], \\ N/2 & \text{if } 0 < p_1 = p_2 < N/2, \\ N & \text{if } p_1 = p_2 = (0 \text{ or } N/2 \text{ if } N \text{ is even.}) \end{cases}$$

$$\sum_{t=1}^{N} \sin\left(\frac{2\pi p_1 t}{N}\right) \sin\left(\frac{2\pi p_2 t}{N}\right) = \begin{cases} 0 & \text{if } 0 \leq p_1 \neq p_2 \leq [N/2], \\ N/2 & \text{if } 0 < p_1 = p_2 < N/2, \\ 0 & \text{if } p_1 = p_2 = (0 \text{ or } N/2 \text{ if } N \text{ is even.}) \end{cases}$$

$$\sum_{t=1}^{N} \sin\left(\frac{2\pi p_1 t}{N}\right) \cos\left(\frac{2\pi p_2 t}{N}\right) = 0 \text{ for all } p_1, p_2.$$

A.2 Delta Functions

The following are some basic functions that are needed for the proof of theorems included in previous chapters. The definitions were taken from Brillinger (1981, chapter 2) and are reproduced here because we found it difficult to obtain a copy of Brillinger (1981).

Kronecker delta

$$\delta\{\alpha\} = \begin{cases} 1 & \text{if } \alpha = 0 \\ 0 & \text{otherwise.} \end{cases} \tag{A.1}$$

Kronecker comb

$$\eta\{\alpha\} = \begin{cases} 1 & \text{if } \alpha \equiv 0(\mod 2\pi) \\ 0 & \text{otherwise.} \end{cases} \tag{A.2}$$

Dirac delta function

$$\delta(\alpha), -\infty < \alpha < \infty, \tag{A.3}$$

with the property

$$\int_{-\infty}^{\infty} f(\alpha)\delta(\alpha)d\alpha = f(0) \tag{A.4}$$

for all functions $f(\alpha)$ continuous at 0.

Dirac comb

$$\eta(\alpha) = \sum_{j=-\infty}^{\infty} \delta(\alpha - 2\pi j), \text{ for } -\infty < \alpha < \infty, \tag{A.5}$$

with the property

$$\int_{-\infty}^{\infty} f(\alpha)\eta(\alpha)d\alpha = \sum_{j=-\infty}^{\infty} f(2\pi j) \tag{A.6}$$

for all suitable functions $f(\alpha)$.

A.3 Relevant Distributions

In this section, we provide definitions of the complex normal multivariate distribution and the complex Wishart distribution.

The Complex Normal Distribution Let $N_k(\mu, \Sigma)$ denotes a k vector–valued normal distribution with mean μ and covariance matrix Σ. Let $\mathbf{X}$ be a k complex vector–valued variate, then $\mathbf{X}$ is said to be a complex k vector–valued normal variate denoted by $N_k^{\mathbb{C}}(\mu, \Sigma)$, if

$$\begin{bmatrix} \mathrm{Re}\mathbf{X} \\ \mathrm{Im}\mathbf{X} \end{bmatrix} = N_{2k} \left(\begin{matrix} \mathrm{Re}\mu, \\ \mathrm{Im}\mu, \end{matrix} \frac{1}{2} \begin{bmatrix} \mathrm{Re}\Sigma & -\mathrm{Im}\Sigma \\ \mathrm{Im}\Sigma & \mathrm{Re}\Sigma \end{bmatrix} \right)$$

From the above definition, one can conclude that

$\mathbb{E}[(\mathbf{X} - \mu)\overline{(\mathbf{X} - \mu)}^{\top}] = \Sigma$ and that $\mathbb{E}[(\mathbf{X} - \mu)(\mathbf{X} - \mu)^{\top}] = \mathbf{0}$.

The Complex Wishart Distribution If $\mathbf{X}_1, \ldots, \mathbf{X}_m$ are independent $N_k^{\mathbb{C}}(\mathbf{0}, \Sigma)$ variates, then the $k \times k$ matrix-valued random variable $\mathbf{W} = \sum_{j=1}^{m} \mathbf{X}_j \overline{\mathbf{X}_j^{\top}}$ is said to have a complex Wishart distribution of dimension k and degrees of freedom m, and is written as $W_k^{\mathbb{C}}(m, \Sigma)$. This distribution was introduced by Goodman (1963), it is an extension of the Wishart distribution. Now, if we write $\mathbf{W} = ||\mathbf{W}_{jkR} + i\mathbf{W}_{jkI}||$, where R, I in the subscript denote the real part and the imaginary part, respectively. The joint distribution of the distinct elements of the matrix $\mathbf{W}$ is called a *complex Wishart distribution.* The probability density function of the joint distribution is given by

$$f_{\mathbf{W}}(V) = |V| \mathfrak{I}(\Sigma) \exp\{-\mathrm{tr}(\Sigma^{-1} V)\}$$

where,

$$\mathfrak{I}^{-1}(\Sigma) = \pi^{\frac{1}{2}k(k-1)} |\Sigma|^m \prod_{j=0}^{k-1} \Gamma(m - j),$$

and $|V|$ denotes the determinant of the matrix V. In addition, Γ is the gamma function. The density $f_{\mathbf{W}}(V)$ is defined over the domain where V is Hermitian positive semi-definite.

A.4 Linear and Space Invariant Operators

An important class of operators consists of those that are *linear* and *space invariant* (see Brillinger, 1970). Let $\mathfrak{B}$ be an operator whose domain, $\mathbb{D}$, is a process $X(\mathbf{a}), \mathbf{a} \in \mathbb{R}^2$. The operation is linear if

$$\mathfrak{B}[b_1 X_1 + b_2 X_2](\mathbf{a}) = b_1 \mathfrak{B}[X_1](\mathbf{a}) + b_2 \mathfrak{B}[X_2](\mathbf{a}),$$

where b_1, b_2 are constants and X_1, X_2 are in $\mathbb{D}$.

The operation is space invariant, if

$$\mathfrak{B}[\mathbb{T}^{\mathbf{u}} X](\mathbf{a}) = \mathfrak{B}[X](\mathbf{a} + \mathbf{u}),$$

where $\mathbb{T}^{\mathbf{u}} X(\mathbf{a}) = X(\mathbf{a} + \mathbf{u})$.

Appendix B

Cumulants

B.1 Definition and Properties

It is well known that the characteristic function, $\Psi(t)$, of a given distribution determines the distribution uniquely. In addition, knowing the distribution function enables us to calculate the moments of all orders of the given distribution by using the Taylor expansion of the function, if such an expansion exist.

Therefore, if we are interested in determining the joint distribution of products of random variables, as it is the case here, then it is sufficient to establish the characteristic function of the product. However, in most cases, it is algebraically difficult to do so. Such a problem can be simplified by using the log transform, which maps products to sums.

Hence, instead of calculating the characteristic function, one determines its log transform, $\log \Psi(t)$, known as the *cumulant generating function* (see Kendall and Stuart, 1963, chapter 3). Since the log transform is a one to one transformation then the cumulant generating function also determines the distribution of a given random variable uniquely.

Next following the notation in Brillinger (1981, chapter 2), *cumulants* are defined by analogy to the moments of a distribution.

Definition B.1.1 *Let* $(Y_1, \ldots, Y_r)$ *be an* r *variate random variable with* $\mathbb{E}|Y_j|^r < \infty$ *for* $j = 1, \ldots, r$, *where the* Y_j *are real or complex and* $\mathbb{E}Y = \int y dF(y)$. *The* r^{th}*–order joint cumulant,* $Cum(Y_1, \ldots, Y_r)$, *of* $(Y_1, \ldots, Y_r)$ *is given by the coefficient of* $i^r t_1 \cdots t_r$ *in the Taylor series expansion of* $\log(\mathbb{E}\exp i \sum_{j=1}^{r} Y_j t_j)$ *about the origin.*

However, authors such as Brillinger (1981) and Kendall and Stuart (1963) give the above definition as a theorem after defining the cumulant function of several variables as below.

Definition B.1.2 *Let* $(Y_1, \ldots, Y_r)$ *be as above, then*

$$Cum(Y_1, \ldots, Y_r) = \sum (-1)^{p-1}(p-1)! \, (\mathbb{E}\prod_{j \in \nu_1} Y_j) \ldots (\mathbb{E}\prod_{j \in \nu_p} Y_j), \qquad \text{(B.1)}$$

where the summation extends over all partitions $(\nu_1, \ldots, \nu_p)$, $p = 1, \ldots, r$, *of* $(1, \ldots, r)$.

A special case occurs when $Y_j = Y$, $j = 1, \ldots, r$. The definition gives then the cumulant of order r of a univariate random variable.

Note that for $r = 1, 2, 3$ Definition B.1.2 implies that

$$\begin{aligned}
\mathrm{Cum}\{Y\} &= \mathbb{E}\{Y\}, \\
\mathrm{Cum}\{Y_1, Y_2\} &= \mathbb{E}\{Y_1 Y_2\} - \mathbb{E}\{Y_1\}\mathbb{E}\{Y_2\}, \\
\mathrm{Cum}\{Y_1, Y_2, Y_3\} &= \mathbb{E}\{Y_1 Y_2 Y_3\} - \mathbb{E}\{Y_1 Y_2\}\mathbb{E}\{Y_3\} - \mathbb{E}\{Y_1 Y_3\}\mathbb{E}\{Y_2\} - \\
&\qquad \mathbb{E}\{Y_2 Y_3\}\mathbb{E}\{Y_1\} + \mathbb{E}\{Y_1\}\mathbb{E}\{Y_2\}\mathbb{E}\{Y_3\}.
\end{aligned}$$

Next, we list some properties of cumulant functions.

1. $\text{Cum}(a_1 Y_1, \ldots, a_r Y_r) = a_1 \cdots a_r \text{Cum}(Y_1, \ldots, Y_r)$ for $a_1, \ldots, a_r$ constants.

2. The function $\text{Cum}(Y_1, \ldots, Y_r)$ is symmetric in its arguments.

3. If any group of the Y's is independent of the remaining Y's, then $\text{Cum}(Y_1, \ldots, Y_r) = 0$.

4. For the random variable $(Z_1, Y_1, \ldots, Y_r)$,

$$\text{Cum}(Y_1 + Z_1, Y_2, \ldots, Y_r) = \text{Cum}(Y_1, Y_2, \ldots, Y_r) + \text{Cum}(Z_1, Y_2, \ldots, Y_r).$$

5. For μ constant and $r = 2, 3, \ldots$

$$\text{Cum}(Y_1 + \mu, Y_2, \ldots, Y_r) = \text{Cum}(Y_1, Y_2, \ldots, Y_r).$$

6. If the random variables $(Y_1, \ldots, Y_r)$ and $(Z_1, \ldots, Z_r)$ are independent then,

$$\text{Cum}(Y_1 + Z_1, \ldots, Y_r + Z_r) = \text{Cum}(Y_1, \ldots, Y_r) + \text{Cum}(Z_1, \ldots, Z_r).$$

7. $\text{Cum}(Y) = \mathbb{E}(Y)$.

8. $\text{Cum}(Y, \bar{Y}) = \text{Var}(Y)$.

9. $\text{Cum}(Y, \bar{Z}) = \text{Cov}(Y, Z)$.

B.2 Important Lemma

In this section, we supply a lemma that enables us to determine the cumulants for a random variable in a systematic manner. This lemma is due to Leonov and Shiryaev (1959) for real random variables but was extended by Brillinger

and Rosenblatt (1967) to the complex case. First, we introduce some relevant definitions.

Definition B.2.1 *Consider a (not necessarily rectangular) two way table*

$$\begin{array}{ccc} (1,1) & \dots & (1,k_1) \\ (2,1) & \dots & (2,k_2) \\ \vdots & \vdots & \vdots \\ (J,1) & \dots & (J,k_J) \end{array} \tag{B.2}$$

and a partition of its elements into disjoint sets $\{ P_1 , P_2 , \dots , P_m \}$ *two sets of the partition* P_{i_1} *and* P_{i_2} *are said to* ***hook*** *if there exist* $(j_1, j_2) \in P_{i_1}$ *and* $(j_3, j_4) \in P_{i_2}$ *such that* $j_1 = j_3$.

Definition B.2.2 *Two sets* $P_{i'}$ *and* $P_{i''}$ *are said to* ***communicate*** *if there exists a sequence of sets* $P_{i'} = P_{i_1}, P_{i_2}, \dots , P_{i_r} = P_{i''}$ *such that* P_{i_j} *and* $P_{i_{j+1}}$ *hook for each* j.

Definition B.2.3 *A partition is said to be* ***indecomposable*** *if all its sets communicate.*

Result 1 *If the rows of the above table are denoted by* $R_1, \dots , R_J$ *then* $\{ P_1, \dots , P_m \}$ *is indecomposable if and only if there exists no sets* $P_{i_1}, \dots , P_{i_n}$ $(n < m)$ *and rows* $R_{j_1}, \dots , R_{j_p}$ $(p < J)$ *with*

$$P_{i_1} \cup \dots \cup P_{i_n} = R_{j_1} \cup \dots \cup R_{j_p}$$

Lemma B.2.1 *Given an array* $||Y_{mn}||, n = 1, \dots , K_m$ *and* $m = 1, \dots , J$ *of random variables consider the* J *complex random variables*

$$z_m = \prod_{n=1}^{K_m} Y_{mn}.$$

The joint J^{th}-order cumulant $Cum\{z_1, \ldots, z_J\}$ is given by

$$\sum_{\nu} C_{\nu_1} \ldots C_{\nu_p} \tag{B.3}$$

where $C_\nu = Cum\{Y_{a_1}, \ldots, Y_{a_m}\}$ when $\nu = (a_1, \ldots, a_m)$ the a's being pairs of integers taken from the above table and the summation extends over all indecomposable partitions of the above table.

Result 2 *For a Normal variable X, it can be easily shown that cumulants of order greater than two vanish (see Kendall and Stuart, 1963, chapter 5). Hence, to show that a variable is normally distributed it is sufficient to show that the cumulants of order greater than two vanish. This is so because the Normal distribution is determined by its moments.*

Appendix C

Tree Species (Continued)

In this appendix we provide exploratory cross-spectral analyses for Species 2, 4,..., 9, 13 and 14 that are listed in Table 6.1. In addition, the joint properties of species that belong to the same family are studied.

C.1 Species 2: Gaulette

Figure C.1(a) is the graph of Gaulette versus altitude pattern. Figure C.1(b) has two peaks at the frequencies $(0, 1)$ and $(1, -1)$. This indicates that Gaulette resembles a cluster process repeating once in the SN direction and along the direction of the 135° angle. These peaks are significant at the 5% and 10% level, respectively.

Henceforth, we will only report significant features of the species studied, obvious interpretations will be omitted. However, for completeness we will provide all the essential figures associated with each species.

The co-spectrum, Figure C.1(c), has peaks at $(0, 1)$ and $(1, -1)$. The quadrature spectrum, Figure C.1(d), has troughs at $(1, 1), (0, 1)$, and a peak at $(1, 0)$. The phase and coherency spectra are given in Figures C.1(e) and

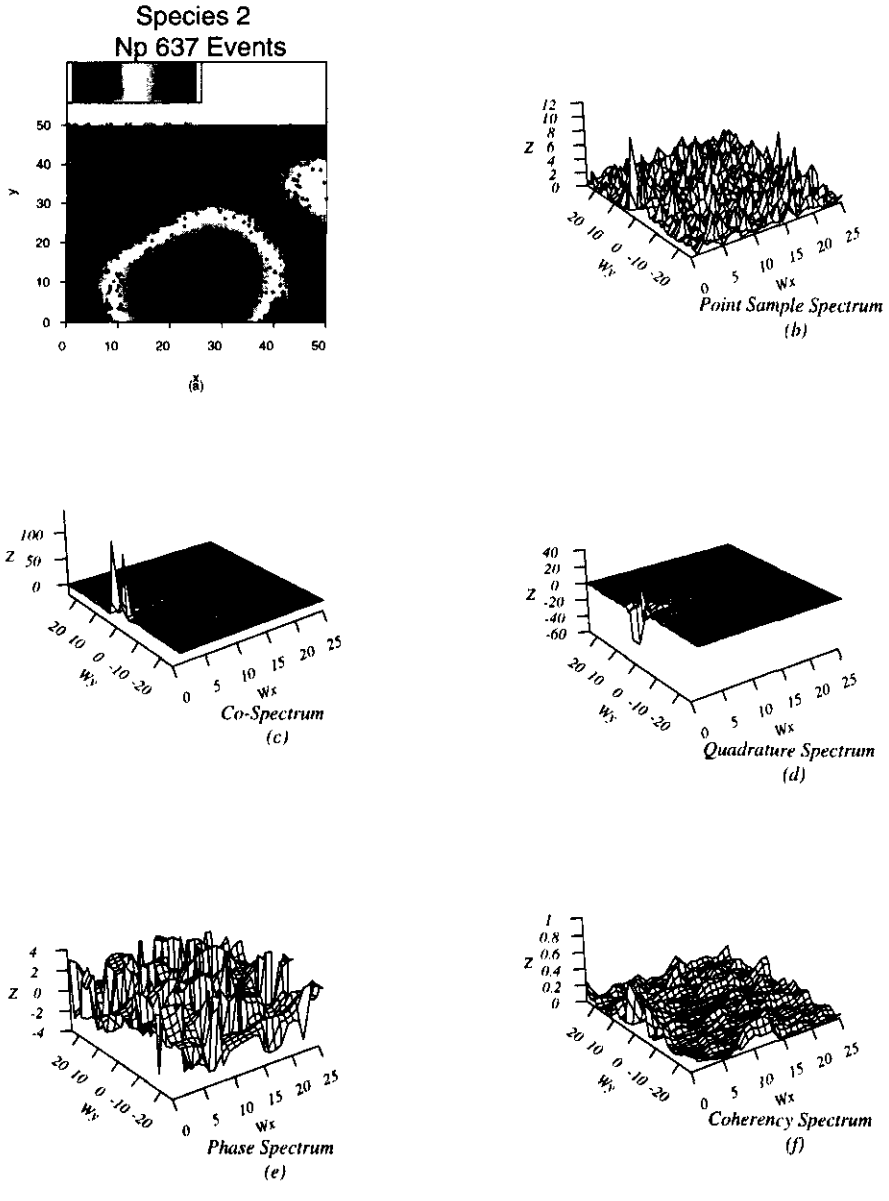

Figure C.1: (a) Gaulette versus altitude pattern; (b) raw auto-periodogram of the point pattern; (c) and (d) raw co- and quadrature spectra; (e) and (f) smoothed phase and coherency spectra using Method A four times.

(f), respectively.

Figure C.2 is the profile of the zero coherency test for Gaulette versus altitude pattern for $p = 0, \ldots, 15$. Figures C.3(a) and (b) represent the adjusted phase spectra in the WE/SN directions for the frequencies where concentration of significant ordinates was observed in the zero coherency test. Note that coherency is concentrated along the frequencies $(p = 1, q = \{-2, \ldots, 2\})$ and $(q = 2, p = \{0, \ldots, 4\})$. The slope in the SN direction for the frequency band $p = 1$ is -0.12, and the slope in the WE direction for the frequency band $q = 2$ is -0.11. Thus Gaulette is to the east of the altitude data by 0.6m and to its north by 0.55m.

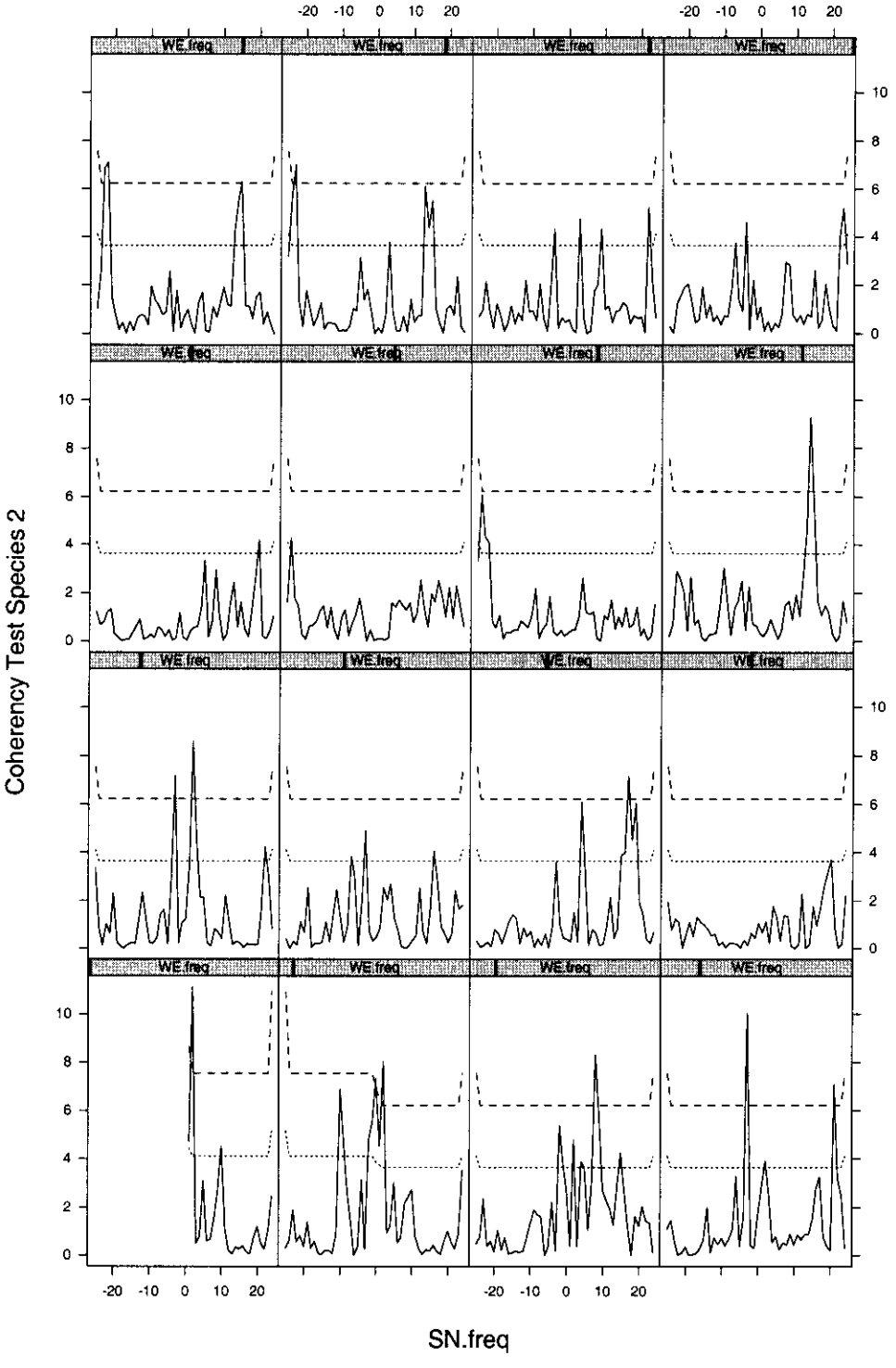

Figure C.2: Profile of the zero coherency test statistic spectrum for Gaulette versus altitude pattern for $p = 0, \ldots, 15$, solid line, and the corresponding upper 5/1% critical point of the F distribution, dotted/dashed line.

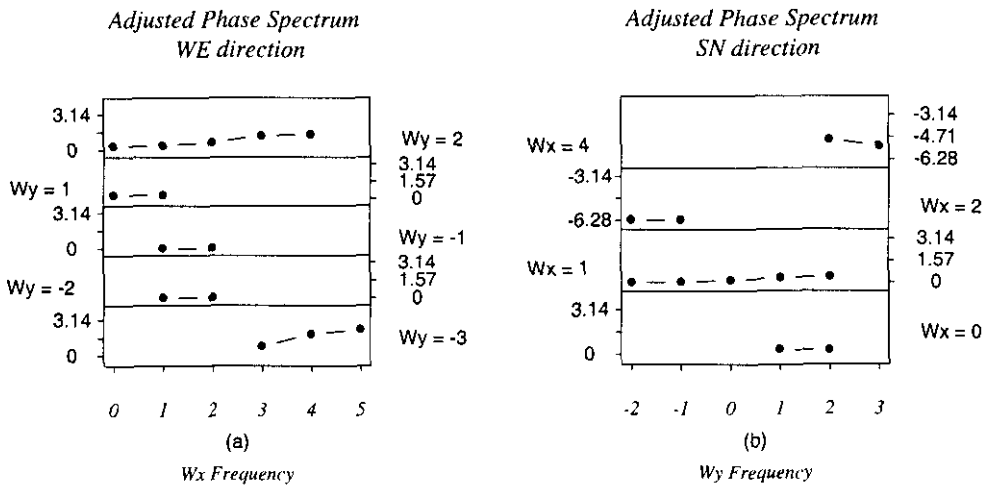

Figure C.3: (a) and (b) Profile of the adjusted phase spectrum (Gaulette versus altitude pattern) in the WE and SN directions for the frequencies $p = 0, 1, 2, 4$ and $q = -3, -2, -1, 1, 2$.

C.2 Species 4: Palmiers

The locations of Palmiers are presented in Figure C.4(a) superimposed on altitude values. The raw auto-periodogram of the point pattern, Figure C.4(b), has peaks at $(4, 1)$ and $(1, -1)$. The former frequency was found to be the only significant frequency at the 5% level among the frequencies investigated.

Figure C.4(c) is the co-spectrum, and it possesses a trough at $(1, -1)$ and a peak at $(1, 0)$. The quadrature spectrum has peaks at $(1, -1)$, $(0, 1)$ and a trough at $(1, 1)$, see Figure C.4(d). The phase and coherency spectra are represented in Figures C.4(e) and (f), respectively.

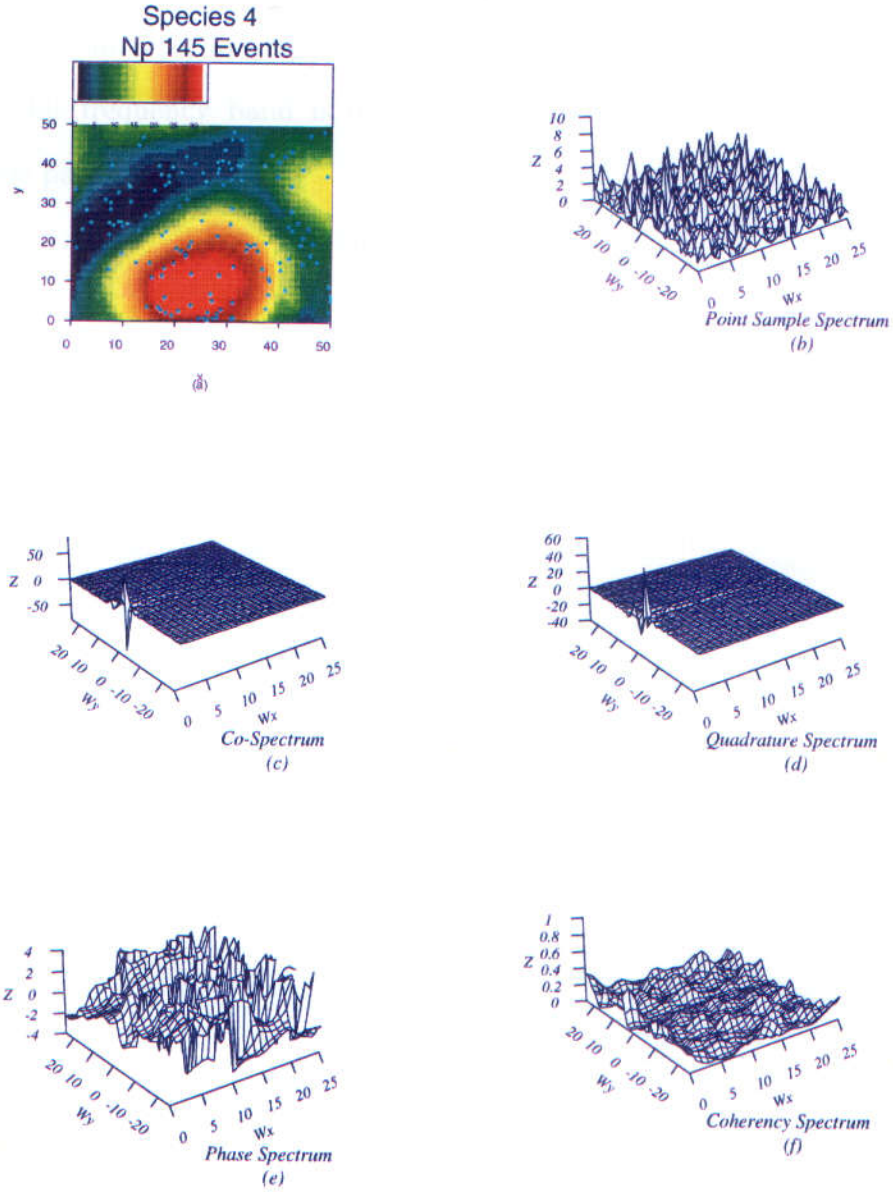

Figure C.4: (a) Palmiers versus altitude pattern; (b) raw auto-periodogram of the point pattern; (c) and (d) raw co- and quadrature spectra; (e) and (f) smoothed phase and coherency spectra using Method A four times.

The profile of the zero coherency test for $p = 0, \ldots, 15$, is provided in Figure C.5. From this figure we note that the coherency is significantly different from zero, at the 5% level, for $(q = 4, p = \{0, 1, 2\})$. The slope along this frequency band is 0.67. Thus Palmiers lie to the west of the altitude pattern by 3.35m.

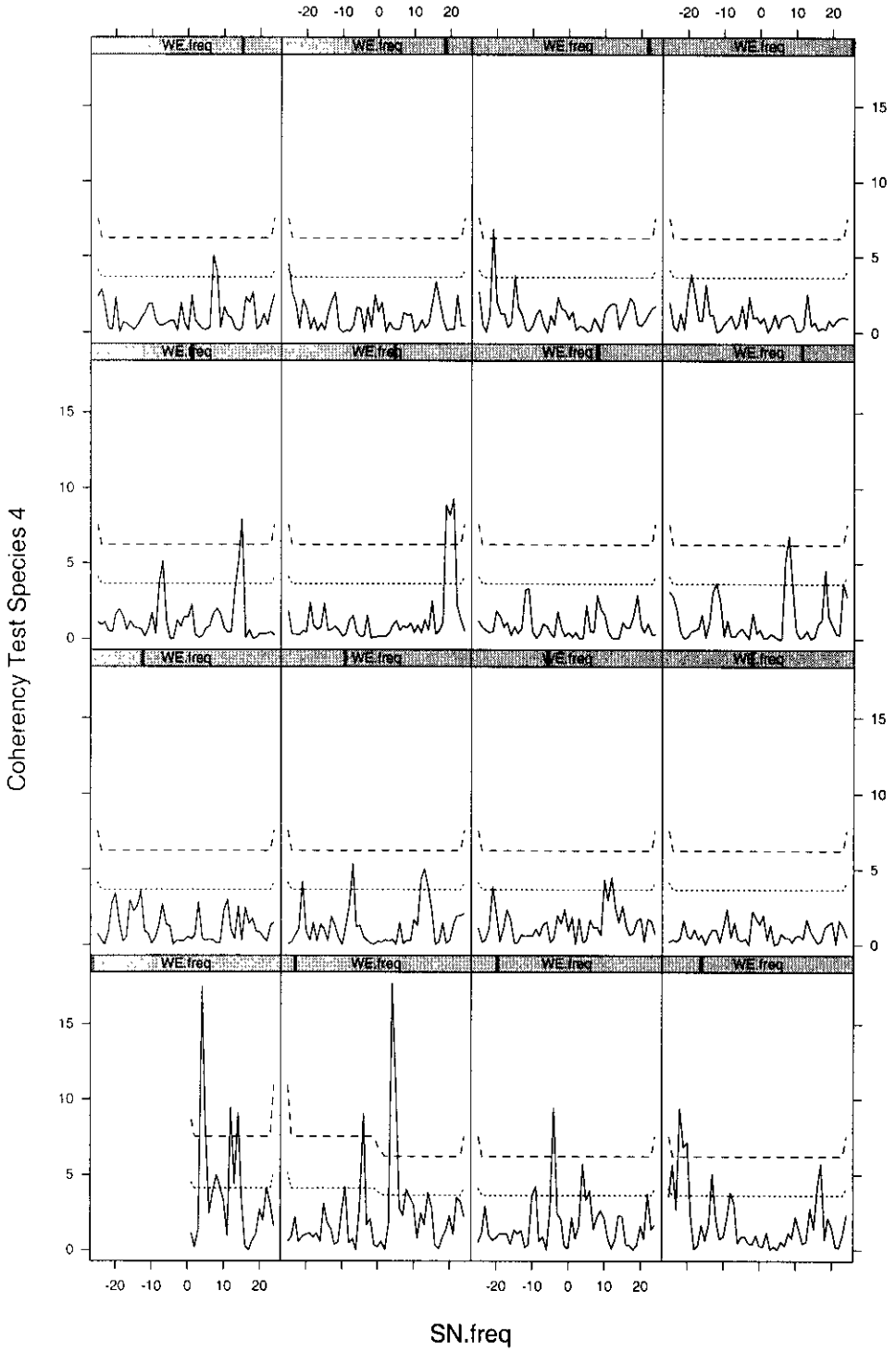

Figure C.5: Profile of the zero coherency test statistic spectrum for Palmiers versus altitude pattern for $p = 0, \ldots, 15$.

C.3 Species 5: Encens

Figure C.6(a) gives the locations of Encens together with altitude values. The sample point spectra, Figure C.6(b), has peaks at $(1, 0)$, $(20, -11)$, $(0, 2)$ and $(0, 1)$. The peak at $(1, 0)$ is significant at the 5% level. However, given that the number of events is 131, the frequency range is restricted so that the significance of the frequency $(20, -11)$ cannot be assessed.

A peak is observed at $(0, 1)$ in the co-spectrum, Figure C.6(c), and a trough is observed at $(1, -1)$. The quadrature spectrum, Figure C.6(d), has a major trough at $(1, 0)$. Figures C.6(e) and (f) represent the phase and coherency spectra, respectively. The coherency is significantly different from zero at the 5% level for the frequency band ($p = \{0, \ldots, 4\}, q = 3$). The slope of the adjusted phase spectra in the SN direction for this frequency band is -1.24.

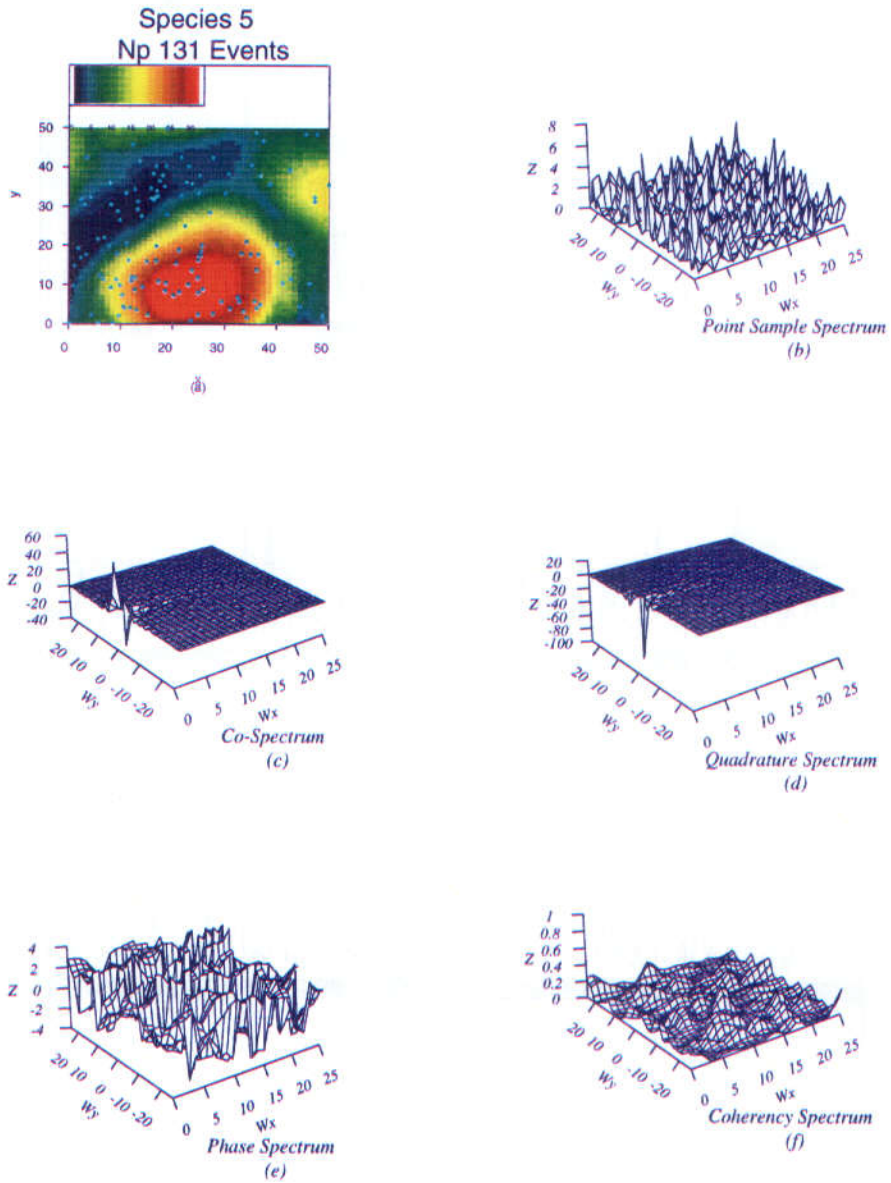

Figure C.6: (a) Encens versus altitude pattern; (b) raw auto-periodogram of the point pattern; (c) and (d) raw co- and quadrature spectra; (e) and (f) smoothed phase and coherency spectra using Method A four times.

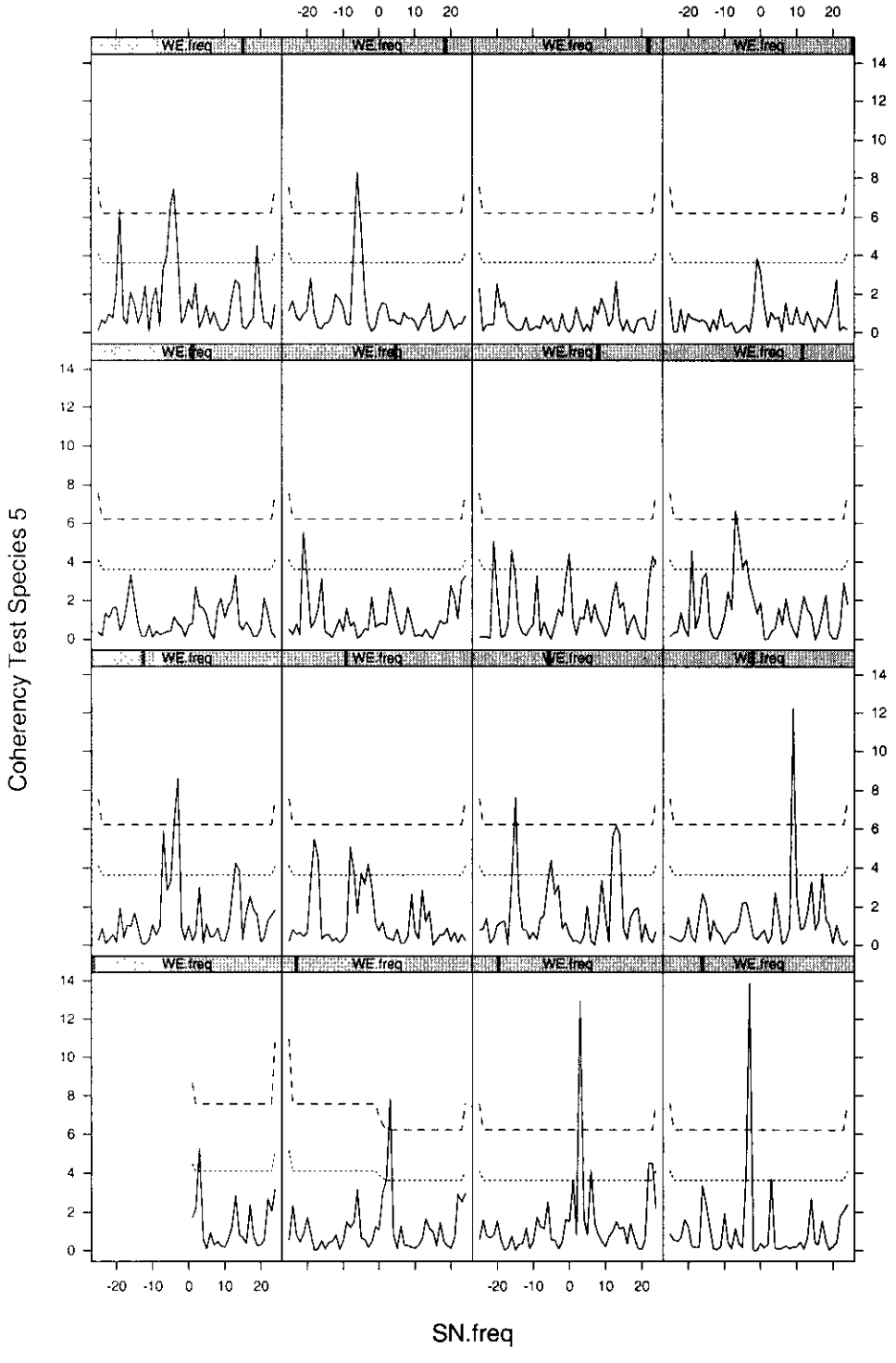

Figure C.7: Profile of the zero coherency test statistic spectrum for Encens versus altitude pattern for $p = 0, \ldots, 15$.

C.4 Species 6: Tosso Passa

The point pattern of Tosso Passa is presented in Figure C.8(a) together with altitude values of the study region. The auto-periodogram of the point pattern, Figure C.8(b), has peaks at $(17, 15)$ and $(1, -2)$. However, the null hypothesis of CSR was not rejected at the 10% significance level.

The co-spectrum, Figure C.8(c), possesses major troughs at $(0, 1)$, $(1, -1)$ and a minor peak at $(1, 0)$. The quadrature spectrum, Figure C.8(d), exhibits troughs at $(1, 0), (0, 1)$, and peaks at $(1, -1)$, $(0, 2)$. The detection of these peaks and troughs, despite failing to reject the null hypothesis of CSR of the point pattern, might be attributed to the simple structure of the lattice pattern. The phase and coherency spectra are provided in Figures C.8(e) and (f), respectively. The profile in Figure C.9 reveals that there is no concentration of coherency. Thus Tosso Passa is not (highly) correlated with altitude data.

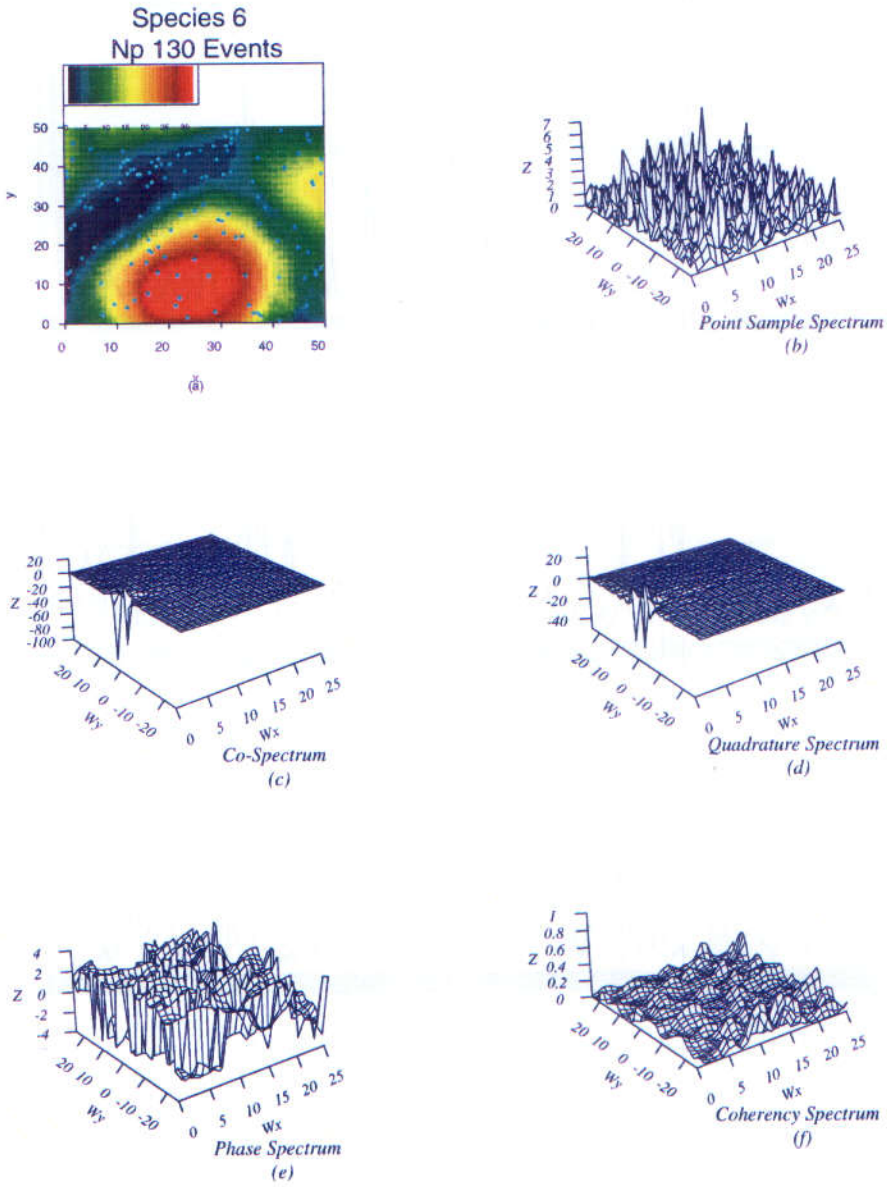

Figure C.8: (a) Tosso Passa versus altitude pattern; (b) raw auto-periodogram of the point pattern; (c) and (d) raw co- and quadrature spectra; (e) and (f) smoothed phase and coherency spectra using Method A four times.

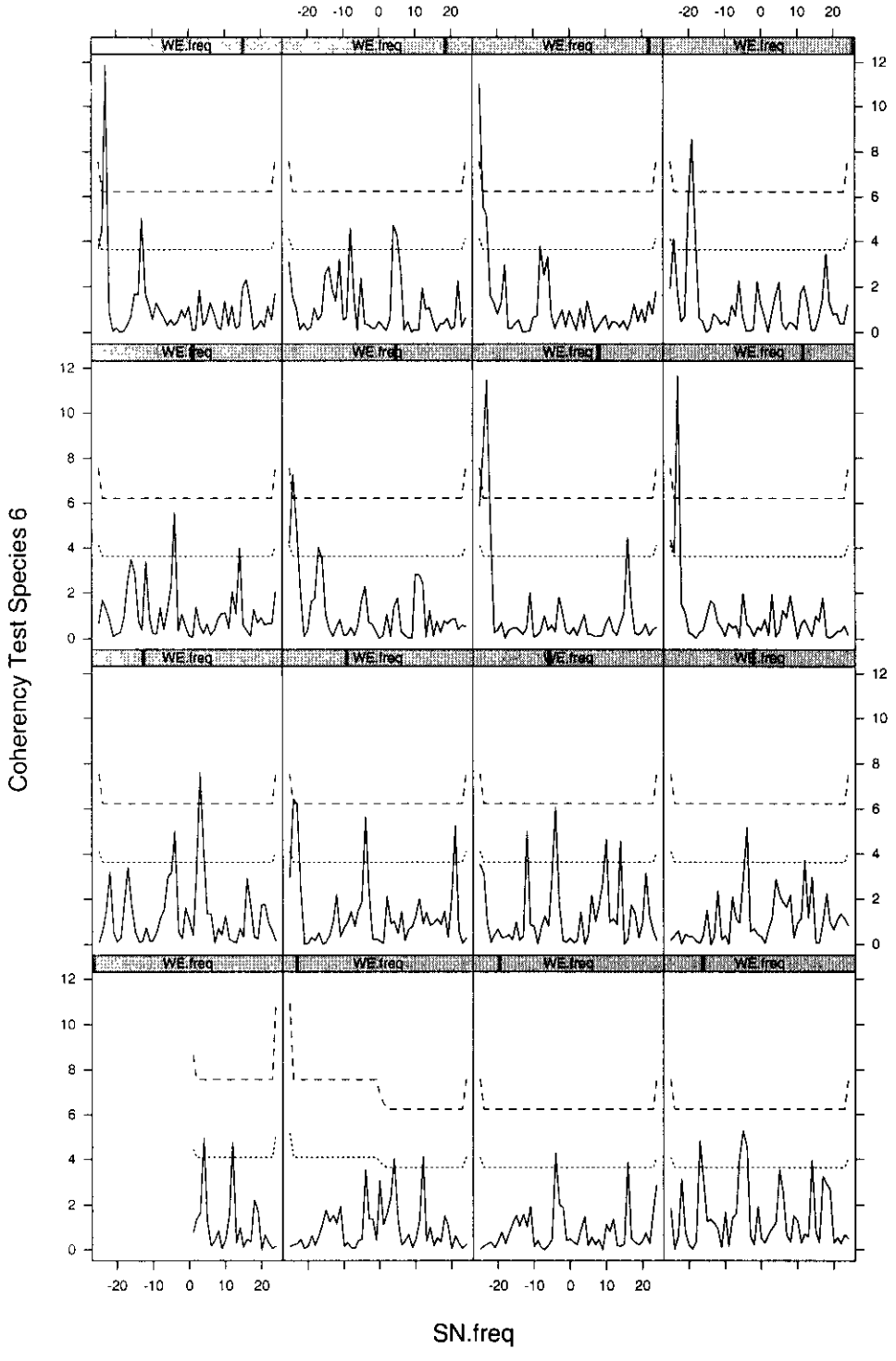

Figure C.9: Profile of the zero coherency test statistic spectrum for (Tosso Passa) versus altitude pattern for $p = 0, \ldots, 15$.

C.5 Species 7: Boco

Figure C.10(a) gives the locations of Boco superimposed on altitude values. Figure C.10(b) represents the auto-periodogram of the point pattern. This periodogram exhibits peaks at $(1, -1)$ and $(9, -13)$. The peak at $(1, -1)$ is significant at the 1% level.

The co-spectrum has peaks at $(1, -1)$, $(1, 1)$ and $(0, 1)$, see Figure C.10(c). Figure C.10(d) represents the quadrature spectrum which exhibits a trough at $(0, 1)$ and two peaks at $(1, -1)$ and $(1, 0)$.

The phase and coherency spectra are presented in Figures C.10(e) and (f), respectively. Concentration of non-zero coherency, around relatively low frequencies, is observed along the frequency band $(p = 2, q = \{-2, \ldots, 2\})$, see Figure C.11. The slope of the adjusted phase spectra in the SN direction for this frequency band is 0.52.

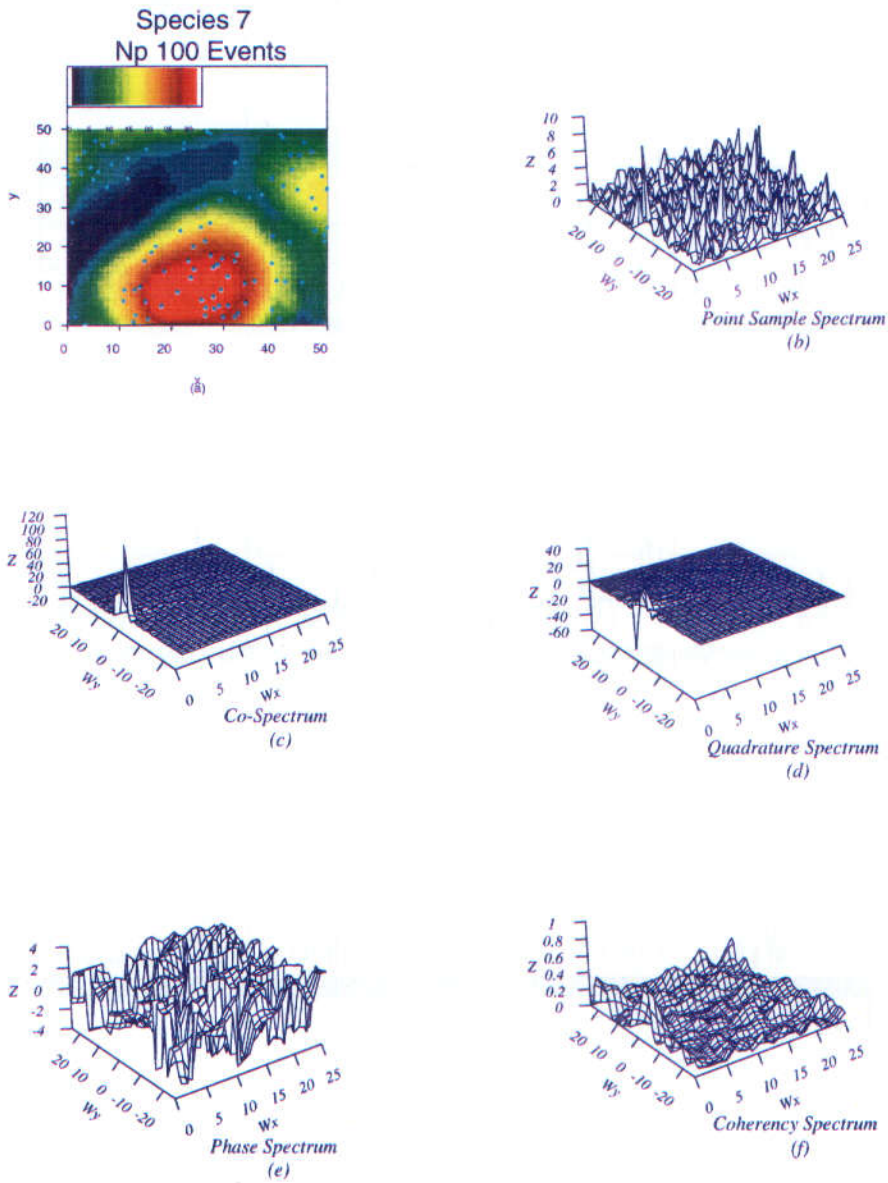

Figure C.10: (a) Boco versus altitude pattern; (b) raw auto-periodogram of the point pattern; (c) and (d) raw co- and quadrature spectra; (e) and (f) smoothed phase and coherency spectra using Method A four times.

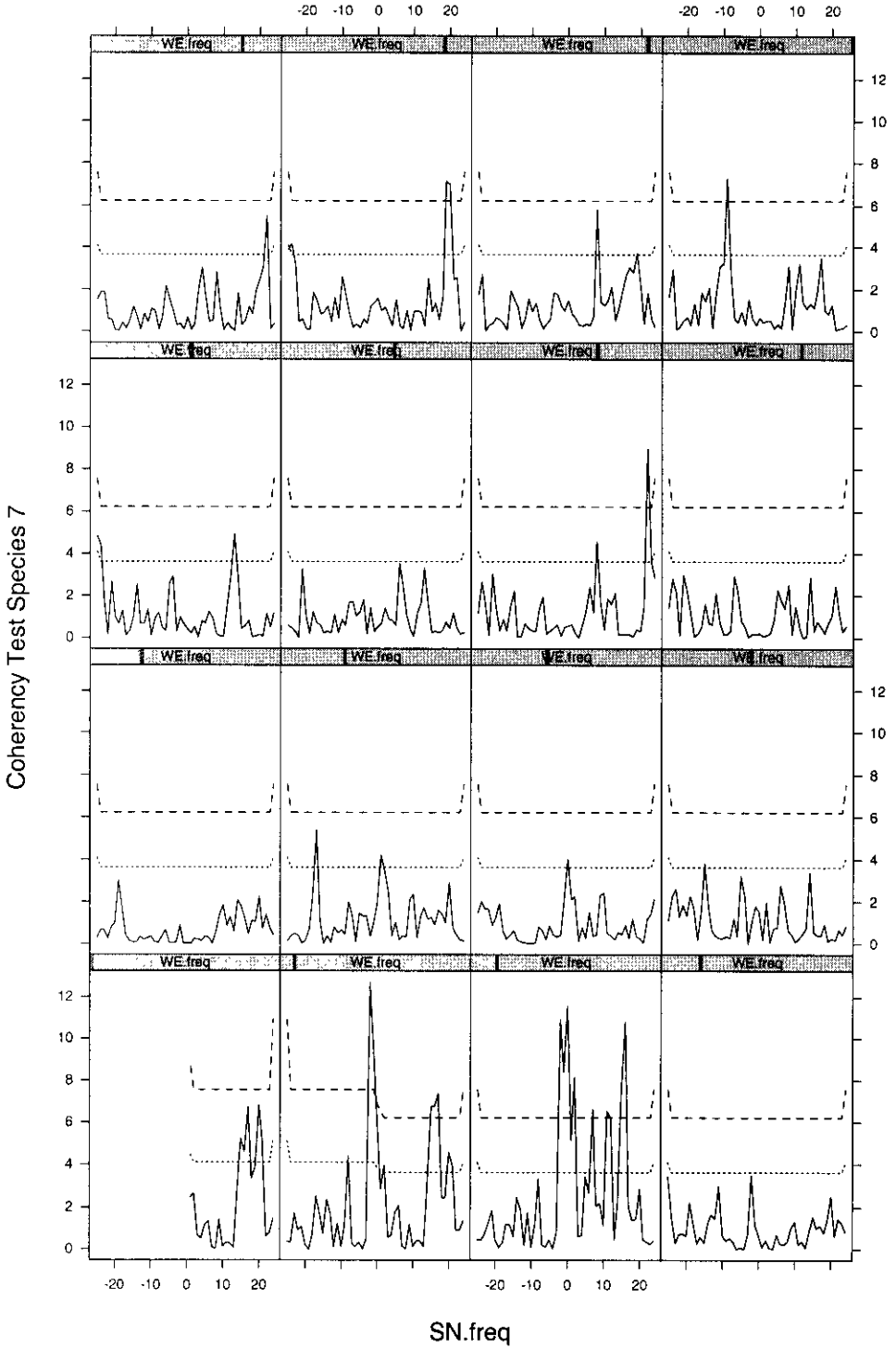

Figure C.11: Profile of the zero coherency test statistic spectrum for Boco versus altitude pattern for $p = 0, \ldots, 15$.

C.6 Species 8: Manil Marecage

The pattern of the locations of Manil Marecage superimposed on altitude is presented in Figure C.12(a). Figure C.12(b) is the auto-periodogram for the point pattern. The peak at $(1, 0)$ is the only significant low frequency at the 5% level.

Figure C.12(c) represents the co-spectrum which possesses troughs at $(1, 0)$ and $(0, -1)$. The quadrature spectrum, Figure C.12(d), exhibits a major peak at $(0, 1)$ and two other minor peaks at $(1, -1)$ and $(1, 1)$. The graphs of the phase and coherency spectra are given in Figures C.12(e) and (f), respectively. The profile of the zero coherency test in Figure C.13 indicates that the correlation detected above is not strong.

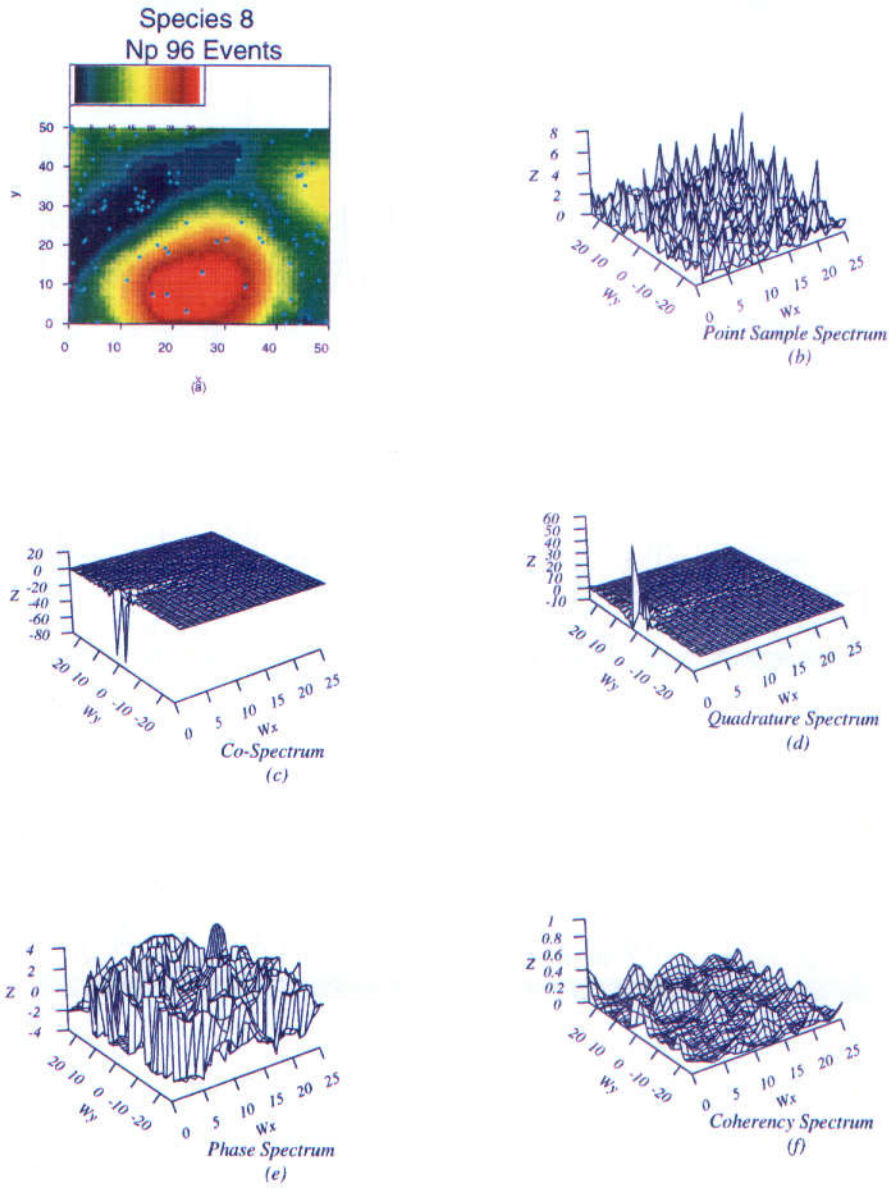

Figure C.12: (a) Manil Marecage versus altitude pattern; (b) raw auto-periodogram of the point pattern; (c) and (d) raw co- and quadrature spectra; (e) and (f) smoothed phase and coherency spectra using Method A four times.

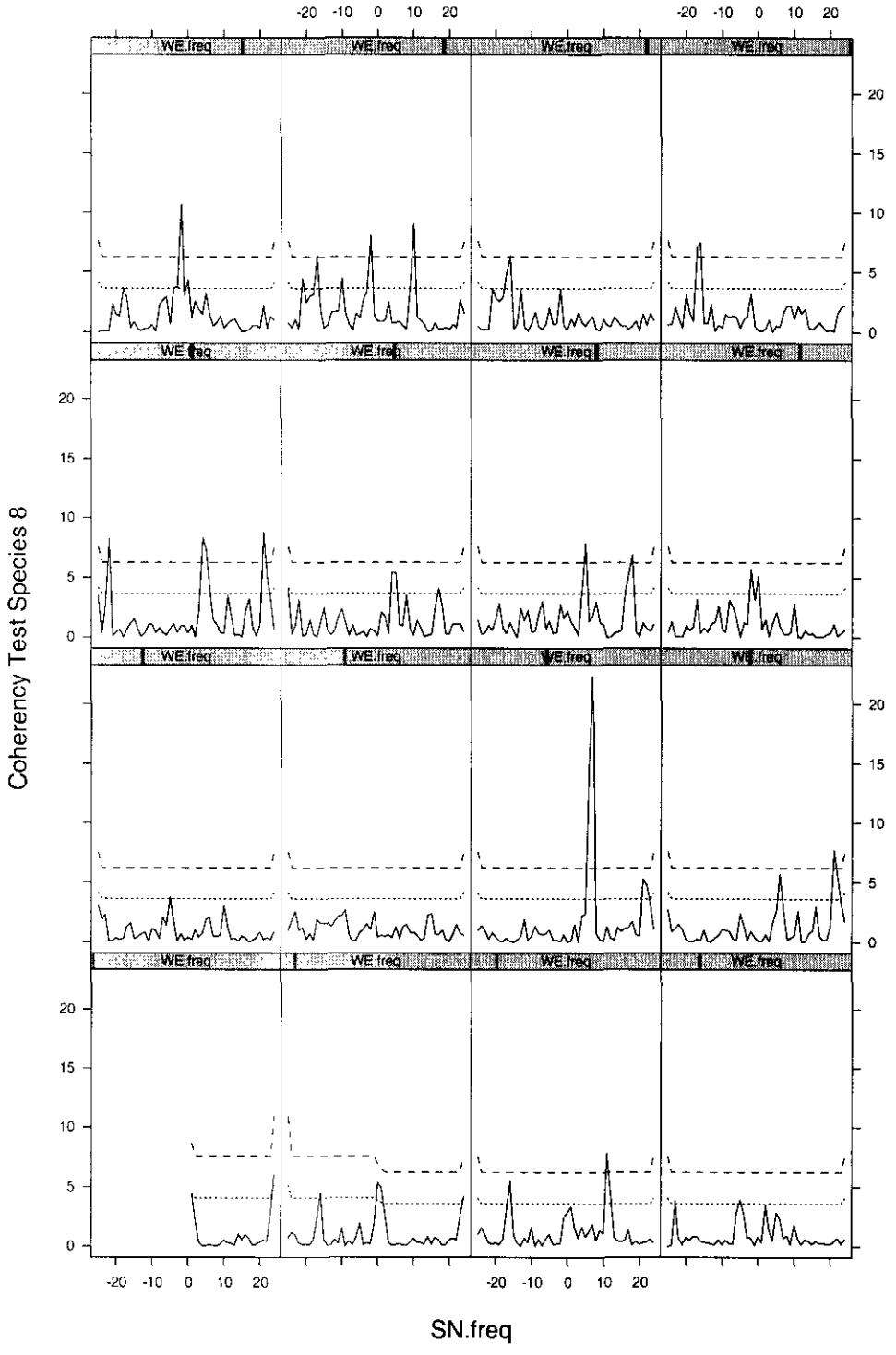

Figure C.13: Profile of the zero coherency test statistic spectrum for Manil Marecage versus altitude pattern for $p = 0, \ldots, 15$.

C.7 Species 9: Gonfolo Rose

Gonfolo Rose versus altitude pattern is provided in Figure C.14(a). The auto-periodogram for the point pattern, Figure C.14(b), exhibits peaks at $(1,1)$ and $(13,23)$. The former peak is significant at the 1% level. The significance of the latter peak cannot be assessed since the number of events in the point pattern 84 implies that we can only investigate the frequency band $(p = \{0,\ldots,4\}, q = \{-4,\ldots,3\})$.

Figure C.14 (c) is the co-spectrum of the point-lattice pattern. It possesses peaks at $(0,1)$, $(1,1)$ and $(1,0)$. The quadrature spectrum, Figure C.14(d), has a peak at $(0,1)$ and troughs at $(1,0)$, $(1,-1)$ and $(1,1)$. The spectra of phase and coherency are presented in Figures C.14(e) and (f), respectively. Figure C.15 represents the profile of the zero coherency test. Note that at the 5% significance level coherency is concentrated around the frequencies $(p = 2, q = \{-1,0,1\})$ in the SN direction and $(p = \{2,3\}, q = -1)$ in the WE direction. Calculating the slope of the adjusted phase spectrum in the SN direction for the frequency band $(p = 2, q = \{-1,0,1\})$ yields -1.52. The slope in the WE direction for the frequency band $(p = \{2,3\}, q = -1)$ is 0.12.

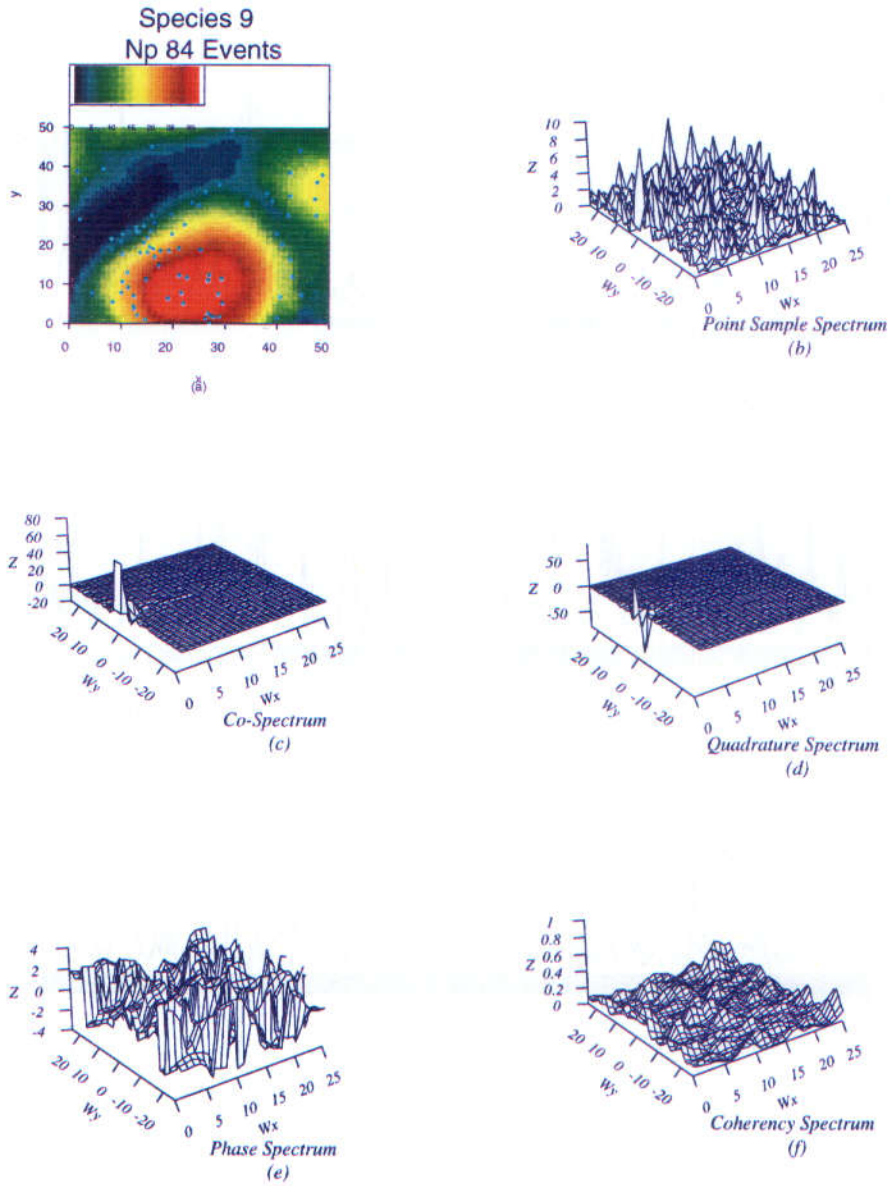

Figure C.14: (a) Gonfolo Rose versus altitude pattern; (b) raw auto-periodogram of the point pattern; (c) and (d) raw co- and quadrature spectra; (e) and (f) smoothed phase and coherency spectra using Method A four times.

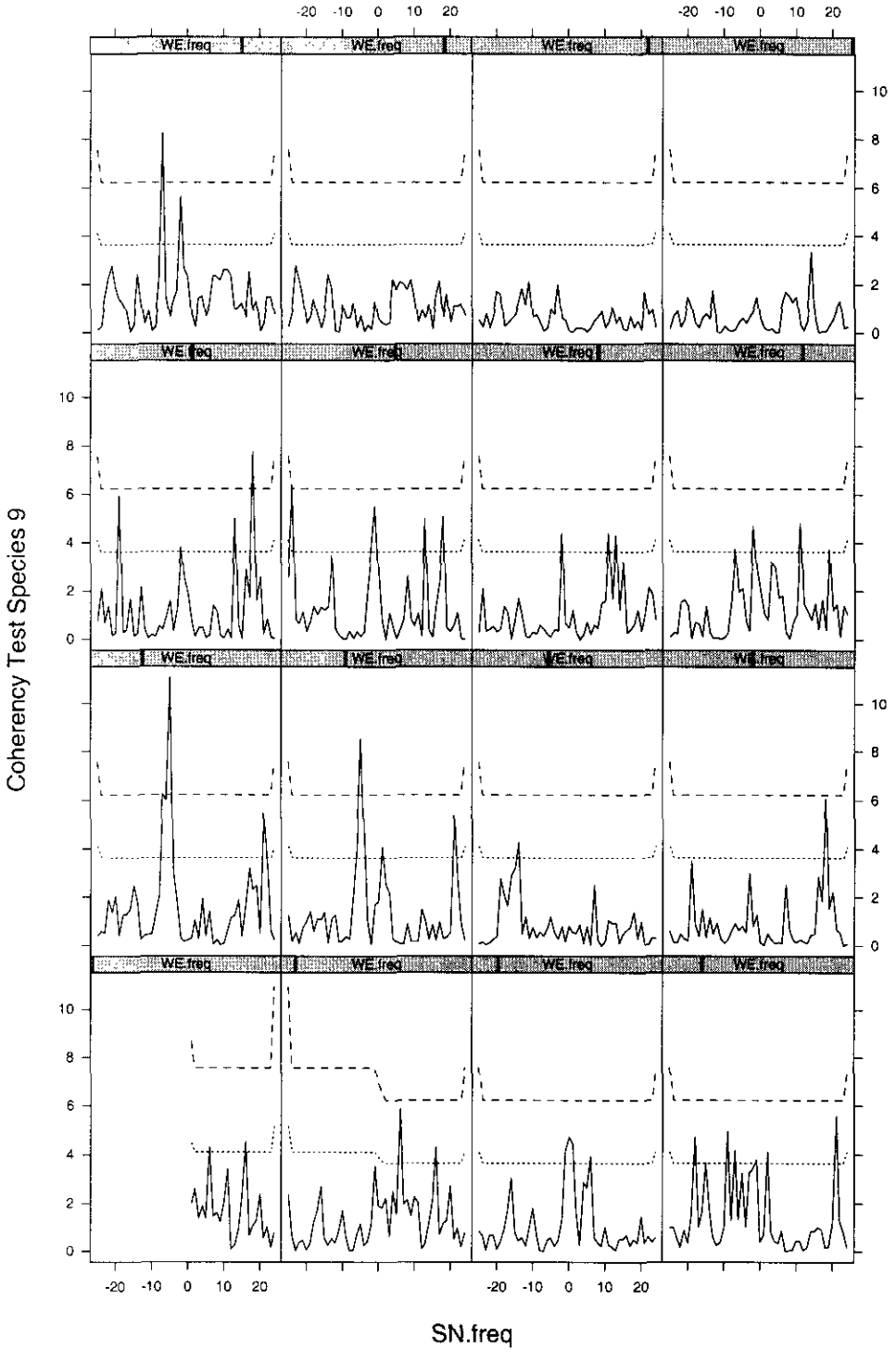

Figure C.15: Profile of the zero coherency test statistic spectrum for Gonfolo Rose versus altitude pattern for $p = 0, \ldots, 15$.

C.8 Species 13: Cedres

The locations of the point pattern formed by the Cedres are presented in Figure C.16(a). The auto-periodogram for the point pattern, Figure C.16(b), has a major peak at $(1, 1)$. This peak is significant at the 1% level, moreover the frequency $(3, 0)$ is significant at the 5% level. Peaks are detected at $(1, 1)$ and $(0, 1)$ in the co-spectrum, Figure C.16(c). The quadrature spectrum, Figure C.16(d), exhibits a major trough at $(1, -1)$ and two minor troughs at $(1, 0)$ and $(0, 1)$.

The graphs of phase and coherency spectra are provided in Figures C.16(e) and (f), respectively. Figure C.17, the profile of the zero coherency test for this species versus altitude pattern, indicates that the coherency is different from zero for couple of sparse low frequencies.

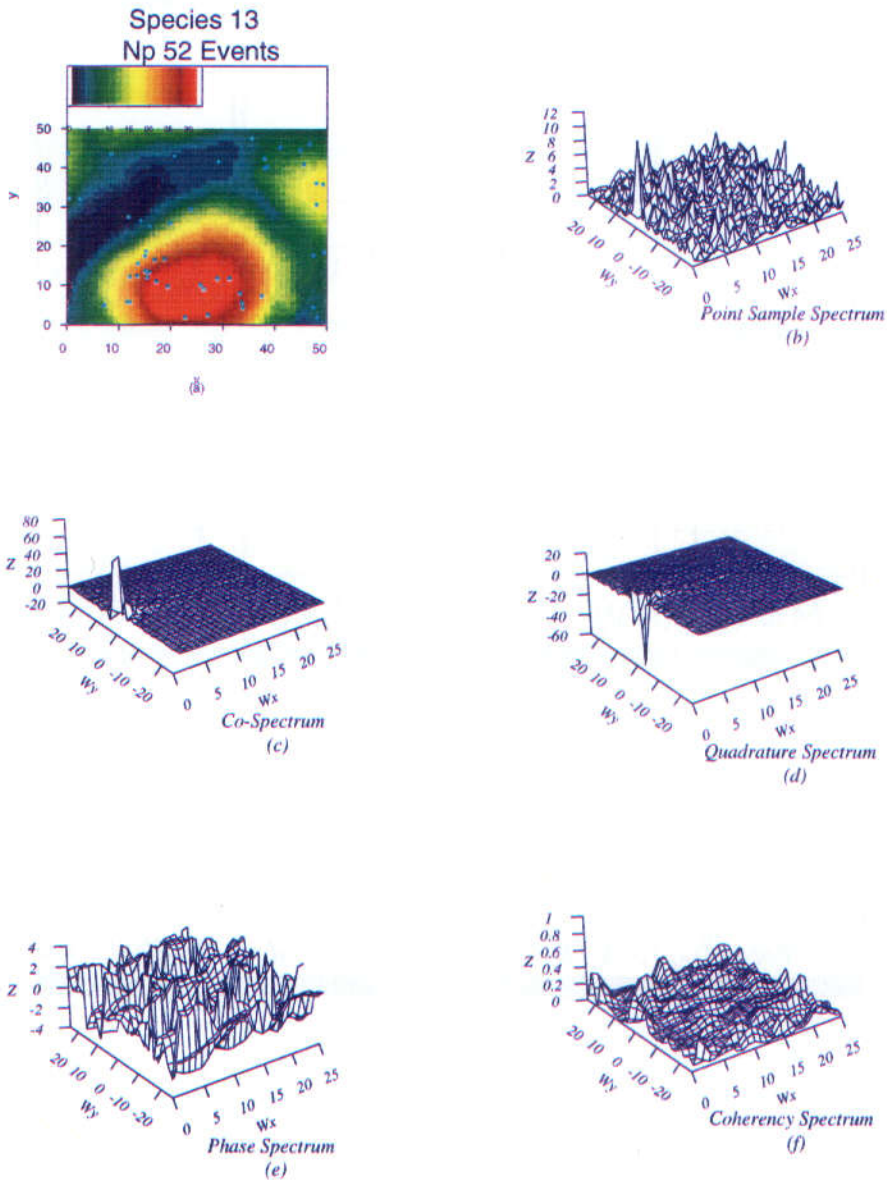

Figure C.16: (a) Cedres versus altitude pattern; (b) raw auto-periodogram of the point pattern; (c) and (d) raw co- and quadrature spectra; (e) and (f) smoothed phase and coherency spectra using Method A four times.

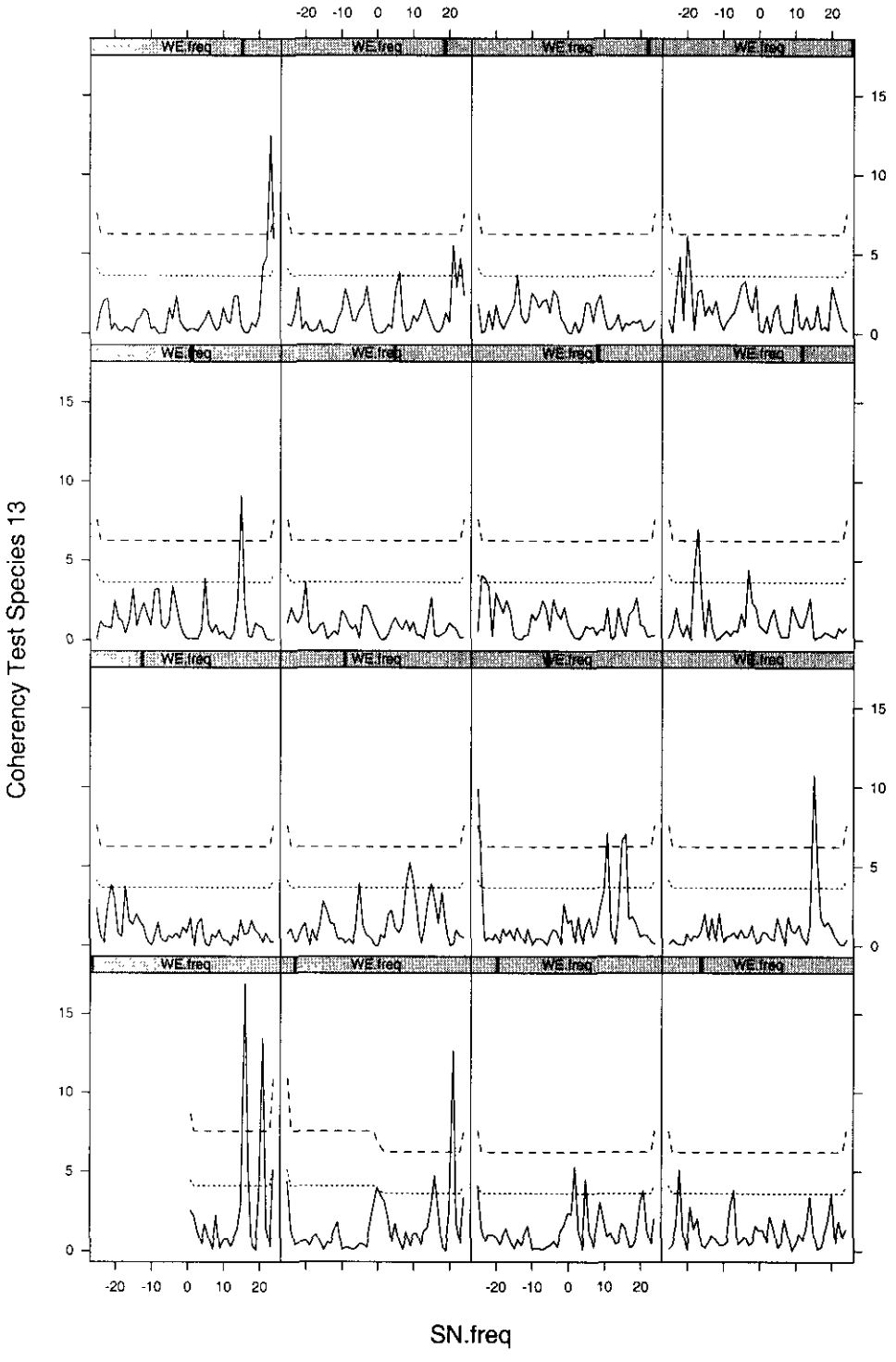

Figure C.17: Profile of the zero coherency test statistic spectrum for Cedres versus altitude pattern for $p = 0, \ldots, 15$.

C.9 Species 14: Angelique

The locations of Angelique are presented in Figure C.18(a). Figure C.18(b) gives the graph of the auto-periodogram of the point pattern. Peaks are detected at $(1,-2),(2,0),(1,2),(0,1)$ and $(0,2)$. The first two of these peaks are significant at the 1% level and the fourth at the 5% level.

The co-spectrum, Figure C.18(c), has peaks at $(1,0),(0,1)$ and a trough at $(0,2)$. The quadrature spectrum, Figure C.18(d), has a major trough at $(0,1)$ and a minor peak at $(1,0)$.

The phase and coherency spectra are presented in Figures C.18(f) and (f), respectively. Concentration of coherency is detected along the frequencies $(p = \{1,2\}, q = \{-10,\ldots,-3\})$ and $(p = \{0,1,2\}, q = 3)$, see Figure C.19. The slope of the adjusted phase spectrum in the WE direction for the frequency band with $q = 3$ is 0.25, and the slopes of the adjusted phase spectrum in the SN direction for the frequency bands with $p = 1,2$ are 0.11 and 0.27, respectively.

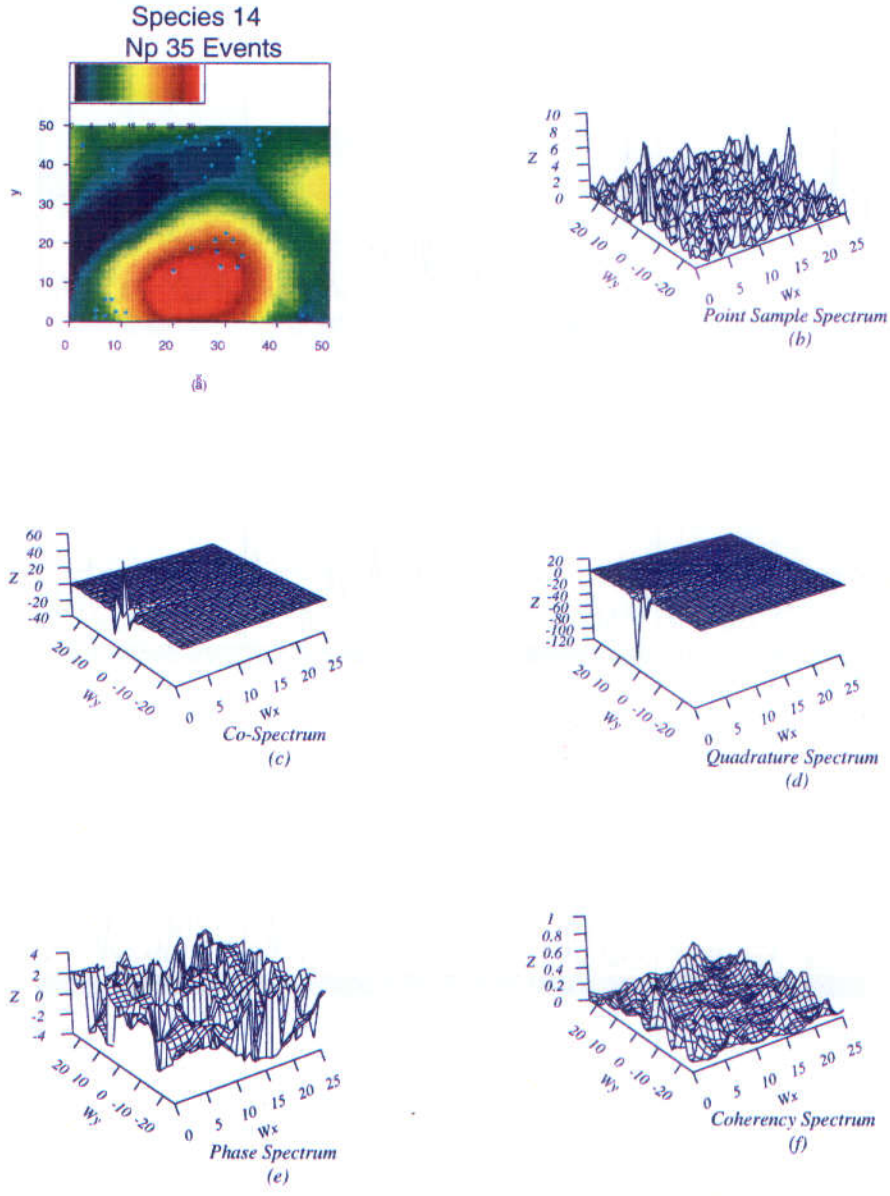

Figure C.18: (a) Angelique versus altitude pattern; (b) raw auto-periodogram of the point pattern; (c) and (d) raw co- and quadrature spectra; (e) and (f) smoothed phase and coherency spectra using Method A four times.

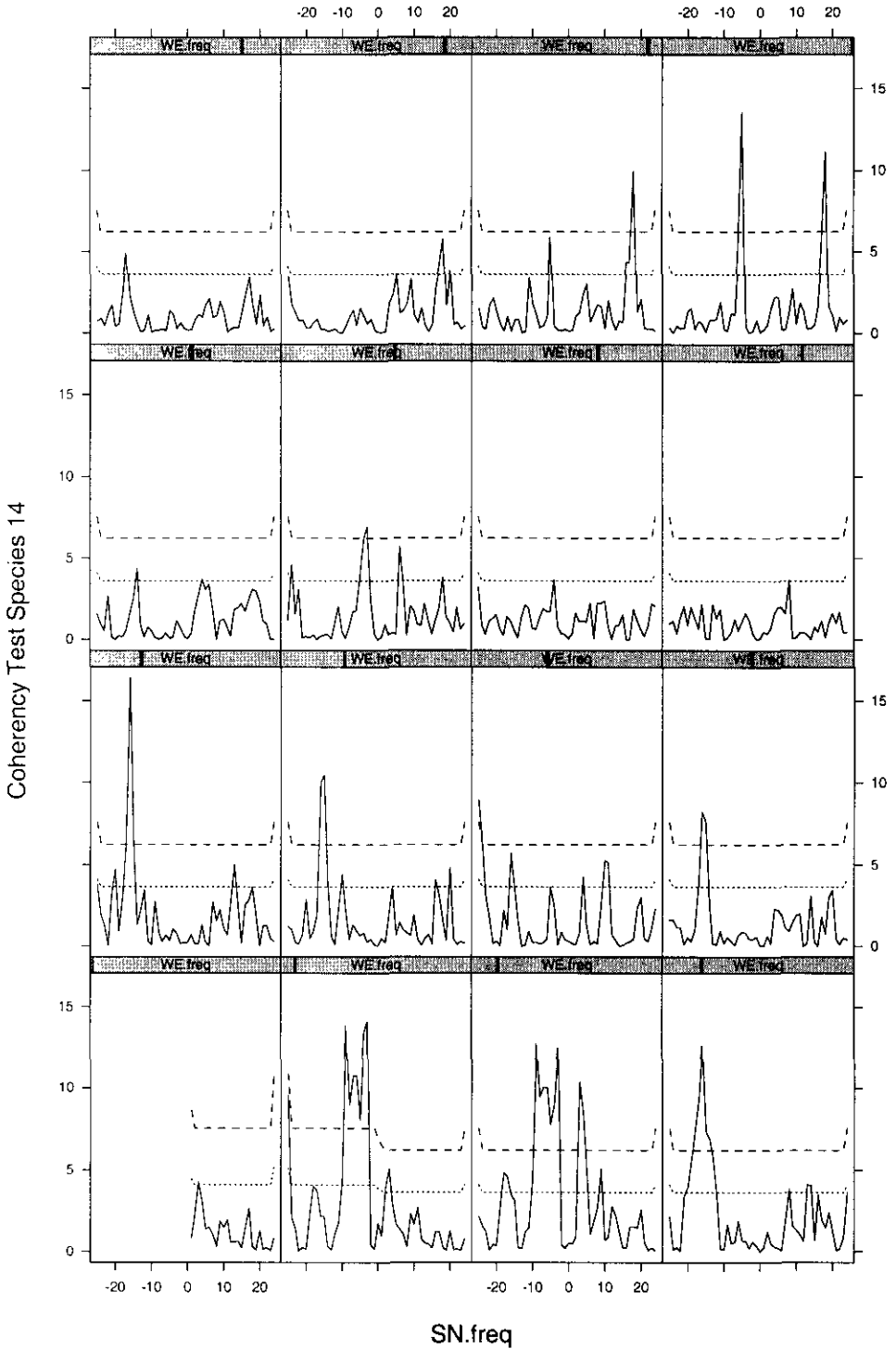

Figure C.19: Profile of the zero coherency test statistic spectrum for Angelique versus altitude pattern for $p = 0, \ldots, 15$.

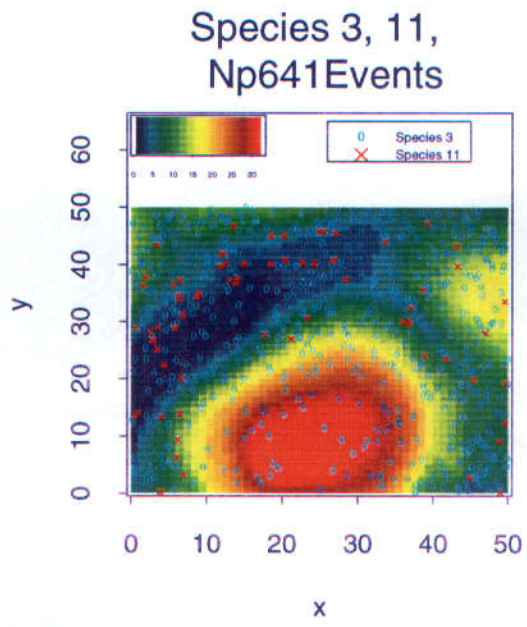

Figure C.20: The joint pattern of Species 3 and 11 together with altitude.

C.10 Species 3 and 11: *Lecythidaceae*

In this section, Species 3 and 11 from the *Lecythidaceae* family are joined to form one species, and the cross-spectral analysis of the resulting point-lattice pattern is investigated. The joint pattern for the tree species and the altitude data is presented in Figure C.20.

The auto-periodogram for the joint point pattern is presented in Figure C.21(a). The peaks in this periodogram are detected at $(0, 1)$ and $(1, 0)$. The co-spectrum, Figure C.21(b), exhibits major troughs at $(0, 1)$ and $(1, -1)$. The quadrature spectrum, Figure C.21(c), exhibits a trough at $(0, 1)$, and a peak at $(1, 0)$. The phase and coherency spectra are presented in Figures C.21(d) and (e), respectively.

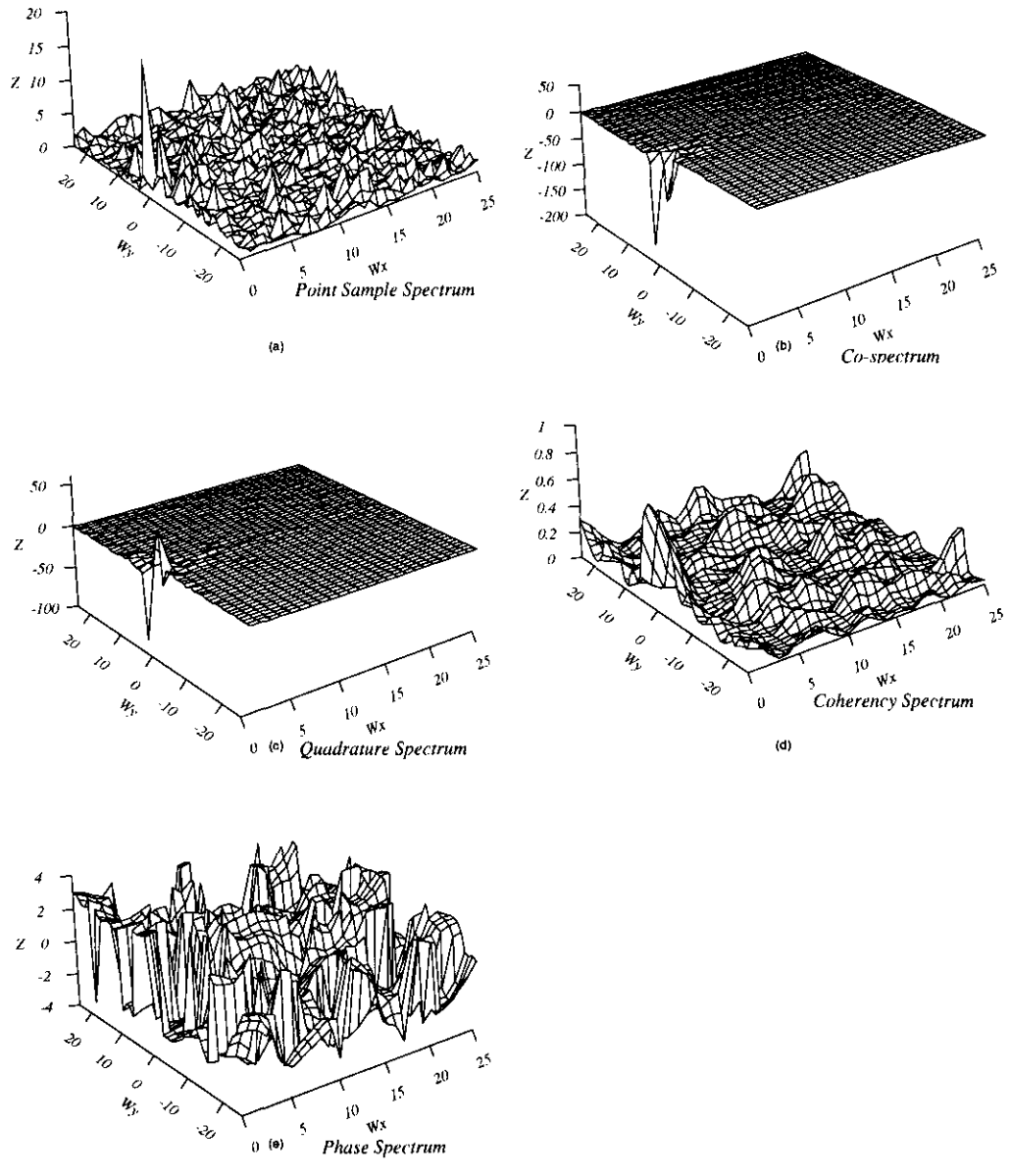

Figure C.21: (a) raw auto-periodogram of the point pattern of the joint pattern for Species 3 and 11, (b) and (c) raw co- and quadrature spectra; (d) and (e) smoothed phase and coherency spectra using method A four times.

The profile of the zero coherency test statistic, Figure C.22, indicates that there is concentration of significant ordinates at the 1% level at the frequencies $(p = 0, q = \{1, 2, 3\})$, $(p = 1, q = \{-1, \ldots, 3\})$ and $(p = 2, q = \{-1, \ldots, 2\})$. Figures C.23(a) and (b) represent the profiles of the adjusted phase spectra in the WE direction and SN direction for the previously mentioned frequencies, respectively. The slopes in the WE direction for $q = -1, \ldots, 3$ are 0.29, 0.92, 1.61, 1.58 and 1.14, respectively. The slopes in the SN direction for $p = 0, 1, 2$ are -0.53, -0.9 and -0.37, respectively.

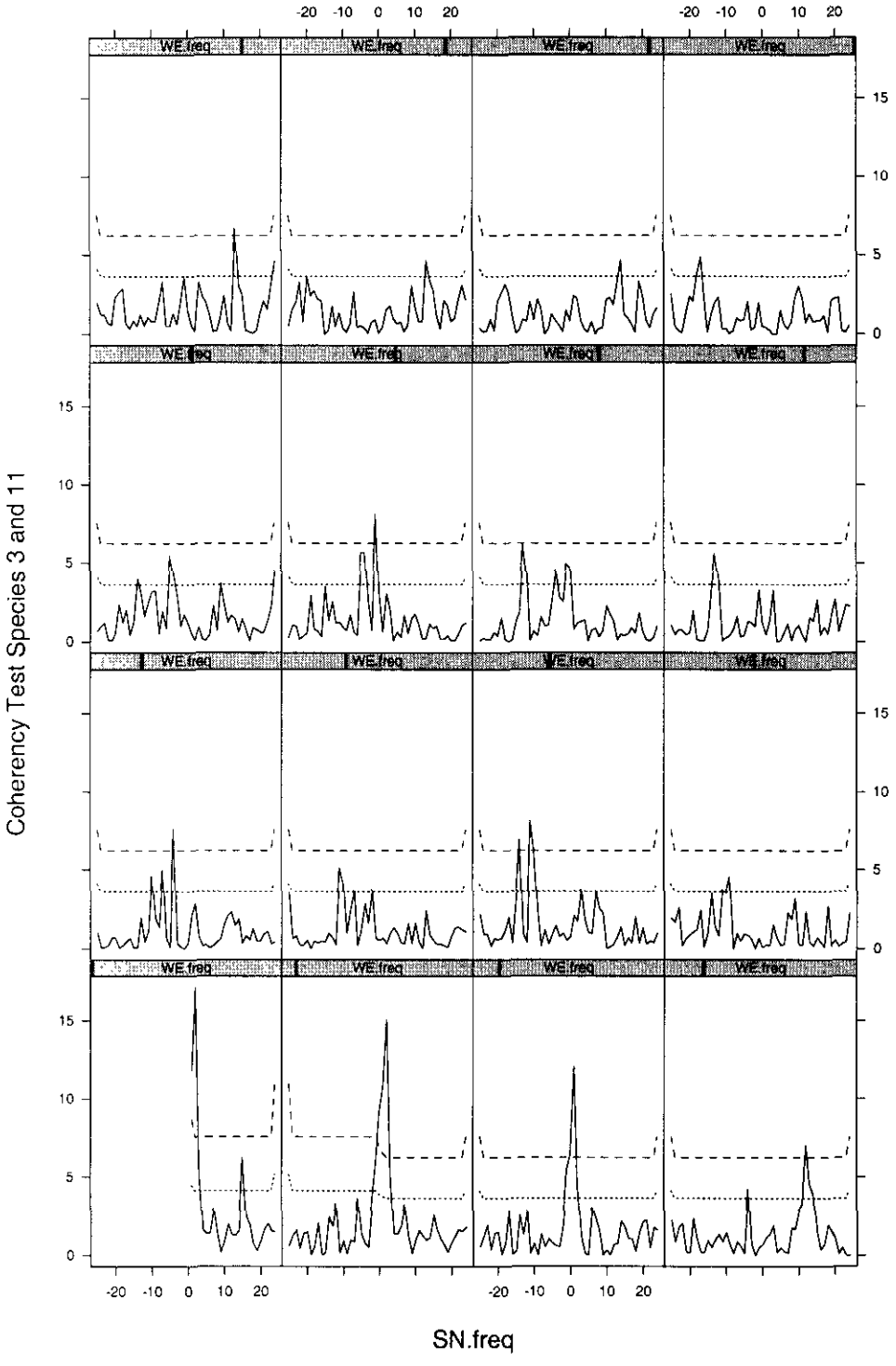

Figure C.22: Profile of the zero coherency test statistic spectrum for Species 3 and 11 versus altitude pattern for $p = 0, \ldots, 15$.

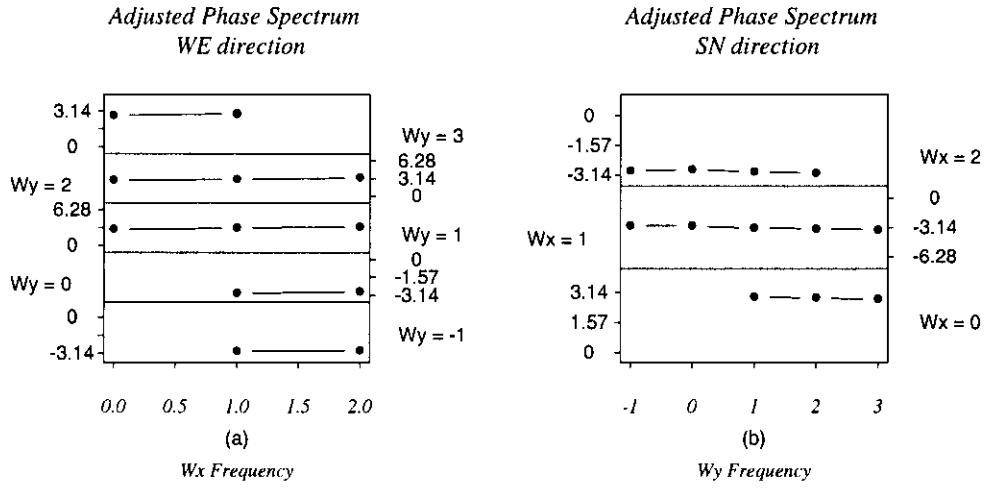

Figure C.23: (a) and (b) Profile of the adjusted phase spectrum for Species 3 and 11 versus altitude pattern in the WE and SN directions for the frequencies $p = 0, 1, 2$, and $q = -1, \ldots, 3$.

C.11 Species 10 and 14: *Leguminosae-Caesalpineaceae*

Figure C.24 represents the point pattern formed by Species 10 and 14 together with altitude data. The sample point pattern is presented in Figure C.25(a). Peaks are detected at $(0, 1)$, $(1, -1)$ and $(1, 0)$.

The co-spectrum, Figure C.25(b), also exhibits peaks at the above frequencies. The quadrature spectrum, Figure C.25(c), exhibits a major trough at $(1, -1)$ and a peak at $(0, 1)$. Figures C.25(d) and (e) represent the phase and coherency spectra. Figure C.26 represents the profile of the zero coherency test statistic. It indicates that coherency is concentrated around

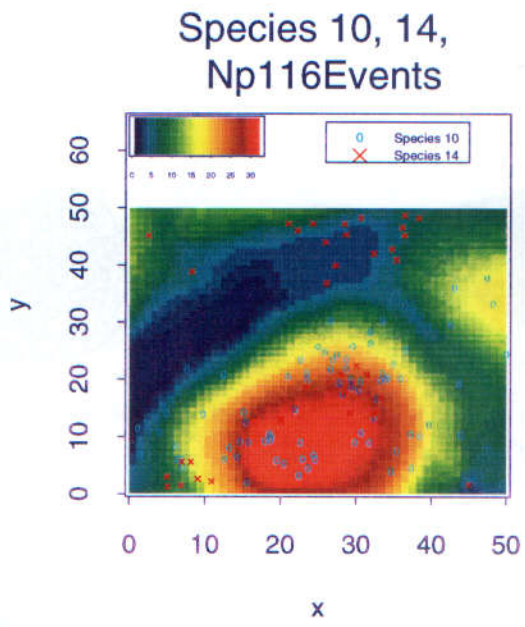

Figure C.24: The joint pattern for Species 10 and 14, in addition to altitude.

the frequencies $(p = 1, q = \{-5, \ldots, 2\})$ and $(p = 2, q = \{-4, \ldots, 0\})$. The slopes of the adjusted phase spectrum in the SN direction for $p = 1, 2$ are -3.1 and -4.3, respectively.

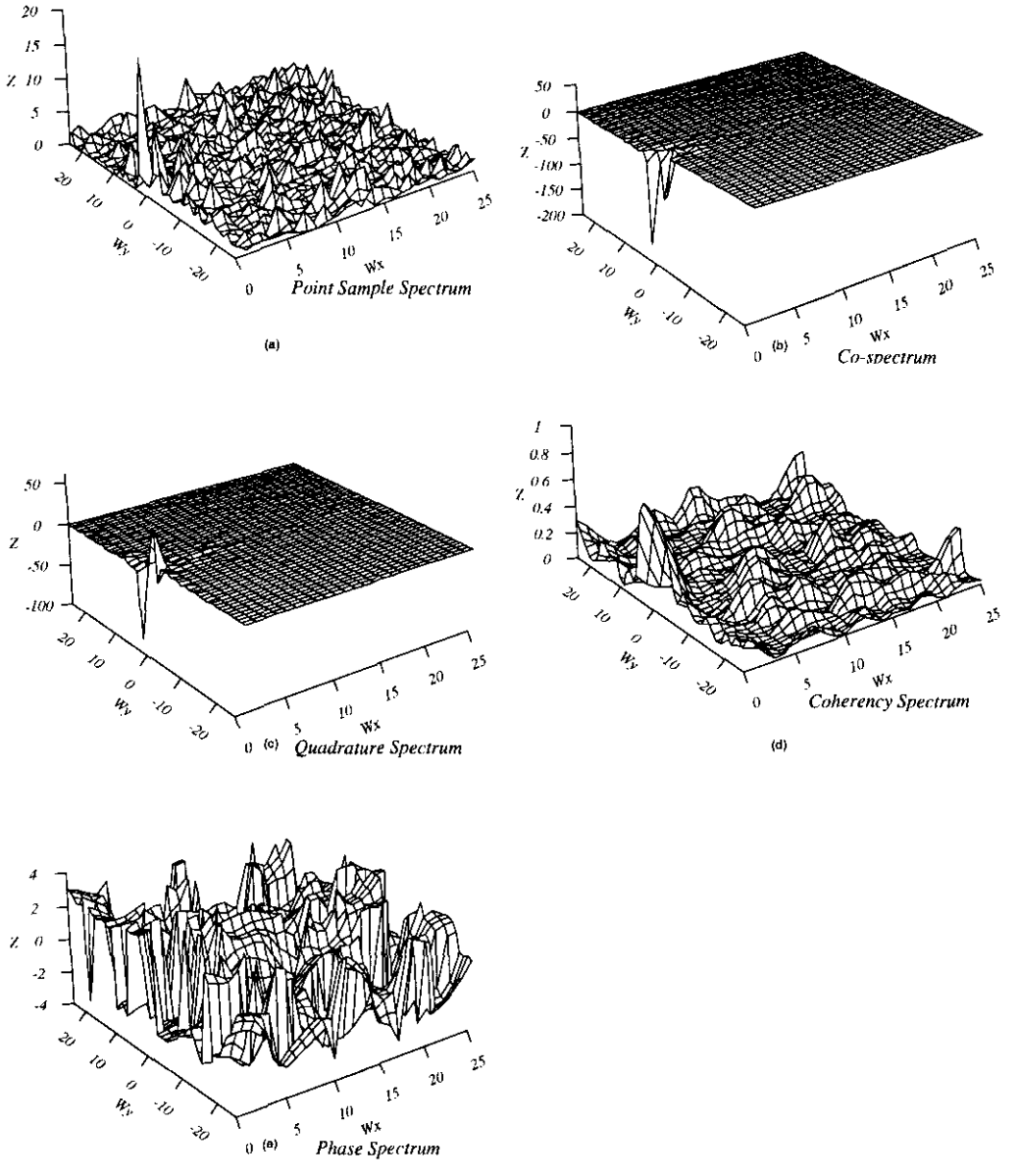

Figure C.25: (a) raw auto-periodogram of the point pattern of the joint pattern for Species 10 and 14; (b) and (c) raw co- and quadrature spectra; (d) and (e) smoothed phase and coherency spectra using Method A four times.

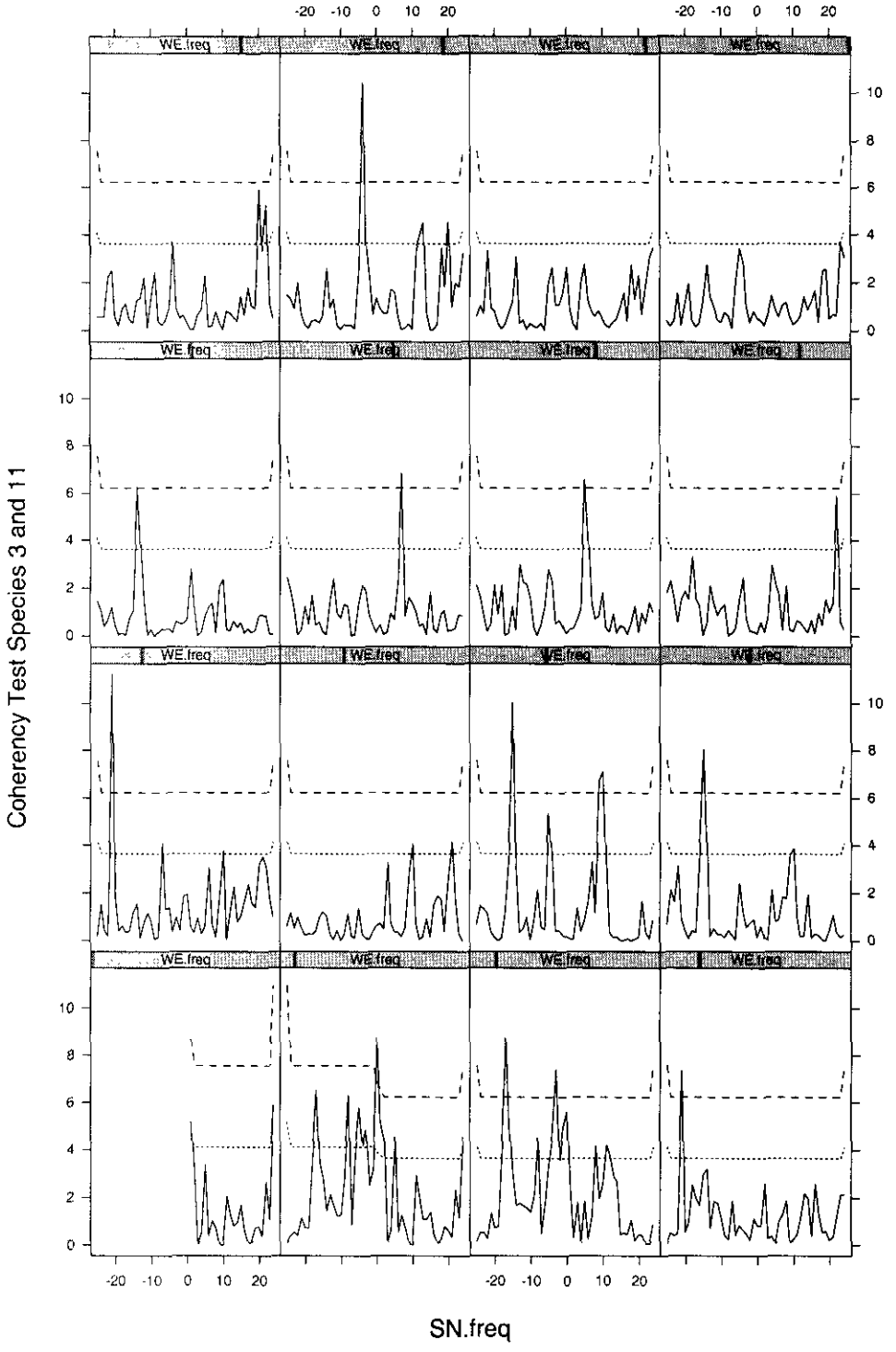

Figure C.26: Profile of the zero coherency test statistic spectrum for Species 10 and 14 versus altitude pattern for $p = 0, \ldots, 15$.

Bibliography

Augustin, N. H., Mugglestone, M. A. and Buckland, S. T. (1996). An Autologistic model for the Spatial Distribution of Wildlife. *Journal of Applied Ecology*, vol. 33, pp. 339-347.

Bartlett, M. S. (1963). The Spectral Analysis of Point Processes. *Journal of the Royal Statistical Society*, Series B, vol. 25, no. 2, pp. 264-296.

Bartlett, M. S. (1964). The Spectral Analysis of Two-Dimensional Point Processes. *Biometrika*, vol. 51, no. 3 and 4, pp. 299-311.

Bartlett, M. S. (1967). The Spectral Analysis of Line Processes. *Proceedings of the fifth Berkeley Symposium on Mathematical Statistics and Probability*, vol. 3, pp. 135-153.

Bartlett, M. S. (1975). *The Statistical Analysis of Spatial Pattern.* Chapman and Hall.

Bartlett, M. S. (1978). *An Introduction to Stochastic Processes: With Special Reference to Methods and Applications.* Cambridge University Press, third edition.

Berman, M., Bischof, L.M., Davies, S. J., Greeen, A. A., and Craig, M.(1994). Estimating Band-to-band Misregistrations in Aliased Imagery. *CVGIP: Graphical Models and Image Processing*, vol. 56, pp. 479-493.

Brigham, E. O. (1988). *The Fast Fourier Transform and Its Applications.* Prentince-Hall International.

Brillinger, D. R. (1969). Asymptotic Properties of Spectral Estimates of Second Order. *Biometrika*, vol. 56, no. 2, pp. 375-390.

Brillinger, D. R. (1970). The Frequency Analysis of Relations Between Stationary Spatial Series. *In: Proceedings of the Twelfth Biennial Seminar of the Canadian Mathematical Congress on Time Series and Stochastic Processes; Convexity and Combinatorics*, Edited by Ronald Pyke, Canadian Mathematical Congress, Montreal, Canada, pp. 39-81.

Brillinger, D. R. (1972). The Spectral Analysis of Stationary Interval Functions. *In: Proceedings of the Sixth Berkeley Symposium on Mathematical Statistics and Probability*, vol. 1, pp. 483-513.

Brillinger, D. R. (1976). Estimation of the Second–Order Intensities of a Bivariate Stationary Point Process. *Journal of the Royal Statistical Society*, Series B, vol. 38, pp. 60-66.

Brillinger, D. R. (1981). *Time Series: Data Analysis and Theory.* Expanded Edition, Holden-Day Series in Time Series Analysis.

Brillinger, D. R. (1983). The Finite Fourier Transform of a Stationary Process. *Handbook of Statistics*, vol. 3, Time Series in the Frequency Do-

main, editors Brillinger, D. R. and Krishnaiah, P. R.; Elsevier Science Publishers B. V., Amsterdam, pp. 21-37.

Brillinger, D. R. (1994). Time Series, Point Processes and Hybrids. *Canadian Journal of Statistics*, vol. 22, no. 2, pp. 177-206.

Brillinger, D. R. and Rosenblatt, M. (1967). Asymptotic Theory of Estimates of k-Th Order Spectra. *In: Spectral Analysis of Time Series*, edited by Harris, B.; J. Wiley, New York, pp. 153-188.

Buckland, S. T. and Elston, D. A. (1993). Empirical Models for the Spatial Distribution of Wildlife. *Journal of Applied Ecology*, vol. 30, pp. 478-495.

Chan, Y. T., Hattin, R. V., and Plant, J. B. (1978). The Least Squares Estimation of Time Delay and Its Use in Signal Detection. *IEEE Transactions on Acoustics, Speech and Signal Processing*; vol. 26, no. 3, pp. 217-222.

Chatfield, C. (1989). *The Analysis of Time Series: an Introduction.* Chapman and Hall, fourth edition.

Cliff, A. D. and Ord, J. K. (1981). *Spatial Processes: Models and Applications.* Pion Limited.

Cox, D. R. and Lewis, P. A. W. (1968). *The Statistical Analysis of a Series of Events.* Methuen and Co, first published 1966.

Cressie, N. A. C. (1991). *Statistics for Spatial Data.* Wiley.

Dessard, H. (1996). Estimation de L'intensite Local d'un Processus Ponctuel de Cox: Application a L'analyse Spatiale d'un Inventaire Forestier. PhD thesis, Université de Montpellier II, France, Unpublished.

Dessard, H. and Goulard, M. (1998). Estimation of Relationships Between a Cox Point Process Intensity and a Random Field. Unpublished Working Paper, INRA and CIRAD-Forêt, France.

Diggle, P. J. (1983). *Statistical Analysis of Spatial Point Patterns.* Academic Press.

Diggle, P. J. (1985). A Kernel-Method For Smoothing Point Process Data. *Journal of the Royal Statistical Society*, Series C, vol. 34, no. 2, pp. 138-147.

Diggle, P. J. (1990). *Time Series a Biostatistical Introduction.* Oxford Science Publications.

Diggle, P. J., and Marron, J. S. (1988). Equivalence of Smoothing Parameter Selectors in Density and Intensity Estimation. *Journal of the American Statistical Association*, vol. 83, no. 403, pp. 793-800.

Diggle, P. J., and Milne, R. K. (1983). Bivariate Cox Processes: Some Models for Bivariate Spatial Point Patterns. *Journal of the Royal Statistical Society*, Series B, vol. 45, pp. 11-21.

Fisher, R. A. (1929). Tests of Significance in Harmonic Analysis. *Proceedings of the Royal Society*, Series A, vol. 125, pp. 54-59.

Fisher, N. I. and Lee, A. J. (1983). A Correlation Coefficient for Circular Data. *Biometrika*, vol. 70, no. 2, pp. 327-332.

Fisher, N. I. and Lee, A. J. (1992). Regression Models for an Angular Response. *Biometrics*, vol. 48, pp. 665-677.

Ford, E. D. and Renshaw, E. (1984). The Interpretation of Process from Pattern Using Two-Dimensional Spectral Analysis: Modelling Single Species Patterns in Vegetation. *Vegetatio*, vol. 56, pp. 113-123.

Forget, P. M. , Mercire, F. and Collinet, F. (1999). Spatial Patterns of Two Rodent-Dispersed Rainforest Trees Carapa Procera (Meliaceae) and Voucapoua Americana (Caesalpiniaceae) in French Guiana. *Journal of Tropical Ecology*, vol. 15, no. 3, pp. 301-314.

Glasbey, C.A. and Horgan, G. W. (1995). *Image Analysis for the Biological Sciences*. Wiley.

Glasbey, C. A. and Mardia, K. V. (2000). A Statistical Approach to Image Warping. *Journal of the Royal Statistical Society, series B*. (submitted)

Goodman, N. R. (1963). Statistical Analysis Based on a Certain Multivariate Complex Gaussian Distribution (An Introduction). *Annals of Mathematical Statisitcs*, vol. 34, pp. 152-177.

Goulard, M., Pagès, L. and Cabanettes, A. (1995). Marked Point Process: Using Correlation Functions to Explore a Spatial Data Set. *Biometrical Journal*, vol. 37, pp. 837-853.

Gould, A. L. (1969). A regression model for angular variates. *Biometrics*, vol. 25, pp. 683-670.

Grenander, U. and Rosenblatt, M. (1957). Some Problems in Estimating the Spectrum of Time Series. *Proceedings of the 3rd Berkeley Symposium on Statistics and Probability*, University of California Press, Berkeley.

Haile, M. (1994). Observation of Convective Storms Over the Sahelian Zone. PhD Thesis, University of Reading, UK, Unpublished.

Hammond, D. S., Gourlet-Fleury S., van der Hout, P., ter Steege, H., Brown, V. K. (1996). A Compilation of Known Guianan Timber Trees and the Significance of Their Dispersal Mode, Seed Size and Taxonomic Affinity to Tropical Rain Forest Management. *Forest Ecology and Management*, vol. 83, pp. 99-116.

Hamon, B. V. and Hannan, E. J. (1974). Spectral Estimation of Time Delay for Dispersive and Non-dispersive Systems. *Applied Statistics*, vol. 23, no. 2, pp. 134-142.

Hannan, E. J. (1970). *Multiple Time Series*. John Wiley.

Hannan, E. J. and Thomson,P. J.(1988). Time Delay Estimation. *Journal of Time Series Analysis*, vol. 9, pp. 21-33.

Jenkins, G. M. and Donald, D. G. (1968). *Spectral Analysis and Its Applications*. Holden-Day.

Johnson, R. A. and Wehrly, T. E. (1978). Some Angular-Linear Distributions and Related Regression Models. *Journal of the American Statistical Association*, vol. 73, no. 363, pp. 602-606.

Kendall, M. G. and Stuart, A. (1963). *The Advanced Theory of Statistics: Distribution Theory*. Charles Griffin and Company, second edition, vol. 1.

Kuglin, C. D. and Hines, D. C. (1975). The Phase Correlation Image Alignment Method. In *Proceedings of the IEEE 1975 International Conference on Cybernetics and Society*, pp. 163-165.

Leonov, V. P. and Shiryaev, A. N. (1959). On a Method of Calculation of Semi-Invariants. *Theory of Probability and Its Applications*, vol. 4, no. 3, pp. 319-329.

Lewis, P. A. W. and Shelder,G. S. (1979). Simulation of Non-Homogenuous Poisson Processes by Thinning. *Naval Research Logisitcs Quarterly*, vol. 26, no. 3, pp. 403-413.

Mugglestone, M. A. (1990). Spectral Analysis of Spatial Processes. PhD Thesis, University of Edinburgh, UK, Unpublished.

Mugglestone, M. A. and Renshaw, E. (1996a). A Practical Guide to the Spectral Analysis of Spatial Point Processes. *Computational Statistics and Data Analysis*, vol. 21, pp. 43-65.

Mugglestone, M. A. and Renshaw, E. (1996b). The Exploratory Analysis of Bivariate Spatial Point Patterns Using Cross-Spectra. *Environmetrics*, vol. 7, pp. 361-377.

Mugglestone, M. A., and Renshaw, E. (2000). Spectral Tests of Randomness for Spatial Point Patterns. *Ecological and Environmental Statistics*, to appear.

Mugglestone, M. A. and Taylor, P. C. (1994). Investigating Spatial Patterns of Convective Storms in the Sahel Region of Africa: Tests for Random Labelling of Storm Initiation Sites Relative to Storm Duration. University of Reading, Department of Applied Statistics, Technical Report no. 94/10, Unpublished.

Nason, G. P., and Silverman, B. W. (1994). The Discrete Wavelet Transform in S. *Journal of Computational and Graphical Statistics*, vol. 3, pp. 163-191.

Ogata, Y. (1981). On Lewis' Simulation Method for Point Processes. *IEEE Transactions on Information Theory*, vol. IT-27, no. 1, pp. 23-31.

Penttinen, A., Stoyan, D., and Henttonen, H. M. (1992). Marked Point-Processes in Forest Statistics. *Forest Science*, vol. 38, no. 4, pp. 806-882.

Priestley, M. B. (1981a). *Spectral Analysis and Time Series Volume 1: Univariate Series.* Academic Press.

Priestley, M. B. (1981b). *Spectral Analysis and Time Series Volume 2: Multivariate Series, Prediction and Control.* Academic Press.

Rayner, J. N. (1971). *An Introduction to Spectral Analysis.* Pion.

Renshaw, E. (1999). Two-Dimensional Spectral Analysis for Marked Point-Processes. submitted for publication.

Renshaw, E. and Ford, E. D. (1983). The Interpretation of Process from Pattern Using Two-Dimensional Spectral Analysis: Methods and Problems of Interpretation. *Applied Statistics*, vol. 32, no. 1, pp. 51-63.

Rigas, A. G. (1983). Point Processes and Time Series Analysis: Theory and Applications to Complex Physiological Problems. PhD Thesis, University of Glasgow, UK, Unpublished.

Rigas, A. G. (1996). Estimation of Certain Parameters of a Stationary Hybrid Process Involving a Time Series and a Point Process. *Mathematical Biosciences*, vol. 133, pp. 197-218.

Ripley, B. D. (1981). *Spatial Statistics.* Wiley Series.

Robinson, P. M. (1983). Review of Various Approaches to Power Spectrum Estimation. *Handbook of Statistics*, vol. 3, Time Series in the Frequency Domain, editors Brillinger, D. R. and Krishnaiah, P. R.; Elsevier Science Publishers B. V., Amsterdam, pp. 343-366.

Upton, G. J. G. and Fingleton, B. (1995). *Spatial Data Analysis by Example vol. 1: Point Pattern and Quantitative Data.* Wiley, reprint.

Wand, M. P. (1994). Code for Bivariate Plug-in Bandwidth Selection. Australian Graduate School of Management, Unpublished.

Wand, M. P. and Jones, M. C. (1994). Multivariate Plug-in Bandwidth Selection. *Computational Statistics*, vol. 9, pp. 97-116.

Wand, M. P. and Jones, M. C. (1995). *Kernel Smoothing*. Chapman and Hall.

Whittle, P. (1952). The Simultaneous Estimation of a Time Series Harmonic Components and Covariance Structure. *Trabajos. Estadist.*, vol. 3, pp. 43-57.